

Visualisation and profiling of lipids in single biological cells using Time-of-Flight Secondary Ion Mass Spectrometry

**A thesis submitted to The University of Manchester
for the degree of Doctor of Philosophy
in the Faculty of Engineering and Physical Sciences**

2011

Hua Tian

School of Chemical Engineering and Analytical Science

Contents

FIGURES	5
TABLES	8
ABBREVIATIONS	9
ABSTRACT	11
DECLARATION	12
COPYRIGHT STATEMENT	12
DEDICATION	13
ACKNOWLEDGEMENTS	14
CHAPTER 1 LITERATURE REVIEW	15
1.1 INTRODUCTION	15
1.1.1 <i>History of SIMS -- instrumentation and primary ion sources</i>	16
1.1.2 <i>The generation of secondary ions</i>	19
1.1.2.1 Sputtering	19
1.1.2.2 Ionisation	20
1.1.2.2.1 Nascent ion molecule model	20
1.1.2.2.2 The desorption ionisation model	21
1.1.3 <i>Basic equations</i>	21
1.2 LIPIDOMICS AND TOF-SIMS	22
1.2.1 <i>Lipid classification and functions</i>	22
1.2.2 <i>System-level approaches in lipid research</i>	26
1.2.2.1 Contemporary techniques in lipidomics	26
1.2.2.2 Identification and imaging with ToF-SIMS	32
1.2.2.2.1 Sample considerations	32
1.2.2.2.2 Untargeted analysis	34
1.2.2.2.3 Targeted analysis	38
1.2.2.3 Problems and challenges for ToF-SIMS	41
1.2.2.3.1 Peak identification	41
1.2.2.3.2 Mass resolution and spatial resolution	43
1.2.2.3.3 Ion suppression and enhancement from the chemical environment	44
1.3 AIM OF THE STUDY	44
REFERENCES	45
CHAPTER 2 INSTRUMENTATION	52
2.1 BIOToF-SIMS INSTRUMENT	52
2.1.1 <i>Operation mechanism</i>	53
2.1.2 <i>Main components</i>	53
2.1.2.1 Primary ion gun	53
2.1.2.1.1 Liquid metal ion gun	53
2.1.2.1.2 Polyatomic C ₆₀ ⁺ Gun	54

2.1.2.2 ToF mass analyser	55
2.1.2.3 MCP detector.....	56
2.1.2.4 Electron Flood Gun	57
2.1.2.5 Sample stage and sample stub.....	57
2.2 J105 3D CHEMICAL IMAGER.....	58
2.2.1 Overview of the J105 3D Chemical Imager	58
2.2.2 Unique features.....	59
2.2.2.1 DC PI beam with corresponding high lateral resolution and fast duty cycle.....	59
2.2.2.2 Buncher-ToF with corresponding high mass resolution and transmission	61
2.2.2.3 Reliable sample handling system	62
2.2.2.4 MS/MS analysis	63
REFERENCE	64
CHAPTER 3 LIPIDOMICS STUDY OF XENOPUS LAEVIS EMBRYO.....	65
3.1 INTRODUCTION.....	65
3.1.1 From fertilisation to early embryo development of <i>Xenopus laevis</i> eggs	65
3.1.2 Lipids profiling and imaging of <i>Xenopus laevis</i> eggs.....	67
3.1.3 Aim of the project.....	70
3.2 MATERIAL AND METHODS.....	71
3.2.1 Total lipids extraction	71
3.2.2 Sampling of <i>Xenopus laevis</i> embryos	72
3.2.2.1 Dejelling of <i>Xenopus laevis</i> egg	72
3.2.2.2 Freeze the biological process of zygotes and embryos	72
3.2.2.3 Optimised procedure for sampling zygotes and embryos	73
3.2.2.4 Serial cryosections of zygote	74
3.2.3 ToF-SIMS analysis.....	75
3.3 RESULT AND DISCUSSION	76
3.3.1 Effects of dejelling on fertilisation and development of <i>Xenopus laevis</i> egg.....	76
3.3.2 Spectra interpretation of lipids extraction	77
3.3.3 Topography effects on spherical sample.....	89
3.3.4 Lipids map of <i>Xenopus laevis</i> zygote/embryo in time course study.....	95
3.3.4.1 Lipid composition in two hemispheres of the zygote	95
3.3.4.2 Monitoring the lipids distribution on the animal hemisphere of zygotes sampled shortly after fertilisation.....	98
3.3.4.3 Subcellular signalling upon the fertilisation of <i>Xenopus laevis</i> eggs	104
3.3.4.4 Monitoring the lipids distribution on <i>Xenopus laevis</i> embryo through the early development stages	107
3.4 SUMMARY	112
REFERENCES	113
CHAPTER 4 SUBCELLULAR IMAGING USING DYNAMIC SECONDARY ION MASS SPECTROMETRY	118
4.1 INTRODUCTION.....	118
4.1.1 Mouse embryonic fibroblast cells and Raf kinase	118
4.1.2 NIH 3T3 BXB-ER cells in response to the Raf/ERK activation.....	119
4.1.3 SIMS imaging on submicron scale	121

4.1.4 Aim of the project	123
4.2 MATERIALS AND METHODS	124
4.2.1 Cell culture	124
4.2.2 Sample preparation	124
4.2.2 Confocal microscopy and ESEM analysis	126
4.2.3 Imaging ToF-SIMS analysis.....	126
4.3 RESULT AND DISCUSSION	127
4.3.1 Sensitivity and stability of fluorophore-MitoTracker Red CMXRos.....	127
4.3.2 Morphological changes of NIH 3T3 BXB-ER cells following Raf/ERK activation in sample Group A.....	129
4.3.3 Time course study of mitochondrial rearrangement using confocal microscopy and ToF-SIMS in sample Group B	132
4.4 SUMMARY	144
REFERENCE	144
CHAPTER 5 CONCLUSION AND FUTURE WORK	147
5.1 XENOPUS LAEVIS EMBRYO	147
5.2 FIBROBLAST NIN/3T3 CELLS	148
5.3 FUTURE WORK	148
5.3.1 Fundamental questions	148
5.3.2 Further biological applications	149
REFERENCES	151
APPENDIX I.....	152
APPENDIX II.....	155

Figures

Fig. 1.1 Schematic of single cells imaging using ToF-SIMS.....	15
Fig. 1.2 Secondary ion signal intensities are plotted against the primary ion dose during the alternative bombardment by Au_3^+ and C_{60}^+	18
Fig. 1.3 Molecular dynamics simulation of inorganic and organics under the bombardment of polyatomic projectiles.....	19
Fig. 1.4 Schematic presentation of the Nascent ion molecule model emission with the aid of Me^+ emission	21
Fig. 1.5 The major classes of lipids and their cellular distribution in eukaryotic cell	24
Fig. 1.6 The structure of cell membrane	24
Fig. 1.7 Schematic of tissue section imaging using matrix-assisted laser desorption ionization mass spectrometry	28
Fig. 1.8 Ion images of a sagittal rat brain section	30
Fig. 1.9 The procedures of cells preparation for ToF-SIMS analysis.	32
Fig. 1.10 NanoSIMS analysis of a freeze-dried, phase-separated supported lipid bilayer	35
Fig. 1.11 3D biochemical images of freeze-dried <i>Xenopus laevis</i> oocyte focused C_{60}^+ primary ion beam on a conventional ToF-SIMS instrument..	36
Fig. 1.12 3D C_{60}^+ cellular imaging of frozen-hydrated HeLa-M cells using the J105 3D Chemical Imager.	37
Fig. 1.13 ToF-SIMS images (three-color overlays) of a whole mouse section.	38
Fig. 1.14 Images of unwashed and argon blow-dried 3T3F442A cells treated with ^{13}C -oleate.....	39
Fig. 1.15 ToF-SIMS analysis of a strongly paired mated <i>T. thermophila</i>	39
Fig. 1.16 Au_3^+ SIMS mass spectrum in positive ion mode of a mouse brain tissue section.	43
Fig. 1.17 Demonstrate the necessity of maintaining high mass resolution while imaging.....	43
Fig. 2.1 Schematic drawing of BioToF-SIMS	52
Fig. 2.2 The mechanism of the ToF-SIMS	53
Fig. 2.3 Schematic of liquid metal ion gun	54
Fig. 2.4 Schematic of C_{60} gun ion optics.....	55
Fig. 2.5 Schematic of ToF mass analyser.....	56
Fig. 2.6 Microchannel plates.	57
Fig. 2.7 Sample holder for the BioToF-SIMS	58
Fig. 2.8 Illustration of the Ionoptika J105 3D Chemical Imager.	59
Fig. 2.9 +SIMS spectra of two biomolecules using the J105 3D Chemical Imager and the BioToF-SIMS	61
Fig. 2.10 Sample holders for the J105 3D Chemical Imager.	63
Fig. 3.1 Cleavage and gastrulation of the <i>Xenopus laevis</i> embryo..	66
Fig. 3.2 Simulation of the distributions of Ca^{2+} (top) and IP3 (bottom) in an axisymmetric, three-dimensional sphere at 60, 100, 140 and 180 s after wave initiation.....	67
Fig. 3.3 Morphology of the outer surface of the <i>Xenopus laevis</i> egg.....	69
Fig. 3.4 Morphological changes on egg surface of <i>Rana pipiens</i> at the site of sperm entry shortly after the insemination.....	70

Fig. 3.5 Single <i>Xenopus laevis</i> embryo preparation for ToF-SIMS.....	74
Fig. 3.6 Fish gelatine sections of <i>Xenopus laevis</i> zygote 10min after fertilisation in the microtome chamber	75
Fig. 3.7 The development of <i>Xenopus laevis</i> zygotes dejellied 7 min post-insemination in early stages.	77
Fig. 3.8 +SIMS Spectra of lipids extraction from <i>Xenopus laevis</i> zygote 10 min after fertilisation...83	
Fig. 3.9 -SIMS spectra of lipids extraction from <i>Xenopus laevis</i> zygote 10 min after fertilisation. ...85	
Fig. 3.10 Fragmentation of the major classes of lipids in biological cell membrane.....86	
Fig. 3.11 Relative intensities of selected lipid ions from lipids extraction of <i>Xenopus laevis</i> zygotes 10 min post insemination.	89
Fig. 3.12 The \pm SIMS spectra of the residue from <i>Xenopus laevis</i> zygotes 10 min post-insemination after lipids extraction	89
Fig. 3.13 Simulated electric fields in ToF-SIMS for insulating particle over a conducting substrate..	90
Fig. 3.14 Sphere sample under the extraction field.	90
Fig. 3.15 Images (+SIMS) of <i>Xenopus laevis</i> zygote 10 min post-insemination selected for comparison study of secondary ion yields variation using the BioToF-SIMS.....	91
Fig. 3.16 Comparing the yields of total and selected ions cross the animal hemisphere of <i>Xenopus laevis</i> zygote 10 min post-insemination using the BioToF-SIMS.	92
Fig. 3.17 Images (+SIMS) of <i>Xenopus laevis</i> 32 cells embryo selected for comparison study of secondary ion yields variation using the J105 3D Chemical Imager	93
Fig. 3.18 Comparing the yields of total and selected ions cross the animal hemisphere of <i>Xenopus laevis</i> 32 cells embryo using the J105 3D Chemical Imager	94
Fig. 3.19 Intensity variation of ion m/z 91.0 ⁺ across the surface of spherical sample in relation to the corresponding incident angles of primary ion beam	95
Fig. 3.20 +SIMS spectra of animal hemisphere of <i>Xenopus laevis</i> zygote 10 min post-insemination using the BioToF-SIMS.....	96
Fig. 3.21 Relative intensities of selected ions from the animal and vegetal hemispheres of <i>Xenopus laevis</i> zygote sampled 10 min after insemination using the BioToF-SIMS.....	97
Fig. 3.22 Total positive ion and selected ion images (+SIMS) of the animal hemisphere of <i>Xenopus laevis</i> zygote 10 min after insemination using the BioToF-SIMS..	98
Fig. 3.23 Total ion and selected ion images (\pm SIMS) of the animal hemisphere of <i>Xenopus laevis</i> zygote sampled 10 min post-insemination using the BioToF-SIMS.	99
Fig. 3.24 Total ion and selected ion images (+SIMS) of the animal hemisphere of <i>Xenopus laevis</i> zygote 10 min post-insemination using the J105 3D Chemical Imager.....	100
Fig. 3.25 PCA plot of SIMS data of single <i>Xenopus laevis</i> zygote 10 min post-insemination.....	101
Fig. 3.26 Changes of selected ions across one gametes fusion site on the animal hemisphere of <i>Xenopus laevis</i> zygote 10 min post-insemination.....	102
Fig. 3.27 3D visualization of depth profile of <i>Xenopus laevis</i> zygote sampled 10 min post-insemination using the J105 3D Chemical Imager	103
Fig. 3.28 Total ion and selected ion images (+SIMS) of the animal hemisphere of <i>Xenopus laevis</i> egg control samples using the J105 3D Chemical Imager	104

Fig. 3.29 Changes of selected ions during depth profiling of <i>Xenopus laevis</i> zygote 10 min post-insemination using the BioToF-SIMS	105
Fig. 3.30 Changes of ion concentrations of selected ions in serial sections of <i>Xenopus laevis</i> zygote 10 min after fertilisation using the J105 3D Chemical Imager..	106
Fig. 3.31 Total ion and selected ion images (+SIMS) in serial sections of <i>Xenopus laevis</i> zygote 10 min after fertilisation using the J105 3D Chemical Imager...	107
Fig. 3.32 Total optical, total ion and selected ion images (+SIMS) of animal hemisphere of <i>Xenopus laevis</i> embryos in different cleavage stages using the J105 3D Chemical Imager.	108
Fig. 3.33 Total ion and selected ion images (+SIMS) of animal hemisphere of <i>Xenopus laevis</i> blastula embryo 5.5 h post-insemination using the J105 3D Chemical Imager.....	110
Fig. 3.34 Depth profiling in the central area of <i>Xenopus laevis</i> blastula embryo 5.5 h post-insemination using the J105 3D Chemical Imager.	111
Fig. 3.35 Changes of relative intensities and distributions of selected ions along with depth profiling of <i>Xenopus laevis</i> blastula embryo 5.5 h post-insemination using the J105 3D Chemical Imager	112
Fig. 4.1 NIH 3T3 BXB-ER cells and the c-Raf-1 derived BXB-ER fusion protein.	119
Fig. 4.2 C-RAF activation changes mitochondrial subcellular distribution.....	120
Fig. 4.3 BXB-ER activation induces chromatin rearrangement and reduced nuclear diameter	121
Fig. 4.4 Qualitative co-localization of DNA and RNA through simultaneous NanoSIMS imaging of RNA and DNA.....	122
Fig. 4.5 ToF-SIMS imaging (c-f) confocal laser scanning imaging (a, b) were obtained from the same position of a methanol/acetic acid fixed cell sample	123
Fig. 4.6 The structure of MitoTracker Red CMXRos and the conjugation with peptide.....	127
Fig. 4.7 +SIMS spectrum of MitoTracker Red CMXRos using the J105 3D Chemical Imager.....	128
Fig. 4.8 \pm SIMS spectra of MitoTracker Red CMXRos using the BioToF-SIMS.....	128
Fig. 4.9 Depth profiling of MitoTracker Red CMXRos film.	129
Fig. 4.10 Comparing the morphological changes of NIH 3T3 BXB-ER cells without and following Raf/ERK activation using the J105 3D Chemical Imager	130
Fig. 4.11 ToF-SIMS analysis of B22 cells and PCA data processing	133
Fig. 4.12 Fluorescence images of NIH 3T3 BXB-ER cells stained with MitoTracker Red CMXRos at varying concentrations 200, 400, 600 nM using confocal microscopy	135
Fig. 4.13 3D depth fluorescence images taken from the yellow frame area of B26 cells	136
Fig. 4.14 Depth profiling of B23 cells in positive ion mode using the J105 3D Chemical Imager...	138
Fig. 4.15 PCA data processing of depth 3 and 4 of B23 cells	139
Fig. 4.16 ESEM image of B23 cells	140
Fig. 4.17 Depth profiling of B24 cells in positive ion mode using J105 3D Chemical Imager.....	142
Fig. 4.18 The summed positive ion spectra from the pixels containing the fluorescence dye ions.	143
Fig. 4.19 Structure of cardiolipin (CL) and possible fragment by loss of fatty acid chain and phosphate.	144
Fig. 5.1 PCA analysis of <i>Xenopus laevis</i> embryos in 2 cells, 4 cells and 16 cells stages.....	150

Tables

Table 1.1 Comparison of imaging mass spectrometries.....	31
Table 1.2 Characteristic fragments of biomolecules in ToF-SIMS spectra.....	42
Table 2.1 IOG C60-40 operation conditions with 40 keV C ₆₀ ⁺ ion beam	60
Table 2.2 Signal to noise levels on the J105 3D Chemical Imager and the BioToF-SIMS	61
Table 2.3 Mass accuracy of several biomolecules using J105 3D Chemical Imager.....	62
Table 3.1 Lipid composition of plasma membrane of <i>Xenopus laevis</i> oocytes	68
Table 3.2 The effect of dejellying on the fertilisation rate of <i>Xenopus laevis</i> eggs	77
Table 3.3 Peaks assignment of lipids extraction from <i>Xenopus laevis</i> zygote 10 min post- insemination in positive and negative SIMS	87
Table 4.1 Cell treatments in Group A.....	125
Table 4.2 Cell treatments in Group B.....	126
Table 4.3 Peak assignment of the fluorescent probe MitoTracker Red CMXRos	128

Abbreviations

AFM	atomic force microscopy
AP IR-MALDI	atmospheric pressure infrared matrix-assisted laser desorption ionization
9-AA	9-aminoacridine
2-AeP	2-aminoethylphosphonolipids
BPH	benign prostatic hyperplasia
CL	cardiolipin
¹³ C18-DSPC	¹³ C-labeled 1,2-distearoylphosphatidylcholine
DAG	diacylglycerol
DEMS	deuterium exchange mass spectrometry
DESI	desorption electrospray ionization
DHB	2,5-dihydroxy benzoic acid
DI	desorption ionisation
DMEM	Dulbecco's modified Eagle medium
DMSO	dimethyl sulfoxide
DPDME	dipalmitoylphosphatidyl-dimethylethanolamine
DPPC	dipalmitoylphosphatidylcholine
DPPG	dipalmitoylphosphatidylglycerol
DPPNME	dipalmitoylphosphatidyl-N-monomethylethanolamine
ERK	extracellular signal-regulated kinases
E.S.A	electrostatic analyser
ESEM	environmental scanning electron microscope
ESI	electrospray ionization
FCS	Fetal Calf Serum
FFPE	formaldehyde-fixed and paraffin-embedding
GC	gas chromatography
HEPES	N-(2-Hydroxyethyl)piperazine-N'-(2-ethanesulfonic acid) sodium salt
GC-MS	gas chromatography-mass spectrometry
GFP	green fluorescent protein
GPA/PA	phosphatidic acid
GPCho	glycerophosphocholine
GPEtn	glycerophosphoethanolamine
GPIns	glycerophosphoinositol
GPGro	glycerophosphoglycerol
GPSer	glycerophosphoserine
IMS	imaging mass spectrometry
J105	J105 3D Chemical Imager
IP3	inositol-1,4,5-trisphosphate
LB	Langmuir Blodgett
LC-MS	liquid chromatography-mass spectrometry
LMIG	liquid metal ion gun

MAG	monoacylglycerol
MALDI	matrix-assisted laser desorption ionization
mc	maximum counts
MCP	microchannel plate
MTBE	methyl- <i>tert</i> -butyl ether
NAFLD	nonalcoholic fatty liver disease
¹⁵ N-DLPC	¹⁵ N labelled 1,2-dilauroylphosphatidylcholine
NMR	nuclear magnetic resonance
OCT	optimal cutting temperature compound
PBS	phosphate buffer saline
PC12	rat pheochromocytoma
PCA	principal component analysis
PDMS	polydimethylsiloxane
PI(s)	primary ion(s)
PIP	phosphatidylinositolphosphates
PMMA	polymethylmethacrylate
PS	polystyrene
PTFE	Poly(tetrafluoroethylene)
PVC	poly(vinyl chloride)
SAC	sample analysis chamber
SEM	scanning electron microscopy
SI(s)	secondary ion(s)
SIMS	secondary ion mass spectrometry
SM	sphingomyelin
SPM	scanning probe microscopy
ST	sulfatide
TAG	triacylglycerol
TD	Transient Digitizer
TDC	Time-to-Digital converter
TEM	transmission electron microscopy
TLC	thin layer chromatography
TMRE	tetramethylrhodamine ethyl ester
ToF	Time-of-Flight
ToF-SIMS	Time-of-Flight secondary ion mass spectrometry
UHV	ultra high vacuum

Abstract

Imaging Time-of-Flight secondary ion mass spectrometry (ToF-SIMS) has been developed to perform 2D imaging and depth profiling of biological systems with micron or submicron scale lateral resolution, which can be attributed to the advent of polyatomic ion beam particularly C_{60}^+ and new concept of ToF-SIMS instrument, the J105 3D Chemical Imager (J105). These recent advances in ToF-SIMS have opened a new dimension for biological analysis. In this study, 2D and 3D imaging have been performed on two biological systems, *Xenopus laevis* (*X. laevis*) zygote/embryo and murine embryonic fibroblasts NIH 3T3 BXB-ER cells to explore the capability of ToF-SIMS to handle the biological samples with extreme topography and high resolution depth profiling of microdomains, which still represent major challenges for the ToF-SIMS.

The study on *X. laevis* embryo explored the capability of ToF-SIMS to handle spherical samples (approx. 1-1.2 mm in diameter), identify lipid species in mixtures of lipid extraction from the zygotes and image of an intact embryo in 2D/3D during dynamic biological events, e.g., fertilisation and early embryo development. For the first time the J105 and conventional BioToF-SIMS instrument were employed for the study of developmental biology. The major classes of lipid were identified through multiple lipid assay in a single analytical run using ToF-SIMS. Topography effects of the embryo were assessed through imaging a single intact zygote/embryo that revealed secondary ions loss at the edge of the single cell. However, the topography effects on the mass resolution could be minimised using the J105. Moreover, *in situ* lipid profiling of the zygote revealed different lipid compositions and intensities on the membrane of the animal and vegetal hemispheres. Furthermore, high resolution imaging and depth profiling that performed on a single intact cell in a time course study visualised the egg-sperm fusion sites on the membrane of the zygote 10 min post-insemination and lipids arrangement on the membrane of the embryo through the early development stages. Subcellular signalling upon the fertilisation was also spatially located on the serial cryosections of a single zygote.

With the NIH 3T3 BXB-ER cells, the study firstly adopted a finely focused C_{60}^+ beam to track morphological changes and rearrangement of subcellular organelle mitochondria (0.5-2 μ m) in response to the activation of Raf/ERK (extracellular signal regulated kinase) pathway using the J105. The SIMS images of the unlabelled cells showed the shifting of membrane distribution and nuclei shrinking following Raf/ERK activation. The mitochondria fluorescence probe within the cells were located 3-dimensionally using confocal microscopy and ToF-SIMS, which revealed the distribution pattern of condensing in the two sides of the nuclei following the Raf/ERK activation. Coupled with scanning electron microscopy (SEM), the three imaging modes showed good agreement in cellular morphological changes and subcellular mitochondrial rearrangement without or following Raf/ERK activation, demonstrating an integrated approaching to study the biological processes at subcellular dimension.

Declaration

No portion of the work referred to in this thesis has been submitted in support of an application of another degree or qualification of this or any other university, or other institution of learning.

Copyright statement

i. The author of this thesis (including any appendices and/or schedules to this thesis) owns certain copyright or related rights in it (the “Copyright”) and she has given The University of Manchester certain rights to use such Copyright, including for administrative purposes.

ii. Copies of this thesis, either in full or in extracts and whether in hard or electronic copy, may be made only in accordance with the Copyright, Designs and Patents Act 1988 (as amended) and regulations issued under it or, where appropriate, in accordance with licensing agreements which the University has from time to time. This page must form part of any such copies made.

iii. The ownership of certain Copyright, patents, designs, trade marks and other intellectual property (the “Intellectual Property”) and any reproductions of copyright works in the thesis, for example graphs and tables (“Reproductions”), which may be described in this thesis, may not be owned by the author and may be owned by third parties. Such Intellectual Property and Reproductions cannot and must not be made available for use without the prior written permission of the owner(s) of the relevant Intellectual Property and/or Reproductions.

iv. Further information on the conditions under which disclosure, publication and commercialisation of this thesis, the Copyright and any Intellectual Property and/or Reproductions described in it may take place is available in the University IP Policy (see <http://www.campus.manchester.ac.uk/medialibrary/policies/intellectual-property.pdf>), in any relevant thesis restriction declarations deposited in the University Library, The University Library’s regulations (see <http://www.manchester.ac.uk/library/aboutus/regulations>) and in The University’s policy on presentation of Theses.

This thesis is dedicated to my family.

Where there is a will, there is a way.

Acknowledgements

It would not have been possible to have the opportunity to work at Manchester Surface Analysis Research Centre (SARC) and write this doctoral thesis without the help and support of the kind people around me. It is possible to just give particular mention to only some of them here.

Above all, I am sincerely and heartily grateful to my supervisor, Dr. Nicholas Lockyer and Prof. John Vickerman for their support, particular the valuable discussions and patience they showed me throughout my thesis writing, not to mention the efforts they have made to provide training, facilities, advice and guidance during my PhD study. The good advice, help in the lab and sharing of precious experiences of instrument operation from Dr. John Fletcher have been invaluable, for which I am extremely grateful. Also I would like to thank Dr. Alex Henderson who has devoted time to help with the data processing and provided valuable suggestions.

I gratefully acknowledge the Royal Society of Chemistry Analytical Trust Fund and the University of Manchester for funding this project.

I owe earnest thanks to my fellow PhD students and friends Alessia Longobardo and Edward Jackson for the encouragement and friendship, especially the great support and company during my illness and thesis writing, for which my mere expression of thanks does not suffice. It is a great pleasure to thank Dr. Sadia Rabbani for the help with the experiment and valuable discussion, Jimmy Moore for the kind help with data processing, and other SARC members for the help with my work. I would also thank previous SARC member Dr. Steve Wong for valuable discussion and the efforts made to proof-read my thesis.

The two projects presented in the thesis are in cooperation with Prof. Nancy Papalopulu and Dr. Josip Lovric. I would like to thank them for providing samples and experiment facilities. I am truly thankful to Dr. Raphael Thuret who spent precious time to help me with every detail of the frog embryos sampling. I am glad to have worked with Ricardo Rodriguez-Enriquez and Pedro Olivares-Chauvet on fibroblast cells culture and confocal imaging. Many thanks to Dr. Patrick Hill for help with ESEM imaging and my friend Mingcheng Wu for the help with lipids extraction.

Among my friends in Manchester, Hui Wang, Xuejiao Yang, Bo Yuan, Jie Gao and many others, I am sincerely thankful for the great joys we share and helping each other. I will always treasure the time having all of you around.

Last but by no means least, I am truly indebted and thankful to my parents and my brother for their unequivocal support. Their love for me will always encourage and propel me.

Chapter 1 Literature review

1.1 Introduction

Imaging mass spectrometry (IMS) has drawn increasing interest from biological and pharmaceutical studies due to its unique combination of non-presumptive detection of multiple bio-substances with high resolution imaging of their spatial distributions. Time-of-Flight secondary ion mass spectrometry (ToF-SIMS), a variant of IMS, is operated by rastering a focused high-energy primary ion (PI) beam (atomic ion beam, e.g., Ga^+ , Cs^+ , Au^+ , or cluster beams, e.g., Au_3^+ , C_{60}^+) which impinges the sample surface and then collecting emitted 'secondary' ions (SIs) pixel by pixel (or by voxel). These SIs are analysed by a Time-of-Flight mass spectrometer to determine their elemental, isotopic, or molecular composition, thus generating a compositional map in 2 or 3 dimensions (2D or 3D) (as in Fig. 1.1).

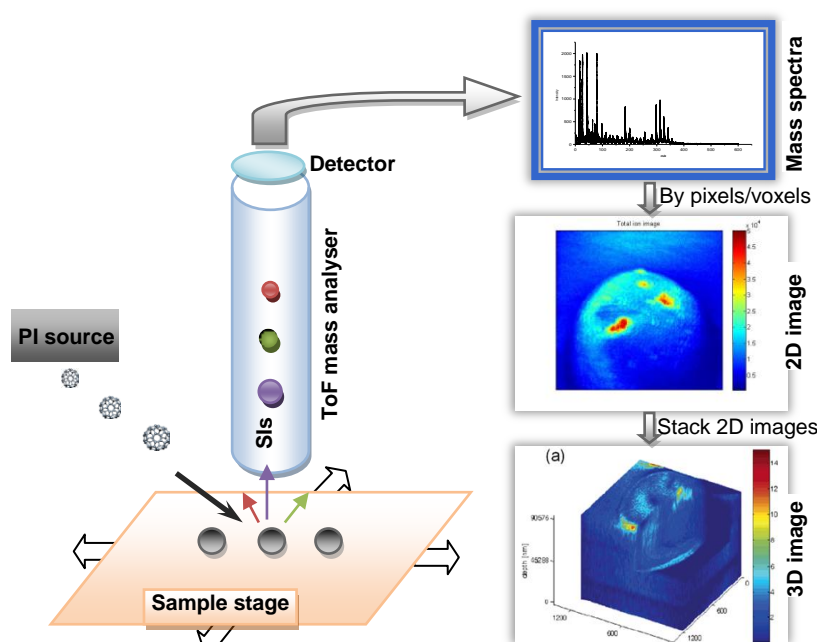


Fig. 1.1 Schematic of single cells imaging using ToF-SIMS. SIs, secondary ions; PI, primary ion.

With the advances of the technique, ToF-SIMS displays some advantages over other imaging techniques, e.g., high chemical sensitivity, high lateral resolution (~ 100 nm with cluster ion beams) and molecular depth profiling for 3D visualisation of biological systems. These have led to successful applications of the technique to lipidomics study on a wide range of cells and tissues, gaining insights into biological events, disease progression at molecular level to aid disease diagnosis, treatment and drug development. However, the optimum sample shape is flat in ToF-SIMS analysis due to topography effects for most ion beam probe based instruments, which presents difficulties for real world biological analysis. On the other hand, the challenges still remain in term of high resolution molecular depth profiling of biological specimens.

The previous work on single *Xenopus laevis* (*X. laevis*) oocyte analysis and a decade of technique improvements in our lab have shown the possibility to probe large spherical samples, achieving 3D imaging at high resolution using a focused C_{60}^+ PI beam. As extensions of previous work, the two projects presented in this thesis aimed to explore the capabilities of ToF-SIMS to manipulate

biological samples with extreme topography and obtain high resolution depth profiling of microdomains with two biological systems, *X. laevis* embryo and murine embryonic fibroblasts NIH 3T3 BXB-ER. More importantly, this study further explored using ToF-SIMS to monitor dynamic biological processes, e.g., fertilisation and cleavage during early developmental stages of *X. laevis* egg and ongoing mitochondrial remodelling in NIH 3T3 BXB-ER cells responding to the external Raf/ERK activation.

1.1.1 History of SIMS -- instrumentation and primary ion sources

Based on the discovery of the positive ions and neutral atoms releasing from a metal surface after vigorous bombardment of cathode rays by Thomson in 1910 [1], the emitted positive ions (or negative ions depending on the electron affinity) were defined as 'secondary ions'. These can yield direct information of the chemical composition of the surface. The fact that the constituents from almost all solid surfaces, even those that are thermally unstable and cannot be vaporized, are emitted as intact neutral particles and SIs following such bombardment, inspired the construction of new analytical instruments. However, not until 1949, with the improved vacuum pump technology stabilizing the SIs during the extraction and their flight path, was the first prototype SIMS developed by Herzog and Viehböck at the University of Vienna, Austria [2]. With high flux of PIs, typically Cs^+ , O_2^+ , many monolayers of the sample surface can be removed, so called 'dynamic SIMS'; and accordingly, the local chemical information as function of depth can be determined, termed 'depth profiling'. This operation mode was largely successful in elemental analysis with many routine applications established in materials science and semi-conductor industry [3].

On the other hand, when applied to organic analysis, the high dose of PI caused detrimental chemical damage to the sample. Benninghoven defined the phenomenon using the 'damage cross-section', σ , determined by the average surface area damaged by a single ion impact, i.e., the area modified in such a way that the considered secondary ion cannot be generated from this area subsequently [4]. Later Benninghoven introduced the method of 'static SIMS' with a recommended PI dose density below 10^{13} ions/cm² in 1969. The static SIMS mode ensured that a particular surface region will not receive more than one PI impact, making SIMS is a truly surface analysis technique [5]. But the concept did not advance SIMS very far, because low PI dose results in low SI emission. If considering the limited surface area has very limited number of atoms and molecules available for analysis (e.g., 10^6 particles for a $1\text{ }\mu\text{m}^2$ surface area [6]), and the ionisation probabilities for most surface constituents are less than 10^{-4} [7], it is immediately clear that the detectable SIs are very few. The situation was even more exaggerated by the magnetic double focusing sector field mass spectrometer and quadrupole spectrometers employed in 1960s and 1970s respectively [8, 9], owing to their low detection sensitivity arising from limited mass range, low transmission, and sequential mass scanning mode. However, in 1980s, a most significant improvement, the adoption of ToF mass analyzer, offered an almost ideal solution to enhance the detection sensitivity by many orders of magnitude. Shortly after the ToF-SIMS instrument was assembled at the University of Münster, Germany by Benninghoven, Niehus and Steffens, and also by Charles Evans & Associates in USA. In the next two decades, with the mature charge neutralisation techniques, static ToF-SIMS were widely used in surface analysis of various inorganic or organic materials to understand the SIMS process and the influence of various factors on 'secondary ion yields', defined as the fraction of sputtered species in form of SIs [7]. The single

celled *Paramecia* were also imaged to locate elements and biomolecules using a Ga^+ PI beam [10, 11]. At that time, the frequently used ion sources were gas sources (e.g., Ar^+ , Xe^+) and the liquid metal ion source (e.g., Cs^+ , Ga^+ , In^+). However, the trial experiments with organic molecules and biological samples yielded extreme low SIs and limited mass range less than $\sim m/z$ 300 due to the in-source fragmentation [11]. The urgency to develop new PI sources in order to bring about the efficient sputtering and ionisation has pushed ToF-SIMS through another important technique improvement -- the evolution of PI sources.

The development of PI sources can date back several decades [6]. In the 1970s, Wittmaack [12, 13] demonstrated that sputter yields and SI yields are affected by the mass and number of constituent atoms of projectiles, and made efforts to generate polyatomic ion sources using convenient technology. Consequently, molecular ion sources (e.g., SF_5^+) were used for SIMS experiments in the 1980s and early 1990s. Around the same time, the Texas A&M group started to explore C_{60}^+ , and jointed with the Institute de Nuclearie for the study of Au_n^+ and several other molecular ion beams. Systematic studies and cross comparison of the new projectiles were followed. Benguerba *et al.* [14] revealed the nonlinear increase of SI yield of molecular ions from organic surfaces along with the number of constituents in Au_n^+ ($n=1-5$) cluster ion beam at the same velocity. The same group then demonstrated that the emission induced by gold clusters was from a depth 50-100 Å in Langmuir-Blodgett films, and with carbon cluster projectile the nonlinear increase effect vanished when using C_n^+ ($n>20$), suggesting that cluster ions with a large number of atoms deposit their energy within a shallow distance of the sample surface and C_{60}^+ could be a candidate for SIMS [15]. Different atomic and molecular PI sources were also compared, e.g., SF_5^+ , SF_6^- and Xe^+ by Szymczak and Wittmaack [16], O^+ , Ar^+ , Xe^+ , O_2^+ , CO_2^+ , SF_5^+ , C_7H_7^+ , $\text{C}_{10}\text{H}_8^+$, C_6F_6^+ , and $\text{C}_{10}\text{F}_8^+$ by the Benninghoven group [17], confirming the strong SI yield enhancement along with the increasing of the mass for atomic PIs and number of constituents for molecular PIs, as well as smaller increase in damage cross section. Research was also conducted to test the imaging capabilities of PI beams with 15 µm lateral resolution achieved for focused Ar^+ and SF_5^+ , and 1 µm for Au_2^+ [17], this is the first report regarding secondary ion image using gold cluster ion beams.

Owing to the good focusability (<1 µm) of metal cluster ions, as well as them delivering higher yields of SIs of biomaterials (compared to the atomic ion beams), Au_3^+ and Bi_3^+ ion beams were widely adopted in the early 2000s for high resolution imaging of biological specimens [18, 19]. A number of applications to tissue, e.g., rat brain and rat leg section quickly followed as detailed in section 1.2.2.2. Bi_3^+ was particularly favoured because its ion fluence is seven times higher than that of Au_3^+ resulting in shorter analysis duty cycle and improved sensitivity for high mass molecular species [19]. However, these metal clusters still generated considerable damage by implanting ions deeper than just the top surface of the sample and accordingly the chemical nature is altered during depth profiling [3]. Therefore, 3D imaging of subcellular domains with metal cluster beams was hindered. Meanwhile, the Vickerman group started to develop C_{60}^+ ion sources with Ionoptika Ltd, UK [20]. Its excellent capabilities were revealed by depth profiling of organic and biological systems as well as in the molecular dynamic simulation. Jones *et al.* [21] demonstrated the reduced surface damage associated with C_{60}^+ ion sputtering in chemically fixed HeLa cells with the molecular information obtained even following a dose of 10^{15} ions/cm² that is far beyond the static limit. Cheng and Winograd [22] performed molecular depth profiles using C_{60}^+ ion beam on

an organic film made by diluting small peptide molecules into trehalose. The molecular ion of trehalose and the peptide kept at a steady value until the Si substrate was reached. High mass ions up to m/z 830⁺ were recorded. The reduced damage through C₆₀⁺ impact is even more apparent during the alternative bombardment of the same film by Au₃⁺ and C₆₀⁺ as in Fig. 1.2. During the sputtering process C₆₀⁺ projectiles yielded higher molecular ion signals than Au₃⁺, and more notably, C₆₀⁺ is capable of recovering the damage done by Au₃⁺ as molecular ions of both components recovered to different extents after switching from Au₃⁺ to C₆₀⁺ [23]. The reasons why the two projectiles with similar mass behave so differently could be well explained by molecular dynamics simulation by Garrison *et al.* at Penn State University [24]. As in Fig. 1.3 (a), with the same 15 keV impact energy, C₆₀⁺ projectile penetrates through 3 nm of material creating a crater much shallower than Au₃⁺ of 15 nm. More atoms in C₆₀⁺ projectile work simultaneously with less energy per atom for bigger sputtering events and less damage. Delcorte *et al.* [25] firstly simulated fullerene projectile bombardment of organics, confirming the same reaction under C₆₀⁺ impinging [Fig. 1.3 (b, c)].

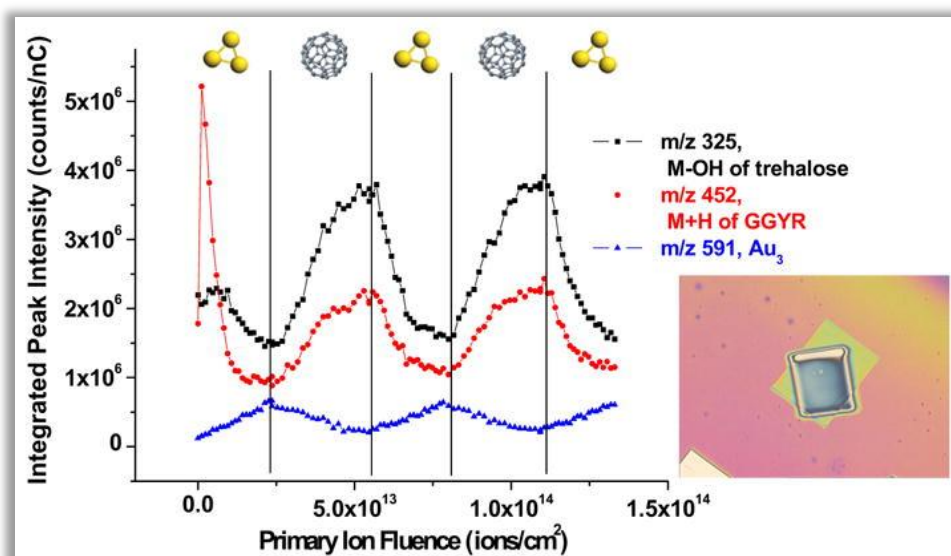


Fig. 1.2 Secondary ion signal intensities are plotted against the primary ion dose during the alternative bombardment by Au₃⁺ and C₆₀⁺. The order of the projectile that is used to sputter for each turn is indicated on the figure. The inset is an optical image of the film after the overlap depth profile experiment. The smaller crater is created by C₆₀⁺ sputtering while the bigger crater on the outside is created by Au₃⁺ sputtering. All of the spectra were taken from the overlapped centre area of 1360×1020 μm². Reproduced from reference [23].

All the results showed fullerene is a promising candidate for molecular depth profiling. However, the drawback of the projectile is the difficulty in focusing this gas phase source compared to the metal cluster beams. The dual beam operation system was thus employed to offset each beam's drawbacks by using C₆₀⁺ to etch between two analysis cycles and another metal cluster ion beam to image. The 2D images acquired in each analysis cycle can be reconstructed to form 3D visualisation. A group of experiments have used this approach for subcellular location of the biomolecules in depths, as summarized in section 1.2.2.2. To avoid the complications of dual beam operation and build more reliable operation system, the Vickerman group dedicated to develop a 40 keV C₆₀⁺ PI source with nanoscale spot size and new concept ToF-SIMS instrument, J105 3D Chemical Imager, which enables a novel 3D imaging mode using the focused C₆₀⁺ ion beam for simultaneous etching and imaging such that the chemical information is collected in voxels rather

than pixels without wasting any of the sample. The applications of this approach in HeLa cells and rat kidney have been published recently and are described in section 1.2.2.2.

Developing new PI sources is always the focus of interest. The more components the cluster projectile has, the higher yields of molecular ions and less damage it can achieve. With this general observation, more giant cluster ion sources emerged very recently, e.g., Ar_n^+ ($n=60-2000$) cluster in the Vickerman group [26], Ar_n^+ ($n=1-1500$) in the Matsuo group [27], Au_{400}^+ at Texas A&M university with imaging capability of 10 μm resolution [28] and a new metal-cluster-complex of $\text{Ir}_4(\text{CO})_7^+$ [29]. Generally, with the right energy and a suitable size, these clusters enable more effective, even ‘fragment-free’ ionisation of organics. However, being difficult to focus down to small sizes and limited mass range (generally below 2000 amu), further development is required for the application to high resolution molecular imaging.

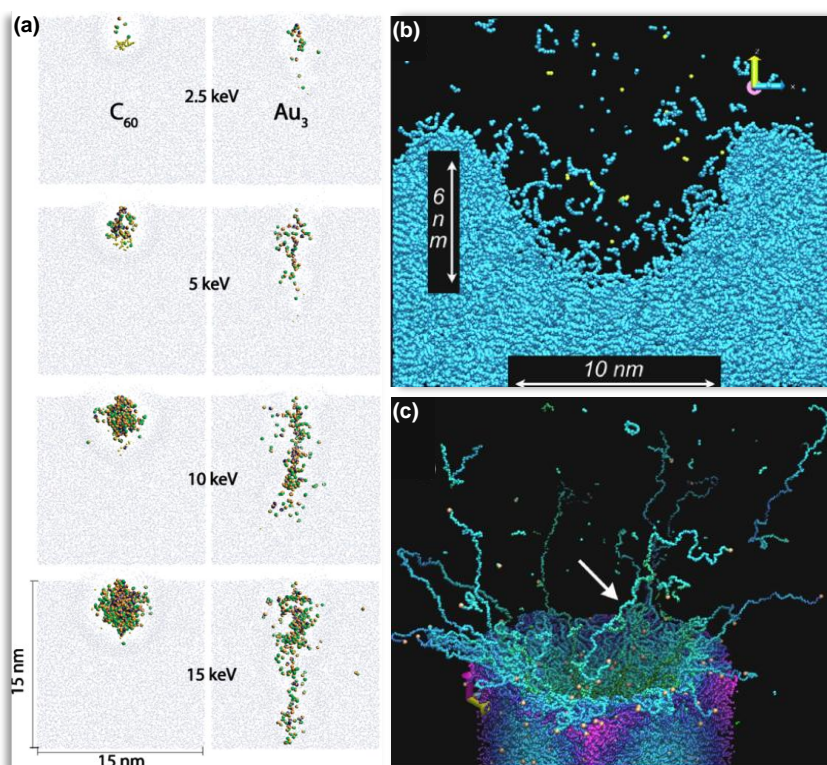


Fig. 1.3 Molecular dynamics simulation of inorganic and organics under the bombardment of polyatomic projectiles. (a), time snapshots of 2.5, 5, 10, and 15 keV C_{60}^+ and Au_3^+ bombardment of pure amorphous water ice. Gray and yellow spheres represent intact water molecules and projectile atoms, respectively, within a 2 nm cross-section through the centre of the substrate at 0.5 ps. Orange, green, and blue spheres represent the fragment species placed back in their initial positions and overlaid on the substrate at 0.5 ps. Reproduced from reference [24]; (b), the crater formed in amorphous icosane ($\text{C}_{20}\text{H}_{42}$) within 3 nm cross-section in the sample after 20 ps following 5 keV C_{60}^+ impinging with a normal incidence; (c), perspective view of the emission of an intact $\text{C}_{249}\text{H}_{500}$ molecule (white arrow) from the crater formed at 20 ps in a polyethylene (PE3; $\text{C}_{249}\text{H}_{500}$) sample. (b, c) are reproduced from reference [25].

1.1.2 The generation of secondary ions

Two processes are vital for the formation SIs, the dynamical process by which atoms and multi-atomic clusters are desorbed and the ionisation process in which a fraction of these sputtered particles become charged [6].

1.1.2.1 Sputtering

The sputtering process central to the SIMS could be elucidated by Sigmund’s linear cascade theory,

which assumed that sputtering occurs by particle bombardment at small incident particle current and fluency, this excludes the situations where there is extensive heating and damage of the target and is close to the criteria for static SIMS [30]. PIs from the source impinge upon the sample and transfer energy to target atoms, both through the direct collisions between the PIs and the atoms in the sample or indirectly through collisions of atoms already in motion with other atoms within the sample (*i.e.*, knock-on effects). Compared to bond energies of sample substances, the PIs typical carrying energies of keV range induce highly energetic collisions directly between the PIs and the atoms in the sample. This results in extensive fragmentation and bond breaking within about 30 Å near the collision site, producing essentially only the emission of atomic particles. When the collision cascade becomes weak, the emission of molecular fragments becomes dominant. Particles produced in approx. the top 2-3 monolayers of the sample have sufficient energy to overcome the surface binding energy and leave the sample as ejected neutral atoms and molecules, electrons, and ions.

The linear cascade theory fit well the experimental data, showing a good description of the dependence of SI yields on primary particle mass and energy in the models of single component materials under the bombardment of medium to high energy particle. However, when it comes to lower energy beams and multi-component materials, the linear cascade theory is not suitable anymore. Seah *et al.* [31] also evaluated the thermal spike model proposed by Sigmund and Claussen, which proved to be consistent with published ion sputtering yields data from mono-elemental solids sputtered by PI clusters, mainly the type of Au_n^+ ($n=1-13$).

1.1.2.2 Ionisation

During the sputtering event, only a small fraction of sputtered particles (10^{-6} - 10^{-1}) are ionised (their positive or negative state depends on their electron configuration) and re-excited through the near surface region to the mass detector. Two models that were proposed to explain the process are described briefly as follows.

1.1.2.2.1 Nascent ion molecule model

Plog and Gerhard [32] developed the model that is a "cold" ion emission from solid surfaces and the SIs were emitted by means of metal oxide species following Ar^+ bombardment (Fig. 1.4). It assumed that a non-adiabatic dissociation of nascent ion molecules occurs outside of the surface potential barrier, and for homogeneous and inhomogeneous matrices the energy distributions of the surface atoms are different. In addition, the energetic ability of becoming an ion latently exists already in the center-of-mass system of the particles. The rapid electronic transitions which occur in the surface region will neutralize any ions before they can escape. For the neutral emission, it depends on the mass ratio of the constituents of the sputtered molecule. Most of the neutral molecules originate from direct emission of ion pairs (*e.g.*, MeO) and keep their molecular character after leaving the surface. Only a few molecules have enough energy to dissociate into their constituents.

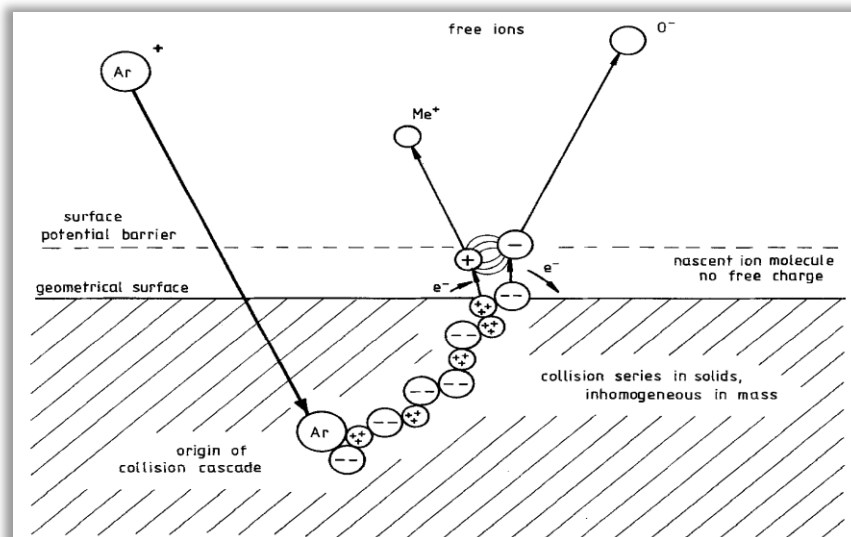


Fig. 1.4 Schematic presentation of the nascent ion molecule model emission with the aid of Me^+ emission. Reproduced from reference [30].

1.1.2.2.2 The desorption ionisation model

The desorption ionisation (DI) model has been advocated by Cooks and Busch [33] for understanding of molecular and cluster ion emission from organic materials. It suggested that the process of desorption and ionisation could be considered separately and seek to rationalize the relative abundances of the ions generally observed in the SIMS spectra. With the initial excitation process, the energy in molecules is transformed into thermal/vibrational motion, the ions C^+ or A^- are then desorbed and transverse the uppermost layers (termed the selvedge) in high abundance reflected in the spectrum. The fragmentation of ions is minimized for the low internal energy and being energized by the collision is unlikely. Neutral molecules are desorbed in high yield but to be detected must undergo an ionisation process (e.g., cationisation).

The model also described how other ions may be formed by chemical reaction, fast ion/molecule reactions or electron ionisation in the selvedge and unimolecular dissociations in free vacuum that is governed by the internal energy of the parent ion. The model was consistent with the fact that in static SIMS little low-mass fragmentation occurs. However, it seemed not totally reasonable to suggest that the initial collision processes cannot produce significant numbers of additional ions relative to those existing in the material.

1.1.3 Basic equations

The yield of SI is strongly influenced by the electric state of the material being analysed and consequently this complicates the quantitative analysis. The basic SIMS equation is as follows:

$$I_s^M = I_p Y_M \alpha^+ \theta_M \eta \quad \text{Equation 1.1}$$

Where I_s^M is the SI current of an element or species M;

I_p is the PI flux;

Y_M is the total sputter yields of species M;

α^+ is the ionisation probability of the M;

θ_M is the fractional concentration of M in the surface layer;

η is the transmission of the analysis system. [6]

Clearly, sensitivity to species M is governed by α^+ and η . Y_M is the total yield of sputtered particles of M including neutral and ionic per primary particle impact. It increases linearly with primary flux, also non-linearly with primary particle mass, charge and energy.

Since the sputtering is a damaging process, the damage cross-section, σ , has been defined. It is related to the SI intensity by the equation:

$$I_M = I_{M0} \exp(-\sigma I_p) \quad \text{Equation 1.2}$$

Where I_M is the SI current of an element or species M after a certain flux of PI;

I_{M0} is the initial SI current of an element or species M;

I_p is the primary particle flux.

It is proved that the larger the fragments, the greater the rate of damage [6].

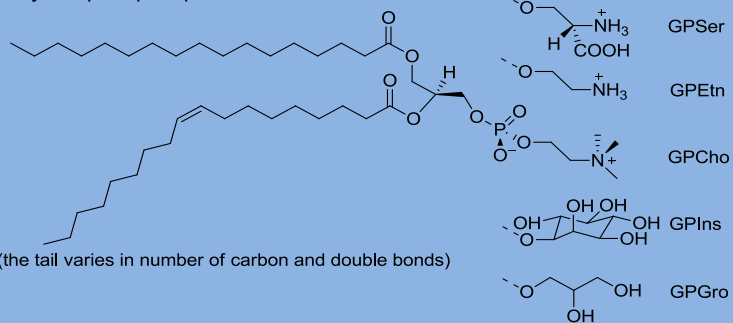
1.2 Lipidomics and ToF-SIMS

The definition of lipidomics has been determined as ‘the full characterization of lipid molecular species and of their biological roles with respect to expression of proteins involved in lipid metabolism and function, including gene regulation’ [34]. It is a newly emerging ‘omics’ field in the last decade driven by the surge of innovation in techniques, e.g., mass spectrometry (MS), nuclear magnetic resonance spectroscopy (NMR), fluorescence spectroscopy, dual polarisation interferometry and computational methods, coupled with the recognition and significance of lipids in neuroscience [35, 36] and in many metabolic diseases, e.g., obesity, atherosclerosis, stroke, hypertension and diabetes [37]. With the same impetus, novel IMS techniques may shed some light on this field owing to their ability to locate the lipids spatially in the biological samples. In this section, current techniques employed to lipids assay of biological systems are reviewed and compared. In particular, the applications of ToF-SIMS to lipid profiling of cells and tissues to assist the understanding of lipid-related biological functions and diseases progression are discussed.

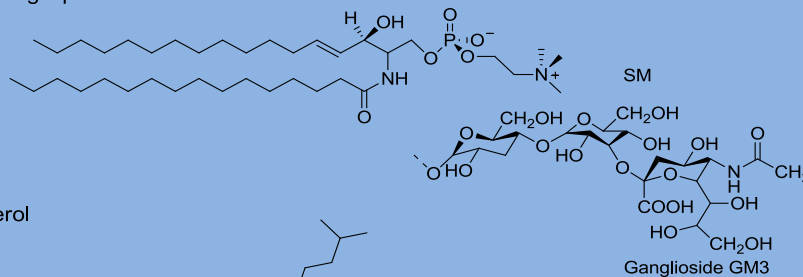
1.2.1 Lipid classification and functions

Lipids, the hydrophobic or amphipathic small molecules, derived from ketoacyl or isoprene subunits, are defined and classified into eight lipid categories according to LIPIDS MAPS Consortium. These include fatty acyls, glycerolipids, glycerophospholipids, sphingolipids, sterol lipids, prenol lipids, saccharolipids and polyketides. Each category comprises various classes and sub-classification to present a full picture of the lipids family [38, 39]. In eukaryotic cells, lipids are well organized in the membrane and cellular organelles. This strict spatial arrangement determines the crucial functions and types of lipids as seen in Fig. 1.5. It demonstrates the structures of lipid categories and representative classes in relation to their certain locations within the cell. Some lipids have exclusive locations for specialized functions, e.g., the mitochondria-specific cardiolipin (CL). The molecular symmetry of CL is necessary for stabilizing and catalyzing the mitochondrial membrane proteins [40]. More interestingly, CL microdomains are revealed as essential activating platforms for apoptotic signals on mitochondria [41].

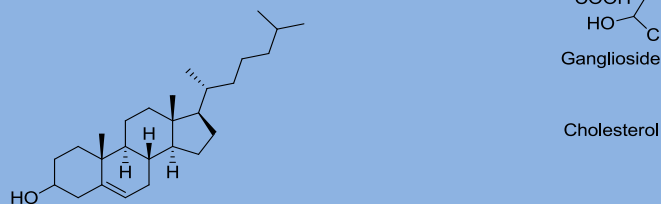
Glycerophospholipids



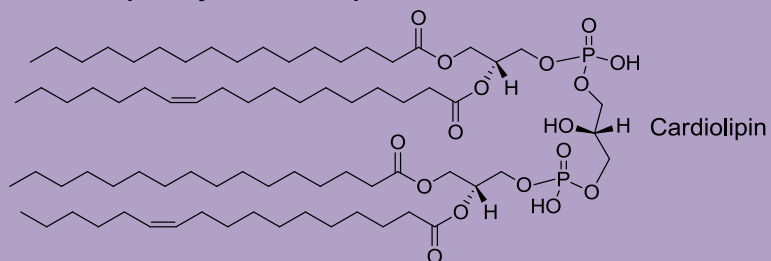
Sphingolipids



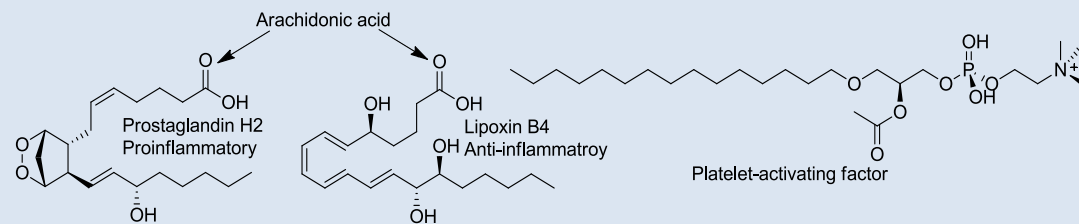
Sterol



Spatially restricted lipids to Mitochondria

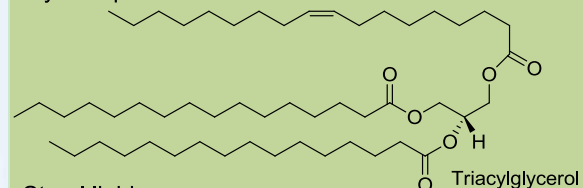


Mediator lipids

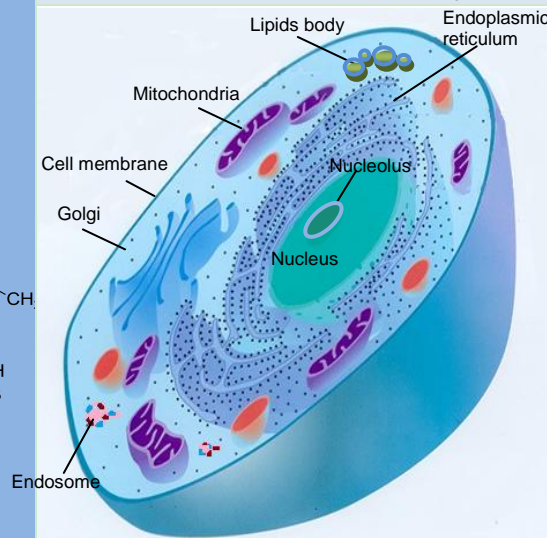
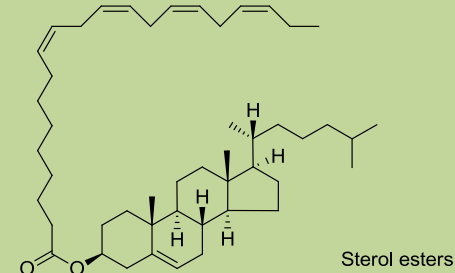


Major components of lipids body

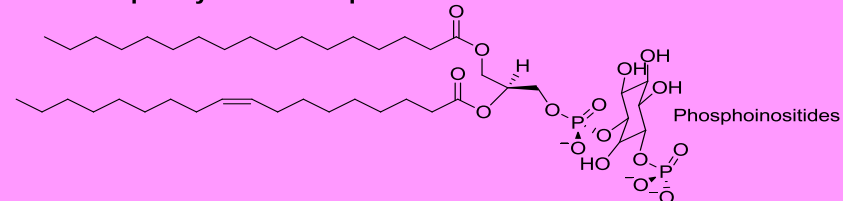
Glycerolipids



Sterol lipids



Spitially restricted lipids to endosomes



Spatially restricted lipids to endosomes

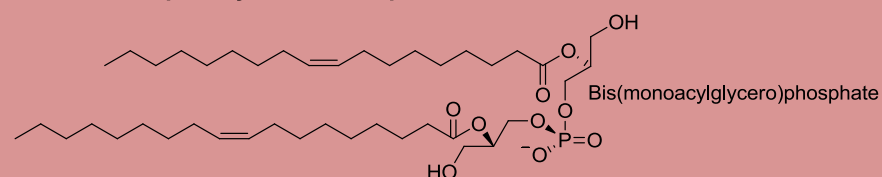


Fig. 1.5 The major classes of lipids and their cellular distribution in eukaryotic cell. Lipids usually with mass below 2000 Da are extremely diverse in chemical structures, resulting from anabolic and catabolic reaction pathways which are greatly affected by complex dietary and physiological control. This complicates the comprehensive understanding and classification of the lipids. Typically, the biomembrane is assembled from glycerophospholipids, sphingolipids and sterols (the structures of these lipids are in dark blue box). GPSer, glycerophosphoserine; GPEtn, glycerophosphoethanolamine; GPCho, glycerophosphocholine; GPIIns, glycerophosphoinositol; GPGro, glycerophosphoglycerol; SM, sphingomyelin). These lipids distribute asymmetrically in the plasma membrane and cellular organelle membranes. Some lipids are exclusive to certain organelles, e.g., CL only exists in mitochondria (as in purple box), bis (monoacylglycerol, MAG) phosphate is in endosomes (structures as in pink and brown box). Special distribution attributes to certain functional domain. Some lipids are metabolised from membrane lipids as second messengers more freely transferring between cellular compartments (as in light blue box). The very neutral lipids, e.g., triacylglycerol (TAG) and sterol-esters, are clustered in the endoplasmic reticulum and lipid body as nutrients. The picture of cell in the middle was reproduced from reference[42]. (The figure is in the previous page).

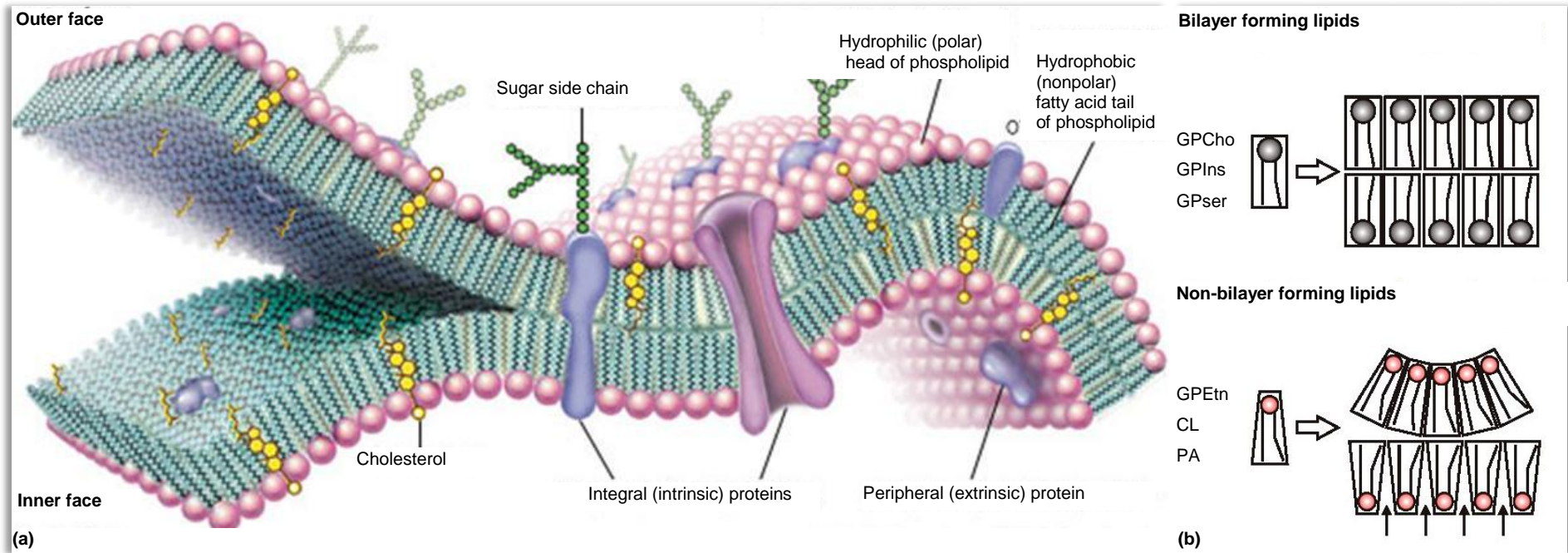


Fig. 1.6 The structure of cell membrane. (a), lipid bilayer structure. Reproduced from reference[43]; (b), bilayer and non-bilayer phospholipids. The conical shape of nonbilayer lipids induces membrane curvature or creates a unique biochemical microenvironment in a planar bilayer, where the hydrophobic parts are exposed between neighbouring phospholipids (marked with arrows). Reproduced from reference[44].

In their most important function, lipids can associate noncovalently to generate the basic bilayer structure of the biomembrane. This flexible bilayer sheet serves as the boundary of cells with external environments for maintaining integral physiochemical properties and creating an interior environment and embedding sites that are necessary for proteins to function and interaction. Recent studies have revealed that the clusters of sphingolipids and cholesterol can form 'raft' microdomains discretely on the plasma membrane that are more mobile and flexible, upon which certain membrane proteins dwell to perform specific functions, *e.g.*, signalling and endocytosis [45-47].

A typical plasma membrane of animal cells is assembled from glycerophospholipids, sphingolipids and sterols [48]. As seen in Fig. 1.5, all three classes of lipids are amphipathic molecules having a hydrophilic head group and hydrophobic tail. The hydrophobic effect and Van der Waals interactions cause the tail groups to self-associate into a bilayer with the polar head groups oriented towards water as shown in Fig. 1.6 (a). The lipids distribute asymmetrically within the two halves of the bilayer. Phosphatidylcholine and sphingomyelin mainly construct the outer leaflet, whereas phosphatidylethanolamine and phosphatidylserine along with phosphatidylinositol are predominant in the inner layer [49]. The asymmetric distribution is partially determined by the natural shapes of the lipids as shown in Fig. 1.6 (b). The conical shape of non-bilayer lipids can induce membrane curvature or budding in the inner leaflet. Cholesterol, having equal molar amount as phospholipids, acts as a 'spacer' between the long nonpolar tails of phospholipids rendering the bilayer the appropriate rigidity and fluidity. The double bonds in lipids fatty acid chains are also related to the membrane fluidity. In a restricted space *cis* bonds prevent the lipids from compact packing, and consequently influence the melting temperature and fluidity of the membrane [50].

Lipid bilayer dimensions vary according to the length of the nonpolar tails and sterols. Containing 16 to 24 carbon atoms in the hydrocarbon chain of phospholipids and sphingolipids, the double hydrocarbon core in the membrane is ~30 Å in width with variations induced by the lipids state and double bonds. Together with the polar headgroups, the bilayer can reach to 45-50 Å [51-53]. However, the width can be extended much more depending on the structure of the polar headgroups. Taking ganglioside GM3 (as in Fig. 1.5) as an example, it is obvious that with the much larger headgroup the dimension of the bilayer expands.

Aside from the construction of the bilayer membrane, lipids play diverse roles in biological systems. A second important role of lipids is to serve as a source of energy, *e.g.*, triacylglycerol (TAG) is the major form of energy stored in mammalian cells. Notably, TAG is rich in egg yolk as a building block for the embryo development. Moreover, lipids are precursors for numerous secondary messengers. Phospholipase-mediated hydrolysis of phosphatidylinositol-4,5-bisphosphate yields diacylglycerol (DAG), inositol-1,4,5-trisphosphate (IP3), and arachidonic acid (AA). All these molecules act as second messengers [54]. With rapid phosphorylation, DAG is transferred to phosphatidic acid (GPA) [55], an important intermediate in phospholipid synthesis and regulation of the enzyme function and bilayer structure [56]. IP3 is metabolized to generate various polyphosphorylated inositols, and IP3 itself is a cellular signalling molecule for regulation of biological processes, *e.g.*, the activation of Ca_2^+ release upon egg fertilisation and regulating cell proliferation [57]. AA can be enzymatically broken down to leukotrienes, prostaglandins and thromboxanes, serving as important modulators in inflammatory processes (as in the light blue box

of Fig. 1.5) [58]. Taking sphingolipids as another example, they are highly bioactive among membrane lipid, and can be enzymatically disassembled into ceramides that are potentially involved in the modulation of cell proliferation, cell cycle arrest and senescence [59]. Sphingosine, one of the metabolites from sphingolipids, coupled with its phosphorylated derivative sphingosine-1-phosphate, regulates the immune cell migration and could be a potential therapeutic target [60]. With regards to phospholipids, they can act as precursors to platelet activating factor and IP3 (the light blue panel in Fig. 1.5) [61].

The crucial role of the lipids is also demonstrated by many human diseases involving aberrant lipid anabolism and catabolism and potential therapeutic interventions that target the lipid signalling pathway for treating cancer, diabetes, neurodegenerative as well as infectious diseases. The balance of IP3 kinase and 3-phosphoinositide phosphatase, as well as the downstream effectors, regulate cell growth and death. These kinase inhibitors are therefore of great interests for development as novel cancer treatments [62, 63]. It is now clear that lipids are closely involved in the energy homeostasis through the breakdown of dietary fat (mainly TAG) into fatty acids, as well as the uptake, transport and storage of fatty acids. One anti-obesity strategy is to inhibit the digestive lipases for the purpose of reducing TAG utilization, *e.g.*, the commercial medicine Orlistat (Roche) [64]. There are also exciting opportunities for developing novel neuroprotective therapies due to the evident mechanisms of lipid metabolic disorders and imbalanced lipids-protein interactions, *e.g.*, aberrant cholesterol breakdown is linked to Alzheimer's disease [65], mutations in α -synuclein, a family of neuronal proteins binding to fatty acids and lipids to regulate the oligomerization, is attributed to early-onset Parkinson's disease in rare familial cases [66, 67], and cholesterol, glycosphingolipids and sphingosine are found in disorder in lysosomal storage disease especially in Niemann-Pick disease type C [68, 69].

1.2.2 System-level approaches in lipid research

In biological research, there is always the requirement to locate biomolecules or drugs for understanding their functioning and metabolism pathway. This urged the transferring of the lipid assays from non-imaging compositional analysis to imaging analysis in a wide range of biological samples, preferably with chemical specification. The following section briefly summarizes the current techniques employed in lipidomics studies with emphasis on the novel technique -- imaging ToF-SIMS, as well as the challenges and issues encountered with the application.

1.2.2.1 Contemporary techniques in lipidomics

MS based non-imaging techniques. Qualitative and quantitative approaches for lipid composition are the starting point of lipidomics. Mass spectrometry (MS) has played a central role in fundamental lipid studies. The traditional strategy for lipid detection and also as the platform for the LIPIDS MAPS Consortium is MS coupled with chromatographic separation, *e.g.*, thin layer chromatography (TLC), gas chromatography (GC) or high performance liquid chromatography (HPLC) [70]. Tandem MS is also applied on request to enable precursor ion scanning and precise structural identification especially coupled with the 'soft ionisation' methods, *e.g.*, electrospray ionisation (ESI) as it generates molecular or quasi-molecular ions and gives very little structural information. Through the selection of a particular precursor ion (a component of the normal mass spectrum) formed from a molecule or a mixture of molecules and its activation, usually by one or

more collisions with a neutral gas or a solid material, Tandem MS can generate characteristic product fragment ions for enhanced structure determination [71]. An essential process before this analysis is lipid extraction from the biological samples by a mixed solvents system following Folch [72], Lees and Sloane Stanley [73] or Bligh and Dyer [74] recipes with further tweaking to suit each lipid class [75]. During the extraction, the internal standards, typically deuterium-labelled lipids, are added for quantitative analysis. The issues in MS analysis are mainly caused by the incomplete extraction due to polar lipids (e.g., phosphoinositol) being lost in the water phase during the phase partition. In addition, high chemical background induced by fast-atom bombardment and chemical ionisation was also a problem in the early days [76, 77]. Since the 1980s, technological advances have allowed shotgun lipidomics [78] based on ESI [79]. The shotgun approach enables the simultaneous analysis of the lipids with no need for chromatographic separation and provides lipids class favoured analysis named 'intrasource separation' (negatively charged lipids, e.g., PI, PG, PS are analysed in negative mode; a base (e.g., LiOH) added secondly to promote weakly anionic lipids like PE; and then polar lipids are assayed in positive mode) [80]. The extraction-based sample preparation is the same as the traditional strategy, thus the spatial distribution of lipids in the biological system is lost. The complicated lipid compositions and ionisation suppression further pose problems for identifying the low abundance lipids in biological samples and for quantitative analysis.

These MS based techniques have established the solid foundation of the lipidomics approach for biological and pharmaceutical studies. The high-throughput lipids profiling of the mammalian macrophage showed significant remodelling of the subcellular lipodome that might reflect mitochondrial oxidative stress and the release of arachidonic acid from the ER in response to cell activation [81]. Particular patterns of lipid species could be an indicator of diseases progression, e.g., cholesterol links to Alzheimer's disease [65, 82], lysophospholipids to cancer [83] and DAG with periodontal tissue disease [84], which further assist disease diagnosis and drug development [85]. All these studies promoted the new concept of system biology approaches, which highly relies on MS-based technique for the global metabolomics profiling in living systems [86].

Rapid advances in technology have brought a number of new application and ionisation methods. Isotope labelled exogenous substances, e.g., deuterium exchange mass spectrometry (DEMS) is employed for lipids conformation and membrane interactions [87]. Ambient ionisation methods that are capable of analysing biomedical samples in their native state are introduced including desorption electrospray ionisation (DESI) in 2004 [88] and laser ablation with electrospray ionisation (LAESI) in 2007 [89]. These methods brought MS to the real biological world with minimum sample preparation; however the detected lipid class are limited to phospholipids due to the type of spray solution.

Chromatographic separations. It is worth mentioning that TLC, GC and HPLC have been employed separately for a long time and well established for quantitative analysis of various classes of lipid compounds. GC analysis is routine approach for fatty acids. The major limitation for chromatographic separation is the moderate sensitivity and throughput capacity [90], along with the complicated sample pre-processing, e.g., chemical derivatization of fatty acids for GC.

Nuclear magnetic resonance (NMR) spectroscopy. Belonging to the non-imaging analysis

techniques, NMR spectroscopy (^1H -NMR, ^{13}C -NMR) is a powerful tool to unveil the molecular structure of purified lipids and the dynamics of lipid membrane [91]. It has been successfully used in characterization of the mechanism of transmembrane protein regulation and ion channels, as well as metabonomic studies [92]. Compared with mass spectrometry, it requires a large quantity of sample and only has low sensitivity. Moreover, the restricted movement of lipids in the bilayer results in poor structure identification [91].

Fluorescence spectroscopy. The fluorescence probes (lipids and/or proteins), e.g., Nile red, Mitotracker and green fluorescent protein are used for *in vivo* detection of lipid heterogeneity and membrane protein/lipid interactions [93, 94]. However, the technique suffers from indirect chemical localization and limited availability of the tags and lipids antibodies. Moreover, the fluorescence tags could alter the chemical properties of the target molecules subsequently perturb the cellular functions [95, 96].

Atomic force microscopy (AFM). AFM can provide microscopic information of topography of biological systems and allows *in situ* investigations under near physiological conditions. It has found further applications in monitoring dynamic biological events, e.g., membrane bilayer alteration, remodelling or digestion following various external stimuli of drugs, proteins activation, nanoparticles and solvents [97, 98].

Scanning electron microscopy (SEM). SEM is another alternative method to provide topographical and morphological information. However, along with AFM, these two techniques share the same drawback of non-chemical specificity [99, 100].

Imaging Mass spectrometry (IMS). IMS has significant advantages in terms of spatial location of various lipid species which provide direct information of the crucial roles of lipids in diseases and cell apoptosis. MALDI-MS and ToF-SIMS, two essential types of IMS, have been developed over decades to explore the biological field, as discussed below.

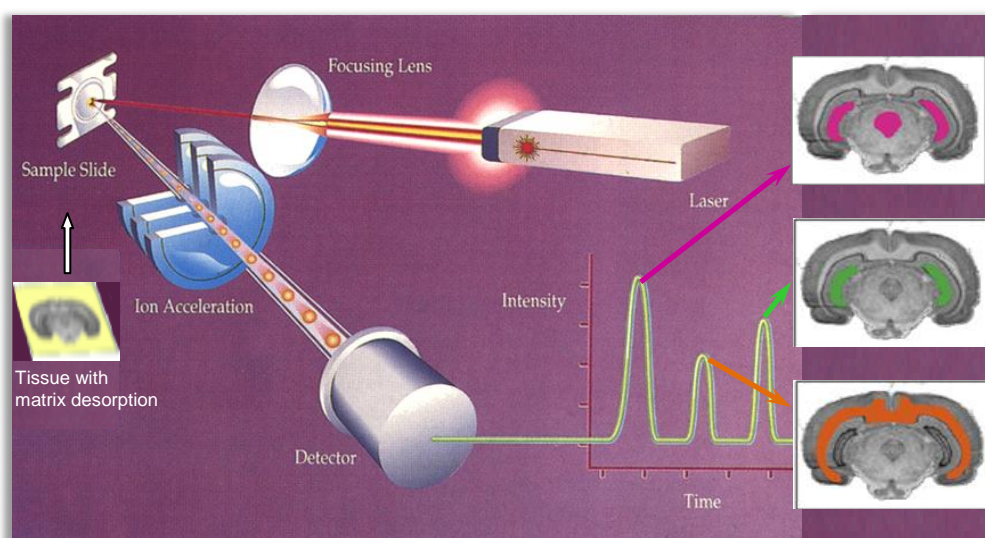


Fig. 1.7 Schematic of tissue section imaging using matrix-assisted laser desorption ionisation mass spectrometry (MALDI-MS). Reproduced from reference [101].

MALDI pulses a focused laser beam to ablate the sample surface following the matrix desorption, and the resulting ions are detected using a mass spectrometer. Typically spatial resolution $\sim 10\ \mu\text{m}$

is used to generate sufficient SIs signals for 2D molecular imaging as shown in Fig. 1.7. Matrix selection and homogeneous deposition onto the sample surface is a crucial step for MALDI analysis. Several commonly used matrixes are 2,5-dihydroxy benzoic acid (DHB), *o*-cyano-4-hydroxycinnamic acid and 9-aminoacridine (9-AA) [102], which serve to absorb the energy of primary UV laser pulses and ionize the analyte. The desorbed ions from the sample surface are mainly singly protonated even electron ions or adducts with alkali metals. The application of MALDI used to focus on peptide/protein localisation in biological tissues [103], and has extended to drug and lipids distributions in biological systems [104].

For proteins and peptides, MALDI-IMS is capable of analysing them directly or following enzymatic on-tissue digestion. With enzymatic digestion, the sensitivity is improved and sample complexity is reduced to avoid the ion suppression effect. The proteome/peptidome and their variation has been localised in various disease tissues, including Alzheimer's disease, Parkinson's disease, Fabry's disease, kidney diseases and many types of cancer. Djidja *et al.* [105] used matrix-assisted laser desorption/ionisation-ion mobility separation-mass spectrometry (MALDI-IMS-MS) to assess a wide range of tumour tissues, facilitated by tissue micro-array technologies. Combined with PCA data analysis, the study helped to generate the tumour classification based on the protein profile pattern.

Various lipids have been detected in healthy/diseased tissues and single cells using MALDI-MS. GPCho, SMs, and sterols can be ionized in positive ion mode. GPIIns, GPSer, and STs ionize well in negative ion mode. GPEtn can be detected in both polarities. Touboul *et al.* [106] first demonstrated the possibility of detection of free fatty acid using MALDI in rat brain section sprayed with 9-AA matrix as shown in Fig. 1.8 (d-f). Compared with ToF-SIMS images of section from same rat brain in Fig. 1.8 (h-n), MALDI identifies more molecular ions of phospholipids in positive mode and has comparable imaging capability with the similar focus-sized laser beam as to a Bi_3^{2+} beam. A few trials of single cell analyses were also performed using MALDI-MS. Ferreira *et al.* [107] analysed intact single embryo and oocyte. This direct lipids profiling revealed SM, GPCho and TAG species. Coupled with PCA analysis, the characteristic lipid profiles of gametes and embryos was revealed to respond to modifications due to developmental stages and in vitro culture conditions of bovine embryos. However, single cell studies with MALDI-MS were carried out multiple lipids assay rather than imaging mode due to the poorer spatial resolution.

MALDI has also been used to track metabolomics and pharmaceuticals. The general problem in this kind of study is that low mass compounds suffer from interferences with MALDI matrix. However, the studies have demonstrated that tandem MS or high resolution MS is efficient to isolate the target compounds from matrix [108], or applying the surfaces instead of the matrix on sample surface could be another solution [109]. MALDI-MS has been used to visualize the distribution of drugs and their metabolites in tissue, *e.g.*, anticancer drug vinblastine in the whole rat body [110], and platinum anticancer drug oxaliplatin in rat kidney [111].

With technique advances, MALDI has evolved to perform ambient analysis, *e.g.*, atmospheric pressure Infrared MALDI (AP IR-MALDI). The newly developed DESI and LAESI imaging are also capable of analysis at atmospheric pressure. A comparison of current MS based imaging technologies is present in Table 1.1.

It is obvious there is no one technique that can do all the jobs as each has advantages and downsides. Within the techniques for lipids assay, IMS is the only method which enables to simultaneously obtain the chemical information and spatial distributions over the surface or within the depth of biological specimens. Particularly, the higher spatial resolution and equivalent sensitivities in chemistry has enabled ToF-SIMS to detect more subtle microdomains of biological systems. The following section 1.2.2.2 focuses on the application of ToF-SIMS in various model and real biological systems.

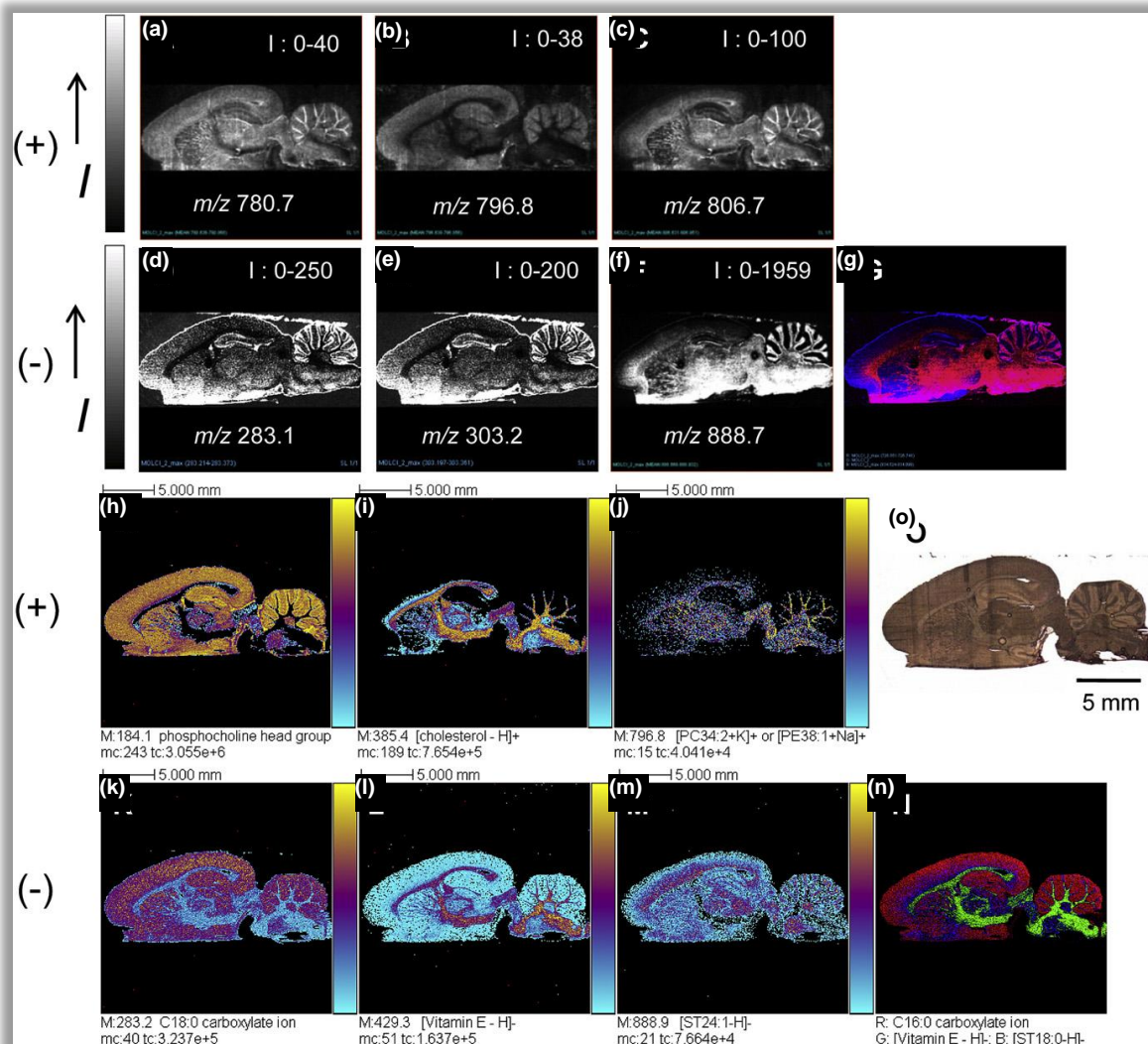


Fig. 1.8 Ion images of a sagittal rat brain section. (a-c): MALDI-ToF positive ion images. (a), m/z 780.7⁺ ([GPCCho 36:5+H]⁺); (b), m/z 796.8⁺ ([GPEtn 40:4+H]⁺ or [GPEtn 38:1+Na]⁺ or [PC 34:2+K]⁺); (c), m/z 806.7⁺ ([GPEtn 44:12+H]⁺ or [GPCCho 38:6+H]⁺). Images have 106×237 pixels with a pixel size of 100 μ m. (d-g): MALDI-ToF negative ion images. (d), m/z 283.1⁻ (fatty acid carboxylate [C18:0-H]⁻); (e), m/z 303.2⁻ ([C20:4-H]⁻); (f), m/z 888.7⁻ ([sulfatide (ST) d18:1/24:1-H]⁻); (g), two colour overlay between MALDI-ToF ion images of [GPEtn 36:2-H]⁻ (m/z 726.6⁻) in red and of phosphatidylserine [GPSer 40:6-H]⁻ (m/z 834.7⁻) in blue. Images have 214×408 pixels with a pixel size of 50 μ m. The value of intensity 'I' indicated in white in each image corresponds to the minimum and the maximum intensities in a pixel. (h-j): ToF-SIMS positive ion images. (h), m/z 184.1⁺ (phosphocholine head group); (i), m/z 385.4⁺ ([cholesterol-H]⁺); (j), m/z 796.8⁺ ([GPEtn 40:4+H]⁺ or [GPEtn 38:1+Na]⁺ or [GPCCho 34:2+K]⁺). (k-n): ToF-SIMS negative ion images. (k), m/z 283.2⁻ (fatty acid carboxylate [C18:0-H]⁻); (l), m/z 429.3⁻ ([vitamin E-H]⁻); (m), m/z 888.9⁻ ([ST d18:1/24:1-H]⁻); (n), three colour overlay between ToF-SIMS ion images C16:0 carboxylate ion (red), vitamin E (green) and [ST d18:1/18:0-H]⁻ (blue). For all ToF-SIMS images: PI Bi₃²⁺, 50 keV, 3.4×10^8 ions/cm², area 22.4×22.4 mm², 256×256 pixels, pixel size: 87.5×87.5 μ m². The amplitude of the colour scale corresponds to the maximum number of counts mc and could be read as [0, mc]. 'tc' is the total number of counts recorded for the specified m/z (it is the sum of counts in all the pixels). (o), optical ion image of the sagittal rat brain section. Reproduced from reference [106].

Table 1.1 Comparison of imaging mass spectrometries

Method	Ionisation	Sample preparation	Mass range	LOD	Imaging lateral resolution	Depth profiling; quantitative	In vivo	Biological application	Limitations
MALDI	Pulsed laser beam excites the matrix or nanoparticles coated on the biosamples to form ions [112, 113].	The tissue embedded into OCT or FFPE and then microtome sectioned to 2-20 μm sections onto conductive substrates (steel plate, ITO glass slide), followed by electrospraying matrix (DHB, 9-AA) or nanoparticles.	~100 kDa, small molecule as well with appropriate matrix	1fmol /pixel	25-100 normally, 10 μm is the smallest been reported	2D; semi-quantitative	Vacuum analysis N	Peptides and proteins in large tissue samples; recently used in lipidomics to visualize various lipids and metabolites in tissue [114], even in single embryo [115].	Matrix affects; relatively poor resolution.
AP IR-MALDI	Mid-infrared laser excites water molecules to eject the plume off the sample [116, 117].	Direct sampling of frozen sample to conductive substrates.	~3 kDa	1fmol /pixel	40 μm with oversampling	2D; semi-quantitative	Ambient analysis Y	Biological samples with sufficient water content, e.g., plants, fruits [116, 117].	Sample restriction.
ToF-SIMS	PI beam (e.g., Cs^+ , Bi_3^+ , Au_3^+ , C_{60}^+) directly bombards the samples and generate SIs.	Tissue sections as in MALDI without matrix coating. Single cells are chemically or cryo-fixed, followed by freezing-drying or keep frozen hydrated.	<2000 Da	ppm	Nanometre-scale, smallest beam size of 30 nm from Cs^+ ion beam	2D & 3D depth profiling; semi-quantitative	Vacuum analysis N	Tissue sections and single cells for locating various lipids and metabolites [118]. Also proteins, blood markers [119].	Limited m/z , etc, as in detailed 1.2.2.3.
DESI	Charged droplets of mixed solvent impacts the sample to eject secondary droplets [88, 120].	Direct sampling under ambient conditions, tissue section as standard procedure as used in MALDI.	~66 kDa	4 fmol	200-400 μm	2D, 3D realized by serial sectioning; quantitative	Ambient analysis Y	A number of applications on tissues, e.g., 3D reconstruct of mouse brain [121].	Analyte wash effects; sensitive to the surface; ill-defined sampling area [122].
LAESI	Mid-infrared laser beam (2.94 μm wavelength) excites water molecule in samples to eject the plumes. The plumes are then coalesced and ionized by charged electrospray droplets [89].	Direct sampling onto conductive substrates.	~66 kDa	8 fmol	300-400 μm	N/A; quantitative	Ambient analysis Y	biological samples with sufficient water content, e.g., plants [89].	Limited mass range; sample restriction.

OCT, optimal cutting temperature compound; FFPE, formaldehyde-fixed and paraffin-embedding; DHB, 2,5-dihydroxybenzoic; 9-AA, 9-aminoacridine.

1.2.2.2 Identification and imaging with ToF-SIMS

1.2.2.2.1 Sample considerations

Sample preparation is the key to successful analysis as ToF-SIMS is highly surface sensitive and operated in high vacuum that is obviously not a biological friendly environment. Thus careful sample preparation is required to ensure that the investigation reveals the pristine information on the biological samples. Different strategies have been developed to handle the samples mainly in the form of tissue sections or single cells from the standpoint of preservation of their native state as close as possible, whilst meeting the sample handling requirements of ToF-SIMS. For cell samples, the developed methods are shown in Fig. 1.9 mainly based on the procedure of cell washing, preservation and drying or keeping the sample frozen-hydrated.

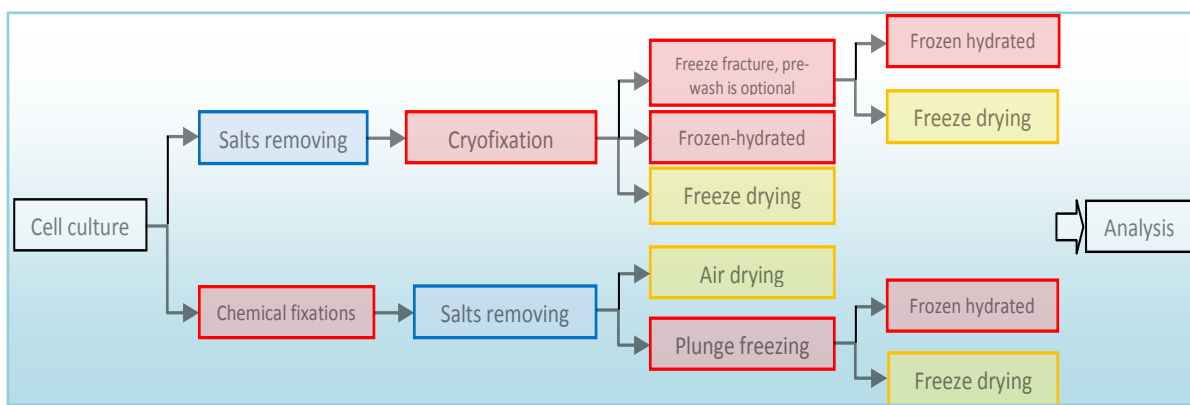


Fig. 1.9 Procedures for cell preparation for ToF-SIMS analysis. The blue boxes indicate the step of removing the salts, red boxes present different strategies to preserve the original chemical information, while the yellow boxes represent sample drying with different methods. The sample can also be analyzed in the frozen hydrated state, which requires the cryogenic sample stage in the ToF-SIMS instrument.

Removing the salts arising from the culture media is a crucial step before any further treatment as the salts could suppress the ionisation of the biomolecules and cover the original chemical information. Due to the osmotic pressure, any inappropriate wash would cause cell bursting or lysing. Several washing media have been used, *e.g.*, water [123] and iso-osmotic solutions represented by sucrose, PBS, Tris, HEPES, magnesium acetate, sodium chloride, ammonium acetate and ammonia formate [124, 125]. Water washing is simple and leaves no residue but is only useful for the cells like frog embryo which itself resists the osmotic pressure. For other small cells, it causes cytoplasm leaks to smear the subcellular structure. The iso-osmotic solutions (*e.g.*, sucrose, PBS, Tris, HEPES and sodium chloride) can keep the cell integrity after the replacement with the cell culture medium, however, the residues of these chemicals on the samples have been found in the SIMS spectrum which complicates the data interpretation. Only ammonium acetate and ammonium formate solution at approx. 0.15 M could replace the salts without leaving residue on the sample because of their volatility in vacuum [126]. These two chemicals have also been used to assist ionisation in negative mode by forming salt adducts in ESI [127, 128], but no study regarding ammonia salts formation in ToF-SIMS was reported. Cell swelling was observed within a minute after exchanging the culture medium with ammonia formate solution, while live/dead-cell staining indicated the cells remained alive [125]. Instead of washing cells, Parry and Winograd [129] pre-incubated the cells with trehalose followed by freezing drying to preserve cell integrity.

However, another study revealed that the trehalose has an effect on membrane resistance of prepubertal ovine oocyte but not on following fertilisation and development [130].

Stopping the biological processes and preserve the cells in a native state is conventionally performed by cryofixation or chemical fixation in SIMS. Cryofixation requires plunge freezing the sample into liquid cryogen (nitrogen, propane, 2-methylbutane, etc); most frequently used chemical fixatives are aldehydes or alcohol, with only a few studies using osmium tetroxide as comparison [125]. Malm *et al.* [125] compared two fixation methods on human fibroblasts both subjected to freezing drying, suggesting glutaraldehyde fixation is better to keep the fine structure of the cell membrane, while cryofixation can maintain diffusible ions (e.g., Na^+ , K^+) along with higher ion yields of GPCho molecular ion. Both methods are capable of retaining lipids distribution and large-scale cell morphology. The finding is in agreement with the observation of Grovenor *et al.* [131]. For subcellular exploration, Chandra [132, 133] developed a simple sandwich freeze-fracture method without prewashing the cells. The SIMS analysis showed close-to-nature K^+/Na^+ ratio and well preserved subcellular structures confirmed by SEM and fluorescence imaging. However, the reproducibility of the fracture method was questioned, and the fracture plane is mostly within the membrane bilayer and the cytoplasm is still not exposed [133]. Rabbani *et al.* [134] reported a newly developed mouse trap device to fracture HeLa cells inside the instrument automatically. The HeLa cells were grown on the mouse trap and freeze fractured *in situ* to expose the nuclear structure, followed by analysis in the frozen-hydrated state. This approach was proved to benefit the subcellular structural imaging compared with formalin fixed, freeze-dried cells. There are other techniques developed to preserve biological samples, e.g., high pressure freezing (HPF). HPF can preserve the ultrastructure larger than a few micrometres and prevent ice crystal damage in thick samples [135]. The technique is widely employed by electron microscopy, only Nygren *et al.* [136] applied it to prepare tissue for ToF-SIMS. Sosinsky *et al.* [137] revealed that chemical fixation coupled with HPF works better than chemical fixation alone on ultrastructure preservation through SEM imaging.

Following the preservation, the cell can be analysed in frozen-hydrated or dried state. The sample drying procedure is usually performed within the ToF-SIMS instrument under controlled low temperature or in a freeze dryer to prevent the water or contaminant in the air from condensing onto the sample surface. Alternatively, the samples can be air-dried. Berman *et al.* [124] described a simple blow dry procedure after salt washing using an inert gas (e.g., N_2) for fast sample preparation. Although the distribution of diffusible subcellular elements is lost, the morphology is still retained for investigation. Actually for both frozen hydrated or dried samples, flash freezing is necessary to prevent obscuring the biological features [138].

Besides cellular preparation, there are several other issues that can also affect the SIMS analysis. Before the sample is transferred to the instrument, the contamination from the atmosphere or lab environment should be avoided. One of the notorious contaminants in the lab is polydimethylsiloxane (PDMS) which has strong peaks at m/z 73⁺, 147⁺, 207⁺, 75⁻, 149⁻, and 223⁻. Transferring the sample with the protection of inert gas and minimal contact with lab facilities can minimize the chances of being contaminated. The topography should also be considered as the SIs yields can be affected. ToF-SIMS still favours flat samples to avoid possible beam shadowing effects, which is in conflict with the fact that real cells and tissues are always topographically

challenging. Investigation has been performed on spherical objects [118] or metal wires [139] to understand topography effects and produce possible solutions. The special designs of the J105 3D Chemical Imager offers solutions to circumvent topography effects to some extent, as described in Chapter 2. During the SIMS analysis, the insulated biosamples can cause severe charging, which further requires the sample to be mounted on the conductive substrate and as thin as possible, in addition, the electron flood gun can be used to neutralize the charges, as detailed in Chapter 2.

To prepare tissue samples for ToF-SIMS, the developed method is based on histological sectioning and similar to tissue sectioning in MALDI without matrix coating (Table 1.1). However, the embedding matrix (e.g., fish gelatine and paraffin) used to enclose the tissues or organs in standard sectioning should be skipped when preparing the tissue sections for ToF-SIMS. The frozen samples can be directly glued onto the microtome with a small amount of OCT that avoids the matrix smudging across the sample surface during the cutting.

1.2.2.2.2 Untargeted analysis

Historically, SIs available for imaging were in the low mass range of m/z 100-200 due to the in-source fragmentation induced by atomic PI sources. Therefore the application of ToF-SIMS in the biological field was hampered until the advent of commercial polyatomic ion sources. Because the polyatomic ions greatly enhanced SI emission of organics and delivered higher mass biomolecules, it showed great potential for analysis of biological specimens. A wide range of biological samples have now been subject to investigation using ToF-SIMS. There is a type of study related to lipid standards, lipid models, tissue sections and even single cells in order to understand the fragmentation pattern of biomolecules under PI bombardment and comprehensive lipids assay. All these can be classified as fundamental untargeted analysis.

Lipids standards and model systems. Roddy *et al.* [140] studied the fragmentation of dipalmitoylphosphatidylcholine (DPPC) in the frozen-hydrated state under the sputtering of Ga^+ and In^+ ions. The DPPC molecular ion was seen in the spectrum though in very low intensity, the ion formation can be attributed to the proton in water matrix compared with the dry sample. Ostrowski *et al.* [141] confirmed the signature peaks of six membrane lipids including phosphatidylcholine, phosphatidylglycerol, phosphatidylserine, phosphatidylinositol, cholesterol and ST using an In^+ ion source. These characteristic peaks can be used to distinguish the membrane lipids either separately or in a mixture. This work further showed the 40-1000 fold enhancements in signals from the lipids by using a C_{60}^+ ion source versus a Ga^+ ion source.

The model systems that simulate cell membrane were also widely studied. Bourdos *et al.* [142] assessed Langmuir Blodgett (LB) films comprising DPPC, dipalmitoylphosphatidylglycerol (DPPG), and the lung surfactant protein (SP-C) as lung surfactant model. Except for DPPG, fingerprint fragments of other components were all found in the SIMS spectrum, and the SI imaging revealed heterogeneous distribution of the components within the film upon the compression, which proved the hypothesis that lung compression causes non-DPPC components to leave the monolayer. LB films with DPPC, DPPE, and cholesterol in different amount were also investigated by the Winograd group [143]. Probing the membrane composition on the nanoscale length, high resolution is a prerequisite. Kraft *et al.* [144] demonstrated high resolution (100 nm lateral resolution) imaging of phase-separated model lipid bilayer containing ^{15}N labelled 1,2-dilauroylphosphatidylcholine

(^{15}N -DLPC) and ^{13}C -labeled 1,2-distearoylphosphatidylcholine ($^{13}\text{C}_{18}$ -DSPC). Within a $20 \times 20 \mu\text{m}^2$ microdomain, it enriched with $^{13}\text{C}_{18}$ -DSPC (by imaging ion $^{13}\text{C}^1\text{H}^-$), as well as dispersed ^{15}N -DLPC (represent by $^{12}\text{C}^{15}\text{N}^-$ signal) as seen in Fig. 1.10. Further quantitative analyses calibrated using sets of lipid bilayers that systematically varied in isotopic composition, revealed that the $^{13}\text{C}_{18}$ -DSPC/ ^{15}N -DLPC ratio was typically $\sim 9:1$ in gel phase.

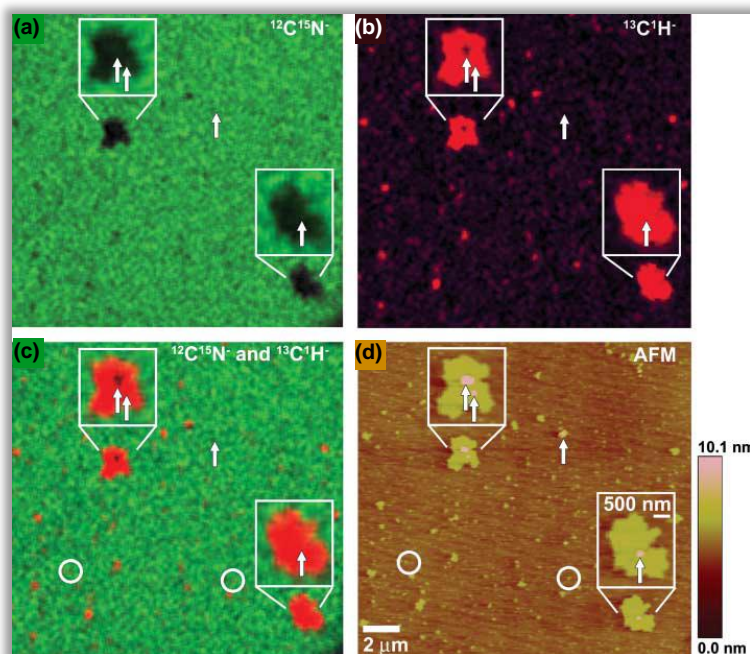


Fig. 1.10 NanoSIMS analysis of a freeze-dried, phase-separated supported lipid bilayer composed of ^{15}N -DLPC and $^{13}\text{C}_{18}$ -DSPC (a-c) and AFM image of the same bilayer location (d). Lateral resolution is 100 nm using a caesium PI beam. (a), the normalized $^{12}\text{C}^{15}\text{N}^-$ SI signal intensity (green) reveals the distribution of ^{15}N -DLPC in this area; (b), the normalized $^{13}\text{C}^1\text{H}^-$ SI signal (red) shows the distribution of $^{13}\text{C}_{18}$ -DSPC in the membrane; (c), overlay of the two lipid-specific ion signals; (d), comparison of the AFM image of the membrane topography that was acquired at the same sample location prior to SIMS analysis. Arrows indicate objects in the AFM image that are unlabeled debris, not labelled domains, and their locations in the SIMS images. Reproduced from reference [144].

Liposomes are also a useful model for cell membranes and investigation of membrane dynamics. Cannon *et al.* [145] used $20 \mu\text{m}$ liposomes prepared with cholesterol and either DPPC, dipalmitoylphosphatidyl-N-monomethylethanolamine (DPPNME) or dipalmitoylphosphatidyl-dimethylethanolamine (DPDME). Upon the fusion of the liposomes the samples were frozen in a time course. The SIMS analysis revealed interesting lipid distribution at the fusion point, showing the heterogeneous lipids at the junction, and redistribution until a homogeneous phase formed.

Single cell imaging. A number of groups have put considerable effort into chemical imaging of the membrane and interior of single cells using ToF-SIMS with the achievement of high lateral resolution. The Winograd group have pioneered single cell imaging using the freeze-fracture method. Hydrocarbons in low mass and exogenous molecules were detected across *Paramecium* [146]; phosphocholine and cholesterol were precisely located to outer cell membranes of rat pheochromocytoma (PC12) with the aid of DiL (membrane outer layer fluorescent marker) [147, 148]. These studies also reinforced the idea of high K^+ and low Na^+ as a ‘golden rule’ of successful cells preservation [147]. The fracture device has also been developed for easy and efficient *in situ* manipulation, e.g., spring-loaded trap system. The success of employment of the device to PC12 cells demonstrated PE concentrated domain coupled with less PC which is likely to be the result of

exposure of inner cell membrane [149]. Other groups have used a dual ion beam approach to probe the interior domain in single cells to generate 3D images. Mainly C_{60}^+ ion beam was employed between two analysis cycles as a sputtering source [150-152], as well as focused Ga^+ ion source in high current mode was used to cross-section the cell [153]. The motivation for the dual beams method results from the chemical damage to biosamples induced by atomic and metal cluster ion beams, which inhibits the continuous depth profiling for obtaining molecular information.

The C_{60}^+ ion source is able to reach the perfect equilibrium between damaging and removing materials from a biological system. Its advent added a third dimension to biomolecular imaging. Moreover, a well-focused 40 kV C_{60}^+ ion source was developed by the Vickerman group for single beam 3D imaging [154]. The impressive results include first 3D analysis of *X. laevis* oocyte [123], benign prostatic hyperplasia (BPH) cells [155] and HeLa cells [134, 156]. As seen in Fig. 1.11, the GPCho, DAG, TAG and cholesterol were visualised within 90 μm depths of *X. laevis* oocyte varying in distribution patterns. However, 3D reconstruction of cell image can be problematic without defining the z scale. This becomes even more complicated considering that the sputter rates of various molecules are different. Combined with principal component analysis (PCA) for topography correction, Fig. 1.12 shows the high resolution 3D image of HeLa cells, that demonstrates spatial distributions of membrane (m/z 184.1 $^+$, phosphocholine) and nuclei (m/z 136.1 $^+$, adenine). The data was collected by voxels in that all detectable SIs in each depth are summed up as illustrated in of Fig. 1.12 (a), which is a different acquisition style from the one shown in Fig. 1.11 (a) that collects data only after each sputtering cycle. This new approach ensures that all the ejected ions from the sample are collected without waste of valuable information between two analysis cycles. Moreover, the focused C_{60}^+ ion beam has comparable lateral resolution with metal clusters ion beam (e.g., Au_3^+) but higher SI yields, offering novel molecular depth profiling at high resolution.

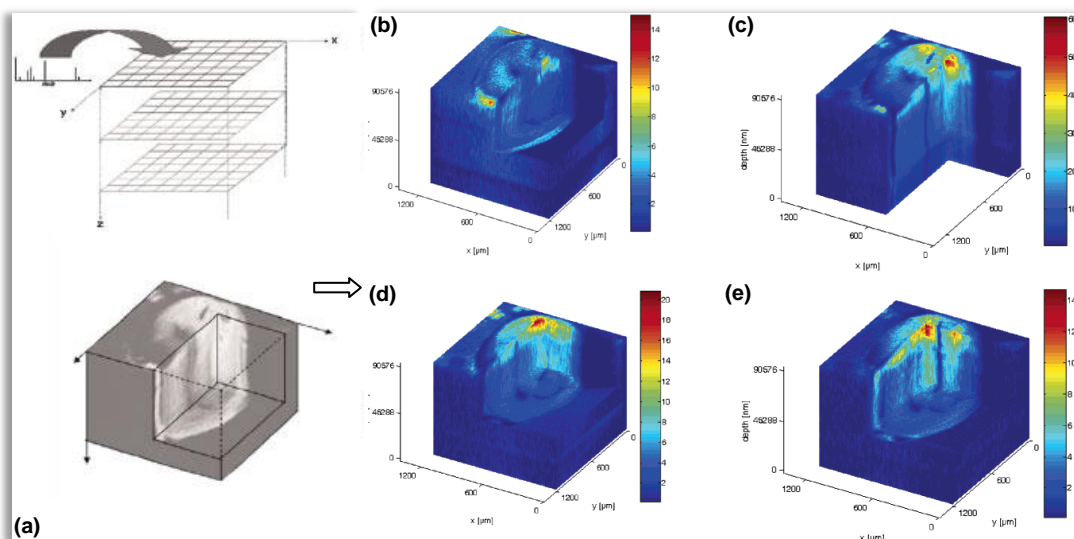


Fig. 1.11 3D biochemical images of freeze-dried *Xenopus laevis* oocyte using focused C_{60}^+ primary ion beam on a conventional ToF-SIMS instrument. (a), alternative sputtering and data acquisition; biomolecular changes showing changes in (b), phosphocholine peaks m/z 58 $^+$, 86 $^+$, 166 $^+$, and 184 $^+$; (c), signal summed over the m/z range 540-650 $^+$; (d), signal summed over the m/z range 815-960 $^+$; (e), cholesterol peak at m/z 369 $^+$. Colour scale normalized for total counts per pixel for each variable (m/z range). Reproduced from reference [123].

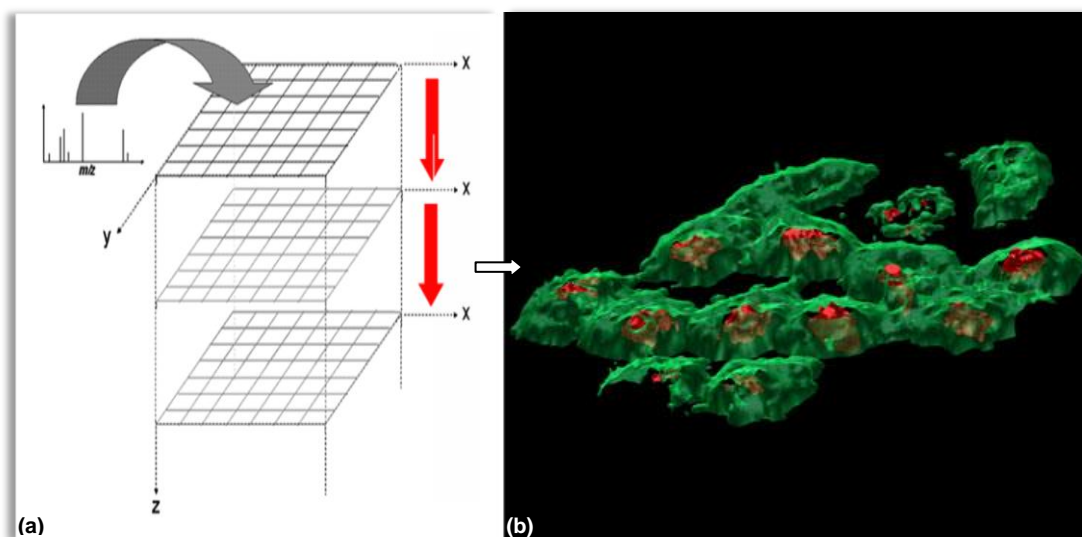


Fig. 1.12 3D C_{60}^+ cellular imaging of frozen-hydrated HeLa-M cells using the J105 3D Chemical Imager. (a), simultaneous data acquisition and sputtering; (b), 3D visualisation of the membrane (green, m/z 184.1 $^+$, phosphocholine) and nucleus (red, m/z 136.1 $^+$, adenine) chemistry in the frozen-hydrated HeLa-M cells following the use of PCA to identify the interface between the cells and the substrate to allow more representative data reconstruction. The visualised area is the same as the analysis area in the SIMS experiment, $250 \times 250 \mu\text{m}^2$, but inclined in order to aid 3D visualisation. Reproduced from reference [156].

Tissue imaging. These untargeted analyses using ToF-SIMS were designed to determine the lipids composition and their spatial distribution on the well established tissue models, including rat and mouse brain, cerebellum, kidney and leg sections. Touboul *et al.* [157] firstly measured rat brain section using a micrometre focused Au_3^+ ion beam at very low dose of 10^7 ions/cm 2 . Brunelle [158] worked on the same model system using Au_3^+ cluster beam. Phospholipids, cholesterol, vitamin E and fatty acid were recorded with high mass ions up to m/z 769 $^+$ in positive and m/z 892 $^-$ in negative mode. A more focused Bi_3^+ ion beam was employed later by the same group to generate detailed images of a rat brain section with an ultimate spatial resolution of 400 nm [159]. Jones *et al.* [160] adopted a C_{60}^+ ion beam to chemically map the rat brain section. The signals from the sample were stable even beyond the static limit dose, allowing continuous profiling in z depth. Thus cholesterol migration to the sample surface was revealed by comparison with frozen-hydrated sample; the *in vivo* dosed drugs in the sample were found to be likely binding to cholesterol. Kensey [161] acquired high-resolution chemical images of a complete sagittal section of the brain from the zebra finch, *Taeniopygia guttata*, which is a songbird with specific neural and developmental functions ascribed to discrete ‘song control nuclei’ of the forebrain. The result revealed a relative increase of palmitic acid C16:0 and oleic acid C18:1 in song control nuclei versus the surrounding tissue, along with the low level of phospholipids. The results are valuable to assess changes in lipid content during song circuit development and song learning of zebra finch.

In parallel with MALDI for locating the peptide, rat cerebellum section was analysed with ToF-SIMS using a Bi_3^+ beam. Phosphocholine, cholesterol and galactosylceramide with carbon chain lengths C18:0 (N-stearoyl galactosylceramide) and C24:0 (N-lignoceroylgalactosylceramide) with C24:0 (hydroxy-lignoceroylgalactosylceramide) were identified and located, as well as the new finding of the organization of myelin in white matter [162]. Nie *et al.* [163] combined ToF-SIMS with scanning probe microscopy (SPM) to probe lipid distribution and subcellular features of neurons in rat brain.

The phase shift images revealed distinctive subcellular features and ion images of CN^- and PO_2^- fragments from ToF-SIMS appear to define some of the subcellular features.

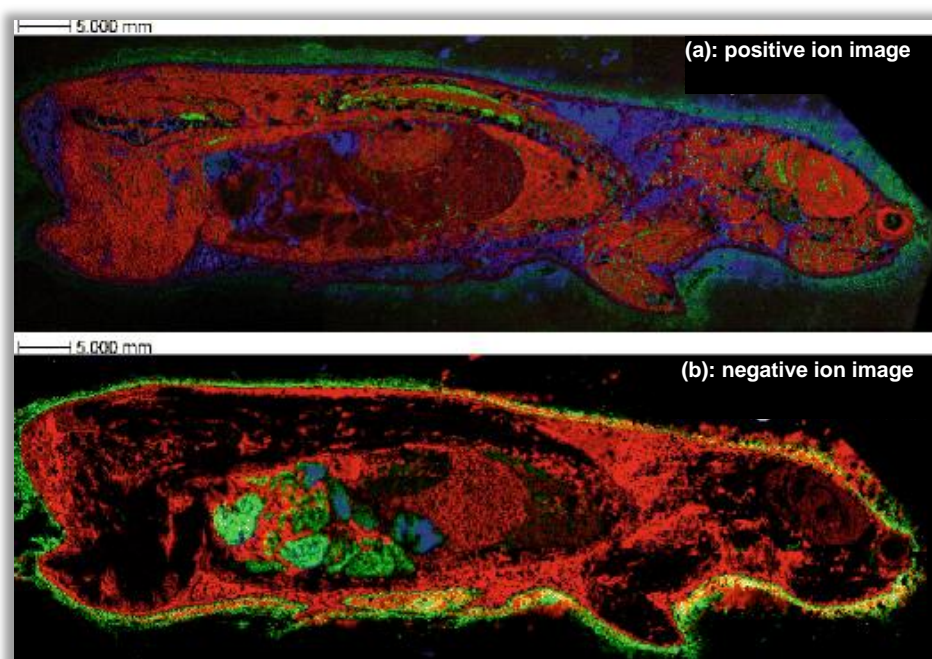


Fig. 1.13 ToF-SIMS images (three-colour overlays) of a whole mouse section. Field of view $84 \times 28 \text{ mm}^2$, 768×256 pixels, pixel size $109 \mu\text{m}$, Bi_3^+ PI fluency $6 \times 10^8 \text{ ions/cm}^2$. (a), positive ion image: red phosphatidylcholine fragment ($m/z 224^+$), green cholesterol ($m/z 369^+$ and 385^+), blue diacylglycerol ($m/z 577^+$); (b), negative ion image: red sum of stearic ($m/z 255^-$) and oleic ($m/z 281^-$) fatty acid carboxylates, green cholesterol sulfate ($m/z 465^-$), blue taurocholic acid carboxylate ($m/z 514^-$). Reproduced from reference [164].

The ToF-SIMS instrument has also been adapted to analyse large tissue sections by means of mosaic imaging. Brunelle and co-worker [164] imaged the whole body mouse section in a length of 7 cm with an accurate spatial resolution of $100 \mu\text{m}$, demonstrating the possibility to locate biomolecules or exogenous chemicals in many organs over the whole body of the animal with no need of *a priori* knowledge (Fig. 1.13). The novel J105 3D Chemical Imager developed in the Vickerman group enables tile images over large sections in a practical time frame without compromising the high lateral resolution. Various model systems including rat brain and kidney were analysed to locate a wide range of lipids up to $m/z 2000$ [165].

These studies with regards to model systems, single cells and tissues are the starting point to collect the biological information for visualization, and fully explore the potential applications of ToF-SIMS to biological and pharmaceutical fields. In the following section the targeted analysis using ToF-SIMS represents some interesting new directions, particularly focused on the exploration of biological processes, diseases and biomarker in different biological systems.

1.2.2.2.3 Targeted analysis

Biological processes in single cell. Cell membrane dynamics are of interest in biology because the various cellular functions are based on them, including fusion (*i.e.* exocytosis) and fission (*i.e.* cell division and endocytosis). However, the lack of suitable methodology makes it difficult to extend the investigations to the cellular scale. With the capabilities of subcellular scale imaging and chemical specification, ToF-SIMS provides the possibility to answer many biological questions. Free fatty acids play crucial roles in many physiological processes. They are released to the blood

bound to albumins and cross the membrane of adipocytes to be stored as TAG. However the transport mechanism across the membrane remains unclear. Kleinfeld and Kampf [166] applied NanoSIMS to investigate fatty acids movement in ^{13}C -oleate:BSA incubated adipocytes cells either dried directly or dried after washing. The intracellular concentrations of $^{12}\text{C}^-$, $^{13}\text{C}^-$, $^{12}\text{C}^{14}\text{N}^-$, $^{13}\text{C}^{14}\text{N}^-$ (or $^{12}\text{C}^{15}\text{N}^-$) were monitored simultaneously. As in Fig. 1.14, it shows a very high $^{13}\text{C}/^{12}\text{C}$ ratio in the lipid droplets. The phenomenon was also reinforced by imaging washed cells, though the overall ratio dropped. Incorporating stable isotopes, the technique demonstrated precisely subcellular tracing of fatty acids with nanoscale lateral resolution despite the lack of molecular ion information.

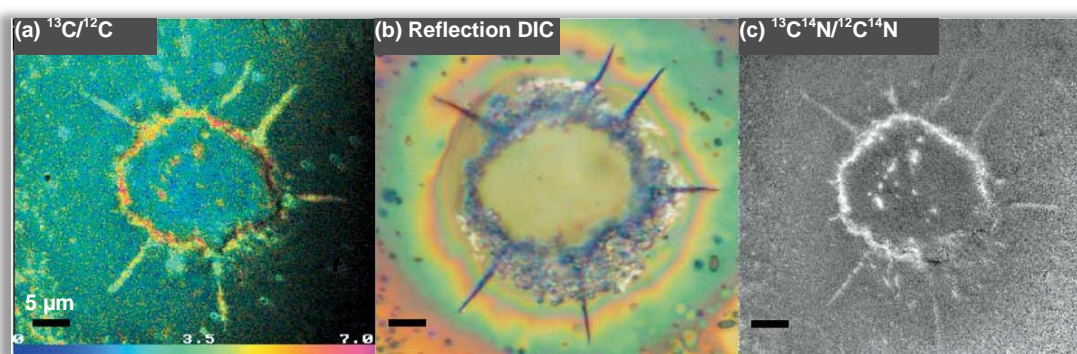


Fig. 1.14 Images of unwashed and argon blow-dried 3T3F442A cells treated with ^{13}C -oleate. (a), a hue saturation intensity (HSI) image of the $^{13}\text{C}/^{12}\text{C}$ ratios; (b), a reflection differential interference contrast (DIC) image of the same cells before analysis with NanoSIMS; (c), the $^{13}\text{C}^{14}\text{N}/^{12}\text{C}^{14}\text{N}$ distribution that reveals the excess ^{13}C in the lipid. (a-c) reveals the peripheral distribution of lipid droplets. The NanoSIMS images are $60 \times 60 \mu\text{m}^2$, 256×256 pixels and were acquired in 40 min. Reproduced from reference [166].

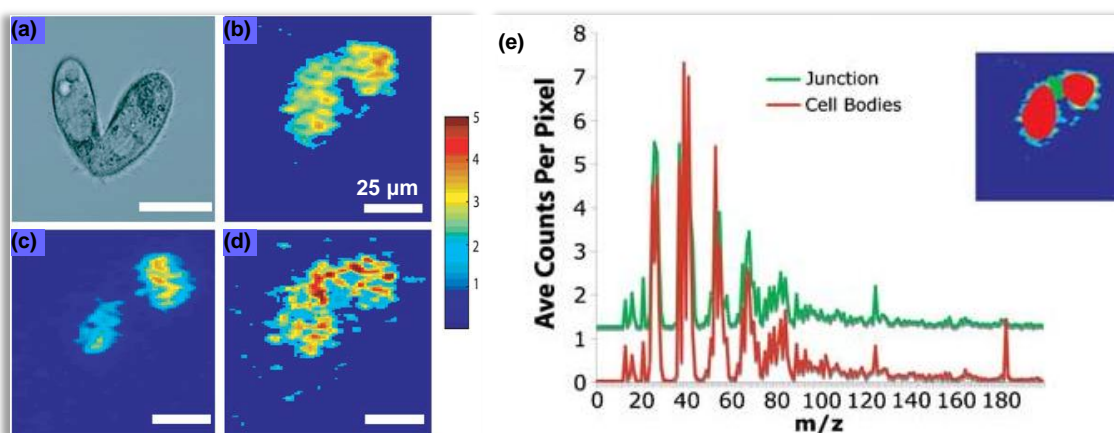


Fig. 1.15 ToF-SIMS analysis of a strongly paired mated *Tetrahymena thermophila*. (a), differential interference contrast microscopy image of a mating cell pair; (b-d), SIMS images of a pair of mating *T. thermophila*. C_5H_9 is mapped in (b), GPCho is in (c), and 2-AeP is in (d) (the intensity in the 2-AeP image has been multiplied by 3); (e), region of interest analysis of the same cells. The mass spectrum from cell bodies is in red, and from the junction is in green. The inset highlights the regions on the SIMS image, red for the cell bodies and green for the junction. Reproduced from reference [167].

Membrane fusion is another interesting dynamic process still lacking total understanding. Ostrowski *et al.* [168] and Kurczy *et al.* [167] studied the membrane fusion site between mating *Tetrahymena* to investigate lipid rearrangement in the fusion junction using ToF-SIMS. Two lipids were found to play important roles in the event, glycerophosphocholine lipids (GPCho, fragment at m/z 184⁺) and the 2-aminoethylphosphonolipids (2-AeP, fragment at m/z 126⁺) (Fig. 1.15). The study revealed that highly contoured non-lamellar lipids, 2-AeP, replaces the lamellar GPCho lipids at the conjugation site during mating. A time course study showed that structural changes in the

membrane preceded chemical changes. The study, for the first time, clearly linked chemical structure with function of different lipids in biological process, providing further understanding based on the chemical visualization of the process. However, it is both a new promising opportunity and great challenge to specify the intact lipids species and proteins involved within the system.

Tissue/disease analysis. The difference in composition and location of lipids could be used to distinguish the normal tissue section from the diseased one. This hypothesis is behind the application of ToF-SIMS to pathology, and the new findings by SIMS imaging could provide further understanding of cellular biochemistry and the mechanism of disease progression. Touboul *et al.* [169] analysed the leg section of Duchenne muscular dystrophy mouse using an Au_3^+ cluster beam. The vastly different ratios of C16:0/C16:1 and C18:0/C18:1 was found in the damaged, under degenerated and stable muscle area respectively. Moreover, the comprehensive mapping of lipid species revealed that the areas under oxidative stress show an accumulation of vitamin E and Coenzyme Q9, which are known as antioxidants. Human striated muscle samples were also subjected to cluster ToF-SIMS imaging using a 25 keV Bi_3^+ ion beam. Characteristic distributions of various lipids were observed. Vitamin E and GPIs had intense distribution within the cells, whereas intact GPCho accumulated over the most damaged areas of the dystrophic muscles, coupled with cholesterol and SM species. The composition of fatty acyl chain depended on the different region, allowing estimation of the local damage extent [170].

Cardiovascular disease, one of the leading causes of death and disability, has also been the focus of ToF-SIMS analysis. The work revealed the pathology of lipid accumulation within the artery wall, e.g., the presence of high amounts of endogenous non-esterified fatty acids was highlighted on carotid atherosclerotic plaque, vitamin E (a putative redox statemarker) was at the innermost areas of the intima with extra-cellular cholesterol accumulation at the edge [171]. In rat aorta and human atherosclerotic plaque, fatty acids, cholesterol, oxysterol and DAG were detected, revealing palmitic/palmitoleic acid and stearic/oleic acid in high concentration especially in the tunica media region of the aorta, and irregular cholesterol distributed in spots and larger elongated regions with DAG in human atherosclerotic plaque [172]. However, further experiments are still required to assess the pathological relevance of the highlighted lipids.

Human liver sections from patients suffering from non-alcoholic fatty liver disease were investigated using a Bi_3^+ ion beam. Debois and coworkers [173] found that small vesicles (size of a few micrometers) scattered on the section accumulated with TAG, DAG, MAG, fatty acids, traces of myristic acid, along with a lessening of vitamin E and a selective macrovacuolar localization of cholesterol in steatosis areas of fatty livers compared to control livers. The ToF-SIMS images further revealed that the accumulation of lipid zonation could be an indicator of steatosis, which was not characterized by the histological control performed on serial tissue sections. The same group also studied Fabry disease (in parallel with MALDI-ToF) [174] to look for the biomarkers.

Magnusson *et al.* [175] evaluated skeletal muscle lipid accumulation associated with obesity using a Bi_3^+ ion source. Compare to the lean wild-type mice, the signal intensities of fatty acids and DAGs were seen to significantly increase in skeletal muscle of the obese *ob/ob* mice. With PCA analysis, the ratio between different fatty acids revealed changes in monounsaturated and polyunsaturated fatty acids, which was also corresponding to ratios of different DAG or PC.

Compared with the wide application of MALDI in cancer research for identification of protein and peptide over various tumour sections [176], ToF-SIMS has been lagging behind in the field. However, no conclusion has been reached so far on which decisive single gene or change/modification of protein expression that could explain complicated cancer progress. Rather than track the proteins, ToF-SIMS/PCA analysis was developed to detect the global changes with subcellular resolution in individual cells, which could bring the breakthrough for potential detection and treatment strategy. Lockyer and Vickerman [177] described the ToF-SIMS/PCA characterisation of prostate cancer cells. Kulp *et al.* [178] used the same method to distinguish three closely-related breast cancer lines. The methodology shows promising application in cancer research in term of identification of subtle changes at the molecular levels aiming to further understand cancer progression and metabolism. Meanwhile, intensive studies of anticancer boronated drugs were carried out using ToF-SIMS to locate the drug distribution in human glioblastoma cell for the evaluation of the drug combination and efficacy [179, 180].

ToF-SIMS has also been used in other areas to target organic molecules, *e.g.*, analysis of thousand years old mummies [181], finger prints for forensic studies [182], and exploration of biomarkers for early life on Earth in fluid inclusions [183]. These diverse applications demonstrate the essence of ToF-SIMS, that is imaging the molecules either inorganic or organic from surface or varying depth of the samples will lead to more opportunities in discovery studies.

1.2.2.3 Problems and challenges for ToF-SIMS

1.2.2.3.1 Peak identification

ToF-SIMS data processing and peak identification is vital to provide chemical information within biological species. A variety of lipids and protein fragments in ToF-SIMS spectra have been assigned accurately with numerous efforts of other researchers [95, 184-188] as summarized in Table 1.2. However, a wealth of information is still left hidden in the spectrum as not all the peaks can be interpreted through the m/z value. Cholesterol is a major constituent of nearly all mammalian cell membranes where its concentration is tightly controlled. In SIMS, cholesterol is fragmented as $[M+H-H_2O]^+$ at m/z 369.4⁺ and $[M-H]^+$ at m/z 385.4⁺. Assisted by MS/MS analysis on a C_{60}^+ /quadrupole ToF-SIMS, the new peak m/z 147.1⁺ is revealed as the most specific diagnostic fragment of cholesterol that offers a 3-fold signal enhancement. Moreover, the new cholesterol fragment (m/z 147.117⁺) can be completely resolved from polydimethylsiloxane (PDMS) fragment (m/z 147.065⁺) with resulting mass resolution $m/\Delta m$ of 8000 [185].

Another concern is the large amount of isomers in lipids, which largely complicated the peak identification. Tandem MS can assist the peak identification by investigating the fragments, but might still not to confirm the identity of the specific lipid. In addition, the intensities decrease rapidly with increasing mass [189], making it difficult to image and map certain molecular ions (Fig. 1.16). Therefore, the future peak assignment work might be facilitated by the application of MS/MS methodology to imaging ToF-SIMS to uncover new and diagnostic peaks in the low mass region.

Table 1.2 Characteristic fragments of biomolecules in ToF-SIMS spectra

Positive <i>m/z</i>	Proposed structure and parent compound	Negative <i>m/z</i>	Proposed structure and parent compound
59	[C ₃ H ₉ N] ⁺ - phosphocholine lipids	30	[CH ₄ N] ⁻ - glycine
86	[C ₅ H ₁₂ N] ⁺ - phosphocholine lipids	63	PO ₂ ⁻ - phospholipids fragment
104	[C ₅ H ₁₄ ON] ⁺ - phosphocholine lipids	68	[C ₄ H ₆ N] ⁻ - proline
124	[C ₂ H ₇ NPO ₃] ⁺ - GPEtn	70	[C ₄ H ₈ N] ⁻ - proline
125	[C ₂ H ₆ PO ₄] ⁺ - phosphoglycerol lipids	79	PO ₃ ⁻ - phospholipids lipids
134	[C ₄ H ₈ NO ₄] ⁺ - alanine or aspartic acid	100	[C ₄ H ₁₀ N ₃] ⁻ - arginine
136	[C ₅ H ₆ N ₅] ⁺ - adenine	104	[C ₅ H ₁₄ NO] ⁻ - phosphocholine lipids
142	[C ₂ H ₉ NPO ₄] ⁺ - GPEtn	112	[C ₅ H ₁₀ N ₃] ⁻ - arginine
143	[C ₂ H ₈ O ₅ P] ⁺ - GPSer	130	[C ₉ H ₈ N] ⁻ - tryptophan
165	[C ₉ H ₁₁ NO ₂] ⁺ - tyrosine, or[C ₂ H ₇ O ₅ PNa] ⁺ - GPSer	159	[C ₁₀ H ₁₁ N ₂] ⁻ - tryptophan
166	[C ₅ H ₁₅ NPO ₃] ⁺ - phosphocholine lipids	175	[C ₆ H ₁₅ N ₄ O ₂] ⁻ - arginine
184	[C ₅ H ₁₅ NPO ₄] ⁺ - phosphocholine lipids	223	[C ₆ H ₈ P O ₇] ⁻ - GPIns
198	[C ₅ H ₁₁ PO ₆] ⁺ - GPGro	231	[C ₁₀ H ₁₉ N ₂ O ₄] ⁻ - proline
206	[C ₅ H ₁₄ PO ₄ Na] ⁺ - phosphoglycerol lipids	251	[C ₁₆ H ₃₃ O ₂] ⁻ - fatty acid C16:2
213	[C ₆ H ₁₄ PO ₆] ⁺ - phosphoglycerol lipids	253	[C ₁₆ H ₃₅ O ₂] ⁻ - fatty acid C16:1
224	[C ₈ H ₁₉ NPO ₄] ⁺ - phosphocholine lipids	255	[C ₁₆ H ₃₇ O ₂] ⁻ - fatty acid C16:0
235	[C ₆ H ₁₃ PO ₆ Na] ⁺ - phosphoglycerol lipids	256	[C ₁₆ H ₃₄ NO] ⁻ - palmitoyl from sphingosine backbone
265	[C ₁₈ H ₃₅ N] ⁺ - SM	277	[C ₁₈ H ₂₇ O ₂] ⁻ - fatty acid C18:3
313	[C ₁₉ H ₃₇ O ₃] ⁺ - MAG C16:0	279	[C ₁₈ H ₂₉ O ₂] ⁻ - fatty acid C18:2
339	[C ₂₂ H ₄₃ O ₂] ⁺ - MAG C18:1	281	[C ₁₈ H ₃₃ O ₂] ⁻ - fatty acid C18:0
341	[C ₂₁ H ₄₁ O ₃] ⁺ - MAG C18:0	303	[C ₂₀ H ₃₆ O ₂] ⁻ - fatty acid chain
369	[C ₂₇ H ₄₅] ⁺ - cholesterol (M-OH)	385	[C ₂₇ H ₄₅ O] ⁻ - cholesterol
385	[C ₂₇ H ₄₅ O] ⁺ - cholesterol (M-H)	429	[C ₂₉ H ₄₉ O ₂] ⁺ - vitamin E
430	[C ₂₉ H ₅₀ O ₂] ⁺ - vitamin E	616	[C ₃₄ H ₆₇ NO ₆ P] ⁻ - SM C34:1 [M-C ₂ H ₂ N(CH ₃) ₃] ⁻
478	[C ₂₃ H ₄₃ PO ₃] ⁺ - phosphoglycerol with palmitate C16:0	642	[C ₃₆ H ₆₉ NO ₆ P] ⁻ - SM C34:1 [M-N(CH ₃) ₃] ⁻
494	[C ₂₃ H ₄₃ PO ₃] ⁺ - phosphoglycerol with palmitate C16:0, O	687	[C ₃₈ H ₇₆ N ₂ O ₆ P] ⁻ - SM C34:1[M-H] ⁻
504	[C ₂₅ H ₄₅ PO ₃] ⁺ - phosphoglycerol with oleate C18:1	771	[C ₅₄ H ₉₁ O ₂] ⁻ - cholesterol [2M-H] ⁻
506	[C ₂₅ H ₄₇ PO ₃] ⁺ - phosphoglycerol with stearate C18:0	795	Coenzyme Q9
520	[C ₂₅ H ₄₅ PO ₃] ⁺ - phosphoglycerol with oleate, O	806	[C ₂₅ H ₄₅ O ₁₁ NS-C ₁₇ H ₃₅] ⁻ - ST C18:0
522	[C ₂₅ H ₄₇ PO ₃] ⁺ - phosphoglycerol with stearate C18:0, O	822	[C ₂₅ H ₄₅ O ₁₁ NS-OC ₁₇ H ₃₅] ⁻ - ST C18:0
548	ceramide 18:0	834	[C ₂₅ H ₄₅ O ₁₁ NS-C ₁₉ H ₃₉] ⁻ - ST C20:0
549	[C ₃₅ H ₆₅ O ₄] ⁺ - DAG C32:1	850	[C ₂₅ H ₄₅ O ₁₁ NS-OC ₁₉ H ₃₉] ⁻ - ST C20:0
551	[C ₃₅ H ₆₇ O ₄] ⁺ - DAG C32:0	857	[C ₁₁ H ₁₆ O ₁₃ P-C ₃₄ H ₆₂] ⁻ - GPIns C36:4
563	[C ₃₆ H ₆₇ O ₄] ⁺ - DAG C33:1	862	[C ₂₅ H ₄₅ O ₁₁ NS-C ₂₁ H ₄₃] ⁻ - ST C22:0
575	[C ₃₇ H ₆₇ O ₄] ⁺ - DAG C34:2	878	[C ₂₅ H ₄₅ O ₁₁ NS-OC ₂₁ H ₄₃] ⁻ - ST C22:0
577	[C ₃₆ H ₆₄ O ₄] ⁺ - DAG C34:1	885	[C ₁₁ H ₁₆ O ₁₃ P-C ₃₆ H ₆₆] ⁻ - GPIns C38:4
601	[C ₃₉ H ₆₉ O ₄] ⁺ - DAG C36:3	887	[C ₁₁ H ₁₆ O ₁₃ P-C ₃₆ H ₆₈] ⁻ - GPIns C38:3
603	[C ₃₉ H ₇₁ O ₄] ⁺ - DAG C36:2	888	[C ₂₅ H ₄₅ O ₁₁ NS-C ₂₃ H ₄₅] ⁻ - ST C24:1
623	[C ₄₁ H ₆₇ O ₄] ⁺ - DAG C38:6	890	[C ₂₅ H ₄₅ O ₁₁ NS-C ₂₃ H ₄₇] ⁻ - ST C24:0
625	[C ₄₁ H ₆₉ O ₄] ⁺ - DAG C38:5	904	[C ₂₅ H ₄₅ O ₁₁ NS-OC ₂₃ H ₄₅] ⁻ - ST C24:1
630	ceramide C24:1	906	[C ₂₅ H ₄₅ O ₁₁ NS-OC ₂₃ H ₄₇] ⁻ - ST C24:0
732	[C ₁₀ H ₁₉ NPO ₈ -C ₃₀ H ₆₀] ⁺ - GPCho C32:1		
734	[C ₁₀ H ₁₉ NPO ₈ -C ₃₀ H ₆₂] ⁺ - GPCho C32:0		
758	[C ₁₀ H ₁₉ NPO ₈ -C ₃₂ H ₆₂] ⁺ - GPCho C34:2		
760	[C ₁₀ H ₁₉ NPO ₈ -C ₃₂ H ₆₄] ⁺ - GPCho C34:1		
782	[C ₁₀ H ₁₉ NPO ₈ -C ₃₂ H ₆₄ Na] ⁺ - GPCho C34:1		
788	[C ₁₀ H ₁₉ NPO ₈ -C ₃₄ H ₆₈] ⁺ - GPCho C36:1		
798	[C ₁₀ H ₁₉ NPO ₈ -C ₃₂ H ₆₄ K] ⁺ - GPCho C34:1		
853	[C ₅₅ H ₉₇ O ₆] ⁺ C52:5/[C ₅₃ H ₉₈ O ₆ Na] ⁺ C50:2 - TAG		
855	[C ₅₅ H ₉₉ O ₆] ⁺ C52:4/[C ₅₃ H ₁₀₀ O ₆ Na] ⁺ C50:1 - TAG		
877	[C ₅₅ H ₉₈ O ₆ Na] ⁺ - TAG C52:4		
881	[C ₅₇ H ₁₀₁ O ₆] ⁺ C54:4/[C ₅₅ H ₁₀₂ O ₆ Na] ⁺ C52:2 - TAG		
883	[C ₅₅ H ₁₀₄ O ₆ Na] ⁺ - TAG C52:1		
885	[C ₅₅ H ₁₀₆ O ₆ Na] ⁺ - TAG C52:0		
903	[C ₅₉ H ₉₉ O ₆] ⁺ - TAG C56:3		
905	[C ₅₉ H ₁₀₁ O ₆] ⁺ - TAG C56:2		

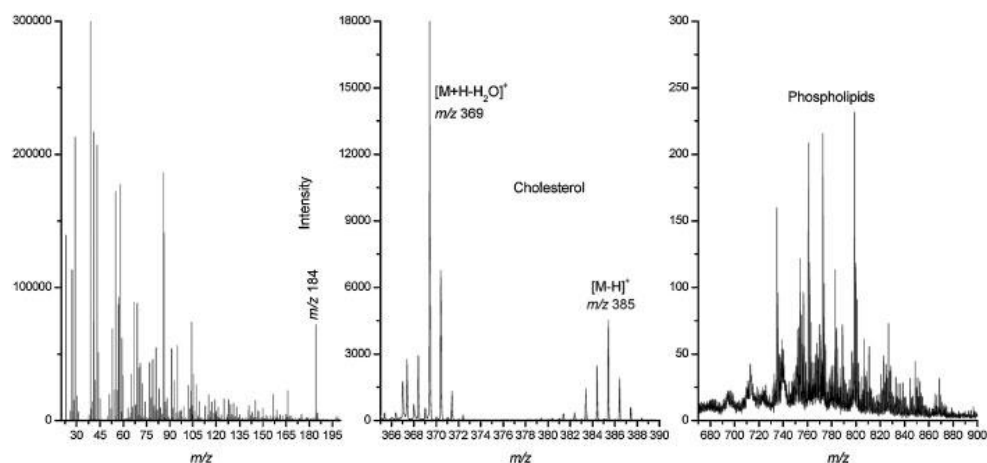


Fig. 1.16 Au_3^+ SIMS mass spectra in positive ion mode of a mouse brain tissue section. It is clear that the number of counts decreases rapidly with increasing mass. Reproduced from reference [189].

1.2.2.3.2 Mass resolution and spatial resolution

To identify unknown peaks and eliminate the isobaric interferences in an incredibly complex system, improved mass resolution is becoming crucial. Especially for biological studies, high mass resolution is necessary for high resolution image. However, for conventional ToF-SIMS, high mass resolution that is achieved using short (ns) PI beam pulses is incompatible with maintaining the high spatial resolution of which the DC PI beam is capable. This could be circumvented by using the continuous PI beam and a linear buncher which are the essence of the design of the new concept J105 3D Chemical imager. The benefits of imaging species with very precise mass have been shown through the study of HeLa cells. The mass spectrum produced from the cells highlights the high mass resolution in the mass region of $m/z\ 86^+$, where an isotope ion of Si_3^+ ($m/z\ 85.93^+$) from the silicon substrate is clearly resolved from characteristic fragment of phosphocholine lipids $[\text{C}_5\text{H}_{12}\text{N}]^+$ ($m/z\ 86.10^+$) and an unassigned ion ($m/z\ 86.03^+$) not only in mass spectrum but also in the three clearly contrasting images at high spatial resolution as shown in Fig. 1.17 [155].

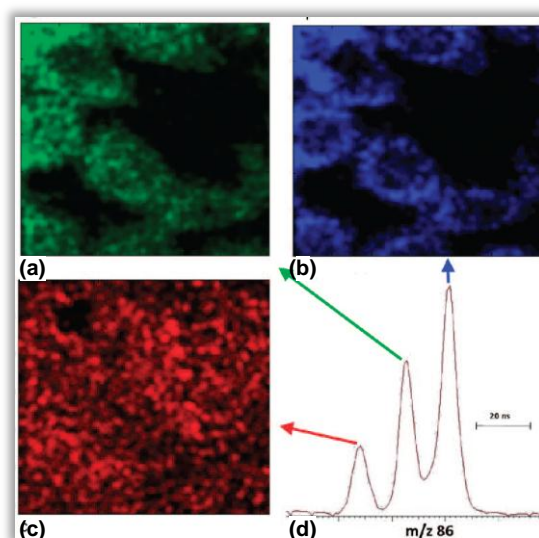


Fig. 1.17 Demonstration of the necessity of maintaining high mass resolution while imaging. All three ions from nominal $m/z\ 86^+$ have distinct differences in localization as single ion image $m/z\ 86.03^+$ (unassigned ion) in (a), phosphocholine lipids fragment $m/z\ 86.10^+$ ($[\text{C}_5\text{H}_{12}\text{N}]^+$) in (b) and $m/z\ 85.93^+$ (Si_3^+) in (c). The mass spectrum of nominal $m/z\ 86^+$ is in (d). Scale bar on the (time) spectrum relates to the arrival time of the ions and indicates that similar resolution in a standard

ToF-SIMS instrument would require <20 ns PI pulses that would not normally be compatible with this level of spatial resolution. Reproduced from reference [155].

On the other hand, the high spatial resolution still presents a big challenge for the application of SIMS to the biological field. Even with the smallest probe size of ~50 nm from a Au_3^+ ion beam and ~1 μm from C_{60}^+ ion beam, it is still difficult to map the detailed arrangement of lipids species in membrane bilayer and subcellular structures, as the lateral resolution is far beyond the microdomain. Besides, given that the finely focused beam is obtained, the less detectable molecules in a small pixel would pose another problem to the detection efficiency.

1.2.2.3.3 Ion suppression and enhancement from the chemical environment

Another issue associated with analysis of complex biological system is the matrix effect when carrying out a SIMS analysis. The effect of two abundant tissue lipids, cholesterol and DPPC, on the atropine $[\text{M}+\text{H}]^+$ signal was assessed by detecting atropine in mixtures with these lipids using ToF-SIMS. It was shown that the DPPC has a strong suppressing effect, which could be attributed to gas phase proton transfer [190]. Piehowski *et al.* [191] reported water can be controllably redeposited onto the sample surface at temperatures below -100 °C in vacuum. The redeposited water increases the ionisation of characteristic fragments of cholesterol 2-fold without loss of spatial resolution. Abundant GPCho, GPEtn lipids and to a lesser extent ceramides could be desorbed and ionized by SIMS, however, the less abundant phospholipids, *e.g.*, PIP and CL were not yet observed, which are much more interesting from a biological point of view [192].

The ion suppression and enhancement complicates the data interpretation and potentially distorts the images. A molecule distributed homogeneously across a surface may be detected with very different intensity from one region to another, solely due to differences in the chemical composition of these areas. Additionally, the compounds responding to the variation in ionisation probability may have strong signals in one polarity while suppressed in other ion polarity, and hence, not be detected. It is for this reason that the data should be collected for the same sample in both polarities to confirm the chemical composition [193].

1.3 Aim of the study

This study focused on visualization and profiling of lipid species using ToF-SIMS instrumentation in two model systems, *X. laevis* egg/embryo and mouse embryonic fibroblast NIH 3T3 BXB-ER, to gain the insights into lipid distribution and rearrangement in the dynamic biological processes, *e.g.*, fertilisation, embryo development in early stages and subcellular mitochondrial rearrangement in reaction to Raf/ERK activation.

The purpose of the study on *X. laevis* egg/embryo was to explore the capability of ToF-SIMS in handling the large spherical sample which is not favoured sample form for ToF-SIMS, establish the reliable sample preparation methodology and assess topography effects of a single intact cell. Moreover, the study was aimed to characterize multiple lipid species from lipid extraction of *X. laevis* zygotes in a single run using ToF-SIMS, and to monitor the distribution and rearrangement of important lipid on the surface of single embryo upon different biological processes including fertilisation and early embryo development through 2D imaging. Meanwhile the study was also to

trace important biomolecules 3-dimensionally in the egg/embryo to further develop an understanding of the issues surrounding 3D SIMS analysis.

With regards to fibroblasts, the study was to explore the possibility of high resolution 3D SIMS imaging with a finely focused C_{60}^+ PI beam to visualize subcellular lipid rearrangement and mitochondria remodelling following Raf/ERK activation. A comparison study was also performed with two other imaging modes, confocal microscopy and SEM, to verify the cell integrity and morphological changes in SIMS images.

References

- [1] Thomson J. J., *Rays of positive electricity*. Phil. Mag., **21**(122): 225-249 (1911).
- [2] Herzog R. F. K. and Viehbock F. P., *Ion source for mass spectrography*. Physical Review, **76**(6): 855-856 (1949).
- [3] Winograd N., et al., *Improvements in SIMS continue: Is the end in sight?* Appl. Surf. Sci., **252**(19): 6836-6843 (2006).
- [4] Benninghoven A., Rüdener F. G., and Werner H. W., *Secondary ion mass spectrometry: basic concepts, instrumental aspects, applications, and trends*. illustrated ed 1987, New York: J. Wiley.
- [5] Benninghoven A., *Analysis of submonolayers on silver by negative secondary ion emission*. Phys. Status Solidi, **34**(2): K169-K171 (1969).
- [6] Vickerman J. C. and Briggs D., *ToF-SIMS: surface analysis by mass spectrometry*. 1st ed 2001, IM.
- [7] Benninghoven A., *Chemical analysis of inorganic and organic surfaces and thin films by static Time-of-Flight secondary ion mass spectrometry (ToF-SIMS)*. Angewandte Chemie International Edition in English, **33**(10): 1023-1043 (1994).
- [8] Wittmaack K., *Pre-equilibrium variation of secondary ion yield*. Int. J. Mass Spectrom. Ion Processes, **17**(1): 39-50 (1975).
- [9] Magee C. W., Harrington W. L., and Honig R. E., *Secondary ion quadrupole mass-spectrometer for depth profiling-design and performance evaluation*. Rev. Sci. Instrum., **49**(4): 477-485 (1978).
- [10] Chandra S., Ausserer W. A., and Morrison G. H., *Subcellular imaging of calcium exchange in cultured cells with ion microscopy*. J. Cell Sci., **102**(Pt3): 417-425 (1992).
- [11] Colliver T. L., et al., *Atomic and Molecular imaging at the single-cell level with ToF-SIMS*. Anal. Chem., **69**(13): 2225-2231 (1997).
- [12] Blank P. and Wittmaack K., *Energy and fluence dependence of the sputtering yield of silicon bombarded with argon and xenon*. J. Appl. Phys., **50**(3): 1519-1528 (1979).
- [13] Wittmaack K., *Secondary-ion emission from silicon bombarded with atomic and molecular noble-gas ions*. Surf. Sci., **90**(2): 557-563 (1979).
- [14] Benguerba M., et al., *Impact of slow gold clusters on various solids: nonlinear effects in secondary ion emission*. Nucl. Instrum. Meth. B, **62**(1): 8-22 (1991).
- [15] Boussofiane-Baudin K., et al., *Secondary ion emission under cluster impact at low energies (5 - 60 keV); influence of the number of atoms in the projectile*. Nucl. Instrum. Meth. B, **88**(1-2): 160-163 (1994).
- [16] Szymczak W. and Wittmaack K., *Evidence for strongly enhanced yields of negative molecular secondary ions due to bombardment with SF_n cluster ions*. Nucl. Instrum. Meth. B, **88**(1-2): 149-153 (1994).
- [17] Stapel D. and Benninghoven A., *Application of atomic and molecular primary ions for ToF-SIMS analysis of additive containing polymer surfaces*. Appl. Surf. Sci., **174**(3-4): 261-270 (2001).
- [18] Davies N., et al., *Development and experimental application of a gold liquid metal ion source*. Appl. Surf. Sci., **203-204**(0): 223-227 (2003).
- [19] Kollmer F., *Cluster primary ion bombardment of organic materials*. Appl. Surf. Sci., **231-232**(0): 153-158 (2004).
- [20] Weibel D., et al., *A C₆₀ primary ion beam system for time of flight secondary ion mass spectrometry: its development and secondary ion yield characteristics*. Anal. Chem., **75**(7): 1754-1764 (2003).
- [21] Jones E. A., et al., *ToF-SIMS analysis of bio-systems: Are polyatomic primary ions the solution?* Appl. Surf. Sci., **252**(19): 6844-6854 (2006).
- [22] Cheng J. and Winograd N., *Depth profiling of peptide films with ToF-SIMS and a C₆₀ probe*. Anal. Chem., **77**(11): 3651-3659 (2005).

- [23] Cheng J., et al., *Direct comparison of Au-3(+) and C-60(+) cluster projectiles in SIMS molecular depth profiling*. J. Am. Soc. Mass. Spectrom., **18**(3): 406-412 (2007).
- [24] Ryan K. E., Wojciechowski I. A., and Garrison B. J., *Reaction dynamics following keV cluster bombardment*. J. Phys. Chem. C, **111**(34): 12822-12826 (2007).
- [25] Delcorte A., et al., *Sputtering of organic molecules by clusters, with focus on fullerenes*. Appl. Surf. Sci., **255**(4): 1229-1234 (2008).
- [26] Rabbani S., et al., *ToF-SIMS with Argon gas cluster ion beams: A comparison with C60+*. Anal. Chem., **83**(10): 3793-3800 (2011).
- [27] Matsuo J., et al., *What size of cluster is most appropriate for SIMS?* Appl. Surf. Sci., **255**(4): 1235-1238 (2008).
- [28] Fernandez-Lima F. A., et al., *Analysis of native biological surfaces using a 100 kV massive gold cluster source*. Anal. Chem., **83** (22): 8448–8453 (2011).
- [29] Fujiwara Y., et al., *Time-of-Flight secondary ion mass spectrometry (ToF-SIMS) using the metal-cluster-complex primary ion of Ir4(CO)7+*. Surf. Interface Anal., **43**(1-2): 245-248 (2010).
- [30] Castner D. G., Belu A. M., and Graham D. J., *Time-of-flight secondary ion mass spectrometry: techniques and applications for the characterization of biomaterial surfaces*. Biomaterials, **24**(21): 3635-3653 (2003).
- [31] Seah M. P., *Analysis of cluster ion sputtering yields: correlation with the thermal spike model and implications for static secondary ion mass spectrometry*. Surf. Interface Anal., **39**(7): 634-643 (2007).
- [32] Plog C. and Gerhard W., *Secondary ion emission by nonadiabatic dissociation of nascent ion molecules with energies depending on solid composition .2. Examination of the new emission conception by model-calculations of Me+ yields and qualitative extension to other kinds of secondary ions*. Zeitschrift Fur Physik B-Condensed Matter, **54**(1): 71-86 (1983).
- [33] Cooks R. G. and Busch K. L., *Matrix effects, internal energies and Ms/Ms spectra of molecular-ions sputtered from surfaces*. Int. J. Mass Spectrom. Ion Processes, **53**: 111-124 (1983).
- [34] [cited 2011 30th Sept.]; Available from: lipidlibrary.aocs.org/lipidomics/omics.html.
- [35] Han X., *Neurolipidomics: challenges and developments*. Front. Biosci., **12**: 2601-2615 (2007).
- [36] Piomelli D., Astarita G., and Rapaka R., *A neuroscientist's guide to lipidomics*. Nat. Rev. Neurosci., **8**(10): 743-754 (2007).
- [37] Warensjo E., et al., *Associations between estimated fatty acid desaturase activities in serum lipids and adipose tissue in humans: links to obesity and insulin resistance*. Lipids Health Dis., **8**:37-42 (2009).
- [38] Dennis E. A., et al., *Update of the LIPID MAPS comprehensive classification system for lipids*. J. Lipid Res., **50**: S9-S14 (2009).
- [39] [cited 2011 6th Oct.]; Available from: www.lipidmaps.org/data/classification/LM_classification_exp.php.
- [40] Schlame M. and Ren M. D., *The role of cardiolipin in the structural organization of mitochondrial membranes*. Biochimica Et Biophysica Acta-Biomembranes, **1788**(10): 2080-2083 (2009).
- [41] Sorice M., et al., *Cardiolipin-enriched raft-like microdomains are essential activating platforms for apoptotic signals on mitochondria*. FEBS Lett., **583**(15): 2447-2450 (2009).
- [42] [cited 2011 7th Oct.]; Available from: www.williamsclass.com/SeventhScienceWork/CellTheoryParts.htm.
- [43] [cited 2011 5th Oct.]; Available from: www.britannica.com/bps/media-view/45550/0/1/0.
- [44] Langer T., Osman C., and Voelker D. R., *Making heads or tails of phospholipids in mitochondria*. J. Cell Biol., **192**(1): 7-16 (2011).
- [45] Brown D. A. and London E., *Structure and function of sphingolipid- and cholesterol-rich membrane rafts*. J. Biol. Chem., **275**(23): 17221-17224 (2000).
- [46] Edidin M., *The state of lipid rafts: From model membranes to cells*. Annu. Rev. Biophys. Biomol. Struct., **32**: 257-283 (2003).
- [47] Simons K., et al., *Lipid rafts as functional heterogeneity in cell membranes*. Biochem. Soc. Trans., **37**: 955-960 (2009).
- [48] Lodish H. F., *Molecular cell biology*. 5th ed 2004, W.H. Freeman and Company.
- [49] Cooper G. M., *The Cell: A Molecular Approach*. 2nd ed 2000, Sunderland (MA): Sinauer Associates.
- [50] Garrett R. and Grisham C. M., *Biochemistry*. 4th ed 2010, Brooks/Cole Pub Co.
- [51] Nagle J. F. and Tristram-Nagle S., *Lipid bilayer structure*. Curr. Opin. Struct. Biol., **10**(4): 474-480 (2000).
- [52] [cited 2011 8th Oct.]; Available from: blanco.biomol.uci.edu/Bilayer_Struct.html.
- [53] London E., *Lipid bilayer structure*. Encyclopedia of Biological Chemistry, **2**: 576-579 (2004).

- [54] Berridge M. J., *Inositol Trisphosphate and Calcium Signaling*. Nature, **361**(6410): 315-325 (1993).
- [55] Topham M. K., et al., *Diacylglycerol kinases*. Cell. Signal., **16**(9): 983-989 (2004).
- [56] Daum G. and Athenstaedt K., *Phosphatidic acid, a key intermediate in lipid metabolism*. Eur. J. Biochem., **266**(1): 1-16 (1999).
- [57] Shears S. B., *How versatile are inositol phosphate kinases?* Biochem. J., **377**(Pt 2): 265-280 (2004).
- [58] Balazy M., *Eicosanomics: targeted lipidomics of eicosanoids in biological systems*. Prostaglandins Other Lipid Mediat., **73**(3-4): 173-180 (2004).
- [59] Reynolds C. P., Maurer B. J., and Kolesnick R. N., *Ceramide synthesis and metabolism as a target for cancer therapy*. Cancer Lett., **206**(2): 169-180 (2004).
- [60] Melendez A. J., *Sphingosine kinase signalling in immune cells: Potential as novel therapeutic targets*. Biochimica Et Biophysica Acta-Proteins and Proteomics, **1784**(1): 66-75 (2008).
- [61] Cummings B. S. and Peterson B. L., *A review of chromatographic methods for the assessment of phospholipids in biological samples*. Biomed. Chromatogr., **20**(3): 227-243 (2006).
- [62] Finan P. M. and Thomas M. J., *PI 3-kinase inhibition: a therapeutic target for respiratory disease*. Biochem. Soc. Trans., **32**: 378-382 (2004).
- [63] Wetzker R. and Rommel C., *Phosphoinositide 3-kinases as targets for therapeutic intervention*. Curr. Pharm. Des., **10**(16): 1915-1922 (2004).
- [64] Hollander P., *Orlistat in the treatment of obesity*. Prim. Care, **30**(2): 427-440 (2003).
- [65] Martins I. J., et al., *Cholesterol metabolism and transport in the pathogenesis of Alzheimer's disease*. J. Neurochem., **111**(6): 1275-1308 (2009).
- [66] Shchepinov M. S., et al., *Isotopic reinforcement of essential polyunsaturated fatty acids diminishes nigrostriatal degeneration in a mouse model of Parkinson's disease*. Toxicol. Lett., **207**(2): 97-103 (2011).
- [67] Bousquet M., Calon F., and Cicchetti F., *Impact of omega-3 fatty acids in Parkinson's disease*. Ageing Res. Rev., **10**(4): 453-463 (2011).
- [68] Zhou S., et al., *Endosomal/lysosomal processing of gangliosides affects neuronal cholesterol sequestration in Niemann-Pick disease type C*. Am. J. Pathol., **179**(2): 890-902 (2011).
- [69] Tangemo C., et al., *Niemann-Pick type C disease: Characterizing lipid levels in patients with variant lysosomal cholesterol storage*. J. Lipid Res., **52**(4): 813-825 (2011).
- [70] Murphy R. C. and Gaskell S. J., *New applications of mass spectrometry in lipid analysis*. J. Biol. Chem., **286**(29): 25427-25433 (2011).
- [71] Shukla A. K. and Futrell J. H., *Tandem mass spectrometry: dissociation of ions by collisional activation*. J. Mass Spectrom., **35**(9): 1069-1090 (2000).
- [72] Folch J., Lees M., and Sloane Stanley G. H., *A simple method for the isolation and purification of total lipides from animal tissues*. J. Biol. Chem., **226**(1): 497-509 (1957).
- [73] Bligh E. G. and Dyer W. J., *A rapid method of total lipid extraction and purification*. Can J Biochem Physiol, **37**(8): 911-917 (1959).
- [74] Watson A. D., *Thematic review series: systems biology approaches to metabolic and cardiovascular disorders. Lipidomics: A global approach to lipid analysis in biological systems*. J. Lipid Res., **47**(10): 2101-2111 (2006).
- [75] Fahy E., et al., *Update of the LIPID MAPS comprehensive classification system for lipids*. J. Lipid Res., **50**: S9-S14 (2009).
- [76] Berry K. A. Z. and Murphy R. C., *Electrospray ionisation tandem mass spectrometry of glycerophosphoethanolamine plasmalogen phospholipids*. J. Am. Soc. Mass. Spectrom., **15**(10): 1499-1508 (2004).
- [77] Pulfer M. and Murphy R. C., *Electrospray mass spectrometry of phospholipids*. Mass Spectrom. Rev., **22**(5): 332-364 (2003).
- [78] Han X. and Gross R. W., *Shotgun lipidomics: electrospray ionisation mass spectrometric analysis and quantitation of cellular lipidomes directly from crude extracts of biological samples*. Mass Spectrom. Rev., **24**(3): 367-412 (2005).
- [79] Fenn J. B., et al., *Electrospray ionisation for mass-spectrometry of large biomolecules*. Science, **246**(4926): 64-71 (1989).
- [80] Han X. and Cheng H., *Characterization and direct quantitation of cerebroside molecular species from lipid extracts by shotgun lipidomics*. J. Lipid Res., **46**(1): 163-175 (2005).
- [81] Andreyev A. Y., et al., *Subcellular organelle lipidomics in TLR-4-activated macrophages*. J. Lipid Res., **51**(9): 2785-2797 (2010).
- [82] Canevari L. and Clark J. B., *Alzheimer's disease and cholesterol: the fat connection*. Neurochem. Res., **32**(4-5): 739-750 (2007).

- [83] Murph M., et al., *Liquid chromatography mass spectrometry for quantifying plasma lysophospholipids: potential biomarkers for cancer diagnosis*. Methods Enzymol., **433**: 1-25 (2007).
- [84] Gronert K., et al., *A molecular defect in intracellular lipid signaling in human neutrophils in localized aggressive periodontal tissue damage*. J. Immunol., **172**(3): 1856-1861 (2004).
- [85] Forrester J. S., et al., *Computational lipidomics: a multiplexed analysis of dynamic changes in membrane lipid composition during signal transduction*. Mol. Pharmacol., **65**(4): 813-821 (2004).
- [86] Dennis E. A., *Lipidomics joins the omics evolution*. Proc. Natl. Acad. Sci. U. S. A., **106**(7): 2089-2090 (2009).
- [87] Harkewicz R., et al., *Arachidonate-derived dihomoprostaglandin production observed in endotoxin-stimulated macrophage-like cells*. J. Biol. Chem., **282**(5): 2899-2910 (2007).
- [88] Takats Z., et al., *Mass spectrometry sampling under ambient conditions with desorption electrospray ionisation*. Science, **306**(5695): 471-473 (2004).
- [89] Nemes P. and Vertes A., *Laser ablation electrospray ionisation for atmospheric pressure, in vivo, and imaging mass spectrometry*. Anal. Chem., **79**(21): 8098-8106 (2007).
- [90] Snyder L. R., Kirkland J. J., and W. D. J., *Introduction to modern liquid chromatography*. 3rd ed 2010, Hoboken, New Jersey: John Wiley & Sons, Inc.
- [91] Gawrisch K., Eldho N. V., and Polozov I. V., *Novel NMR tools to study structure and dynamics of biomembranes*. Chem. Phys. Lipids, **116**(1-2): 135-151 (2002).
- [92] Gawrisch K. and Soubias O., *Structure and dynamics of polyunsaturated hydrocarbon chains in lipid bilayers-significance for GPCR function*. Chem. Phys. Lipids, **153**(1): 64-75 (2008).
- [93] Vaz W. L. C. and Melo E., *Fluorescence spectroscopic studies on phase heterogeneity in lipid bilayer membranes*. J. Fluoresc., **11**(4): 255-271 (2001).
- [94] Garcia-Saez A. J. and Schwille P., *Fluorescence correlation spectroscopy for the study of membrane dynamics and protein/lipid interactions*. Methods, **46**(2): 116-122 (2008).
- [95] Belazi D., et al., *Chemical analysis of osmium tetroxide staining in adipose tissue using imaging ToF-SIMS*. Histochem. Cell Biol., **132**(1): 105-115 (2009).
- [96] Leonard-Latour M., Morelis R. M., and Coulet P. R., *Influence of pyrene-based fluorescent probes on the characteristics of DMPA/DMPC Langmuir-Blodgett films*. Langmuir, **12**(20): 4797-4802 (1996).
- [97] El Kirat K., Morandat S., and Dufrene Y. F., *Nanoscale analysis of supported lipid bilayers using atomic force microscopy*. Biochim. Biophys. Acta, **1798**(4): 750-765 (2009).
- [98] Balashev K., et al., *Novel methods for studying lipids and lipases and their mutual interaction at interfaces. Part I. Atomic force microscopy*. Biochimie, **83**(5): 387-397 (2001).
- [99] Hatziantoniou S., et al., *Visualisation of liposomes prepared from skin and stratum corneum lipids by transmission electron microscopy*. Micron, **38**(8): 777-781 (2007).
- [100] Meyer H. W. and Richter W., *Freeze-fracture studies on lipids and membranes*. Micron, **32**(6): 615-644 (2001).
- [101] [cited 2011 10th Nov.]; Available from: <http://www.protein.iastate.edu/maldi.html>.
- [102] Schiller J., et al., *MALDI-ToF MS in lipidomics*. Front. Biosci., **12**: 2568-2579 (2007).
- [103] Barrera N. P. and Robinson C. V., *Advances in the mass spectrometry of membrane proteins: from individual proteins to intact complexes*. Annu. Rev. Biochem., **80**: 247-271 (2011).
- [104] Touboul D., Brunelle A., and Laprevote O., *Mass spectrometry imaging: Towards a lipid microscope?* Biochimie, **93**(1): 113-119 (2011).
- [105] Djidja M. C., et al., *Novel molecular tumour classification using MALDI-mass spectrometry imaging of tissue micro-array*. Anal. Bioanal. Chem., **397**(2): 587-601 (2010).
- [106] Touboul D., Brunelle A., and Laprevote O., *Mass spectrometry imaging: Towards a lipid microscope?* Biochimie, **93**(1): 113-119 (2011).
- [107] Ferreira C. R., et al., *Single embryo and oocyte lipid fingerprinting by mass spectrometry*. J. Lipid Res., **51**(5): 1218-1227 (2009).
- [108] Cornett D. S., Frappier S. L., and Caprioli R. M., *MALDI-FTICR imaging mass spectrometry of drugs and metabolites in tissue*. Anal. Chem., **80**(14): 5648-5653 (2008).
- [109] Liu Q., et al., *Metabolite imaging using matrix-enhanced surface-assisted laser desorption/ionisation mass spectrometry (ME-SALDI-MS)*. J. Am. Soc. Mass. Spectrom., **20**(1): 80-88 (2009).
- [110] Trim P. J., et al., *Matrix-assisted laser desorption/ionisation-ion mobility separation-mass spectrometry imaging of vinblastine in whole body tissue sections*. Anal. Chem., **80**(22): 8628-8634 (2008).
- [111] Bouslimani A., et al., *Matrix-assisted laser desorption/ionisation imaging mass spectrometry of oxaliplatin derivatives in heated intraoperative chemotherapy (HIPEC)-like treated rat kidney*. Rapid Commun. Mass Spectrom., **24**(4): 415-421 (2010).

- [112] Yates J. R., *Mass spectrometry and the age of the proteome*. J. Mass Spectrom., **33**(1): 1-19 (1998).
- [113] Harada T., et al., *Visualization of volatile substances in different organelles with an atmospheric-pressure mass microscope*. Anal. Chem., **81**(21): 9153-9157 (2009).
- [114] Goto-Inoue N., et al., *Imaging mass spectrometry for lipidomics*. Biochim. Biophys. Acta., **1811**(11): 961-969 (2011).
- [115] Ferreira C. R., et al., *Single embryo and oocyte lipid fingerprinting by mass spectrometry*. J. Lipid Res., **51**(5): 1218-1227 (2011).
- [116] Li Y., Shrestha B., and Vertes A., *Atmospheric pressure molecular imaging by infrared MALDI mass spectrometry*. Anal. Chem., **79**(2): 523-532 (2007).
- [117] Jurchen J. C., Rubakhin S. S., and Sweedler J. V., *MALDI-MS imaging of features smaller than the size of the laser beam*. J. Am. Soc. Mass. Spectrom., **16**(10): 1654-1659 (2005).
- [118] Fletcher J. S., Lockyer N. P., and Vickerman J. C., *Developments in molecular SIMS depth profiling and 3D imaging of biological systems using polyatomic primary ions*. Mass Spectrom. Rev., **30**(1): 142-174 (2010).
- [119] Mazel V., et al., *Identification of Ritual blood in african artifacts using ToF-SIMS and synchrotron radiation microspectroscopies*. Anal. Chem., **79**(24): 9253-9260 (2007).
- [120] Wiseman J. M., et al., *Tissue imaging at atmospheric pressure using desorption electrospray ionisation (DESI) mass spectrometry*. Angewandte Chemie-International Edition, **45**(43): 7188-7192 (2006).
- [121] Eberlin L. S., et al., *Three-dimensional visualization of mouse brain by lipid analysis using ambient ionisation mass spectrometry*. Angew. Chem. Int. Ed., **49**(5): 873-876 (2010).
- [122] Eberlin L. S., et al., *Desorption electrospray ionisation mass spectrometry for lipid characterization and biological tissue imaging*. Biochim. Biophys. Acta., **1811**(11):946-960 (2011).
- [123] Fletcher J. S., et al., *ToF-SIMS 3D biomolecular imaging of Xenopus laevis oocytes using buckminsterfullerene (C60) primary ions*. Anal. Chem., **79**(6): 2199-2206 (2007).
- [124] Berman E. S. F., et al., *Preparation of single cells for imaging/profiling mass spectrometry*. J. Am. Soc. Mass. Spectrom., **19**(8): 1230-1236 (2008).
- [125] Malm J., et al., *Fixation and drying protocols for the preparation of cell samples for time-of-flight secondary ion mass spectrometry analysis*. Anal. Chem., **81**(17): 7197-7205 (2009).
- [126] Kurczy M. E., et al., *Which is more important in bioimaging SIMS experiments-The sample preparation or the nature of the projectile?* Appl. Surf. Sci., **255**(4): 1298-1304 (2008).
- [127] Kerwin J. L., Tuininga A. R., and Ericsson L. H., *Identification of molecular species of glycerophospholipids and sphingomyelin using electrospray mass spectrometry*. J. Lipid Res., **35**(6): 1102-1114 (1994).
- [128] Manicke N. E., et al., *Desorption electrospray ionisation (DESI) mass spectrometry and tandem mass spectrometry (MS/MS) of phospholipids and sphingolipids: ionisation, adduct formation, and fragmentation*. J. Am. Soc. Mass. Spectrom., **19**(4): 531-543 (2008).
- [129] Parry S. and Winograd N., *High-resolution ToF-SIMS imaging of eukaryotic cells preserved in a trehalose matrix*. Anal. Chem., **77**(24): 7950-7957 (2005).
- [130] Berlinguer F., et al., *Effects of trehalose co-incubation on in vitro matured prepubertal ovine oocyte vitrification*. Cryobiology, **55**(1): 27-34 (2007).
- [131] Grovenor C. R. M., et al., *Specimen preparation for NanoSIMS analysis of biological materials*. Appl. Surf. Sci., **252**(19): 6917-6924 (2006).
- [132] Chandra S., *Challenges of biological sample preparation for SIMS imaging of elements and molecules at subcellular resolution*. Appl. Surf. Sci., **255**(4): 1273-1284 (2008).
- [133] Chandra S. and Morrison G. H., *Sample preparation of animal tissues and cell cultures for secondary ion mass spectrometry (SIMS) microscopy*. Biol. Cell, **74**(0): 31-42 (1992).
- [134] Rabbani S., et al., *Exploring subcellular imaging on the buncher-ToF J105 3D chemical imager*. Surf. Interface Anal., **43**(1-2): 380-384 (2010).
- [135] McDonald K. L., *A review of high-pressure freezing preparation techniques for correlative light and electron microscopy of the same cells and tissues*. Journal of Microscopy-Oxford, **235**(3): 273-281 (2009).
- [136] Nygren H., et al., *Imaging ToF-SIMS of rat kidney prepared by high-pressure freezing*. Microsc. Res. Tech., **68**(6): 329-334 (2005).
- [137] Sosinsky G. E., et al., *The combination of chemical fixation procedures with high pressure freezing and freeze substitution preserves highly labile tissue ultrastructure for electron tomography applications*. J. Struct. Biol., **161**(3): 359-371 (2008).
- [138] Todd P. J., et al., *Organic ion imaging of biological tissue with secondary ion mass spectrometry and matrix-assisted laser desorption/ionisation*. J. Mass Spectrom., **36**(4): 355-369 (2001).
- [139] Rangarajan S. and Tyler B. J., *Topography in secondary ion mass spectroscopy images*. J. Vac. Sci. Technol. A, **24**(5): 1730-1736 (2006).

- [140] Roddy T. P., et al., *Proton transfer in time-of-flight secondary ion mass spectrometry studies of frozen-hydrated dipalmitoylphosphatidylcholine*. Anal. Chem., **75**(16): 4087-4094 (2003).
- [141] Ostrowski S. G., et al., *Secondary ion MS imaging of lipids in picoliter vials with a buckminsterfullerene ion source*. Anal. Chem., **77**(19): 6190-6196 (2005).
- [142] Bourdos N., et al., *Analysis of lung surfactant model systems with time-of-flight secondary ion mass spectrometry*. Biophys. J., **79**(1): 357-369 (2000).
- [143] Sostarecz A. G., et al., *Phosphatidylethanolamine-induced cholesterol domains chemically identified with mass spectrometric imaging*. J. Am. Chem. Soc., **126**(43): 13882-13883 (2004).
- [144] Kraft M. L., et al., *Phase separation of lipid membranes analyzed with high-resolution secondary ion mass spectrometry*. Science, **313**(5795): 1948-1951 (2006).
- [145] Cannon D. M., et al., *Molecule specific imaging of freeze-fractured, frozen-hydrated model membrane systems using mass spectrometry*. J. Am. Chem. Soc., **122**(4): 603-610 (2000).
- [146] Colliver T. L., et al., *Atomic and molecular imaging at the single-cell level with ToF-SIMS*. Anal. Chem., **69**(13): 2225-2231 (1997).
- [147] Roddy T. P., et al., *Identification of cellular sections with imaging mass spectrometry following freeze fracture*. Anal. Chem., **74**(16): 4020-4026 (2002).
- [148] Roddy T. P., et al., *Imaging of freeze-fractured cells with in situ fluorescence and time-of-flight secondary ion mass spectrometry*. Anal. Chem., **74**(16): 4011-4019 (2002).
- [149] Lanekoff I., et al., *Time of flight mass spectrometry imaging of samples fractured in situ with a spring-loaded trap system*. Anal. Chem., **82**(15): 6652-6659 (2010).
- [150] Breitenstein D., et al., *The chemical composition of animal cells reconstructed from 2D and 3D ToF-SIMS analysis*. Appl. Surf. Sci., **255**(4): 1249-1256 (2008).
- [151] Nygren H., et al., *Bioimaging ToF-SIMS: High resolution 3D Imaging of single cells*. Microsc. Res. Tech., **70**(11): 969-974 (2007).
- [152] Breitenstein D., et al., *The chemical composition of animal cells and their intracellular compartments reconstructed from 3D mass spectrometry*. Angewandte Chemie-International Edition, **46**(28): 5332-5335 (2007).
- [153] Szakal C., et al., *Compositional mapping of the surface and interior of mammalian cells at submicrometer resolution*. Anal. Chem., **83**(4): 1207-1213 (2011).
- [154] Fletcher J. S., Lockyer N. P., and Vickerman J. C., *C60, Buckminsterfullerene: its impact on biological ToF-SIMS analysis*. Surf. Interface Anal., **38**(11): 1393-1400 (2006).
- [155] Fletcher J. S., et al., *A New Dynamic in mass spectral imaging of single biological cells*. Anal. Chem., **80**(23): 9058-9064 (2008).
- [156] Fletcher J. S., et al., *Three-dimensional mass spectral imaging of HeLa-M cells--sample preparation, data interpretation and visualisation*. Rapid Commun. Mass Spectrom., **25**(7): 925-932 (2011).
- [157] Touboul D., et al., *Tissue molecular ion imaging by gold cluster ion bombardment*. Anal. Chem., **76**(6): 1550-1559 (2004).
- [158] Brunelle A., Touboul D., and Laprevote O., *Biological tissue imaging with time-of-flight secondary ion mass spectrometry and cluster ion sources*. J. Mass Spectrom., **40**(8): 985-999 (2005).
- [159] Touboul D., et al., *Improvement of biological time-of-flight-secondary ion mass spectrometry imaging with a bismuth cluster ion source*. J. Am. Soc. Mass. Spectrom., **16**(10): 1608-1618 (2005).
- [160] Jones E. A., Lockyer N. P., and Vickerman J. C., *Depth profiling brain tissue sections with a 40 keV C60+ primary ion beam*. Anal. Chem., **80**(6): 2125-2132 (2008).
- [161] Amaya K. R., et al., *Lipid imaging in the zebra finch brain with secondary ion mass spectrometry*. Int. J. Mass spectrom., **260**(2-3): 121-127 (2007).
- [162] Borner K., et al., *Distribution of cholesterol and galactosylceramide in rat cerebellar white matter*. Biochimica Et Biophysica Acta-Molecular and Cell Biology of Lipids, **1761**(3): 335-344 (2006).
- [163] Nie H. Y., et al., *Imaging subcellular features of a sectioned rat brain using time-of-flight secondary ion mass spectrometry and scanning probe microscopy*. Appl. Surf. Sci., **255**(4): 1079-1083 (2008).
- [164] Brunelle A. and Laprevote O., *Lipid imaging with cluster time-of-flight secondary ion mass spectrometry*. Anal. Bioanal. Chem., **393**(1): 31-35 (2009).
- [165] Fletcher J. S. and Vickerman J. C., *A new SIMS paradigm for 2D and 3D molecular imaging of bio-systems*. Anal. Bioanal. Chem., **396**(1): 85-104 (2010).
- [166] Kleinfeld A. M., Kampf J. P., and Lechene C., *Transport of ¹³C-oleate in adipocytes measured using multi imaging mass spectrometry*. J. Am. Soc. Mass. Spectrom., **15**(11): 1572-1580 (2004).

- [167] Kurczy M. E., et al., *Mass spectrometry imaging of mating Tetrahymena show that changes in cell morphology regulate lipid domain formation*. Proc. Natl. Acad. Sci. U. S. A., **107**(7): 2751-2756 (2009).
- [168] Ostrowski S. G., et al., *Mass spectrometric imaging of highly curved membranes during Tetrahymena mating*. Science, **305**(5680): 71-73 (2004).
- [169] Touboul D., et al., *Lipid imaging by gold cluster time-of-flight secondary ion mass spectrometry: application to Duchenne muscular dystrophy*. J. Lipid Res., **46**(7): 1388-1395 (2005).
- [170] Tahallah N., et al., *Lipid mapping in human dystrophic muscle by cluster-time-of-flight secondary ion mass spectrometry imaging*. J. Lipid Res., **49**(2): 438-454 (2008).
- [171] Mas S., et al., *Lipid cartography of atherosclerotic plaque by cluster-ToF-SIMS imaging*. Analyst, **132**(1): 24-26 (2007).
- [172] Malmberg P., et al., *Localization of lipids in the aortic wall with imaging ToF-SIMS*. Biochim. Biophys. Acta, **1771**(2): 185-195 (2007).
- [173] Debois D., et al., *In situ lipidomic analysis of nonalcoholic fatty liver by cluster ToF-SIMS imaging*. Anal. Chem., **81**(8): 2823-2831 (2009).
- [174] Touboul D., et al., *MALDI-ToF and cluster-ToF-SIMS imaging of Fabry disease biomarkers*. Int. J. Mass spectrom., **260**(2-3): 158-165 (2007).
- [175] Magnusson Y. K., et al., *ToF-SIMS analysis of lipid accumulation in the skeletal muscle of ob/ob mice*. Obesity (Silver Spring), **16**(12): 2745-2753 (2008).
- [176] McDonnell L. A., et al., *Peptide and protein imaging mass spectrometry in cancer research*. Journal of proteomics, **73**(10): 1921-1944 (2010).
- [177] Lockyer N. P. and Vickerman J. C., *Progress in cellular analysis using ToF-SIMS*. Appl. Surf. Sci., **231**: 377-384 (2004).
- [178] Kulp K. S., et al., *Chemical and biological differentiation of three human breast cancer cell types using time-of-flight secondary ion mass spectrometry*. Anal. Chem., **78**(11): 3651-3658 (2006).
- [179] Allen G. C., et al., *Analysis of boron-10 in soft tissue by dynamic secondary ion mass spectrometry*. Journal of Microscopy-Oxford, **213**: 39-45 (2004).
- [180] Chandra S., et al. *Mapping of intracellular organelles in relation to boron distribution in the same human glioblastoma cell for the evaluation of the efficacy of anticancer boronated drugs* In Proceedings. in International Conference Secondary Ion Mass Spectrometry. SIMS, XII. September 5-10, 1999. Université Catholique de Louvain, Brussels, Belgium.
- [181] Kempson I. M., et al., *Time-of-flight secondary ion mass spectrometry analysis of hair from archaeological remains*. Eur. J. Mass Spectrom., **9**(6): 589-597 (2003).
- [182] Hinder S. J. and Watts J. F., *SIMS fingerprint analysis on organic substrates*. Surf. Interface Anal., **42**(6-7): 826-829 (2010).
- [183] Thiel V. and Sjoval P., *Using Time-of-Flight secondary ion mass spectrometry to study biomarkers*. Annual Review of Earth and Planetary Sciences, **39**: 125-156 (2011).
- [184] Sjoval P., Johansson B., and Lausmaa J., *Localization of lipids in freeze-dried mouse brain sections by imaging ToF-SIMS*. Appl. Surf. Sci., **252**(19): 6966-6974 (2006).
- [185] Piehowski P. D., et al., *MS/MS methodology to improve subcellular mapping of cholesterol using ToF-SIMS*. Anal. Chem., **80**(22): 8662-8667 (2008).
- [186] Richter K., et al., *Localization of fatty acids with selective chain length by imaging time-of-flight secondary ion mass spectrometry*. Microsc. Res. Tech., **70**(7): 640-647 (2007).
- [187] Johansson B., *ToF-SIMS imaging of lipids in cell membranes*. Surf. Interface Anal., **38**(11): 1401-1412 (2006).
- [188] Nygren H. and Malmberg P., *High resolution imaging by organic secondary ion mass spectrometry*. Trends Biotechnol., **25**(11): 499-504 (2007).
- [189] McDonnell L. A. and Heeren R. M. A., *Imaging mass spectrometry*. Mass Spectrom. Rev., **26**(4): 606-643 (2007).
- [190] Jones E. A., Lockyer N. P., and Vickerman J. C., *Suppression and enhancement of non-native molecules within biological systems*. Appl. Surf. Sci., **252**(19): 6727-6730 (2006).
- [191] Piehowski P. D., et al., *Freeze-etching and vapor matrix deposition for ToF-SIMS imaging of single cells*. Langmuir, **24**(15): 7906-7911 (2008).
- [192] Heeren R. M. A., et al., *Why don't biologists use SIMS? A critical evaluation of imaging MS*. Appl. Surf. Sci., **252**(19): 6827-6835 (2006).
- [193] Jones E. A., et al., *Suppression and enhancement of secondary ion formation due to the chemical environment in static-secondary ion mass spectrometry*. J. Am. Soc. Mass. Spectrom., **18**(8): 1559-1567 (2007).

Chapter 2 Instrumentation

ToF-SIMS instrument has evolved into various types (e.g., Q-Star XL hybrid quadrupole time-of-flight mass spectrometer [1]) for adaptation to analyse different inorganic and organic specimens. Dedicated to explore the potential application of ToF-SIMS to biological study since 1990s, the Manchester SIMS group has collaborated with Kore Technology (Cambridge, UK) and Ionoptika Ltd. (Southampton, UK) introducing two SIMS instruments, which have been employed for this study. The BioToF-SIMS is a conventional ToF-SIMS, designed as a high performance static SIMS instrument geared towards large rough biological specimens with laser post-ionisation facility; another is a new generation of dynamic SIMS, the J105 3D Chemical Imager (J105), which has been updated in many aspects compared with the BioToF-SIMS featuring high lateral resolution imaging and depth profiling at high mass resolution. This chapter briefly introduces the two instruments and the benefits that the two systems offer for the imaging of single cells.

2.1 BioToF-SIMS Instrument

The BioToF-SIMS instrument was initially designed and built by the UMIST and the Pennsylvania State University [2]. The current instrument (Fig. 2.1), following further development over the past decade, is equipped with novel heavy ion sources [one is 20 kV liquid metal ion gun (LMIG) with Au_n ($n=1-3$) source, another is 20 kV C_{60} polyatomic ion gun], reflectron time-of-flight mass analyzer with a post acceleration microchannel plate detector and xyz cryogenic sample stage. The instrument comprises several adjoining ultra high vacuum (UHV) chambers separated by vacuum valves, including a sample preparation chamber with fast sample entry lock and dual stage entry port and sample analysis chamber (SAC). The multi-chamber is designed for the fast recovery of vacuum from nearly atmosphere pressure upon the sample entry via the small preparation chamber, whilst maintaining the UHV in SAC (base pressure $\sim 10^{-9}$ mbar) for analysis.

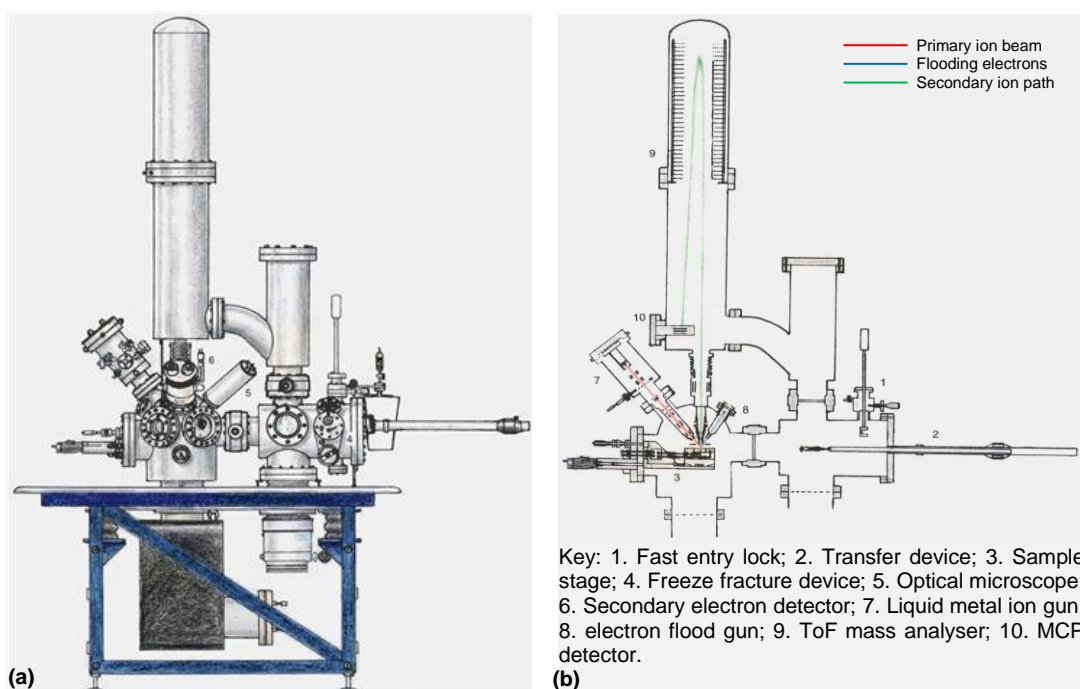


Fig. 2.1 Schematic drawing of BioToF-SIMS. (a), the frontal view; (b), the cut-out view of the BioToF-SIMS imaging system. Reproduced from reference [3].

2.1.1 Operation mechanism

As a conventional ToF-SIMS, the mechanism of operation is illustrated in Fig. 2.2. A focused primary ion (PI) beam is pulsed onto the sample (pulse width a few tens to hundreds nanoseconds) and sputters it. Ejected secondary ions (SIs) are extracted by the extractor and accelerated into a reflectron type mass spectrometer. SIs travel approx. 3 m in reflection through the ToF tube until arriving at the ion detector. Different SIs are separated according to m/z values during the flight and recorded individually as a mass spectrum. The electron flood gun is then introduced after the PI bombardment to stabilize the charged target, ensuring that the next beam bombardment yields signals for the mass spectrum. This analysis is operated in a UHV chamber (*i.e.*, SAC) pumped by an ion/sublimation pump (Varian Triode) in order to focus the PI and SI beam and prevent interfering gases and ions from adsorbing onto the sample surface. The spectra acquired pixel by pixel or as a function of depth can be further generated as 2D or 3D chemical maps of the sample.

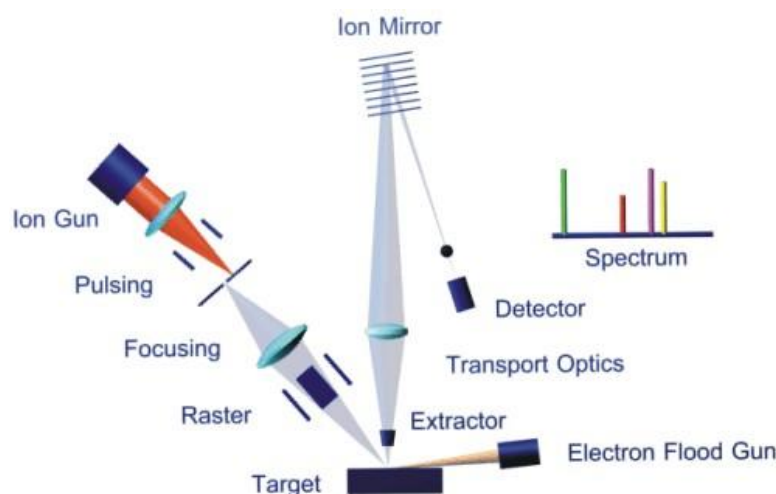


Fig. 2.2 The mechanism of the ToF-SIMS. Reproduced from Reference [4].

2.1.2 Main components

2.1.2.1 Primary ion gun

The criteria for developing an ideal PI gun are whether it is capable of delivering high yield of SIs from various specimens and high lateral resolution imaging. Additionally, the stability and reliability of the device are required. Au_n^+ and C_{60}^+ ion beams are particularly interesting since they enhance molecular SI yields rather than low mass fragments (30-100 fold compared to Ga^+), and have micrometer or submicron probe sizes to match the biological microdomain.

2.1.2.1.1 Liquid metal ion gun

The liquid metal ion gun (LMIG, Ionoptika IOG 25Au) shown schematically in Fig. 2.3 (a) is fitted with a gold germanium eutectic (Au:Ge) source [5], which can greatly reduce operating temperature ($\sim 400^\circ\text{C}$) when compared with pure gold ($>1000^\circ\text{C}$), and consequently reduce source substrate corrosion and extend source lifetime. The source comprises a needle with a reservoir of the Au/Ge alloy and an extractor plate [Fig. 2.3 (b)]. When a current passes through the filament wire, the alloy is heated and the melting metal flows to the tip of the needle. The needle is exposed to a 10-25 kV high voltage while an opposite voltage is on the extractor plate, generating an intense electric field between them. The metal ions therefore move from the tip to form a liquid metal cone, from which positively charged ions are extracted and pass through the aperture in the

extractor plate. The metal ion beam will not emit constantly unless the dynamic equilibrium is reached between the electrostatic forces and the surface tension. The continuous beam is then focused and passed through the apertures down the gun column using two lens and two sets of deflectors. Owing to the alloy reservoir, the source generates mixed mono-atomic and polyatomic ions, e.g., Au^+ , Ge^+ , Au_2^+ , Ge_2^+ , Au_3^+ . These ions are separated by means of a Wien filter which selects certain m/z value ions as the analysis beam. To do so, the voltage applied to the Wien filter is altered, only the ions with right velocity experience the zero force and will be unperturbed to travel through the crossed electromagnetic fields, and the others will be steered away from the straight path line. If the ions are mono-energetic, they can be separated according to the velocities and hence their masses.

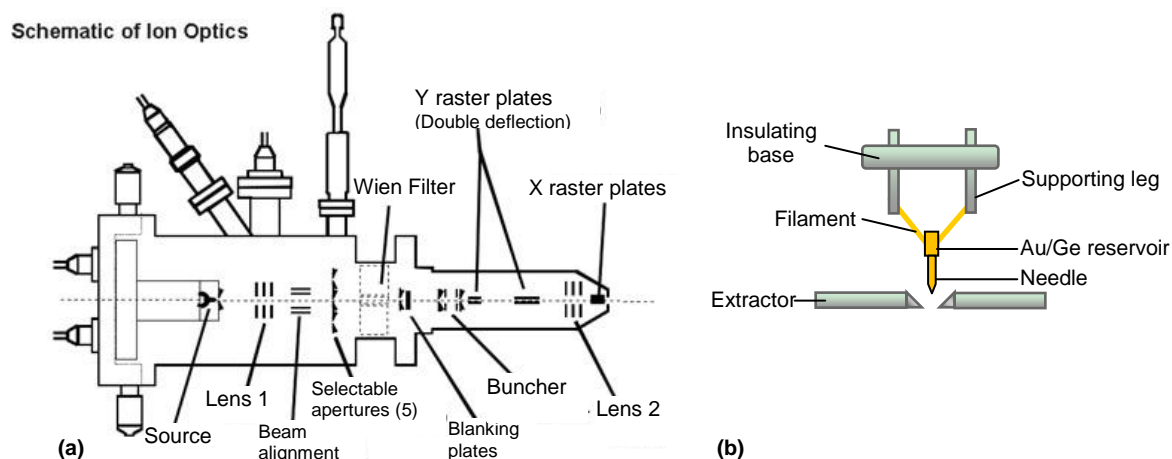


Fig. 2.3 Schematic of Liquid metal ion gun. (a), schematic of ion optics of LMIG. Reproduced from reference [6]; (b), gold germanium eutectic (Au:Ge) source.

Once the continuous PI beam is tuned, it is a requirement of static SIMS to pulse the beam to maintain low ion dose on the sample surface. By exerting a deflecting voltage (~ 200 V) on one of Blanking plates situated along the beam axis, the beam is steered away from the aperture, termed 'blanking'. Applying the same voltage in a short pulse to other plate, the beam is then un-blanked and passes the aperture to reach sample. Furthermore, imaging the sample requires motionless blanking to minimise the sweeping of the beam across the sample during the blanking process. This could occur when Lens 1 focuses the beam into the space between the blanking deflector plates. Lens 2 then forms an image of this point at the sample.

The LIMG offers a wide range of currents (~ 10 nA of Au^+ , ~ 1 nA for Au_3^+) with fine probe capability as small as ~ 50 nm, which could be obtained by finely tuning the beam passing through the smallest aperture situated after Lens 1. However, the beam tuning must be carefully considered according to the specimens and experiment requirements, as the available spatial resolution is always linked to SI signal.

2.1.2.1.2 Polyatomic C_{60}^+ Gun

The C_{60}^+ PI beam gun (Ionoptika IOG-C60-20) is built to expand imaging capability by taking full advantage of the high SI yield and low damage features of C_{60}^+ ion beam. As illustrated in Fig. 2.4, the system is based on the well established technologies of gas guns, e.g., Ar^+ , Xe^+ [7], but with vaporized C_{60} . At the rear of the source C_{60} powder is heated to a temperature of 475°C . Gas phase C_{60} ($\sim 8 \times 10^{-8}$ mbar) is directed into the centre of an ionization cell through a nozzle. A

concentric cylindrical grid accelerates electrons from the filament that surrounds this cell where the collisions occur between low-energy electrons (~ 70 eV) and C_{60} molecules resulting in the formation of C_{60}^+ . Upon ionisation, the C_{60}^+ ion beam is accelerated by a 10–20 kV floating voltage in the source region and extracted by placing an opposite polarity potential on the extractor plate. Neutral elimination is achieved by a 1° bend in the ion optical column. To obtain clean, short pulses of uniform intensity, the beam (mainly C_{60}^+ , C_{60}^{2+} or C_{60}^{3+}) is mass filtered using a Wien filter. The alignment plates and focus lens which are similar to the LIMG allow the beam to be finely tuned for imaging. The original design of C_{60} gun (Fig. 2.4) had two lenses, the current 20 kV C_{60} gun has only one lens, designed for higher current operation.

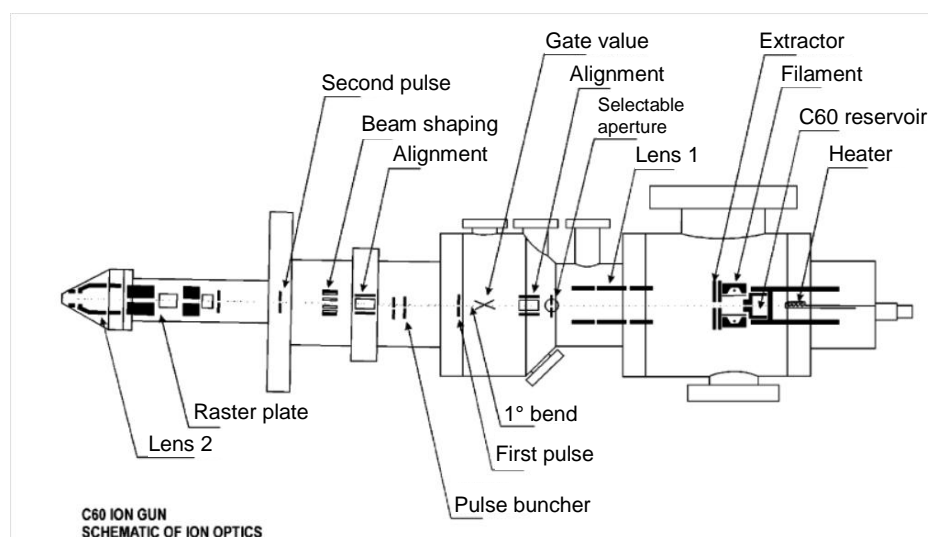


Fig. 2.4 Schematic of C_{60} gun ion optics. Reproduced from reference [7].

It has been proven that monoatomic primary particles penetrate deep into the sample compared to the ejection depth of the SI, resulting in the disrupting the chemistry of the sub-surface as discussed in section 1.1.1. For organic species this disruption causes the breaking of chemical bonds leading to the destruction of the molecular chemistry [8]. On the contrary, the polyatomic beam C_{60}^+ exhibits not only the higher SI yields but also less chemical damage to the subsurface, offering the great potential to maintain reasonable depth resolution during the sputtering and molecular depth profiling to reveal subcellular structures in 3D [9].

2.1.2.2 ToF mass analyser

As a vital technical improvement for ToF-SIMS, time-of-flight mass analyser enables quasi-parallel detection of all masses at high transmission ($>50\%$) and theoretical unlimited mass range (mass range is actually determined by altering the flight time interval and experiment/cycle frequency). The currently used ToF mass analyser (Kore R-500, Fig. 2.5) has a flight path of approx. 3 m in reflection. The SI pulses are accelerated within an electrical field gradient of approx. 250 V/mm to a given a potential 2.5 kV, such that all ions possess the same kinetic energy and then drift through a field free space until getting to the detector. The SIs separation is determined by the flight time and hence the masses. The flight time, t , is determined as follows:

$$t = L \left(\frac{m}{2zV} \right)^{1/2} \quad \text{Equation 2.1}$$

Where, t is the flight time; m/z is mass to charge ratio; L is the length of flight path; V is the acceleration voltage.

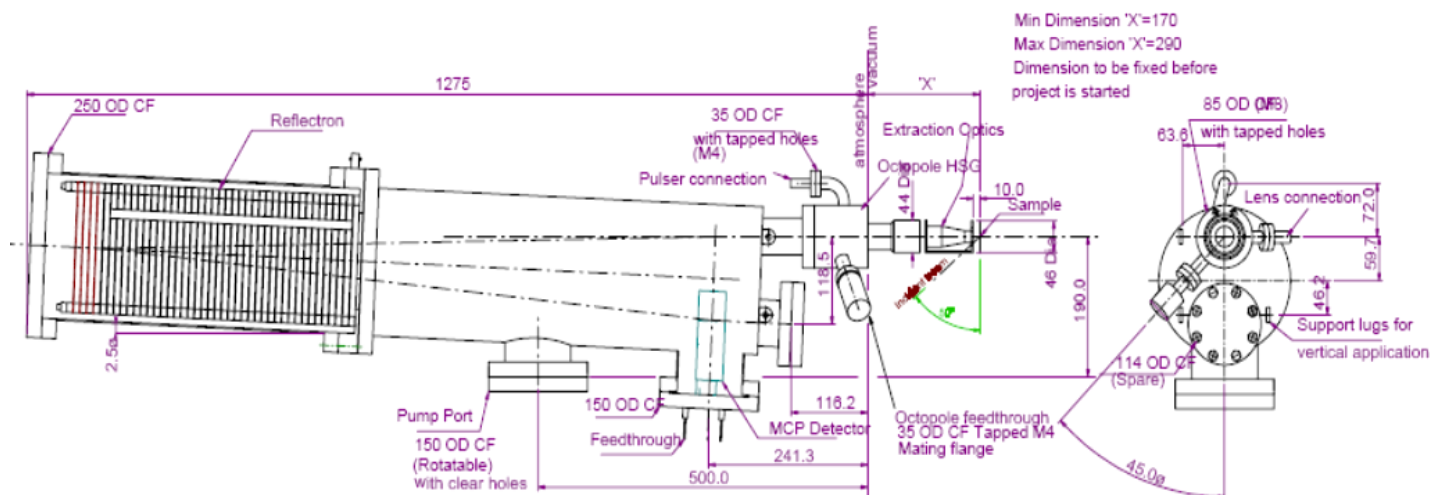


Fig. 2.5 Schematic of ToF mass analyser. Reproduced from reference [10].

The flight tube is inclined at 2.5° in order to split the trajectory of the extracted SIs (which go upwards along the optical axis through the extraction lenses) and the reflected ions (which are directed downwards at a small angle by the reflectron to the detector). The 'reflectron' or 'ion mirror', lying in the upper side of the flight tube with 38 rings and a gridded backplate, is used to compensate the initial energy distribution of the SIs. The more energetic ions penetrate more deeply before being reflected back, thus longer flight path offset their increased velocity. As a result, the ions with the same mass will arrive at the detector simultaneously. This energy compensation gives high mass resolution of up to 10,000 in principle with a sufficiently short PI pulse. However, the necessity of pulsing the PI beam to allow the registration of SIs flight times results in a low duty cycle. Additionally, mass resolution also depends on many other factors, e.g., the time resolution of the detector system.

2.1.2.3 MCP detector

At the end of flight path of SIs, there are a microchannel plate (MCP) detector and a counting device to register the SI events. The detector consists of two microchannel plates with angled channels rotated 180° from each other producing a chevron (V-like) shape as shown in Fig. 2.6. Each microchannel plate comprises a large number of miniature electron multipliers oriented parallel to one another; the channels are in range of 10-100 μm in diameter and have length to diameter ratios between 10 and 100. Channel axes are biased at a small angle ($\sim 8^\circ$) to the MCP input surface [11]. Usually the channel matrix is fabricated from a lead glass, which serves to optimize the secondary electron emission at each channel and renders the channel walls semiconducting, so as to allow charge replenishment from an external voltage source. When the SIs hit the upper plate of a chevron MCP, the emitted electrons strike the channel wall generating an electron cascade. The cascade travels down to the lower plate where the channels have an angle with the upper ones so as to prevent ion feedback, leading to higher multiplied output gains of 10^6 - 10^7 [11]. Through the lower plate, the electrons strike a metal anode and the amplified charge pulse is delivered to counting device.

The detection efficiency falls with increased mass and decreased ion impact energy at the front of the MCP. At an impact energy of 20 keV, the detection efficiency of cationised polystyrene (PS) oligomers is approximately 80% at mass 10,000 amu, whereas at 5 keV it falls to $\sim 5\%$ [12]. A gain

curve is a simple method to determine the correct voltage to operate the MCP for a given efficiency. To detect large ions, high impact energy is required to kinetically initiate secondary electron emission, thus post-acceleration is applied by supplying a voltage ~ 20 kV of opposite charge to the SIs directly before the detector plates. The voltage ensures unity detection efficiency up to a mass of 4000 amu, which covers the mass range typically accessible in a SIMS experiment [12].

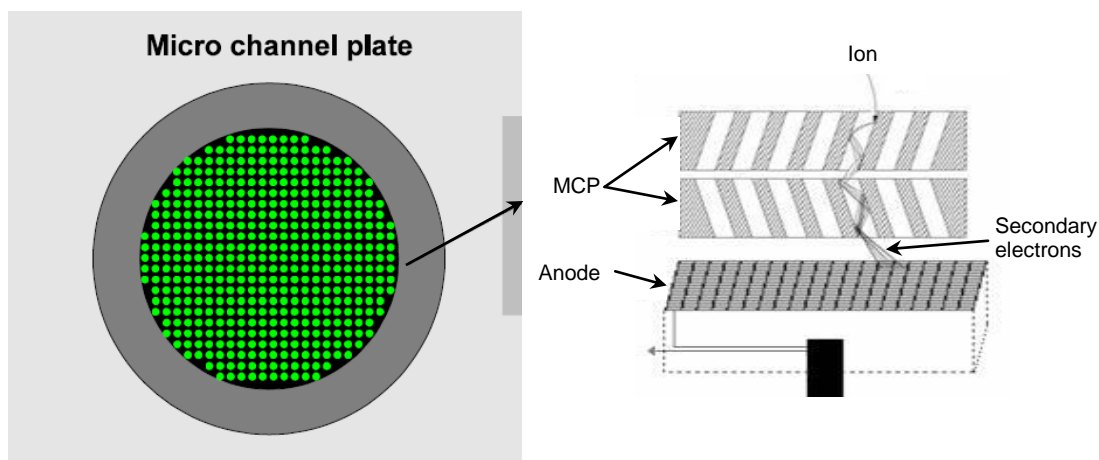


Fig. 2.6 Chevon type microchannel plates. The impact of a single ion within one of the channels causes an electron cascade leading to a greatly multiplied signal output. In the system within the detector of the BioToF-SIMS instrument a second plate receives the electron output of the first, and thus the signal is further enhanced yielding measurable signal from single ion impacts. Reproduced from reference [13].

After passing through an inverting preamplifier with a gain of $-40\times$, the signal is recorded by Time-to-Digital converter (TDC) with a time resolution of 1 ns (FAST Comtec, Germany). When a signal above the threshold voltage (~ 10 mV) is detected the computer registers as a hit. The threshold voltage should be set to maximize the sensitivity and minimize the noise levels. A transient digitizer (TD) with 2 ns time resolution (Signatec Ltd) is used to record both the time and magnitude of each hit in experiments where the simultaneous arrival of multiple ions would cause the saturation of TDC, e.g., in laser post-ionisation experiments.

2.1.2.4 Electron Flood Gun

The Electron Flood Gun is used to emit low-energy electrons (~ 25 eV) in order to stabilize a charged sample. The potential of an insulated sample surface rises during the analysis cycle because the positive PI beam inputs the positive charges whilst SI and secondary electrons are emitted. This moves the kinetic energy of ions beyond the limit of the analyzer and causes the loss of the SIMS spectrum. Gilmore and Seah [14] suggested a dose of 6×10^{18} electrons/m² as an upper limit for the analysis of fragmentation of PS, Poly(vinyl chloride) (PVC), polymethylmethacrylate (PMMA) and Poly(tetrafluoroethylene) (PTFE).

2.1.2.5 Sample stage and sample stub

The sample is usually loaded on the substrate (silica wafer, glass slide, etc) and then mounted on top of a 2 cm \times 2 cm \times 1.5 cm copper stub (Fig. 2.7). This sample stub can be inserted into sample stage and clamped in place by a piston, securing good electronic conduction and thermal contact with the stage. For rigidity and vibration stability towards high lateral resolution imaging of large biospecimens (e.g., tissues), the stage is designed with a relatively large range of motion (x and y:

± 10 mm, z : ± 1 mm) using roller bearing translators and can be positioned precisely using digital micrometers and with the aid of an optical and video microscope.

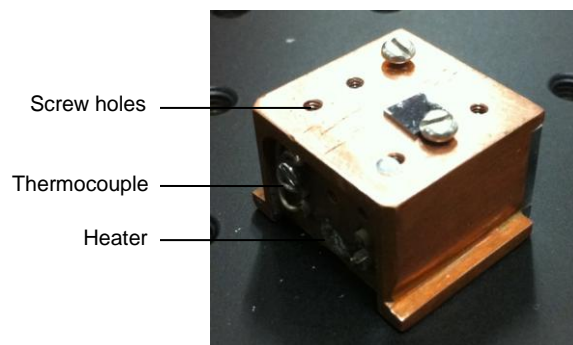


Fig. 2.7 Sample holder for the BioToF-SIMS. This version has additional features for the *in situ* freeze fracture procedure.

The stage can be biased a ± 2500 V depending on the SI polarity of interest and operated with DC or pulsed mode. By setting the pulse width, it ensures that only the SI ejected by the PI beam to be detected, noise to be reduced, as well as allows low energy electron flooding particularly when sample charging occurs. The pulsed stage can be set to either delayed or non-delayed relative to the primary beam. The former biases the stage voltage on after the PI beam impact to get sharper peak shape in the mass spectrum, while for the latter the stage potential is applied at the same time as primary beam pulse, resulting in SI flight time distributions that match the PI pulse width.

Both the stage and the sample can be cooled to cryogenic temperatures (~ -150 °C) and controlled by flowing cooled nitrogen through the gas line incorporated in the stage. The temperature can be measured by the thermocouples and a heater coil. The cold stage is most beneficial for the analysis of volatile materials and biological samples which require a cold hydrated environment to preserve the pristine chemical gradients.

2.2 J105 3D chemical imager

The conventional ToF-SIMS design pulses the PI beam onto the sample surface, which is at the cost of slow duty cycle, and lower lateral resolution than the DC PI beam capable of (*i.e.*, secondary electron/ion image). Moreover, if pulsing a focused C_{60}^+ ion beam, the resulting low current and degraded lateral resolution would be incompatible with molecular depth profiling at high lateral resolution, of which the C_{60}^+ ion beam has shown great potential to [15]. To circumvent the principal drawbacks of the conventional ToF-SIMS and take full advantage of C_{60}^+ ion beam, the Vickerman group at the University of Manchester entered into collaboration with Ionoptika Ltd. (Southampton, UK) and SAI Ltd. (Manchester, UK) to develop new concept of ToF-SIMS instrument and a 40 kV C_{60} PI gun. The outcome, the J105 3D Chemical Imager, operates with a DC PI beam and bunches SI into a harmonic field ToF mass analyser. This operation mode offers a better mass resolution without sacrificing the lateral resolution, improved duty cycle and independence of sample topography, as discussed in the following section 2.2.2.

2.2.1 Overview of the J105 3D Chemical Imager

The schematic of the J105 is shown in Fig. 2.8. A PI beam (C_{60}^+ or Au_n^+ ($n=1-3$), 10–40 keV) operated in DC mode impinges the sample surface to generate a continuous supply of SI. The SI beam is cooled in a RF only quadrupole by colliding with filler gas (*e.g.*, high purity N_2) and then

further energy filtered by an electrostatic analyser (E.S.A), preparing the SIs at 100 eV with energy spread of 1 eV before the linear buncher. A portion of SI approx. 300 mm long is then injected into the buncher and the buncher gate is turned off. Upon the closure of the gate the buncher fires by instantaneously applying an accelerating field. This creates a time focus of SIs at the entrance of the ToF analyser (harmonic field reflectron). The SIs undergo half a period of simple harmonic motion in the analyser before impacting the detector with the same time spread as the time focus from the buncher.

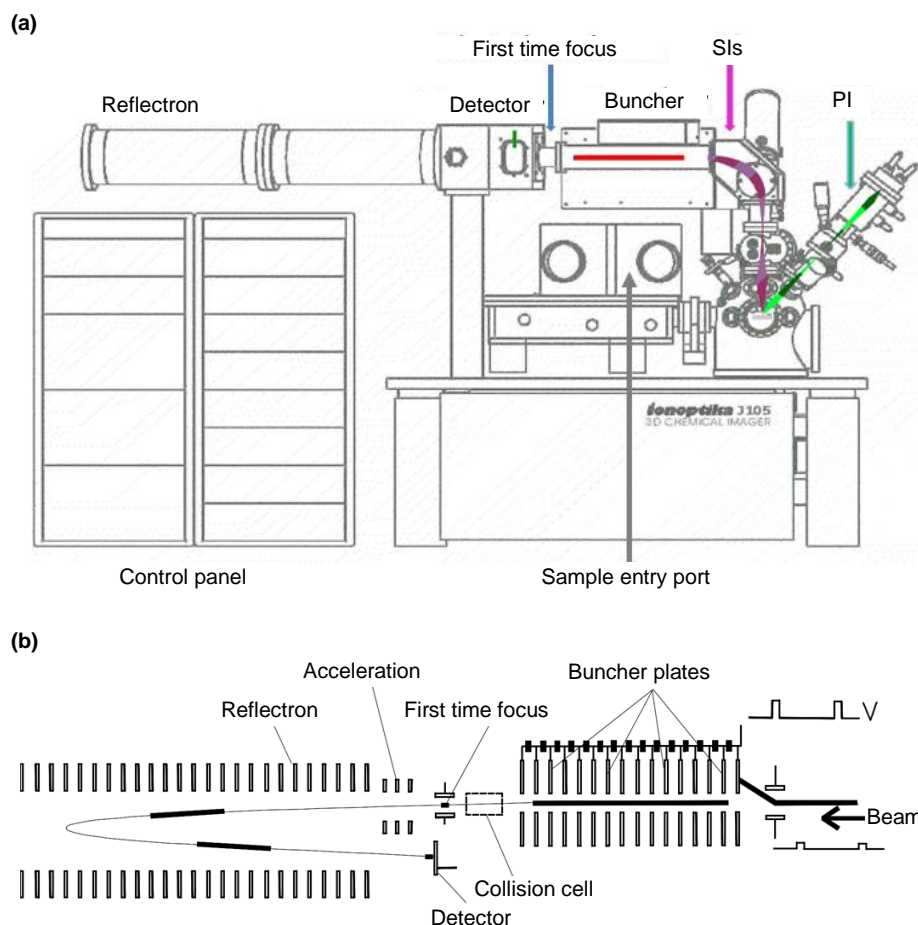


Fig. 2.8 Illustration of the Ionoptika J105 3D Chemical Imager. (a), the front view; (b), schematic of the mass spectrometry showing the coupling of the buncher to the harmonic reflectron. The collision cell is for dissociation during MS/MS experiments. Reproduced from reference [16].

2.2.2 Unique features

2.2.2.1 DC PI beam and corresponding high lateral resolution and fast duty cycle

Aimed to increase duty cycle and attain high lateral resolution, the J105 is initially equipped with a 40 kV C_{60} PI gun (IOG C60-40, Ionoptika Ltd, UK) and 40 kV Au LIMG (IOG Au40, Ionoptika Ltd, UK) operating in DC mode. Now the Au LIMG has been replaced by a new Ar cluster ion gun (GCIB 20). In this study with emphasis on the subcellular imaging of biological samples, the C_{60}^+ PI beam is mainly adopted.

The IOG C60-40 has the same C_{60} source and similar structure as IOG C60-20 installed in BioToF-SIMS but much more improved in terms of focusing and beam energy. The ion gun runs the anode voltage up to 40 kV and provides the impact energy up to 120 keV when selecting C_{60}^{3+} ion beam. Singly, doubly, and triply charged C_{60} ions are mass filtered by a Wien filter. The ion beam is

steered by two pairs of alignment plates and focused using two electrostatic lenses. The DC beam of C_{60}^+ ion can be focused down to 500 nm, the normal operation conditions under different adjustable aperture is shown in Table 2.1.

Table 2.1 IOG C60-40 operation conditions with 40 keV C_{60}^+ ion beam

Adjustable aperture (μm)	Current (nA)	Spot size (μm)
1000	1.056	40
300	0.100	15
100	0.045	08
100	0.005	03
30	0.001	0.8
10	0.0006	0.5

The data is provided by Ionoptika Ltd, UK.

With the continuous PI beam, imaging mode with the C_{60}^+ ion beam can be performed at high lateral resolution without the degradation as encountered when pulsing the PI beam on a conventional ToF-SIMS instrument. Additionally, the continuous SIs can be generated beyond the static limit due to the low chemical damage of the C_{60}^+ ion beam, which greatly increases the duty cycle and correspondingly shortens the analysis time. 2D imaging of a $100 \times 100 \mu\text{m}^2$ sample using a focused C_{60}^+ ion beam with target current of 10 pA operating on the BioToF-SIMS (50 ns pulse width and 10 kHz frequency) would take 9 h for PI dose up to 1×10^{13} ions/ cm^2 . The analysis time would be reduced to 16 s if operating on the J105 (DC beam and 10 kHz frequency) with exactly the same experiment parameters. Upon acquiring a sequence of 2D images under the same condition to generate a 3D image at an ion dose of 1×10^{15} ions/ cm^2 , an impractical time (over a month) would be required using the BioToF-SIMS in contrast to 30 min with the J105. It is obvious that 3D imaging particularly benefits from this operation mode with the J105 in terms of an affordable analysis time frame, less exposure time of biological specimens in vacuum, and more importantly, high lateral resolution depth profiling by a single beam. A focused C_{60}^+ ion beam in DC mode enables reasonable erosion depth into the sample in short time and continuously emit SIs from precise location (*i.e.*, voxel) for analysis without damage to the subsurface of the sample; accordingly the simultaneous etching and analysing is achieved using a single beam, and chemical information is detected by voxels rather than pixels without waste any of the sample [17]. In this way, the necessity of the dual beams analysis (usually C_{60}^+ ion beam to etch and a focused Bi_3^+ or Au_3^+ ion beam to analyse) adopted by conventional ToF-SIMS for 3D imaging is also bypassed.

The DC C_{60}^+ ion beam also contributes to higher SIs signal level compared with the pulsed beam on BioToF-SIMS. Rabbani [18] compared several biomolecules reacting to the same bombardment with both the J105 and BioToF-SIMS. Take arginine and cholesterol for examples (Fig. 2.9), the higher intensities of molecular ions are observed using the J105 than the BioToF-SIMS. The analyses of the same samples were conducted using same ion beam with the same impact energy, which ruled out other influence factors to ion intensity than the instrument design and operation, so that the intensity increasing can be attributed to the DC beam operation. The spectra in Fig. 2.9 also reveal different noise to signal ratios with two instruments. The signal to noise ratio is defined as signal power to noise power corrupting as outlined in Table 2.2. Apparently, the J105 has better capability to resolve the signal from noise.

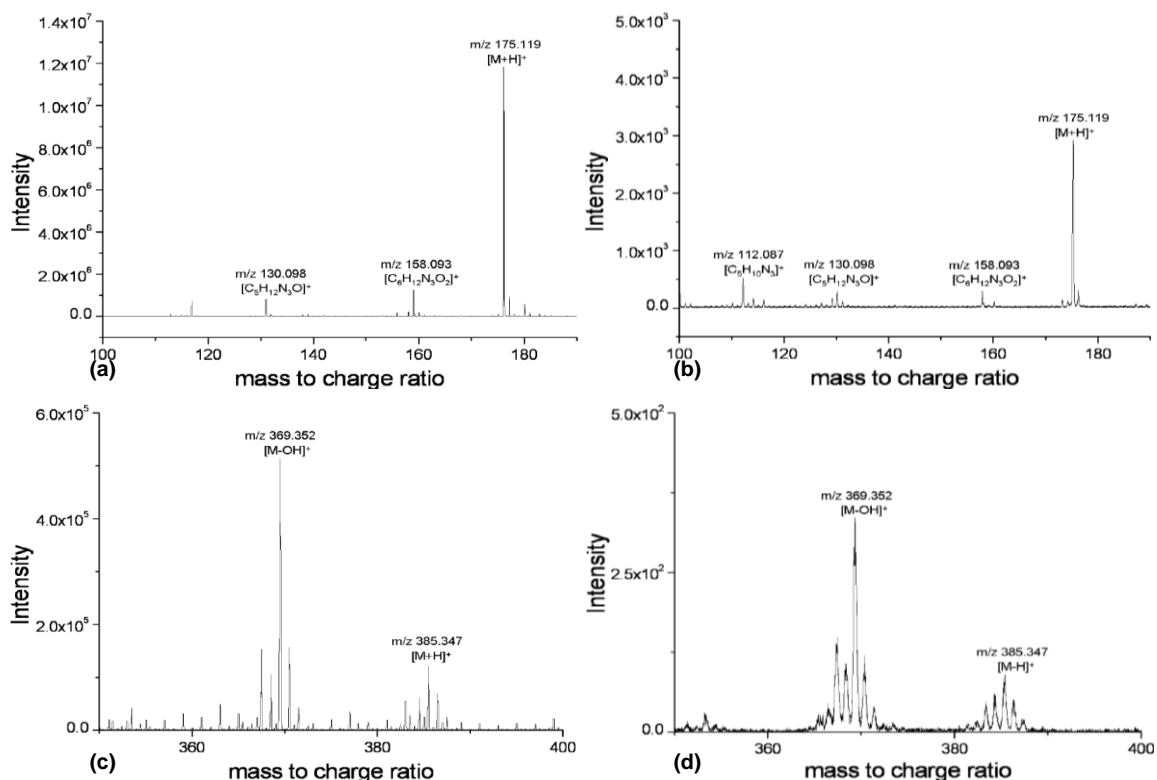


Fig. 2.9 +SIMS spectra of two biomolecules using the J105 3D Chemical Imager and the BioToF-SIMS both with 20 keV C_{60}^{+} ion beam at an ion dose of 1×10^{13} ions/cm². Spectra acquired with the J105 are arginine in (a) and cholesterol in (c); spectra with the BioToF-SIMS are arginine in (b) and cholesterol in (d). On comparison of the surface spectra, the higher intensities of molecular ions are observed using the J105 than with the BioToF-SIMS. DC C_{60}^{+} ion beam on the J105 generates continuous SIs from the sample that increases signal levels while prevent chemical damage accumulation. With the BioToF-SIMS, the generated SI has to be detected before the pulsed PI beam strikes again. Hence, the BioToF-SIMS has a much lower duty cycle and lower SI intensities. Reproduced from reference [18].

Table 2.2 Signal to noise levels on the J105 3D Chemical Imager and the BioToF-SIMS

<i>m/z</i>	Signal to noise level on J105	Signal to noise level on BioToF
175.119	5272	47
136.076	978	92
452.226	1500	65

Reproduced from reference [18].

2.2.2.2 Buncher-ToF with corresponding high mass resolution and transmission

Instead of extracting the SIs directly to the reflectron ToF analyser on the BioToF-SIMS, the J105 has the pretreatment for SIs before enter the buncher-ToF analyser, which is to prepare SIs at an energy of 100 eV through RF only quadrupole and E.S.A. The current buncher has 30 electrodes plates with an aperture for the SIs pass. Each plate can be adjusted separately to form an optimised accelerating field for better mass resolution.

The buncher, 300 mm long, is designed to collect SIs for 90 μ s, and then the buncher gate is blanked by a 100 V electric field. Next, the buncher 'fires' by applying the accelerating fields from 7 kV at the entrance to 1 kV at the exit within 10 μ s. The process balances kinetic energy of the lagged SIs and faster SIs and creates a time focus point as the SIs with the same *m/z* will be at a certain plane in space at the exit of the buncher. The compressed SI packet with 6 keV energy spread enters into the ToF analyser. In the BioToF-SIMS, SIs are accelerated by a certain electric field and end up with same kinetic energy, so a standard reflectron ToF is enough to compensate the narrow energy spread (<50 eV) of the ions with the same *m/z*. However, with wide energy

spread as bunched SIs on the J105, a harmonic field ToF mass analyser is required. In the mirror of a "quadratic-field" reflectron the retardation electric potential is proportional to the square of the distance to the mirror entrance, forming a one-dimensional harmonic field, in which the flight time of the ions are decoupled from their kinetic energy. Thus all ions with equal m/z will leave the reflectron and arrive at the detector with the same time spread as when entering it [19]. Consequently, the mass resolution is subject to the time distribution of the compressed SIs and becomes independent of sample topography or sputtering events. Currently, the instrument produces mass resolution of $m/\Delta m \sim 6000$ at 500 amu and is expected to exceed $m/\Delta m$ of 10,000. A mass accuracy of 5 ppm is obtained [17] and analysis of phosphocholine lipids, vitamin E and cholesterol shows the mass accuracy of fragments ion and molecular ions in Table 2.3. In addition, mass calibration can be done using one standard compound (e.g., Csl) in one spectrum unlike the BioToF-SIMS which needs calibration on each sample to account to topography changes and any sample charging etc.

Table 2.3 Mass accuracy of several biomolecules using J105 3D Chemical Imager

Fragments and parent compound in +SIMS	Observed m/z	Calculated m/z	Mass accuracy /%
$[C_5H_{12}N]^+$ - phosphocholine	86.05	86.10	-0.058
$[C_2H_6PO_4]^+$ - phosphate head group	124.98	125.00	-0.016
$[C_5H_{13}NO_3P]^+$ - phosphocholine or sphingomyelin	166.05	166.06	-0.006
$[C_5H_{15}NO_4P]^+$ - phosphocholine or sphingomyelin	184.05	184.07	-0.011
$[C_8H_{19}PO_4N]^+$ - phosphocholine or sphingomyelin	224.10	224.10	0.000
$[C_{27}H_{45}]^+$ - cholesterol(M-OH)	369.35	369.35	0.000
$[C_{29}H_{50}O_2]^+$ - vitamin E	430.37	430.38	-0.002
$[C_{35}H_{65}O_4]^+$ - phosphocholine	549.49	549.49	0.000
$[C_{37}H_{69}O_4]^+$ - phosphocholine	577.48	577.52	-0.007
$[C_{10}H_{19}NO_8P - C_{32}H_{64}]^+$ - phosphocholine	760.63	760.58	0.0006

The way that the buncher is tuned to collect SIs boosts the transmission of molecular ions while sacrificing that of the fragment ions and elemental ions. All the ions entering the buncher have the same energy, 100 eV (with 1 eV discrepancy), thus their floating velocity is proportional to the reciprocal of root mass. Giving the same flow time, 90 μs , the low mass ions (e.g., mass below 50 amu and instrument operate at 10 kHz) would flee away from the buncher. In addition, the operation frequency of the instrument also affects the low mass ion transmission. If the instrument operates at 10 kHz, the transmission of the low mass ions is 20% with respect to transmission the high mass ions. If the analysis is performed at 5 kHz, the value falls to 10%. This is exhibited in the spectrum as low ion intensity or no ions at all in mass range below m/z 100. This mass range is usually due to the hydrocarbon fragments of biological samples that provides not too much information of diagnostic ions of biomolecules. However, the elemental ions (e.g., Na^+ and K^+) are missed that are of interests for biological samples.

2.2.2.3 Reliable sample handling system

The J105 has been designed to allow easy insertion to the z lift in the preparation chamber and automatic transferral of biological samples to the xyz stage in SAC that is controlled by the sample handling software. Cryogenic facilities are also provided for both z lift and xyz stage. The frozen samples are transferred to an argon pre-purged glove box mounted over the sample insertion port. Coupled with a cryo-shield in the preparation chamber, water condensation can be avoided. Then the z lift rises to a load lock and the samples are placed directly onto this stage during insertion, followed by rapidly transferring to the xyz sample stage. With PT100 temperature sensor, both

stages can be pre-cooled or heated as required. This benefits the analysis of biological samples in frozen-hydrated state or *in situ* freeze fracture.

The stage can also perform automatic freeze fracture using a 'mousetrap' device inside the instrument. The sample is fast frozen inside the hinge (alternatively the cells can be cultured directly onto the hinge) and loaded on the sample holder under LN_2 (Fig. 2.10). Under argon protection, the sample holder is loaded onto z stage, and inside the preparation chamber, the trigger is then pressed to release the upper side of the hinge by a sprung flipper. The sample is therefore fractured and transferred to the pre-cooled stage for analysis. Compared with previous design of *in-vacuo* freeze fracture of two silicon sharps used in BioToF-SIMS, the performance with mousetrap is more reliable and convenient. Moreover, it retains two surfaces of fractured sample for analysis.

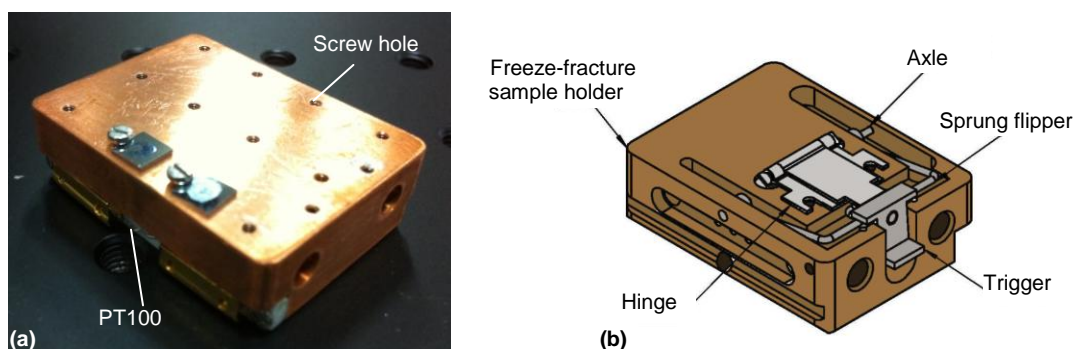


Fig. 2.10 Sample holders for the J105 3D Chemical Imager. (a), the copper sample holder with dimensions of 40 mm×30 mm×12 mm for room temperature and normal cold stage analysis; (b), the freeze-fracture hinge on the copper sample holder with dimensions of 40 mm×30 mm×12 mm. Reproduced from Sample Handling Manual courtesy of Ionoptika.

Owing to the precise movement of xyz stage (x and y: ± 10 cm, z: ± 5 cm, accuracy: 1 μm) controlled by the sample handling software, the instrument can perform tiling imaging. The mosaic images are acquired from consecutive squares of the sample surface together to form a more detailed chemical map over relatively large area. In this way, the pixel size and the lateral resolution of the PI beam are better matched, so that a large area analysis can be conducted without losing information between pixels.

2.2.2.4 MS/MS analysis

The J105 instrument is capable of MS/MS analysis for both fundamental studies related to sputtering and SI formation and molecular identification. This is very important for the analysis of complex biological samples with a large amount of unknown compounds. The SIs exiting the buncher pass through a collision cell containing a suitable gas (e.g., helium, nitrogen and argon). The collision energies are in the range of 1-7 keV resulting from the acceleration field of the buncher, which is enough to disassociate all the species. Since the collisions take place in a field free region of the instrument, the parent ion and associated daughter ions continue to travel with the same velocity. Following a short ToF region, a timed ion gate (4 amu) is used to select the parent-daughter combination of interest for the ToF analyzer.

There are other devices offering conveniences for analysis. The camera 1 and camera 2 are installed in the load lock and SAC respectively. The sample picture can be taken using the camera 1 and saved to sample handling software for the navigation of the sample stub. Camera 2

can be used to monitor the samples under investigation and assist to confirm the PI beam bombardment area. Additionally, there is an electron gun and secondary electron detector (SED) similar to the BioToF-SIMS for charge neutralisation and direct secondary electron/ion imaging.

To sum up, the new concept buncher-ToF SIMS instrument -- J105 3D Chemical Imager uses the continuous PI beam and bunches SI, which display several advantages particularly for bio-specimens analysis, e.g., high lateral resolution imaging without compromising high mass resolution, much higher duty cycle accordingly practical analysis time for 3D imaging without switching to dual beam analysis, and high lateral resolution molecular depth profiling. In addition, the mass resolution is decoupled with sample topography effect. These new features of the J105 offer the possibility to investigate the two biological systems presented in this thesis, as one aims to investigate *Xenopus laevis* embryo with extreme topography, and another to track subcellular mitochondria (0.5-2 μm) in the depths of murine fibroblast cells.

Reference

- [1] Carado A., et al., *Cluster SIMS with a hybrid quadrupole time-of-flight mass spectrometer*. Appl. Surf. Sci., **255**(4): 1610-1613 (2008).
- [2] Braun R. M., et al., *Performance characteristics of a chemical imaging time-of-flight mass spectrometer*. Rapid Commun. Mass Spectrom., **12**(18): 1246-1252 (1998).
- [3] Wong S., *Development of an imaging ToF-SIMS system and its application to self-assemble monolayer and multilayers*, 2001, UMIST, Manchester, UK.
- [4] [cited 2008 10th Aug.]; Available from: http://www.fkf.mpg.de/ga/machines/sims/How_does_TOF_SIMS_work.html.
- [5] Davies N., et al., *Development and experimental application of a gold liquid metal ion source*. Appl. Surf. Sci., **203-204**(0): 223-227 (2003).
- [6] Hill R. and Blenkinsopp P. W. M., *The development of C60 and gold cluster ion guns for static SIMS analysis*. Appl. Surf. Sci., **231-232**(0): 936-939 (2004).
- [7] Weibel D., et al., *A C60 primary ion beam system for time of flight secondary ion mass spectrometry: its development and secondary ion yield characteristics*. Anal. Chem., **75**(7): 1754-1764 (2003).
- [8] Fletcher J. S., Lockyer N. P., and Vickerman J. C., *C60, buckminsterfullerene: its impact on biological ToF-SIMS analysis*. Surf. Interface Anal., **38**(11): 1393-1400 (2006).
- [9] Szakal C., et al., *Surface sensitivity in cluster-ion-induced sputtering*. Phys. Rev. Lett., **96**(21): 216104 (2006).
- [10] [cited 2008 10th July]; Available from: <http://www.kore.co.uk/cop.html>.
- [11] Wiza J. L., *Microchannel plate detectors*. Nucl. Instrum. Methods Phys. Res., Sect. A, **162**: 587-601 (1979).
- [12] Gilmore I. S. and Seah M. P., *Ion detection efficiency in SIMS: Dependencies on energy, mass and composition for microchannel plates used in mass spectrometry*. Int. J. Mass spectrom., **202**(1-3): 217-229 (2000).
- [13] [cited 2011 15th Oct.]; Available from: www.geos.ed.ac.uk/facilities/ionprobe/SIMS4.pdf.
- [14] Gilmore I. S. and Seah M. P., *Investigating the difficulty of eliminating flood gun damage in TOF-SIMS*. Appl. Surf. Sci., **203-204**(0): 600-604 (2003).
- [15] Fletcher J. S., et al., *Uncovering new challenges in bio-analysis with ToF-SIMS*. Appl. Surf. Sci., **255**(4): 1264-1270 (2008).
- [16] Fletcher J. S., et al., *A new dynamic in mass spectral imaging of single biological cells*. Anal. Chem., **80**(23): 9058-9064 (2008).
- [17] Fletcher J. S. and Vickerman J. C., *A new SIMS paradigm for 2D and 3D molecular imaging of bio-systems*. Anal. Bioanal. Chem., **396**(1): 85-104 (2010).
- [18] Rabbani S., *Advances in Time-of-flight secondary ion mass spectrometry for the analysis of single cells on a sub-cellular scale*, 2010, University of Manchester.
- [19] Andersen U. N., et al., *In-series combination of a magnetic-sector mass spectrometer with a time-of-flight quadratic-field ion mirror*. Rev. Sci. Instrum., **69**(4): 1650-1660 (1998).

Chapter 3 Lipidomics study of *Xenopus laevis* embryo

3.1 Introduction

Xenopus laevis (*X. laevis*) eggs and embryos in the early cleavage stages are important model systems in developmental biology. They have a relatively large size (approx. 1-1.2 mm in diameter) allowing convenient manipulation [1] and can be easily obtained. Additionally, the ability to replicate the DNA semi-conservatively in the unfertilised egg, and the rapid cleavage in early stages of embryo development make this model an almost ideal single-cell expression system [2]. Since the 1970s, there have been remarkable developments in the methods used to study this model system, by which the microscopists examine the morphology and cellular structures using scanning electron microscopy (SEM) [3, 4] and confocal microscopy [5], and it has become possible to investigate the intricate nature of subcellular organelles and the biological processes using new fixing and staining technologies [6]. However, the previous studies on this model suffered from a lack of chemical information using SEM and confocal microscopy or the loss of the spatial distribution of biomolecules using liquid chromatography-mass spectrometry (LC-MS). In this study, a novel technique, imaging Time-of-Flight secondary ion mass spectrometry (ToF-SIMS) was employed to gain new insights into the lipids composition and spatial distributions during the biological events, *e.g.*, fertilisation and the early embryo development. Meanwhile, the capability of SIMS to handle the real biological samples was explored, in this case, a textured spherical sample. This introduction briefly summarizes the fertilisation and early embryo development of *X. laevis* eggs, as well as the techniques employed previously to study morphological changes during these biological processes and the lipid composition of the egg.

3.1.1 From fertilisation to early embryo development of *Xenopus laevis* eggs

The *X. laevis* eggs have a distinct polarity, one dark pigmented 'animal' pole and one white 'vegetal' pole. The vegetal hemisphere is filled with a large amount egg yolk, lipids and proteins, providing the developing embryo with the building blocks and energy metabolites after fertilisation [7]. The fertilisation of eggs is initiated with sperm entry, and followed by a sequence of events: the male and female gametes undergo fusion in the microvillar-rich region on the egg surface, and the haploid sperm and egg nuclei fuse to form the diploid zygote nucleus. For *Rana pipiens*, the fusion site is exclusively in the animal hemisphere [8], and for *X. laevis*, the studies have indicated significantly higher number of sperms binding to the animal hemisphere [9, 10].

Fertilization activates those molecules necessary to begin cell cleavage and development. The fertilised egg, *i.e.*, zygote, will undergo the cleavage approx. 1.5-2 h after fertilisation at room temperature that involves rapid and repeated mitotic division up to blastula stage. Cleavage is holoblastic but unequal. As show in Fig. 3.1, the first division is by a vertical furrow or meridional plane which bisects through the centre of animal-vegetal axis giving two equal sized cells called blastomere. Perpendicular to the first meridional plane, the second one launches the second cleavage, resulting in four equal sized blastomeres. The third division by horizontal furrow slightly above the equatorial plane generates four equal pigmented micromeres in animal hemisphere and

four bigger macromeres in vegetal hemisphere. With the fourth division, two vertical planes which pass through one side of median axis of the egg further divide the embryo into 8 micromeres and 8 macromeres leading to 16 cells stage. The fifth division occurs through two horizontal planes resulting in an embryo of 32 cells stage. This ball of cells is called a morula and the process is called morulation. The interval of the divisions is 15 min between the first two divisions, and becomes increasingly longer with the further divisions, e.g., 45 min between the third and fourth divisions and more than 1 h after the fourth division. After the fifth division, the irregular asynchronized division takes place, but the micromeres in the animal hemisphere divide more rapidly than the macromeres in the vegetal hemisphere leaving a mulberry-like appearance in animal pole. Moreover, as the blastomeres become progressively flatter, a fluid-filled cavity called blastocoel is formed in the animal hemisphere. The embryo packed with blastomeres that surround the blastocoel at this stage is called the blastula with at least 128 blastomeres and up to 4,000 of them, accordingly the process is called blastulation.

During the cleavage process, the volume of the embryo will not increase. To an unaided eye, the blastula packed with numerous blastomeres is very similar to an original egg. The formed blastocoel will be essential to allow blastomeres movements during gastrulation. Gastrulation initiates at a point roughly 180 ° opposite sperm entry on the embryo surface, involving blastomeres migration to form three layers namely ectoderm, mesoderm and endoderm as shown in Fig. 3.1 [11]. The further development of the embryo is out of the scope of this introduction.

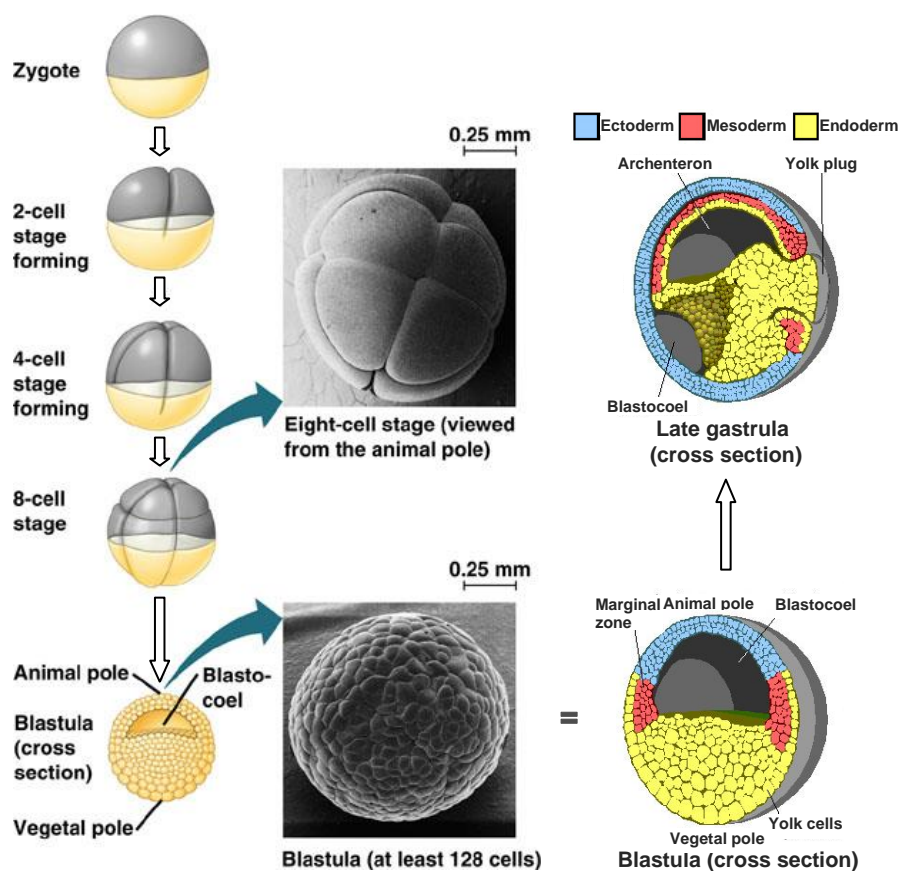


Fig. 3.1 Cleavage and gastrulation of the *Xenopus laevis* embryo. Reproduced from reference [12].

The biological processes are not exclusively associated with DNA, RNA and proteins within the biological system, but also related to ‘small molecules’, a general term used to refer to any compound of molecular weight around 500 Da or less, e.g., biological signalling molecules [13, 14].

The subcellular signalling of interest in this model are calcium and inositol-1, 4, 5-trisphosphate (IP3). Upon the fertilisation of *X. laevis* oocyte, Ca^{2+} wave is initiated from the point of sperm-egg as a single, large wave of elevated free Ca^{2+} . Then it involves an increase in IP3 level due to the sperm-egg interaction, which further activates the endoplasmic reticulum Ca^{2+} release machinery [15]. The 3D simulation of the signalling wave based on the one dimensional experimental data using capillary electrophoresis system is shown in Fig. 3.2. At fertilization, the increase in IP3 mass is estimated to be 200 fmol/egg and it is associated with an increase in $[\text{Ca}^{2+}]$ from 200-400 nM to 1.2-1.4 μM . IP3 increases about four-fold over basal levels and peaks around 5 min after insemination [16, 17]. Calcium ions also give rise to ubiquitous cellular signals, e.g., as the early embryo develops towards and through gastrulation small sporadic calcium transients occurs, the cell cycle of early embryos in the middle of this continuum are correlated with the calcium signals [18, 19]. Most study on the Ca^{2+} and IP3 flux in single fertilised egg adopted capillary electrophoresis method [15] and fluorescent calcium dyes. The green fluorescent protein-tagged constructs have also been proved effective [20, 21]. However, the invasive probe can perturb the microdomains, e.g., the fluorescence dye may cause the redistribution of the chemicals and intervene in the biological processes within the cell [22]. This calls for non-invasive visualization measurements in current biological analysis to locate the small-molecule compounds as that might lead to new biological insights as well as novel probes to perturb enzymes and signalling pathways for potential therapeutic targets [23].

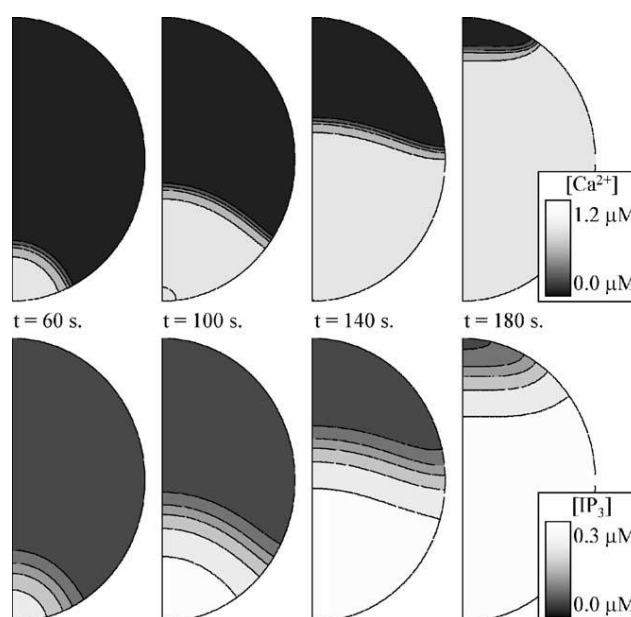


Fig. 3.2 Simulation of the distributions of Ca^{2+} (top) and IP3 (bottom) in an axisymmetric, three-dimensional sphere at 60, 100, 140 and 180 s after wave initiation. Black corresponds to low levels and white indicates high levels of either Ca^{2+} or IP3, as detailed in the figure. Waves were initiated with a 1 μM Ca^{2+} and 0.5 μM IP3 initial condition. Reproduced from reference [15].

3.1.2 Lipid profiling and imaging of *Xenopus laevis* eggs

Since the discovery of phosphoinositide involving in signal transduction [24] and lipids-protein interaction [25], there has been increasing interest in the lipid biochemistry. The location and identification of these biomolecules is essential to the understanding their roles in biological processes, because their locations in a cell membrane, nucleus, or other organelle are responsible for their functions as inter- and intra-cellular communication and signalling [26, 27].

Comprehensive work on the membrane composition of the *X. laevis* oocyte, the immature germ cells arrested at the prophase of the first meiotic cell division [28], has been done by Hill and co-workers [29]. The membrane lipids of the oocytes were extracted conventionally using methanol-chloroform system and examined by electrospray ionization on a triple quadrupole mass spectrometer after either direct infusion or chromatographic separation. Lipids species in mass range of m/z 400-950 were obtained as shown in Table 3.1. In the plasma membrane, it is rich in GPCCho, SM and GPIs, as well as cholesterol comprising approximately 20% of the total lipids extraction. A further study on expressed water and solute transporters in the membrane discovered that the plasma membrane has an extremely effective barrier to the passive diffusion of water. This was attributed to the highly ordered domains formed by the higher than normal concentrations of GPCCho, highly saturated SM and modest cholesterol compared with several other cell types including human red cell plasma membrane. The low-permeability of the oocyte membrane was also proved by other studies [28, 30, 31]. Notably, Kelly *et al.* [28] observed that after 2 h in 10 mOsm buffer, eggs remained intact, while 60.2±7.0% of oocytes had burst. The ability of eggs to maintain volume is speculated to be determined by the gel-like cytoplasm.

Choline Lipids				Ethanolamine Lipids				Anionic Lipids				Other Lipids			
Assignment <i>m/z</i> Mass%				Assignment <i>m/z</i> Mass%				Assignment <i>m/z</i> Mass%				Assignment <i>m/z</i> Mass%			
GPCcho			35.8	GPEtn			21.8	GPSer			5.3	GPGro	16:0-18:1	747	1.3
	16:0-16:1	732	10.5		18:0-18:1	744	14.0		18:1-18:1	786	30.3				3.2
	16:0-18:2	758	18.1		18:2-20:2	770	18.7		18:0-20:4	810	56.4		16:0	572	28.8
	16:0-18:1	760	33.8		18:2-22:6	786	17.2		ND	834	13.2		22:0	656	18.7
	16:0-18:2*	780	19.0		18:1-22:6	788	27.5				6.8		24:1	682	23.4
	18:2-20:4	806	18.5		ND	812	12.4		GPIns	18:0-20:4	885		85.8	24:0	684
		25.8	ND	814	10.1	ND	909	14.1		18:0		3.4			
SM	14:0	675	18.8									22:1		3.0	
	16:0	703	51.6												
	24:1	813	19.3												
	26:4	835	9.8												

Lipid composition excludes cholesterol. GPCCho, glycerophosphocholine; SM, sphingomyelin; GPEtn, glycerophosphoethanolamine; GPSer, glycerophosphoserine; GPIIns, glycerophosphoinositol; GPGro, glycerophosphoglycerol. ND, not determined because signal mass of the initial mass ion was too low to permit other scanning techniques. All ceramides species were detected as Cl^- adducts. * indicates Na^+ adducts. Reproduced from reference [29].

With modern techniques such as SEM and confocal microscopy, the researchers have been trying to image the frog egg and embryo to investigate the mechanism of the biological processes and embryo development. Monroy *et al.* [3] firstly revealed the outer surface of the plasma membrane in *X. laevis* egg by means of SEM. The architecture of the membrane shows dramatic changes before and after fertilisation and as fertilised egg move towards two-cell embryos. As shown in Fig. 3.3, the large hemispherical protrusions on the unfertilised egg gradually become smooth and the microvilli withdraw along with the completion of the fertilisation and first cleavage. This could result from the membrane expansion during cleavage. Moreover, the microvilli could play a role in sperm-egg interaction and consequently disappear after fertilisation.

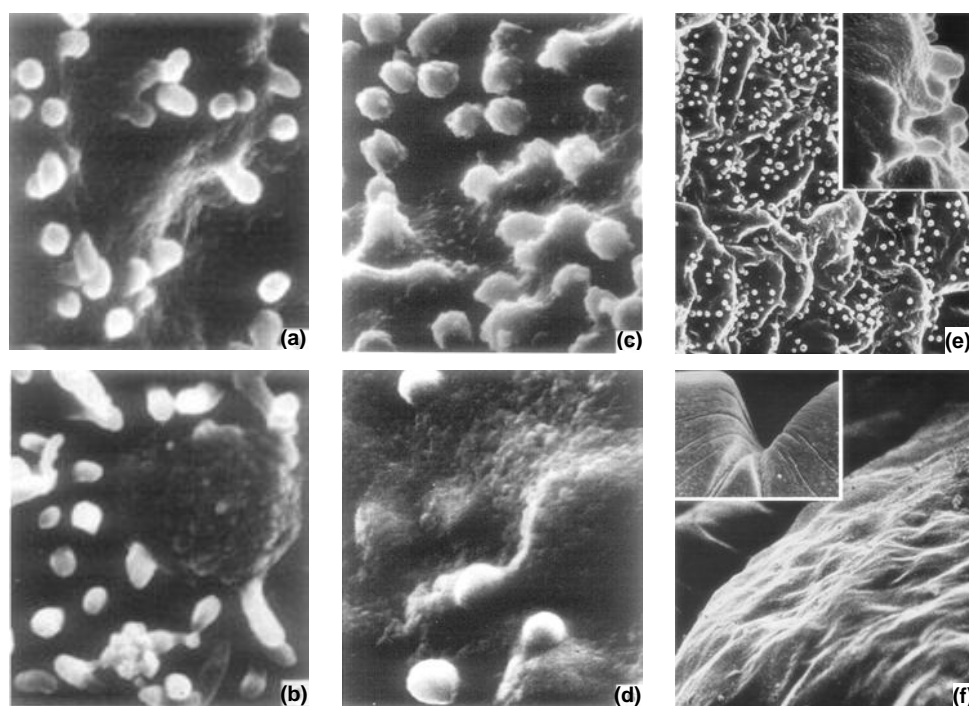


Fig. 3.3 Morphology of the outer surface of the *Xenopus laevis* egg. Images are acquired using a Jeol SEM/ 2.×24000 magnification unless otherwise indicated. (a), unfertilized egg, animal pole in a zone devoid of protrusion; (b), unfertilized egg, vegetal pole showing large protrusions surmounted by microvilli; (c), an zygote 30 min after fertilisation, animal pole; (d), zygote 30 min after fertilisation, vegetal pole; (e), two-cell embryo, surface of animal pole. 2.×5700; Inset, ×29000; (f), two-cell embryo, the smooth surface of the embryo in the vicinity of the cleavage furrow at the vegetal pole. 2.×5700; Inset, ×285. Reproduced from reference [3].

Monroy *et al.* [3] showed the detailed architecture of the membrane during the biological process of fertilisation and cleavage of the zygote. However, the study did not show the sperm entry site on the membrane, which is of particular interest since it determines the plane of bilateral symmetry, and opposite the point of entry, the gray crescent forms, and from where the gastrulation movement initiates [39, 40]. Elinson *et al.* [41] located the site of sperm entry in a time course study on *Rana pipiens* egg using SEM as in Fig. 3.4, showing the sperm entry site changes from a small, microvilli-free structure at 20 min after fertilisation to a clump of elongated microvilli at 40 min, and further to a distinct patch of microvilli by 120 min. Boyle *et al.* [42] first captured the images of the early contact between the sperm head and the plasma membrane of *Xenopus* egg using SEM. The egg fixed 7 min post-insemination shows that the sperm have penetrated the plasma membrane more extensively, and the entry site appears different from the adjacent area, e.g., the microvilli around are fewer in number or disappeared compared with those on the egg fixed 3-5 min post-insemination, and the plasma membrane appears slightly elevated. These studies provided the

images of the morphological changes during the fertilisation. However, SEM imaging requires complicate sample preparation, including chemical fixation (2% glutaraldehyde or 4% formaldehyde), dissection and post fixation (1% OsO₄). In particular, the dissection destroys the integrity of the cell.

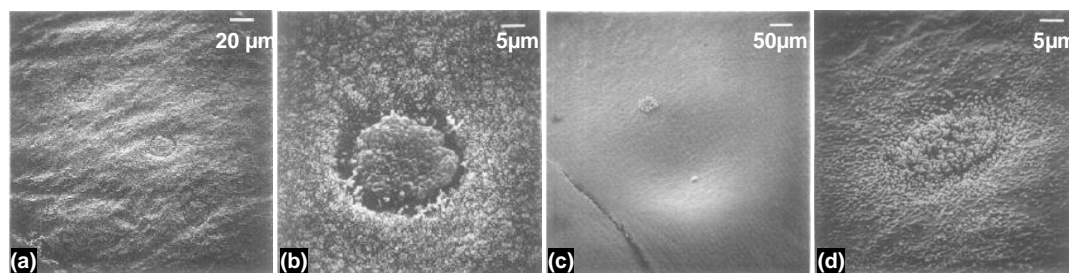


Fig. 3.4 Morphological changes on egg surface of *Rana pipiens* at the site of sperm entry shortly after the insemination. (a), sites of sperm entry on an immature egg. Three sites of sperm entry are seen on this immature egg fixed 10 min after the insemination; (b), egg fixed 20 min after insemination. The small structure attached to the egg surface which has been identified as the site of sperm entry; (c), egg fixed 40 min after insemination. The circular depression is visible on the living egg. A small clump of microvilli is found in the depression; (d), egg fixed 120 min after insemination. Reproduced from reference [41].

Whilst SEM lacks chemical information, immunofluorescence could highlight certain organelles or certain biomolecules within the biosamples. Colombo *et al.* [43] and Roeder *et al.* [44] investigated cortical and subcortical actin filaments and surface microvilli in late stage *X. laevis* oocytes, as well as in unfertilised and fertilised eggs, which predicted the functions of actins in maintaining the polarised organisation and connecting of yolk platelets. However, the immunofluorescence method has been questioned regarding the possible interference of the tags on *in-vivo* function [45-47].

Imaging SIMS, as an emerging tool for biological analysis, has been successfully applied to visualize and chemically map the biological samples including the *X. laevis* oocyte. Fletcher *et al.* [48] measured the 2 and 3 dimensional lipid distribution of freeze-dried *X. laevis* oocyte using conventional BioToF-SIMS. phosphocholine lipids (m/z 58⁺, 86⁺, 166⁺, 184⁺), cholesterol (m/z 369⁺) and fatty acids (m/z 227⁻, 255⁻, 281⁻) was identified and showed different pattern of distributions within the varying depths of the sample. The authors also noted that the investigations were strongly affected by sample topography and the long analysis time, resulting in the secondary ion (SI) signal decrease and changes in sample morphology.

3.1.3 Aim of the project

The aim of the work presented in this chapter was to explore the capabilities of two SIMS instruments, the conventional BioToF-SIMS and new concept J105 3D Chemical Imager (J105), in handling large spherical biological samples, and to establish reliable sample preparation for investigating the lipid composition on the membrane surface and interior of single intact *X. laevis* embryo. In an extension of previous work on lipids profiling of *X. laevis* oocyte using the BioToF-SIMS, lipid variation and rearrangement were further investigated during the dynamic biological process, *e.g.*, the fertilisation and embryo development in early stages. This aimed to provide detailed information that might ultimately lead to a better understanding of these biological processes and in particular the function of lipids in these events. The study involves using both instruments to compare their capabilities of identifying the lipid species in complex mixture and to assess topography effects. 2D and 2D imaging was employed to monitor the embryo development

over time. The intensive imaging work benefits from the special designs of J105, e.g., the buncher-ToF mass spectrometer refocuses the SIs at the entrance of ToF analyser resulting in high mass resolution and independence of sample topography, the DC primary ion beam offers high duty cycle and high lateral resolution making large biosample analyses possible within a practical analysis time frame. The details of the instruments are described in Chapter 2.

3.2 Material and methods

3.2.1 Total lipids extraction

The work started with the analysis of the lipids extraction from *X. laevis* zygote, aiming to explore the capability of the BioToF-SIMS and the J105 to distinguish the lipids species in a complicated chemical environment and provide reference spectra.

Typically, the major classes of lipids from biosamples could be collected via mixed solvents, mainly chloroform/methanol extraction, based on Folch *et al.* [49] and Bligh/Dyer [50] recipes. The work mentioned in the introduction by Hill *et.al.* [29] adopted the conventional methanol-chloroform extraction for lipids assay of *X. laevis* oocytes. The results showed that the membrane is rich in PC, SM and PI. However, the methanol/chloroform solvent system has been criticised for its toxicity and environment hazards, and compared with more recently reported methyl-*tert*-butyl ether (MTBE) extraction, it complicates the lipids layer collection during the phase separation and has a lower lipid recovery [51]. With MTBE method, the low density of lipid-rich organic phase is in the upper layer during the phase separation, which offers convenience for the collection and minimises the losses. Moreover, MTBE is proved to be nontoxic and noncarcinogenic [52].

In the study, MTBE extraction of lipids from *X. laevis* zygote 10 min after fertilization was employed as follows. 10 zygotes 10 min post-insemination of the same batch were washed by HPLC water (Sigma-Aldrich) three times and aspirated to remove all the liquid. Subsequently the cells were homogenised in a glass homogenizer and transferred into a glass tube with a Teflon-lined cap, the remaining were washed with 1.5 mL methanol (Sigma-Aldrich, CHROMASOLV[®] Plus, for HPLC, ≥99.9%) and mixed with the homogenized zygotes into the glass tube. 5 mL MTBE (Sigma-Aldrich, CHROMASOLV[®] Plus, for HPLC, ≥99.9%) was then added into the mixture followed by incubating for 1 h at room temperature on the shaker. Phase separation was induced by adding 1.25 mL MS-grade water. Upon 10 min of incubation at room temperature, the sample was centrifuged at 1000 g for 10 min. The upper phase was collected, and the lower phase was re-extracted with 2 mL of the solvent mixture ($V_{\text{MTBE/methanol}}=10:3$). The total organic phrases were divided into 10 aliquots and dried in a vacuum centrifuge for about 40 min. To speed up sample drying, 20 µL of MS-grade methanol was added to the organic phase individually after 25 min of centrifugation. The lipids extraction were dissolved into 500 µL mixed solvent ($V_{\text{chloroform:methanol:water}}=60:30:4.5$) and stored in -20 °C freezer before analysis [51, 53, 54].

For SIMS analysis, 20 µL solution of the lipid extract acquired in the above procedure were pipetted onto three silicon wafers respectively, left air-drying under an aluminium foil cover in the fume cupboard. Once dried, the samples were loaded onto the sample stub and transferred into the ToF-SIMS instruments immediately for analyses three times in parallel.

3.2.2 Sampling of *Xenopus laevis* embryos

3.2.2.1 Dejellying of *Xenopus laevis* egg

Frog eggs naturally are encapsulated by a thick sticky jelly coat. In the study, this jelly coat must be removed for efficient chemical fixation of the zygotes sampled shortly after insemination (10-40 min) and exposing the embryo surface for SIMS analysis. It is a risk to dejelly the eggs before or shortly after the insemination. It is reported that dejellied eggs are not normally fertilised by sperm but can be artificially activated [55, 56], as the protein rich jelly coat was identified as essential during the fertilisation, influencing the chemoattraction of the sperm to eggs and the sperm binding to vitelline envelope [57, 58]. In addition, if removing the jelly coat after fixation, rolling the eggs during the process would remove attached sperms [42], thus the biological phenomenon would not be fixed for SIMS analysis. However, under a stereomicroscope the sperms were observed navigating through the jelly layers and reaching the vitelline envelope within 2-3 min after addition of the sperm suspension [42]. This implies that the interferences of dejellying could be circumvented by tweaking the timing of this operation. Therefore, of primary importance, the best timing for removing the jelly coat with less perturbation to fertilisation needs to be investigated.

Fertilisation involves four steps: sperm binding, sperm-egg membrane fusion, sperm incorporation and pronuclear migration. It is still ambiguous that the sperm binding to the receptor on the egg inducing phosphoinositide messenger alone is the starting point to activate the egg or whether membrane fusion is required [4]. The first visible sign of egg activation is the movement of pigment granules towards the animal pole termed cortical contraction, which occurs approximately 4 min after fertilisation or 1 min after artificial activation such as pricking [39]. In this study, the fertilisation ratios were investigated upon different dejellying times, before insemination, 5 min and 7 min post-insemination and 40 min post-insemination as control group. Before the insemination, the unfertilised eggs were sorted by removing all bad looking ones, e.g., white and puffy, flattened, activated ones (the animal pole retracted) and those with mottled pigmentation. For eliminating the fake-activated eggs, the fertilisation ratio was calculated by scoring the eggs that have completed the first cleavage divided by the number of total eggs. The results suggested that dejellying the eggs 7 min after the insemination could lead to reasonable fertilisation rate.

3.2.2.2 Freeze the biological process of zygotes and embryos

The zygotes and embryo are very fragile and would burst immediately after leaving the culture media, which left no chance to mount the unprepared cells for SIMS analysis. To freeze the biological processes undergone in the cells and aim to minimize the sample preparation, two strategies were employed, plunge-freezing into liquid nitrogen (LN₂) followed by freeze-drying, or formalin fixation followed by fast freeze and freeze-drying. Difficulties were encountered with the former method. At first, the liquid layer around the cell could not be eliminated completely to avoid cell bursting, resulting in slower freezing step; then the surface of the cells after freeze-drying appeared ridged and distorted using secondary electron microscopy. With regard to the latter method, the limitations of formalin fixation were documented. It has been revealed that formalin fixation is relatively poor at preserving, or preventing the extraction by later processing steps of some classes of molecules such as sugars, and thus these procedures may change the dimensions or arrangements of certain cellular components [59]. There was also report showing

formalin fixation may not keep the cells intact in *Dictyostelium discoideum* tissue [60]. However, Sosinsky *et al.* [61] demonstrated that aldehyde fixation prior to high pressure freezing (HPF) preserves fragile tissues and produces ultrastructural preservation superior to that maintained using chemical fixation along by SEM. Moreover, the obtained cells structure is close to equivalent tissue preserved by HPF alone. In this study, the main targets are the lipids in the membrane, which is not modified chemically by the formalin fixation since formaldehyde reacts with amino, amide and guanidyl group, which yield methylene bridges so to cross-link polypeptide chains [62], anchoring the protein to cytoskeleton and lending mechanical strength and stability to the treated biosamples. The zygote and embryo processed with the formalin fixation are easily manipulated for the later washing procedure without rupture. And further imaging using ToF-SIMS showed the original morphology without wrinkled and distorted surface.

3.2.2.3 Optimised procedure for sampling zygotes and embryos

X. laevis were breed in the Faculty of Life Science at the University of Manchester. The gametes were obtained and insemination was performed using standard procedures as follows [63, 64]. 12-18 h before use, the female frogs were injected subcutaneously with 0.5 ml (500 units) human chorionic gonadotrophin (HCG), and placed in individual tanks containing 5000 mL 1×Marc's modified Ringer's solution (MMR, in mM: 1000 NaCl, 20 KCl, 10 MgCl₂, 20 CaCl₂, 50 Hepes, =10×stock solution, pH 7.5, autoclave before use, dilute accordingly. Except for Hepes purchased from Biomol, the other chemicals were all from Sigma, BioReagent) at 16-18 °C overnight. The laid eggs were then collected in MMR with a wide-bore pipette. Frogs could also be squeezed which often gives the highest quality eggs. Male frogs were sacrificed by lethal injection of 400 µL of 40% Ethyl 3-aminobenzoate methanesulfonate (MS-222, Sigma, 98%). The testis were then dissected and stored in L-15 cell culture media (Sigma, suitable for cell culture) at 4 °C for up to 1 week. Fertilisation was then performed by passing a dilacerated piece of testis over the oocytes for 2 min.

After insemination, the eggs were divided into two groups. One group was dejellied 7 min after the start of insemination by immersing the eggs in 2% L-Cysteine [Sigma, BioUltra, ≥98.5% (RT)] in 0.1×MMR (pH to ~7.5-8.0 with 10 M NaOH) and gently swirling for 2 min. Followed by decanting L-Cysteine solution quickly and washing the eggs with 0.1×MMR three times within 1 min. The eggs were left in fresh 0.1×MMR water. From the point the fertilized eggs were collected using pipette every 10 min until 40 min post-insemination, and immediately fixed with MEMFA [4% (V/V) formaldehyde solution in mM: 2 EGTA, 1 MgSO₄, 20 MOPS, 1.23×10³ CH₂O. All chemicals are from Sigma, EGTA for molecular biology; MgSO₄, BioReagent; Formaldehyde, for molecular biology 36.5-38% in H₂O] for 1.5 h on a shaker and then washed with 1xphosphate buffered saline (PBS) (Sigma, BioReagent, without calcium chloride and magnesium chloride, 10x concentration, diluted accordingly) 4 times and stored in 1x solution in the fridge [65]. Thus, the zygote 10, 20, 30 and 40 min after the insemination were prepared. The other group was dejellied using the same procedure as the first group later at 40 min post-insemination, and left in 0.1×MMR water at room temperature for further cleavage. The healthy embryos at each cleavage stage were selected, and followed by fixation using MEMFA and washing using 1xPBS the same as the first group to prepare the embryos in 2 cells stage, 4 cells stage, 8 cells stage, 16 cells stage, and furthermore, in different cleavage stages. Owing to the eggs artificially fertilised at the same time almost develop synchronically, the embryo of different cell stages could be collected with certain time intervals

under the microscopy which is used to confirm the morphology by comparing with the illustration leaflet of embryo development.

Upon the ToF-SIMS analysis, the samples were quickly washed with HPLC water three times within 60 s due to the resistance of the cell membrane to the osmotic pressure [28, 66], and loaded onto the SIMS sample holder with the animal hemisphere upwards as shown in Fig. 3.5. Followed by aspirating the liquid around the sample and freezing into LN₂, and then the samples were freeze-dried in a Heto DRYWINNER freeze-drier (the School of Chemical Engineering and Analytical Science, The University of Manchester) for at least 6 h. Under the protection of argon gas the dried samples were then inserted into the preparation chamber of SIMS instrument.

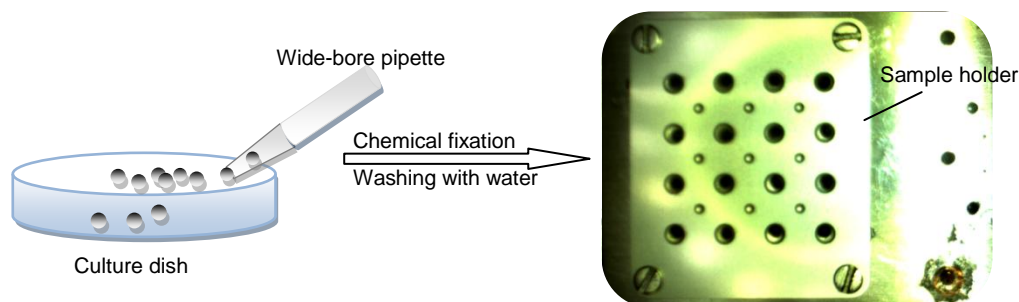


Fig. 3.5 Single *Xenopus laevis* embryo preparation for ToF-SIMS. The embryo has animal hemisphere and vegetal hemisphere. Following the chemical fixation and washing with HPLC water, they are pipetted onto a special sample holder with different hemisphere upwards for analysis.

3.2.2.4 Serial cryosections of zygote

For the large volume *X. laevis* oocyte, the serial cryosections of a single cell facilitate the investigation of the interior directly to locate target compounds. There are several factors that need to be considered with the cell sectioning. Firstly, the embedding matrix should not contaminate the sample and suppress the second ion formation during SIMS analysis. Optimal cutting temperature polymer (OCT), one common matrix, was found in the mass spectrum overlapping with the biomolecular signals [67, 68], e.g., OCT ions at m/z 58⁺, 86⁺, 184⁺, 332⁺ under C₆₀⁺ bombardment are consistent with common biomarkers m/z 86⁺, 184⁺ from phosphocholine lipids. Moreover, OCT sections turned out to be curly and brittle, making it difficult to transfer the section to the substrate. Another frequently used matrix for cryosectioning is fish gelatine. As seen in Fig. 3.6, the fish gelatine section kept flat and linked together as a ribbon so that all the sections from one cell can be transferred to the substrate together. The concentration of the fish gelatine can affect the quality of sections. By comparing embedding cells in fish gelatine with different concentrations 15%, 25% and 30%, the result showed that the sample block with 15% fish gelatine has the right hardness for easily cutting at -26 °C yielding smooth and flat sections. Secondly, the thickness of the section is crucial for keeping the integrity of the cell structure. Li *et al.* [69] suggested 50-100 µm is better to maintain subcellular structure for acquire high resolution atomic force microscopy (AFM) image. Thinner sections could not keep the integrity of the sample, while thicker sections are not ideal for SIMS analysis because of sample charging. In this study, 50 µm thick section was selected for balance both requirements. Thirdly, the transferring of the sections onto the conductive substrate should minimize the disturbance to the cell area so as to avoid chemicals diffusion and contamination. Several methods were used, including using room temperature or pre-cooled substrate to accept the cryosections and using a brush to spread the sections onto the pre-cooled

substrate without touching the cell area. Assisted with the brush, the sections could be spread on to the substrate but not closely stick to it, so that during SIMS analysis in the vacuum environment, they tended to peel off from the substrate and crack. If the cryosections was mounted onto room temperature substrate, it would thaw immediately and leave diffused section onto the substrate (this is the standard procure for biological study). In this study the substrate is cooled in the microtome section chamber for seconds, and then the sections were transferred onto the substrate.

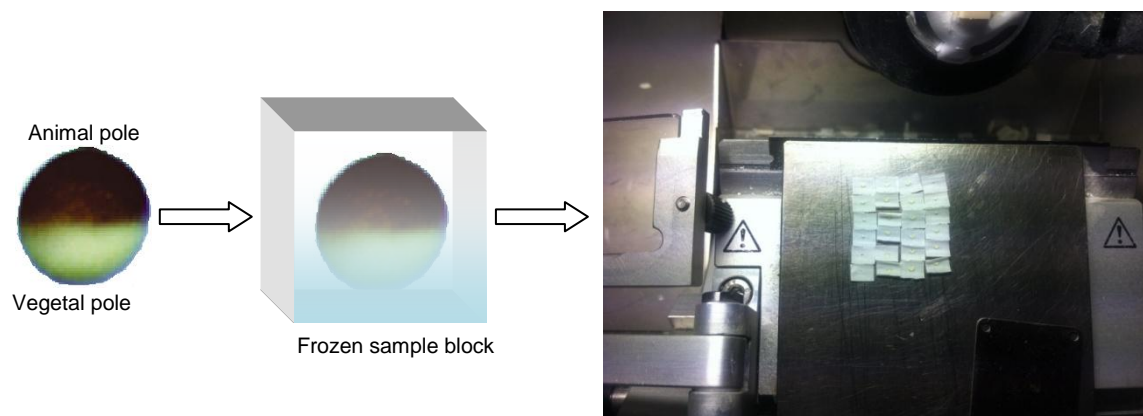


Fig. 3.6 Fish gelatine sections of *Xenopus laevis* zygote 10 min after fertilisation in the microtome chamber. The animal side (black side) of the zygote faces upwards when freezing as in the frozen sample chuck and then sections are cut in an order from the animal side to vegetal side (white side). The sections join together into a ribbon. The bottom right is the steel plate as substrate to accept the sections.

The procedure for single cell sectioning is as follows. The zygotes 10 min post-insemination obtained using the methodology in section 3.2.2.3 were embedded with the 15% fish gelatin (from cold water fish skin, Sigma, Substrates) into the 5×5×5 mm³ plastic moulds and frozen in dry ice for at least 20 min. The frozen sample block was glued onto the sample holder of a Shandon cryotome (the Faculty of Life Science, the University of Manchester) by OCT (Tissue-Tek®, Ted Pella, Inc.). Followed by trimming the sample block until the close to embedded cell, 50 µm thick sections were then cut from animal pole to vegetal pole at -26 °C. The serial sections were transferred onto cold silicon or plain steel plate and sealed into a centrifuge tube immediately. A -80 °C freezer was used to store the samples before analysis.

Prior to SIMS analysis, the serial sectioned sample was quickly transferred into LN₂ and mounted onto the sample holder under LN₂. With the protection of argon gas, the serial sections were inserted into the preparation chamber of SIMS instrument and left freeze-dried inside the instrument.

3.2.3 ToF-SIMS analysis

The BioToF-SIMS and the J105 (the School of Chemical Engineering and Analytical Science, The University of Manchester) were employed for the SIMS analysis. The BioToF-SIMS is equipped with 20 kV C₆₀ gun and 20 kV Au_n (n=1-3) gun both with an incidental angle of 45° and operated in pulsed mode. The J105 is installed with 40 kV C₆₀ gun with 45° angle to the sample surface operating in DC mode. The details of the instrument please refer to Chapter2.

Lipid extract was investigated in both instruments to compare the lipid species that they are able to indentify. Zygotes 10-40 min post-insemination were examined with the BioToF-SIMS, depth

profiling was performed with alternatively Au_3^+ PI beam (for collecting chemical map) and C_{60}^+ PI beam (for etching). Zygote 10 min post-insemination, embryos in different development stages and serial sections were measured with the J105. Charge compensation was performed by pulsing low energy electron gun onto sample surface for the BioToF-SIMS or stage bias 20-30 V for the J105. The detailed instrument settings are mentioned in individual experiments in section 3.3.3.

Owing to the very low initial kinetic energy spread of SIs using the BioToF-SIMS, there is a linear relationship between the time of flight and the square root of m/z . Consequently, the internal mass calibration was made with ions C^+ , CH^+ , CH_2^+ and CH_3^+ in +SIMS spectra, and ions C^- , CH^- and CH_2^- in -SIMS spectra initially. The mass accuracy was further improved by adding identified ions to refine the calibration, e.g., C_7H_7^+ in positive and PO_2^- , PO_3^- in negative spectra. The calibration was made on every spectrum. The single ion images were generated by the BioToF-SIMS software version 9.1 and Matlab 2009. For the J105, the spectra was calibrated externally with ions In^+ , In_2^+ , In_3^+ only once since all the ions were time focused before the mass analyser that eliminates the effects of actual flight distance spreads and sample topography. The images viewing and single ion images generation were performed by Analyze software from SAI Ltd. The further PCA processing was through Matlab 2009 for better contrast or 3D visualization (analysis routines were developed by group members Dr. Alex Henderson and Jimmy Moore). Regarding the signal to noise levels are different with two instruments (refer to section 2.2.2.1), the peaks over 100 counts in the BioToF-SIMS spectra are recognised as real peaks, for the J105, the threshold is over 50 counts.

3.3 Result and discussion

3.3.1 Effects of dejellying on fertilisation and development of *Xenopus laevis* egg

To minimise the disturbance of dejellying to the fertilisation of *X. laevis* eggs, the eggs were dejellied before and after the insemination at different times to optimize the procedure. The fertilisation rate was calculated as in Table 3.2. When removing the jelly coat before insemination, the pigment contraction was seen on the animal hemisphere of the egg indicating the eggs could be activated but no cleavage resulted. The eggs dejellied 7 min post-insemination presents higher ~79% rate than dejellying 5 min after fertilisation, offering better chance to sample the fertilised eggs 10, 20, 30 and 40 min post-insemination for investigation the dynamic fertilisation process on the animal hemisphere. A control group following normal fertilisation procedure with highest fertilisation rate (~96%) is then adopted to sample the embryos at different cleavage stage for the investigation of lipid rearrangement on the membrane during early embryo development.

Dejellying 5 min and 7 min after insemination, the different proportions of eggs were developed into two cell stage after 1.5-2 h incubation, but some of them seem to have developed abnormally as shown in Fig. 3.7. The whole embryo appears bigger and blastomeres loosely packed on the surface as in Fig. 3.7 (c, d) marked with red square frames. The reason of the abnormal development is not clear. Elison *et al.* [70] studied the fertilisation of jellyless oocytes of *Rana pipiens*, showing a very low frequency (5%) of oocytes developed to blastula, but the fertilisation rate was increased with the presence of egg jelly extraction in the medium. This was also proved by Steward-Savage and Grey [71] with the study of fertilisation of denuded *X. laevis* eggs. However, there is no further description regarding the development of the fertilized egg without jelly coat. It is possible that the polyspermy might occur in some eggs when considering dejellying shortly after

insemination could increase the opportunities of sperm-egg interaction. A further investigation will be needed to explain the phenomenon.

Table 3.2 The effect of dejellying on the fertilisation rate of *Xenopus laevis* eggs

Dejelly time	Fertilisation ratio	Note
Before insemination	0	No further division
5 min after insemination	5%	Division stopped in early stage
7 min after insemination	79%	Develop to normal or abnormal embryos as shown in Fig. 3.7 (c,d)
Control group(with jelly coat on until 40 min after insemination)	96%	Cleavage normally

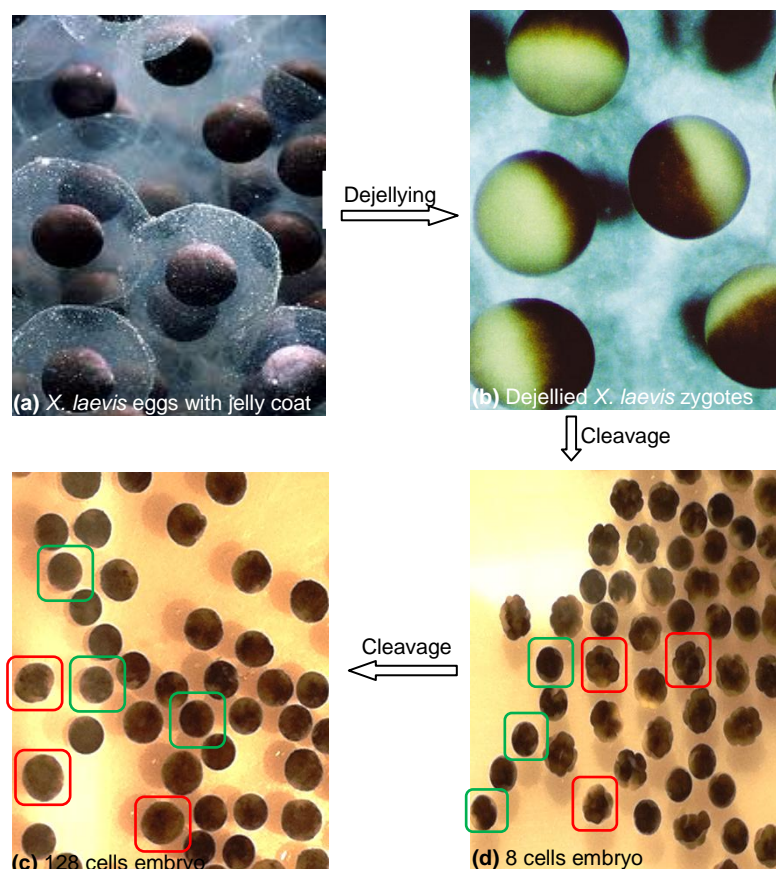


Fig. 3.7 The development of *Xenopus laevis* zygotes dejellied 7 min post-insemination in early stages. (a), Jelly coated eggs; (b), the zygotes dejellied 7 min post-insemination; (c), at least 128 cells embryos; (d), 8 cells embryos. Embryos in the green frame are in normal developmental state, in the red frame are abnormal. The abnormal embryos appear larger than the normal ones, with extruding blastomere cells loosely gathered in the sphere while those are more compactly arranged on the normal embryos. All the cells in photos are approx. 1-1.2 mm in diameter.

3.3.2 Spectra interpretation of lipids extraction

The multiple assay of the total lipids extraction from *X. laevis* zygote 10 min after fertilization was carried out using both BioToF-SIMS and J105 to compare the capabilities of two instruments in characterizing the complex mixtures. More importantly, the identified lipids species would be as reference to track and locate the biomolecules on the single intact *X. laevis* embryo. The positive and negative ion spectra using the BioToF-SIMS and the J105 are shown in Fig. 3.8 and Fig. 3.9 respectively. The peak assignments are listed in Table 3.3 according to lipids categories defined by LIPIDS MAP Consortium (detailed in section 1.2.1). For the comparison of the two SIMS instruments, all m/z values accurate to two places of decimals in mass spectra (Fig. 3.8 and Fig. 3.9) and peak assignments (Table 3.3), and rounded off to one decimal in the description here.

The absence or presence of fragments in the BioToF-SIMS and the J105 spectra are marked with +/- (only in the BioToF-SIMS spectrum), +/+ (in both spectra), -/+ (only in the J105 spectrum).

It is well known that the major classes of lipids in biological membrane (e.g., glycerophospholipids, glycerolipids) can dissociate to unique headgroups and glycerol with fatty acid tails under 'soft' bombardment of polyatomic projectiles. The fragmentations are similar with other ionisation methods such as electrospray (ESI) [72-74]. However, small ions with a mass less than a third of the precursor mass are not normally trapped and detected using a quadrupole ion trap under normal operation of ESI, e.g., m/z 184⁺ is the headgroup derived from phosphocholine lipids. On the contrary, these ions are important in SIMS analysis for peak assignment and mapping the distribution on biological samples. The spectral interpretation was referred to previous works on lipid profiles of either standard lipids or biological samples using ToF-SIMS [75-78], which has been summarized in section 1.2.2.3.1. The lipid fragmentation using ESI was also referenced.

Glycerophosphocholine (GPCho) is one of abundant lipids in the cell membrane, with a quaternary amine in its headgroup as seen in Fig. 3.10. It is clearly seen from the +SIMS spectrum (Fig. 3.8) that the phosphocholine headgroup is ionized well in positive ion mode forming intensive fragments at m/z 86.1⁺, 104.1⁺, 125.0⁺, 166.1⁺, 184.1⁺, 224.1⁺ on both instrument. The glycerol tail is mainly disassembled as monoglycerol phosphate at m/z 459.3⁺ (C20:3), various monoracylglycerol (MAG) and diracylglycerol (DAG) (see MAG and DAG in Table 3.3), potassium salted diracylglycerol phosphate at m/z 721.5⁺ (C16:0/18:2), 723.5⁺ (C16:0/18:1), 732.6⁺ (C16:0/18:0). All these tail fragments could also be shared by other glycerophospholipids. Neutral loss of carboxylic acid from the *sn*-1 or *sn*-2 position results in monoglycerol phosphocholine at m/z 478.45⁺, and loss of ketene (O=C=CH-R) from *sn*-1 or *sn*-2 glycerol position forms ions at m/z 495.3⁺ (C16:0), 521.4⁺ (C18:1), 523.5⁺ (C18:0). This rich structural information helps to identify [M+H]⁺ ions at m/z 732.6⁺ (C16:0/16:1), m/z 758.6⁺ (C16:0/18:2), 760.6⁺ (C16:0/18:1), sodiated molecular ions at m/z 780.6⁺ (C16:0/18:2), 782.3⁺ (C16:0/18:1), 784.6⁺ (C16:0/18:0), potassium salted ion at m/z 798.6⁺ (C16:0/18:1), and m/z 806.6⁺ (C18:2/20:4).

Sphingolipids, especially sphingomyelin (SM), proved to be the source of free ceramides and sphingosine in cell membranes and have powerful second messenger properties [79]. The fragmentation pattern closely follows the related choline-containing lipid, GPCho. SM and GPCho share common fragments derived from the phosphocholine headgroup, e.g., m/z 86.1⁺, 104.1⁺, 125.0⁺, 166.1⁺, 184.1⁺, 206.1⁺, complicating the species separation. However, instead of two fatty acyl group bond to a glycerol back bone, SM has fatty acyl group bonded to a basic nitrogen atom of the long chain base as amide, leading to the unique ions at m/z 265.2⁺ ([C₁₈H₃₅N]⁺, loss of phosphocholine head and neutral loss of the fatty acid as a ketene) to SM in contrast to m/z 224.1⁺ ([C₈H₁₉NPO₄]⁺, phosphocholine with glycerol back bone) to GPCho. The m/z 224.1⁺ usually has reasonable intensity for imaging so that GPCho can be distinguished from SM. Another group of ceramides fragments can also be used to distinguish two lipids as they are unique to sphingolipids, e.g., m/z 417.3⁺, 419.3⁺, 421.3⁺, 423.3⁺. SM is also ionized well in negative ion mode, generating [M-H]⁻ ion and fragments due to the consecutive loss of the carbon chain or N(CH₃)₃ at m/z 687.6⁻, 673.4⁻, 642.5⁻, 616.5⁻.

Glycerophosphoethanolamine (GPEtn), another abundant component in the membrane, has characteristic peaks in +SIMS spectra at m/z 124.1⁺, 142.1⁺ formed by the loss of water and phosphoethanolamine from the headgroup. The further loss of ketene leads to ions at m/z 477.38⁺, 479.23⁺. Molecular ions are formed at m/z 743.5⁺ (C18:0/18:2), 745.6⁺ (C18:0/18:1), 811.7⁺ (C19:1/22:2). The headgroup related fragments in negative ion mode at m/z 196.0⁻ and 140.0⁻ are not well resolved from the background noise.

Glycerophosphoglycerol (GPGro) phospholipids are less abundant than most of the common phospholipid species. These acidic phospholipids also serve as precursors for synthesis of more complex phospholipids, including the cardiolipins found in mitochondria [80]. The headgroup was seen at m/z 198.10⁺ in positive ion mode; in negative ion mode, the representative fragment ions reflecting the glycerol polar headgroup at m/z 227.2⁻ is in low intensity, and m/z 209.0⁻ and 171.0⁻ were not found.

Glycerophosphoserine (GPSer) is an important phospholipid class with a unique characteristic that it is predominantly found expressed on the inner leaflet of normal cells membrane. The precursor of m/z 185.1⁺ was found along with the sodiated peaks at m/z 208.0⁺ in positive ion mode. No headgroup peaks in negative ion mode were seen.

Glycerophosphoinositol (GPIns), containing a polar headgroup of phosphodiester of the six-carbon sugar inositol, is found in all cells. It is the precursor of inositol triphosphate (IP3), an important signalling molecule that could stimulate intercellular calcium release [81]. As a polar lipid, it ionizes well in negative ion mode, giving rise to rather unique ions at m/z 223.1⁻, 241.2⁻, 259.2⁻, 299.2⁻ that correspond to inositol headgroup with phosphate groups. The molecular ion is at m/z 885.4⁻ (16:0/20:4).

Some common fragments are expected due to phospholipids having the same structure of glycerol back bone and phosphate group, e.g., m/z 125.0⁺ [C₂H₆PO₄]⁺, m/z 143.1⁺ [C₂H₈O₅P]⁺, m/z 165.1⁺ [C₂H₇O₅PNa]⁺, m/z 63.0⁻ PO₂⁻, m/z 78.9⁻ PO₃⁻, m/z 137.0⁻ [C₃H₆PO₄]⁻, m/z 153.0⁻ [C₃H₆PO₅]⁻ and m/z 180.9⁻ [C₄H₆PO₆]⁻. Besides, the fatty acyls, the hydrophobic tails of all the lipids are a group of common fragments found mainly between C14-22 as listed in Table 3.3. The intensities of fatty acyls in Fig. 3.9 (a) hint that the C16:0 at m/z 255.2⁻, C18:1 at m/z 281.2⁻ and C18:0 at m/z 283.2⁻ are dominant components. This agrees with the previous finding that frog species oviposit in water has more non-polar lipids with fatty acids tail dominated by C16:0 (38.0±1.7%) and C18:1 (38.2±1.2%), even in polar lipids, the main fatty acids are C16:0 (33.2±0.4%), C18:1 (15.8±0.7%), and C18:2 (16.4±0.2%) [34, 36].

Cholesterol has the characteristic fragments at m/z 369.4⁺ [M+H-H₂O]⁺ and m/z 385.4⁺ [M+H]⁺. Vitamin E molecular peak at m/z 430.4⁺ is observed in +SIMS of the J105 as seen in Fig. 3.8 (b), while submerged in the noise of BioToF-SIMS positive spectra owing to the different signal to noise levels (detailed in section 2.2.2.1). The disadvantage of the higher noise level of the BioToF-SIMS is also reflected in the molecular peak identification, e.g., no GPEtn or GPGro molecular peaks appeared and only some of GPCho molecular ions were seen in +SIMS spectrum Fig. 3.8 (a). Various DAG and TAG species were assigned which benefits from the high mass resolution ($m/\Delta m$ 5000) at mass region over m/z 500⁺ of the J105 3D Chemical Imager, which enables the J105 to separate more species than the BioToF-SIMS (Fig. 3.8). Based on the database of LIPIDS MAPS

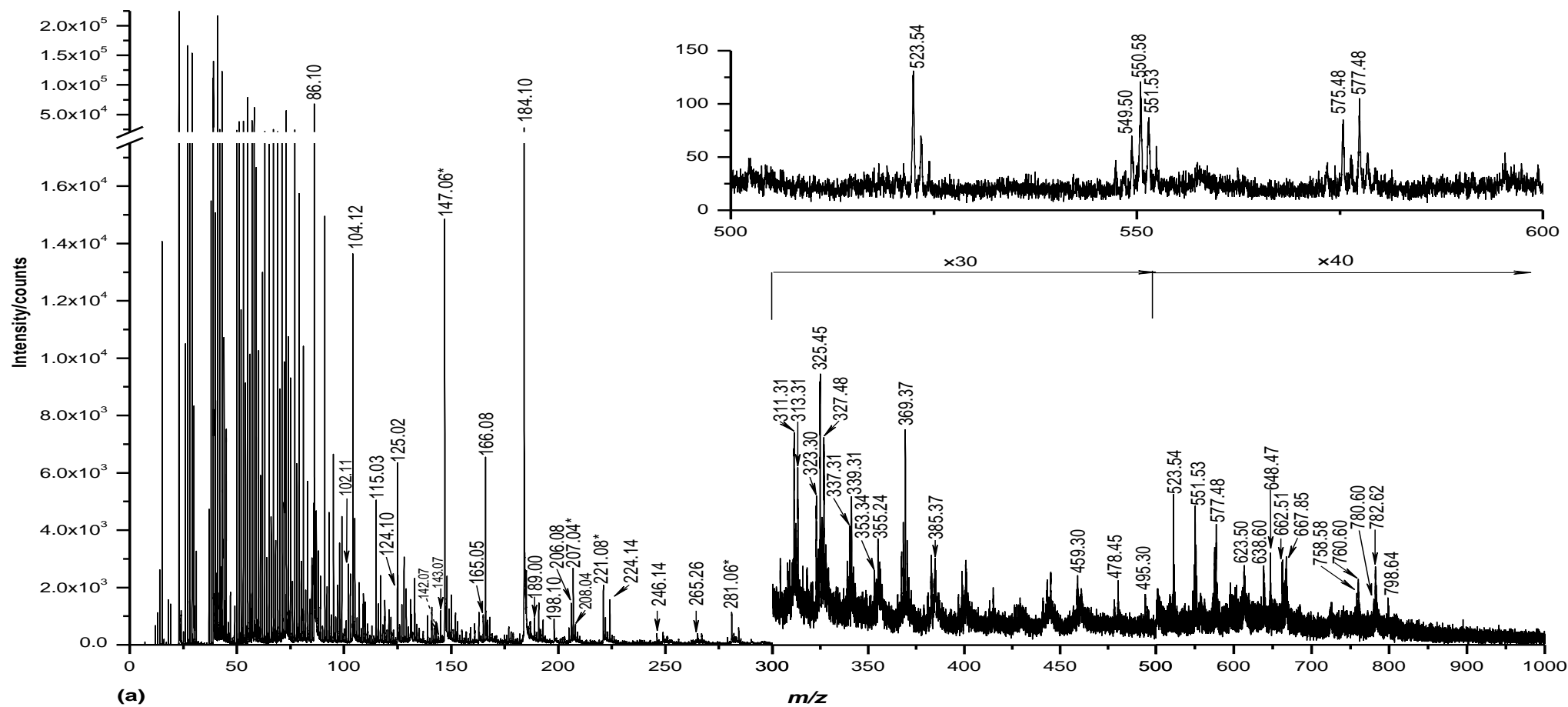
Consortium, m/z 825.7 could be $[C_{53}H_{93}O_6]^+$, TG(16:1/17:2/17:2), m/z 853.7⁺ could be $[C_{55}H_{97}O_6]^+$, TG(17:2/17:2/18:1), m/z 879.7⁺ could be $C_{57}H_{99}O_6^+$ TG(17:2/17:2/20:2), m/z 901.8⁺ could be $C_{58}H_{109}O_6^+$, TG(17:0/18:2/20:0)). The group of DAG and TAG molecules are mainly used to store fat as a source of energy and are abundant in egg yolk for the further development of the embryo.

With the peak by peak scrutiny, the major classes of lipids have been found in the lipids extraction of *X. laevis* zygotes. The characteristic peaks of GPEtn, GPCho, GPSer, GPGro, SM, cholesterol, Vitamin E and DAG were selected for intensity comparison. The average peak intensities of three samples were normalised to the intensity of the highest peak at m/z 184.1⁺ as in Fig. 3.11. The m/z 184.1⁺ is usually the most intense peak in the biological sample compared with other characteristic peaks of lipids species, which indicates high contents of GPCho and SM, the main components in biological membranes. The ion always served as a general biomarker for biological system under SIMS analysis. It is obvious in Fig. 3.11 that the related intensity of m/z 184.1⁺ to that of m/z 369.4⁺ (cholesterol) is 9.0:1, 11.5:1 to m/z 124.1⁺ plus m/z 142.1⁺ (GPEtn), 90.9:1 to m/z 430.4⁺ (vitamin E), which is consistent with the finding by Hill *et al.* [29] that the high concentrations of GPCho and SM and lower levels of GPEtn exist in *X. laevis* oocyte membrane. As SIMS is a semi-quantitative technique, the intensities (counts of SI) are affected by the sputtering yields and ionisation capabilities of certain species, which are variable among different species. Benninghoven [82] revealed up to 4 orders of magnitude difference in ionisation capabilities among several biomolecules, e.g., amino acid and peptide. Although a few quantitative SIMS analyses have been reported [83, 84], but the application are limited to simple systems (e.g. model system with several known components) and elemental analysis. Thus the comparison of different lipid ions provides a rough idea regarding their concentration in the sample. The concentration differences among lipid species might directly related to their function in the biological system. GPCho, SM, and cholesterol were thought to form highly ordered domains through hydrogen bonding and steroid ring group interactions for reasons of optimal acyl chain packing, and the microdomain rafts for the bedding of the protein for signal transferring and intercellular communication [85, 86]. This tightly packed formation might be one reason that the frog membrane can resist osmotic pressure than other type of cells. In addition, the lipids was extracted from the zygote upon 10 min after fertilisation, that was ongoing the most profound biological process of gametes fusion, the arrangement of the high level of GPCho and SM on cell surface and in depths could reflect their functioning during the process as the further experiments revealed in sections 3.3.4.1 and 3.3.4.2.

The BioToF-SIMS +SIMS spectrum in Fig. 3.8 (a) shows polydimethylsiloxane (PDMS) ions appearing at m/z 147.0⁺, 206.9⁺, 281.1⁺, but these are not present in +SIMS spectrum using the J105 in Fig. 3.8 (b). It is likely that the sample was contaminated during the sample transfer to the BioToF-SIMS owing to the exposure to the atmosphere and contact with sample bench. This exposure was avoided when using the J105, in which the sample was isolated in the transferring preparation box and inserted into the instrument under argon protection. The residue after the lipids extraction was also analyzed using the BioToF-SIMS and the \pm SIMS spectra are shown in Fig. 3.12. It is suggested that a small amount of phosphocholine lipids and fatty acyls are left in the precipitate after lipid extraction probably due to incomplete extraction from the *X. laevis* zygote membrane.

In summary, the glycerophospholipids and sphingolipids species determined by +SIMS analysis[Fig. 3.8 (a)] are in good agreement with the results of GC-tandem MS listed in Table 3.1, which implies that SIMS is able to identify lipid species within complex mixtures in a single run, and have similarities in detection with GC-MS instruments. However, what makes SIMS unique are the through-out qualitative analysis of lipids in a single run within very short time (this operation mode is comparable to shotgun lipidomics analysis), and more importantly, the visualization of the diagnostic ions of diverse lipids on the real samples offering more potential in biological study which will be presented by the following experiments of locating the biomolecules in a single intact zygote/embryo. The comparison of the intensities of various lipid ions implies that GPCho and SM are the main components of the lipids extraction this also coincides with the findings of previous work as shown in Table 3.1. However, to enable a more quantitative interpretation of the data the instruments would have to be calibrated against each lipid using various mixtures. This would require a very systematic and substantial programme of research due to the complications of preparing well-mixed multicomponent system for surface analysis under ultrahigh vacuum which is beyond the scope of the present work.

Bio-ToF +SIMS spectrum of lipids extraction from *Xenopus laevis* zygote 10min after fertilisation



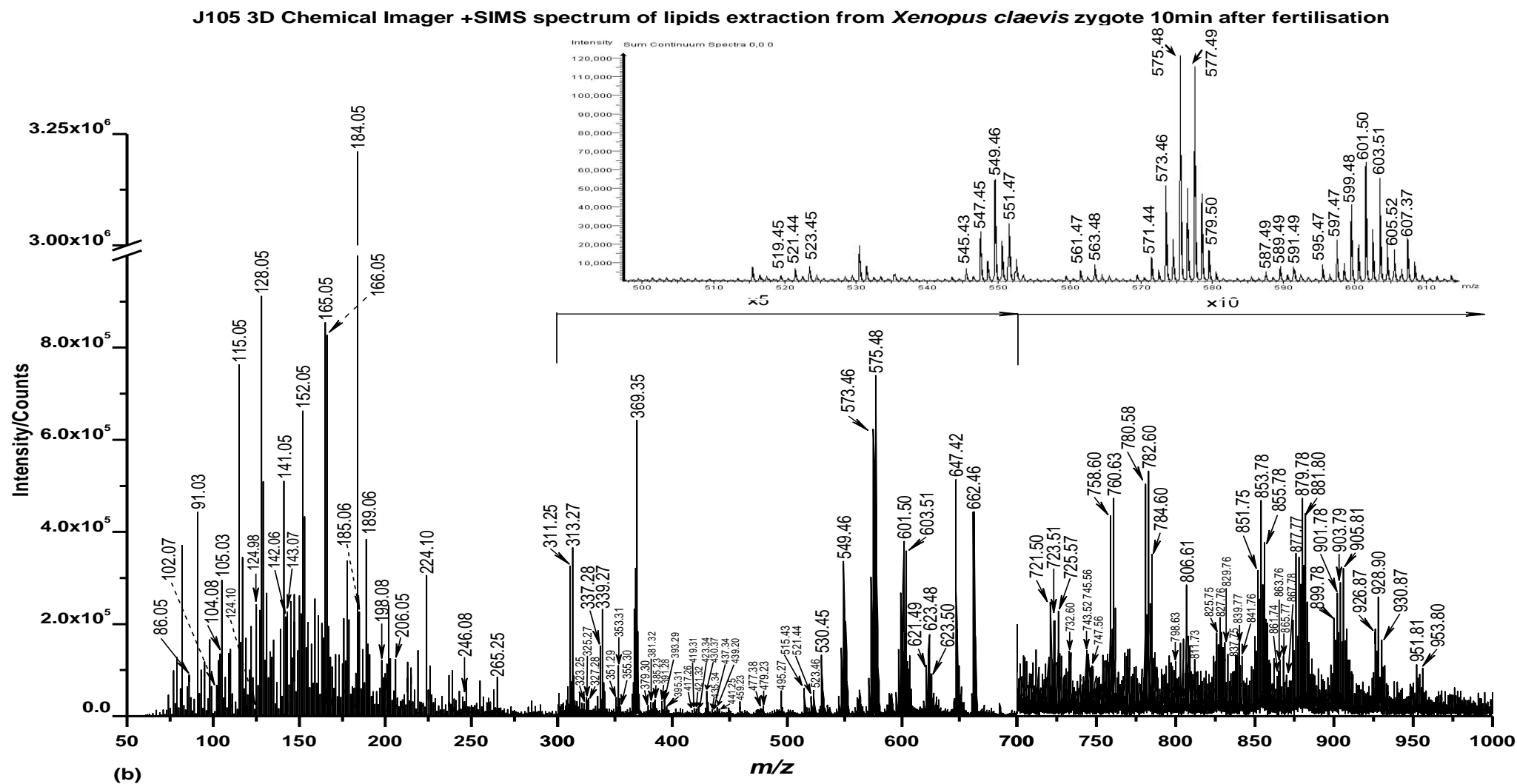
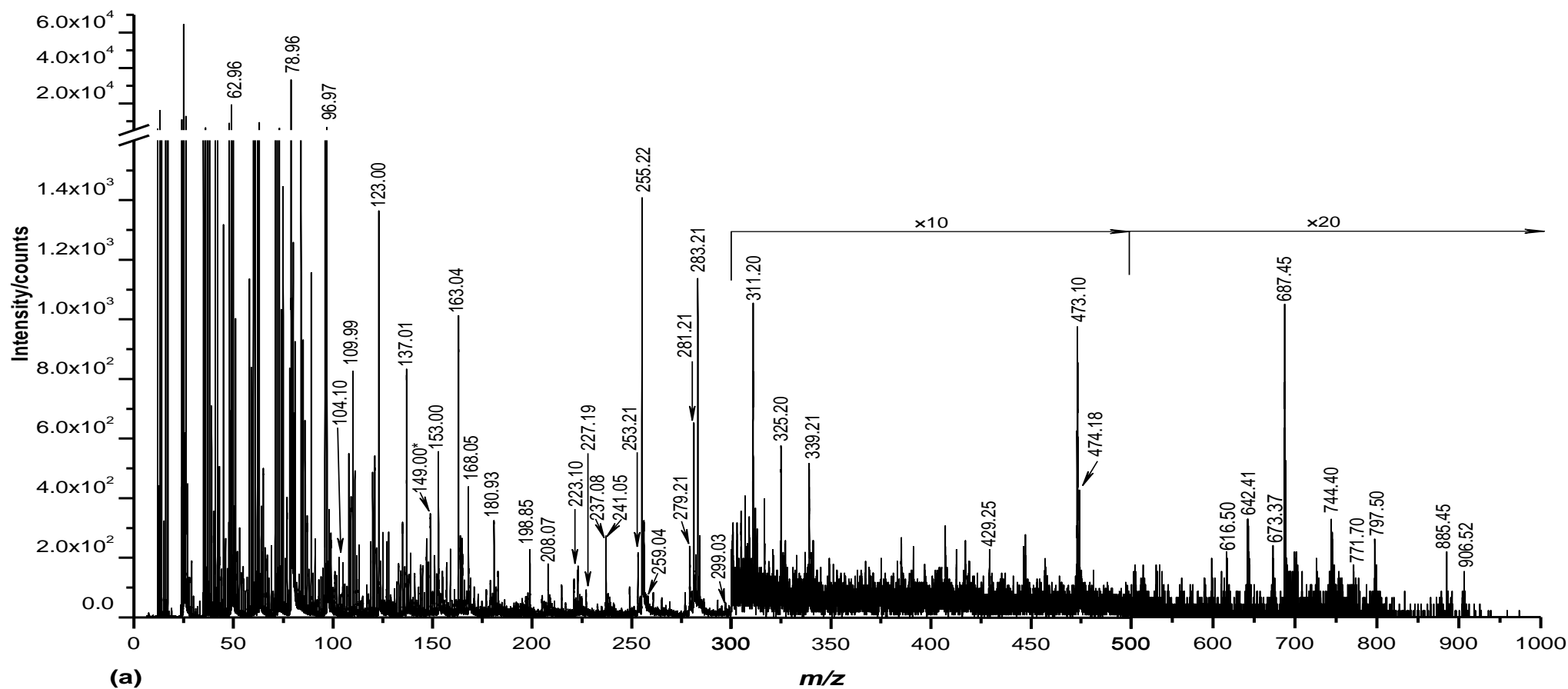


Fig. 3.8 +SIMS Spectra of lipids extraction from *Xenopus laevis* zygote 10 min after fertilisation using the BioToF-SIMS (a) and the J105 3D Chemical Imager (b). Spectral dose for the BioToF-SIMS is 6.67×10^{11} ions/cm² with 20 keV C₆₀⁺ PI beam, and 1.2×10^{13} ions/cm² for the J105 using 40 keV C₆₀⁺ PI beam. The peaks assignment is listed in Table 3.3. * represents PDMS peaks.

Bio ToF -SIMS of lipids extraction from *Xenopus laevis* zygote 10min after fertilisation



J105 3D Chemical Imager -SIMS spectrum of lipids extraction from *Xenopus laevis* zygote 10min after fertilisation

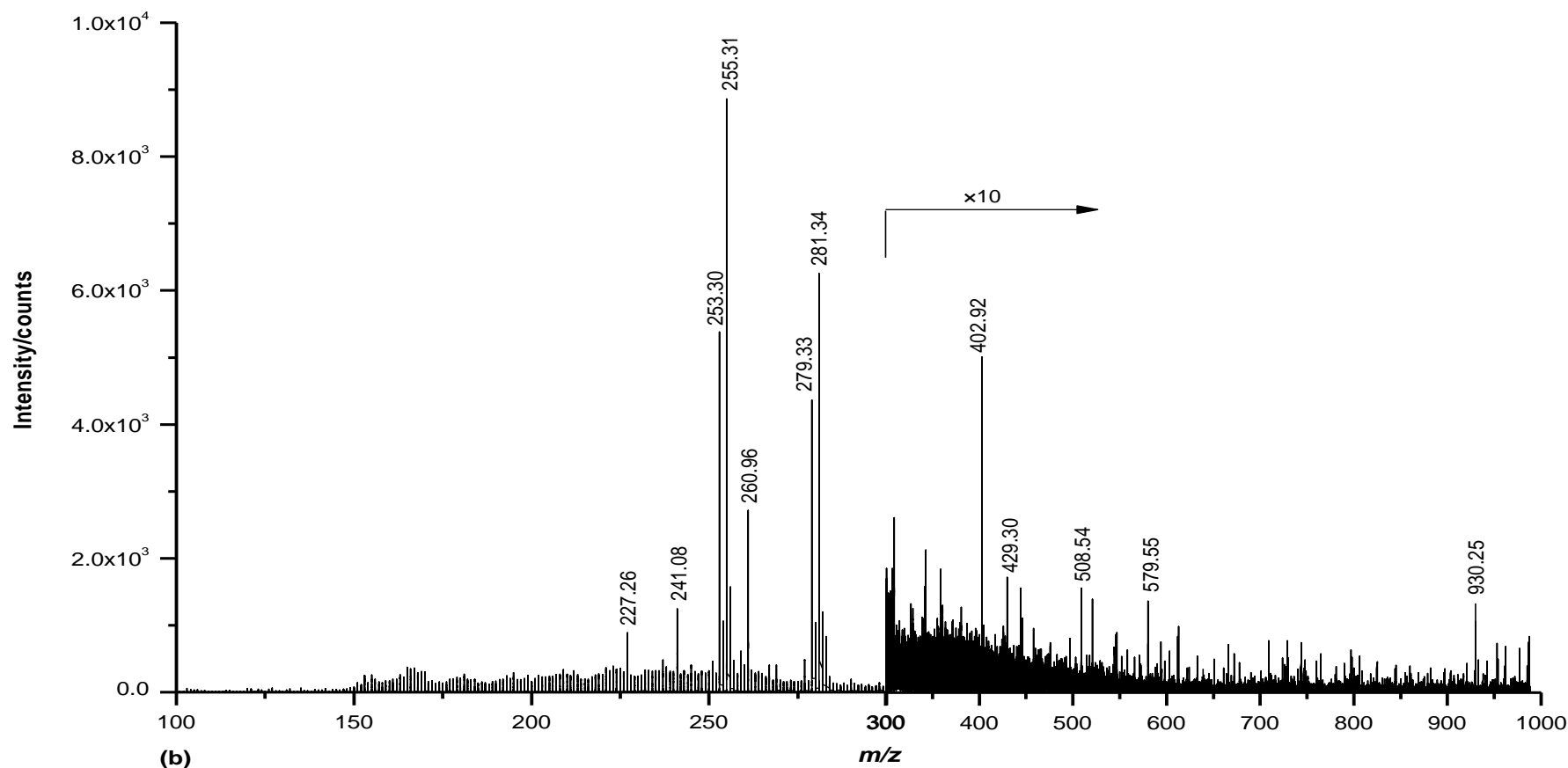
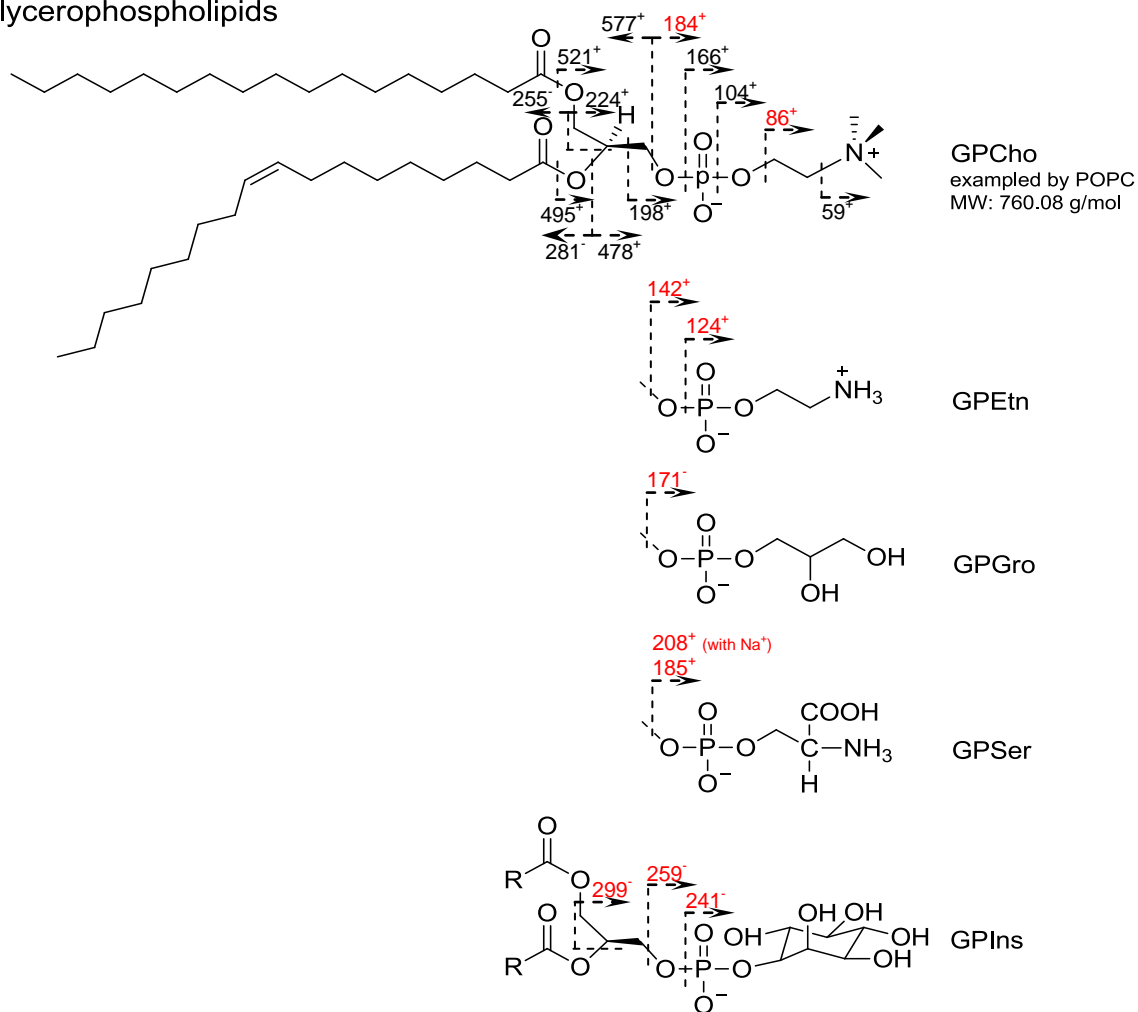


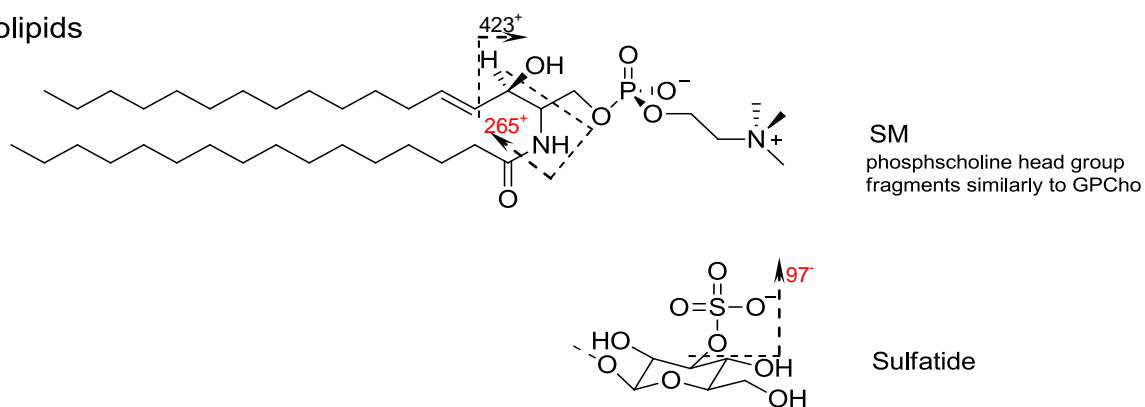
Fig. 3.9 -SIMS spectra of lipids extraction from *Xenopus laevis* zygote 10 min after fertilisation using the BioToF-SIMS (a) and the J105 3D Chemical Imager. Spectral dose for the BioToF-SIMS is 6.67×10^{11} ions/cm² with 20 keV C₆₀⁺ PI beam, and 1.2×10^{13} ions/cm² for the J105 using 40 keV C₆₀⁺ PI beam. The peaks assignment is listed in Table 3.3. * represents PDMS peaks. Because the negative mode of the J105 is still under optimisation, the condition is not ideal for analysis, suffering from low ion transmission and high noise level. As shown in (b), the detectable ions are mainly fatty acids in mass range of m/z 250-290.

Major classes of membrane lipids

Glycerophospholipids



Sphingolipids



Sterol

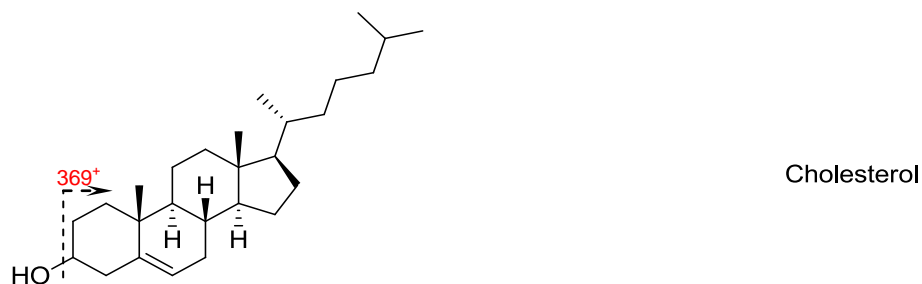


Fig. 3.10 Fragmentation of the major classes of lipids in biological cell membrane.

Table 3.3 Peaks assignment of lipids extraction from *Xenopus laevis* zygote 10 min post-insemination in positive and negative SIMS

Parent compound	+SIMS				-SIMS				
	<i>m/z</i>		Proposed fragments	Note	<i>m/z</i>		Proposed fragments	Note	
	BioToF J105				BioToF J105				
Glycerophosphocholine (GPCho)	86.10	86.05	[C ₅ H ₁₂ N] ⁺	+/+	62.96		PO ₂ ⁻	+/-	
	104.12	104.08	[C ₅ H ₁₄ NO] ⁺	+/+	78.96		PO ₃ ⁻	+/-	
	125.02	124.98	[C ₂ H ₆ PO ₄] ⁺	+/+	104.10		[C ₅ H ₁₄ NO] ⁻	+/-	
	166.08	166.05	[C ₅ H ₁₃ NPO ₃] ⁺	+/+					
	184.10	184.05	[C ₅ H ₁₅ NPO ₄] ⁺	+/+					
	224.14	224.10	[C ₈ H ₁₉ NPO ₄] ⁺	+/+					
	246.14	246.08	[C ₈ H ₁₈ NPO ₄ Na] ⁺	+/+					
	459.30	459.29	[C ₂₃ H ₄₁ O ₇ P] ⁺ C20:3 monoglycerolphosphate	+/+*					
	478.45	478.34	[C ₉ H ₁₇ NPO ₆ -C ₁₅ H ₃₂] ⁺ C16:0 monoacylglycerol-phosphocholines	+/+*					
	495.30	495.27	[C ₉ H ₁₈ NPO ₇ -C ₁₅ H ₃₂] ⁺ C16:0 monoacylglycerol-phosphocholines	+/+*					
		521.44	[C ₉ H ₁₈ NPO ₇ -C ₁₇ H ₃₄] ⁺ 18:1	-/+					
	523.54	523.46	[C ₉ H ₁₈ NPO ₇ -C ₁₇ H ₃₆] ⁺ 18:0	+/+					
		721.50	[C ₃₉ H ₇₁ O ₇ PK] ⁺ 16:0/18:2	-/+					
		723.51	[C ₃₉ H ₇₃ O ₇ PK] ⁺ 16:0/18:1	-/+					
		725.57	[C ₃₉ H ₇₅ O ₇ PK] ⁺ 16:0/18:1	-/+					
		732.60	[C ₁₀ H ₁₉ NPO ₈ -C ₃₀ H ₆₀] ⁺ 16:0/16:1	-/+					
		758.58	758.60	[C ₁₀ H ₁₉ NPO ₈ -C ₃₂ H ₆₂] ⁺ 16:0/18:2	+/+				
		760.60	760.63	[C ₁₀ H ₁₉ NPO ₈ -C ₃₂ H ₆₄] ⁺ 16:0/18:1	+/+				
		780.60	780.58	[C ₄₂ H ₈₁ NPO ₈ Na] ⁺ 16:0/18:2	+/+				
		782.62	782.60	[C ₄₂ H ₈₃ NPO ₈ Na] ⁺ 16:0/18:1	+/+				
			784.60	[C ₄₂ H ₈₅ NPO ₈ Na] ⁺ 16:0/18:0	-/+				
		798.64	798.63	[C ₄₂ H ₈₃ NPO ₈ K] ⁺ 16:0/18:1	+/+				
			806.61	[C ₁₀ H ₁₉ NPO ₈ -C ₃₆ H ₆₂] ⁺ 18:2/20:4	-/+				
Glycerophosphoethanolamine (GPEtn)	124.10	124.10	[C ₂ H ₇ NPO ₃] ⁺	+/+	123.00		[C ₂ H ₆ NPO ₃] ⁻	+/-	
	142.07	142.06	[C ₂ H ₉ NPO ₄] ⁺	+/+					
		477.38	[C ₂₃ H ₄₄ NO ₇ P] ⁺ Monoacylglycerol-phosphoethanolamines C18:2	-/+*					
		479.23	[C ₂₃ H ₄₆ NO ₇ P] ⁺ Monoacylglycerol-phosphoethanolamines C18:1	-/+*					
		743.52	[C ₇ H ₁₂ NPO ₈ -C ₃₄ H ₆₆] ⁺ 18:0/18:2	-/+					
		745.56	[C ₇ H ₁₂ NPO ₈ -C ₃₄ H ₆₈] ⁺ 18:0/18:1	-/+					
		811.73	[C ₇ H ₁₂ NPO ₈ -C ₃₉ H ₇₄] ⁺ 19:1/22:2	-/+					
Glycerophosphoglycerol (GPGro)	198.10	198.08	[C ₅ H ₁₁ PO ₆] ⁺	+/+	227.19	227.26	[C ₆ H ₁₂ PO ₇] ⁻		
		747.56	[C ₈ H ₁₂ PO ₁₀ -C ₃₂ H ₆₄] ⁺ 16:0/18:1	-/+					
Glycerophosphoserine (GPSer)	185.10	185.06	[C ₃ H ₈ NPO ₆] ⁺	+/+					
	208.04		[C ₃ H ₈ NPO ₆ Na] ⁺	+/-					
Glycerophosphoinositol (GPI)					241.22	241.08	[C ₆ H ₁₀ PO ₈] ⁻	+/+	
					259.25		[C ₆ H ₁₂ PO ₉] ⁻	+/-	
					299.22		[C ₉ H ₁₆ PO ₉] ⁻	+/-	
					885.45		[C ₁₁ H ₁₆ O ₁₃ P-C ₃₆ H ₆₆] ⁻ C38:4	+/-	
Sphingolipids	86.10	86.05	[C ₅ H ₁₂ N] ⁺	+/+	62.96		PO ₂ ⁻	+/-	
	102.11	102.07	[C ₅ H ₁₂ NO] ⁺	+/+	78.96		PO ₃ ⁻	+/-	
	104.12	104.08	[C ₅ H ₁₄ NO] ⁺	+/+	96.97		[SO ₄ H] ⁻	+/-	
	166.08	166.05	[C ₅ H ₁₃ NPO ₃] ⁺	+/+	104.10		[C ₅ H ₁₄ NO] ⁻	+/-	
	184.10	184.05	[C ₅ H ₁₅ NPO ₄] ⁺	+/+	616.50		[C ₃₄ H ₆₇ NO ₆ P] ⁻	+/-	
							[M-C ₂ H ₂ N(CH ₃) ₃] SM(34:1)		
	206.08	206.05	[C ₅ H ₁₅ NPO ₄ Na] ⁺	+/+	642.41		[C ₃₆ H ₆₉ NO ₆ P] ⁻ [M-N(CH ₃) ₃] SM(34:1)	+/-	
	265.06	265.25	[C ₁₈ H ₃₅ N] ⁺	+/+*	673.37		[C ₃₇ H ₇₄ N ₂ O ₆ P] ⁻ [M-C ₂ H ₅] SM(34:1)	*+/-	
		417.26	[C ₂₀ H ₃₆ NO ₆ P] ⁺ Ceramide phosphocholines C16:3	-/+*	687.45		[C ₃₈ H ₇₆ N ₂ O ₆ P] ⁻ [M-CH ₃] SM(34:1)	+/-	
		419.31	[C ₂₀ H ₃₈ NO ₆ P] ⁺ Ceramide phosphocholines C16:2	-/+*	906.52		[C ₄₈ H ₉₂ SNO ₁₂] ⁻ [M-H] ⁻ ST	+/-	
		421.32	[C ₂₀ H ₄₀ NO ₆ P] ⁺ Ceramide phosphocholines C16:1	-/+*					
	423.34	[C ₂₀ H ₄₂ NO ₆ P] ⁺ Ceramide phosphocholines C16:0	-/+*						
Sterol lipids	369.37	369.35	[C ₂₇ H ₄₅] ⁺	+/+	771.70		[C ₅₄ H ₉₁ O ₂] ⁻	+/-	
Cholesterol	385.37	385.23	[C ₂₇ H ₄₅ O] ⁺	+/+					
Prenol lipids		430.37	[C ₂₉ H ₅₀ O ₂] ⁺	-/+	429.25	429.30	[C ₂₉ H ₄₉ O ₂] ⁻	+/+	
Vitamin E									
Fatty acyls	435.34		[C ₂₉ H ₄₁ NO ₂] ⁺ C20:5 N-acyl amine	-/+*	251.21	251.30	[C ₁₆ H ₂₇ O ₂] ⁻ C16:2	+/+	
	437.34		[C ₂₉ H ₄₃ NO ₂] ⁺ C20:4 N-acyl amine	-/+*	253.21	253.30	[C ₁₆ H ₂₉ O ₂] ⁻ C16:1	+/+	
	439.20		[C ₂₉ H ₄₅ NO ₂] ⁺ C20:3 N-acyl amine	-/+*	255.22		[C ₁₆ H ₃₁ O ₂] ⁻ C16:0	+/-	
	441.25		[C ₂₉ H ₄₇ NO ₂] ⁺ C20:2 N-acyl amine	-/+*	279.21	279.33	[C ₁₈ H ₃₁ O ₂] ⁻ C18:2	+/+	
					281.21	281.34	[C ₁₈ H ₃₃ O ₂] ⁻ C18:1	+/+	
					283.21		[C ₁₈ H ₃₅ O ₂] ⁻ C18:0	+/-	
					311.20		[C ₂₀ H ₃₉ O ₂] ⁻ C20:0	+/-	
					325.20		[C ₂₁ H ₄₁ O ₂] ⁻ C21:0	+/-	
				339.21		[C ₂₂ H ₄₃ O ₂] ⁻ C22:0	+/-		

Monoacyl-glycerol (MAG)	311.31	311.25	[C ₁₉ H ₃₅ O ₃] ⁺	C16:1	+glycerol backbone	+/+
	313.31	313.27	[C ₁₉ H ₃₇ O ₃] ⁺	C16:0	+glycerol backbone	+/+
	323.30	323.25	[C ₂₀ H ₃₅ O ₃] ⁺	C17:2	+glycerol backbone	+/+
	325.45	325.27	[C ₂₀ H ₃₇ O ₃] ⁺	C17:1	+glycerol backbone	+/+
	327.48	327.28	[C ₂₀ H ₃₉ O ₃] ⁺	C17:0	+glycerol backbone	+/+
	335.31	335.25	[C ₂₁ H ₃₇ O ₃] ⁺	C18:3	+glycerol backbone	+/+
	337.31	337.28	[C ₂₁ H ₃₉ O ₃] ⁺	C18:2	+glycerol backbone	+/+
	339.31	339.27	[C ₂₁ H ₃₉ O ₃] ⁺	C18:1	+glycerol backbone	+/+
	351.29		[C ₂₂ H ₃₉ O ₃] ⁺	C19:2	+glycerol backbone	-/+
	353.34	353.31	[C ₂₂ H ₄₁ O ₃] ⁺	C19:1	+glycerol backbone	+/+*
	355.24	355.30	[C ₂₂ H ₄₃ O ₃] ⁺	C19:0	+glycerol backbone	+/+*
	391.28		[C ₂₅ H ₄₃ O ₃] ⁺	C22:2	+glycerol backbone	-/+*
	393.29		[C ₂₅ H ₄₅ O ₃] ⁺	C22:1	+glycerol backbone	-/+*
	395.31		[C ₂₅ H ₄₇ O ₃] ⁺	C22:0	+glycerol backbone	-/+*
Diacylglycerol (DAG)	515.43		[C ₃₃ H ₆₃ O ₄] ⁺	C30:0		-/+
	519.42		[C ₃₃ H ₅₉ O ₄] ⁺	C30:2		-/+
	545.43		[C ₃₅ H ₆₁ O ₄] ⁺	C32:3		-/+
	547.44		[C ₃₅ H ₆₃ O ₄] ⁺	C32:2		-/+
	549.50	549.46	[C ₃₅ H ₆₅ O ₄] ⁺	C32:1		+/+
	551.53	551.47	[C ₃₅ H ₆₇ O ₄] ⁺	C32:0		+/+
	561.47		[C ₃₆ H ₆₅ O ₄] ⁺	C33:2		-/+
	563.48		[C ₃₆ H ₆₇ O ₄] ⁺	C33:1		-/+
	571.44		[C ₃₇ H ₆₃ O ₄] ⁺	C34:4		-/+
	573.46		[C ₃₇ H ₆₅ O ₄] ⁺	C34:3		-/+
	575.48	575.48	[C ₃₇ H ₆₇ O ₄] ⁺	C34:2		+/+
	577.48	577.49	[C ₃₇ H ₆₉ O ₄] ⁺	C34:1		+/+
	579.50		[C ₃₇ H ₇₁ O ₄] ⁺	C34:0		-/+
	587.49		[C ₃₈ H ₆₇ O ₄] ⁺	C35:3		-/+
	589.49		[C ₃₈ H ₆₉ O ₄] ⁺	C35:2		-/+
	591.49		[C ₃₈ H ₇₁ O ₄] ⁺	C35:1		-/+
	595.47		[C ₃₉ H ₆₃ O ₄] ⁺	C36:6		-/+
	597.47		[C ₃₉ H ₆₅ O ₄] ⁺	C36:5		-/+
	599.48		[C ₃₉ H ₆₇ O ₄] ⁺	C36:4		-/+
	601.50		[C ₃₉ H ₆₉ O ₄] ⁺	C36:3		-/+
	603.51		[C ₃₉ H ₇₁ O ₄] ⁺	C36:2		-/+
	605.52		[C ₃₉ H ₇₃ O ₄] ⁺	C36:1		-/+
	607.37		[C ₃₉ H ₇₅ O ₄] ⁺	C36:0		-/+
	621.49		[C ₄₁ H ₆₅ O ₄] ⁺	C38:7		-/+
	623.48		[C ₄₁ H ₆₇ O ₄] ⁺	C38:6		-/+
	625.50		[C ₄₁ H ₆₉ O ₄] ⁺	C38:5		-/+
Triacylglycerol (TAG)	825.75		[C ₅₃ H ₉₃ O ₆] ⁺	C50:5		-/+
	827.76		[C ₅₃ H ₉₅ O ₆] ⁺	C50:4		-/+
	829.77		[C ₅₃ H ₉₇ O ₆] ⁺	C50:3		-/+
	837.75		[C ₅₄ H ₉₃ O ₆] ⁺	C51:6		-/+
	839.77		[C ₅₄ H ₉₅ O ₆] ⁺	C51:5		-/+
	841.76		[C ₅₄ H ₉₇ O ₆] ⁺	C51:4		-/+
	851.75		[C ₅₅ H ₉₅ O ₆] ⁺	C52:6		-/+
	853.78		[C ₅₅ H ₉₇ O ₆] ⁺	C52:5		-/+
			/[C ₅₃ H ₉₈ O ₆ Na] ⁺	C50:2		-/+
			[C ₅₅ H ₉₉ O ₆] ⁺	C52:4		-/+
	855.78		/[C ₅₃ H ₁₀₀ O ₆ Na] ⁺	C50:1		-/+
	861.74		[C ₅₅ H ₁₀₅ O ₆] ⁺	C52:0		-/+
	863.76		[C ₅₆ H ₉₅ O ₆] ⁺	C53:7		-/+
	865.77		[C ₅₆ H ₉₇ O ₆] ⁺	C53:6		-/+
	867.78		[C ₅₆ H ₉₉ O ₆] ⁺	C53:5		-/+
			[C ₅₅ H ₉₈ O ₆ Na] ⁺	C52:4		-/+
	877.77		/[C ₅₇ H ₉₇ O ₆] ⁺	C54:2		-/+
			[C ₅₅ H ₁₀₀ O ₆ Na] ⁺	C52:3		-/+
	879.78		/[C ₅₇ H ₉₉ O ₆] ⁺	C54:3		-/+
			[C ₅₅ H ₁₀₂ O ₆ Na] ⁺	C52:2		-/+
	881.80		/[C ₅₇ H ₁₀₁ O ₆] ⁺	C54:4		-/+
	899.78		[C ₅₉ H ₉₅ O ₆] ⁺	C56:5		-/+
	901.78		[C ₅₉ H ₉₇ O ₆] ⁺	C56:4		-/+
	903.79		[C ₅₉ H ₉₉ O ₆] ⁺	C56:3		-/+
	905.81		[C ₅₉ H ₁₀₁ O ₆] ⁺	C56:2		-/+
	926.87		[C ₅₉ H ₉₉ O ₆ Na] ⁺	C56:3		-/+*
	928.90		[C ₅₉ H ₁₀₁ O ₆ Na] ⁺	C56:2		-/+*
	930.87		[C ₅₉ H ₁₀₃ O ₆ Na] ⁺	C56:1		-/+*
	951.81		[C ₆₁ H ₁₀₁ O ₆ Na] ⁺	C58:4		-/+*
	953.80		[C ₆₁ H ₁₀₃ O ₆ Na] ⁺	C58:4		-/+*

Notes: +/+, appeared in both the BioToF-SIMS and the J105 SIMS spectra; +/- only appeared in the BioToF-SIMS spectrum; -/+ only appeared in the J105 SIMS spectrum. The ions marked with ' * ' have not been reported in previous ToF-SIMS studies, and the assignments of these ions are based on the LIPID MAPS Consortium.

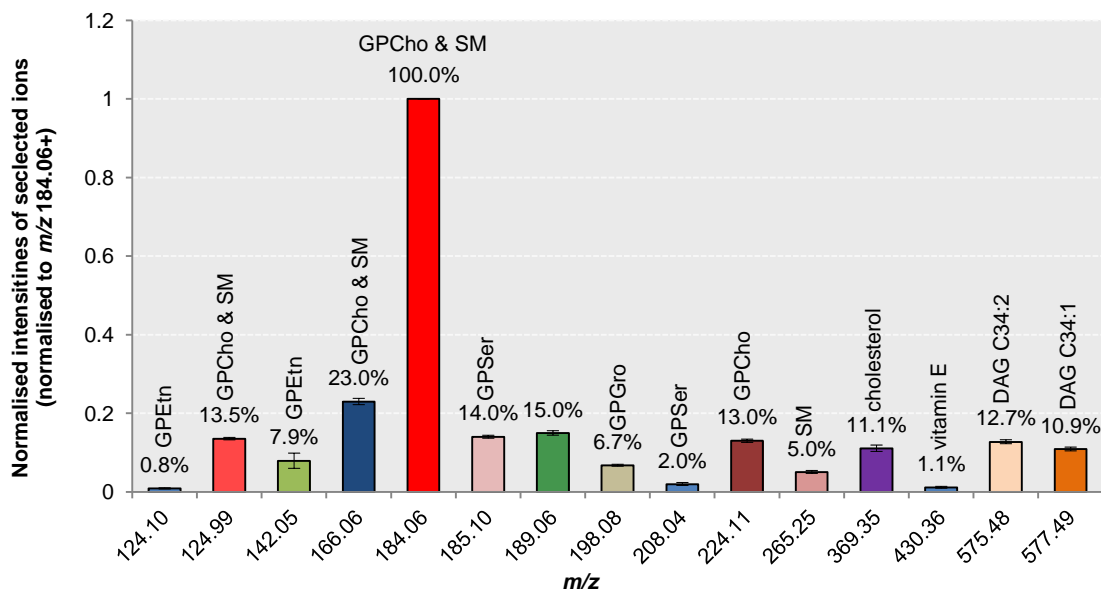


Fig. 3.11 Relative intensities of selected lipid ions from lipid extract of *Xenopus laevis* zygotes 10 min post-insemination. The analysis was performed in positive ion mode using the J105 3D Chemical Imager. Characteristic peaks of various lipids are as follows, m/z 124.10⁺ and 142.05⁺ for GPEtn; m/z 124.99⁺, 166.05⁺, 184.06⁺ and 224.11⁺ for GPCho; m/z 185.10⁺ and 208.04⁺ for GPSer; m/z 198.08⁺ for GPGro; m/z 265.25⁺ for SM; m/z 369.35⁺ for Cholesterol; m/z 430.36⁺ for vitamin E; m/z 575.48⁺ and 577.49⁺ for DAG; m/z 189.06⁺ is unassigned, possible for GPGro.

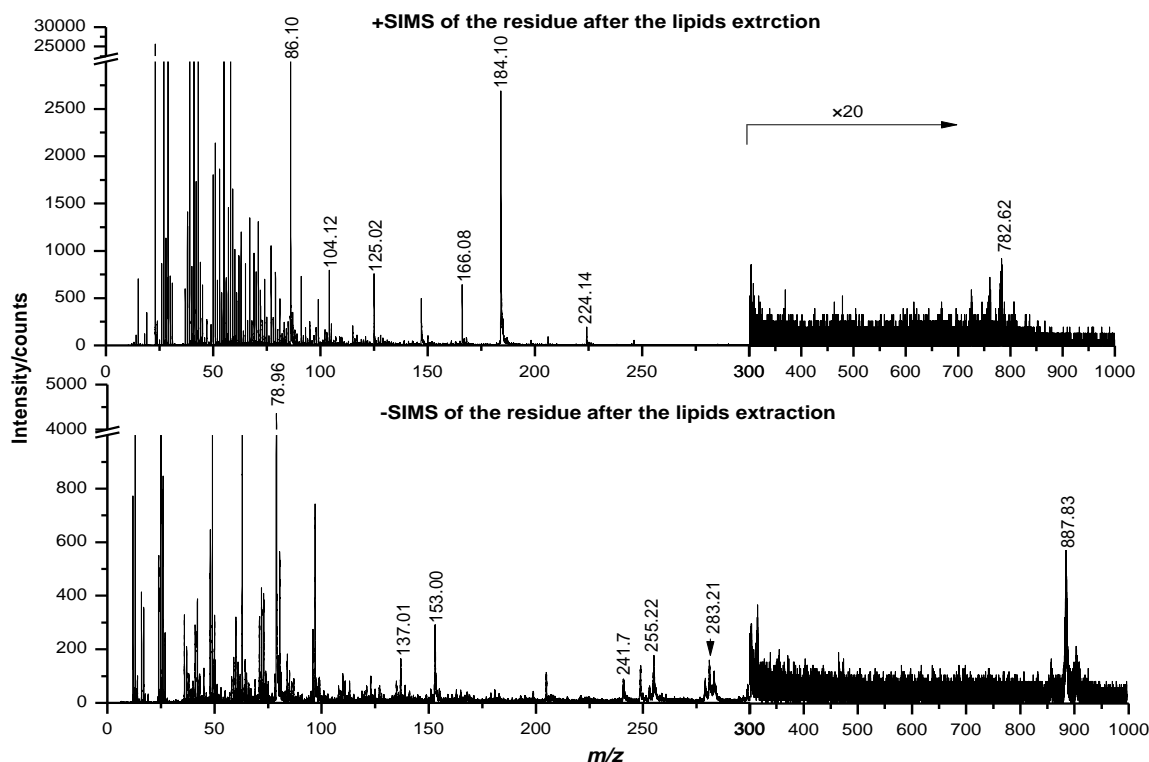


Fig. 3.12 The \pm SIMS spectra of the residue from *Xenopus laevis* zygotes 10 min post-insemination after lipids extraction. Spectral dose is 3.5×10^{11} ions/cm² with 20 keV C₆₀⁺ PI beam using the BioToF-SIMS.

3.3.3 Topography effects on spherical sample

Owing to the extreme topography of the *X. laevis* egg, imaging the cell is quite challenging for both instruments. It is expected that the spot size of the focused beam varies to some extent at different heights of the sample, consequently the spatial resolution and mass resolution are affected. Particularly for the BioToF-SIMS, the ions with the same mass ejected from different sample height

will arrive at detector successively, resulting in broad peaks and low mass resolution. Another effect induced by the topography is varying SI intensity across the sample surface. As in Fig. 3.13, the extraction field is distorted by the insulating sphere sample, so that the extraction efficiency of SI is different across the sample surface. In addition, the edge of the curved sample surface may shadow the SIs ejected by the incident PI beam from being collected by the detector, this is termed 'beam shadow' effect [87]. The J105 as a new generation of SIMS instrument has been improved in several aspects for the analysis of biological samples. The DC PI beam enables high lateral resolution, and buncher-ToF design decouples SI detection from the sample topography effect to some extent. In addition, the dynamic emittance matching (DEM's) as show in Fig. 3.14 (b) reduces the loss of the SI from the edges of the sample surface. In this section, the topography effects were assessed using both instruments through investigation of the variation of SIs yields across the sphere sample surface in 2D image.

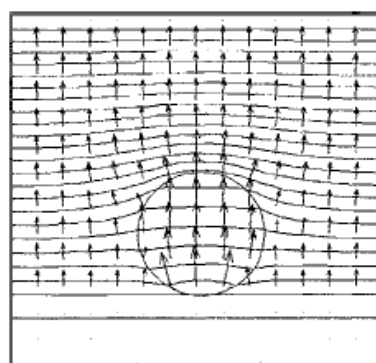


Fig. 3.13 Simulated electric fields in ToF-SIMS for insulating particle over a conducting substrate. Reproduced from reference [87].

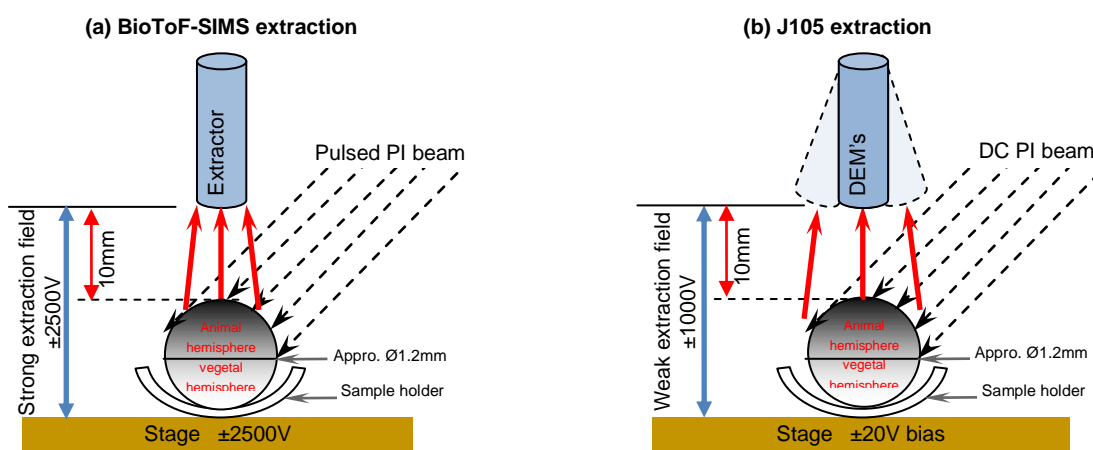


Fig. 3.14 Sphere sample under the extraction field. (a) the BioToF-SIMS extraction. Extraction field is fixed with a strong electric field. (b) the J105 extraction. Dynamic emittance matching (DEM's) extraction and with weak electric field.

Sample height setting. For both instruments, the extraction gap is fixed at 10 mm (Fig. 3.14), and correspondingly some parameters are optimized to maximum extraction efficiency, e.g., extractor lens and stage voltage. The right distance between the extractor and the samples is therefore a prerequisite for the experiments. The sample height is confirmed by checking the optical extraction gate (where beam sputtering and extraction field are aligned), which should appear round in the central of the SIMS image with maximum analysis area. The optical gate checking is easier to perform on flat samples, but for large sphere samples like *X. laevis* embryos, the optical gate has to fall onto the top the sphere in order to distribute the extraction field as broadly as possible. If the

optical gate is focused on the lower part or the side of the sphere, the PI beam could be blocked in the opposite side of the sample, and accordingly the complete loss of SI in some region might occur. In these cases, the optical gates appear as elongated and shrieked.

Delay of stage voltage. Unlike the J105, the mass resolution of the BioToF-SIMS is affected severely by the sample topography due to the discrepancy of flight distances for same mass ions ejected from different heights on the sample resulting in broad peak. This can be compensated by delaying the acceleration voltage applied to the stage by tens of nanoseconds after the PI beam sputters the sample surface [88]. The delay allows SI emitted from different heights to drift freely and consequently energy dispersion of the SI is balanced, followed by accelerating the SI from where the extraction field is less distorted above the sample. For the J105, a different approach is used to avoid the distortion of the extraction field, e.g., applying a lower extraction voltage (± 1000 V), DEM scanning follows the movement of the PI beam and stage bias (± 20 V) to boost the ejected SI towards the extractor [Fig. 3.14 (b)]. The stage bias was also applied for charge compensation.

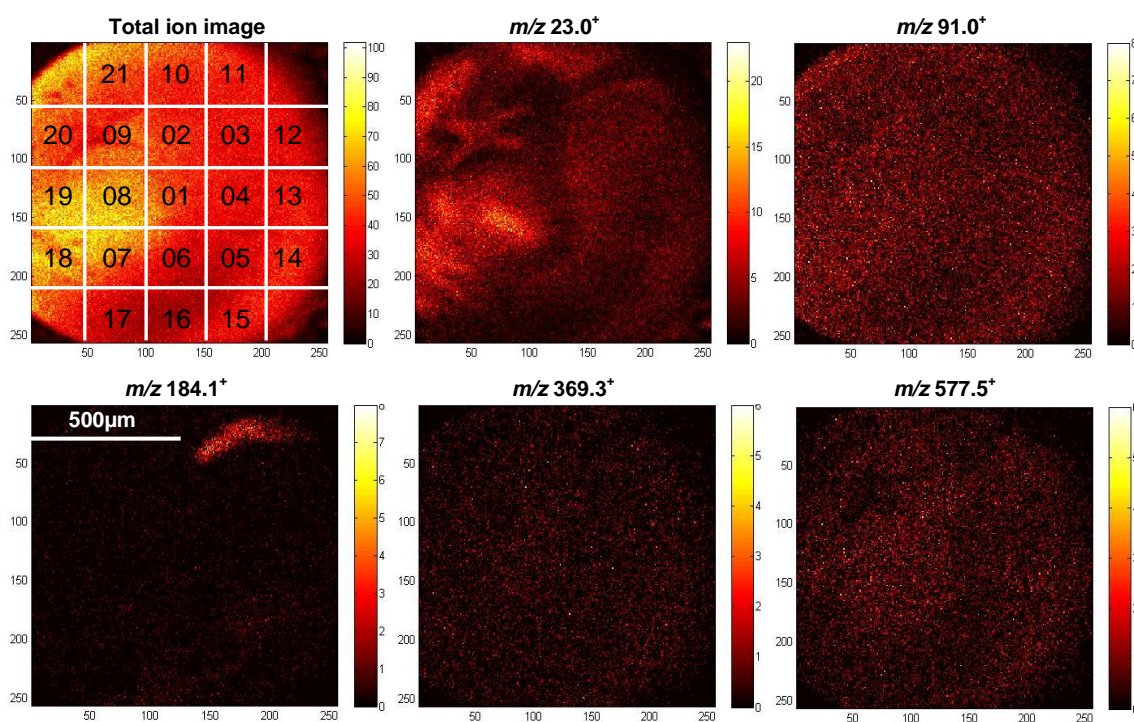


Fig. 3.15 Images (+SIMS) of *Xenopus laevis* zygote 10 min post-insemination selected for comparison study of secondary ion yields variation using the BioToF-SIMS. Spectral dose is 2.09×10^9 ions/cm² over $1000 \times 1000 \mu\text{m}^2$, 256×256 pixels across the image. The total ion image was divided into 25 squares equally. The yields of total SI and selected SI at $m/z 23.0^+$ (Na^+), $m/z 91.0^+$ ($[\text{C}_7\text{H}_7]^+$), $m/z 184.1^+$ (phosphocholine), $m/z 369.3^+$ (cholesterol) and $m/z 577.5^+$ (DAG) are calculated in the squares numbered with 01-21 and plotted in Fig. 3.16. The thermo scale corresponds to the ion intensity and the counts can be read on the scale bar.

With the optimised settings, *X. laevis* zygote 10 min after fertilisation with smooth surface was investigated using the BioToF-SIMS. The total ion image of the cell was divided into equal squares and selected SI yields were calculated in each square to compare the SI loss in different areas on sample surface. The BioToF-SIMS images in Fig. 3.15 show the overall morphology and some features on the membrane of the zygote. The equal squares numbered 01-21 in the total ion image cover most of the cell surface. The yields of total SI and selected SI at $m/z 23.0^+$, $m/z 184.1^+$, $m/z 369.3^+$ and $m/z 577.5^+$ were calculated and plotted in Fig. 3.16. Representing important

salts/biomolecules, these selected ions help to clarify the topography effects with respect to the real distribution of the biomolecules. Particularly, m/z 91.0⁺ [C₇H₇]⁺ is a common hydrocarbon fragment with almost homogenous distribution on biological samples, enabling it to demonstrate how SI signal varies from different areas on the sample surface. It is clear that all SIs have a similar distribution pattern of the yields cross the sample surface, e.g., squares No.12-14 in the edge of the zygote display lower SI yields, whereas highest SI yields occur in squares No.17-18 opposite to No.12-14, and squares No.01-09 in the middle of the zygote surface have the intermediate SI yields. The exception is m/z 184.1⁺ that has highest yield in square No.10, and this is also manifested by the ion image of m/z 184.1⁺ (Fig. 3.15) as a high-intensity patch in No.10 area. The yields of SI at m/z 91.0⁺ and m/z 369.3⁺ that are almost homogeneous on the hemisphere follow the general distribution pattern. This indicates the biological features and spatial distributions are possible to be imaged using single ion images (i.e. m/z 23.0⁺ and m/z 184.1⁺) even though the features locate in the region where the SI loss is significant.

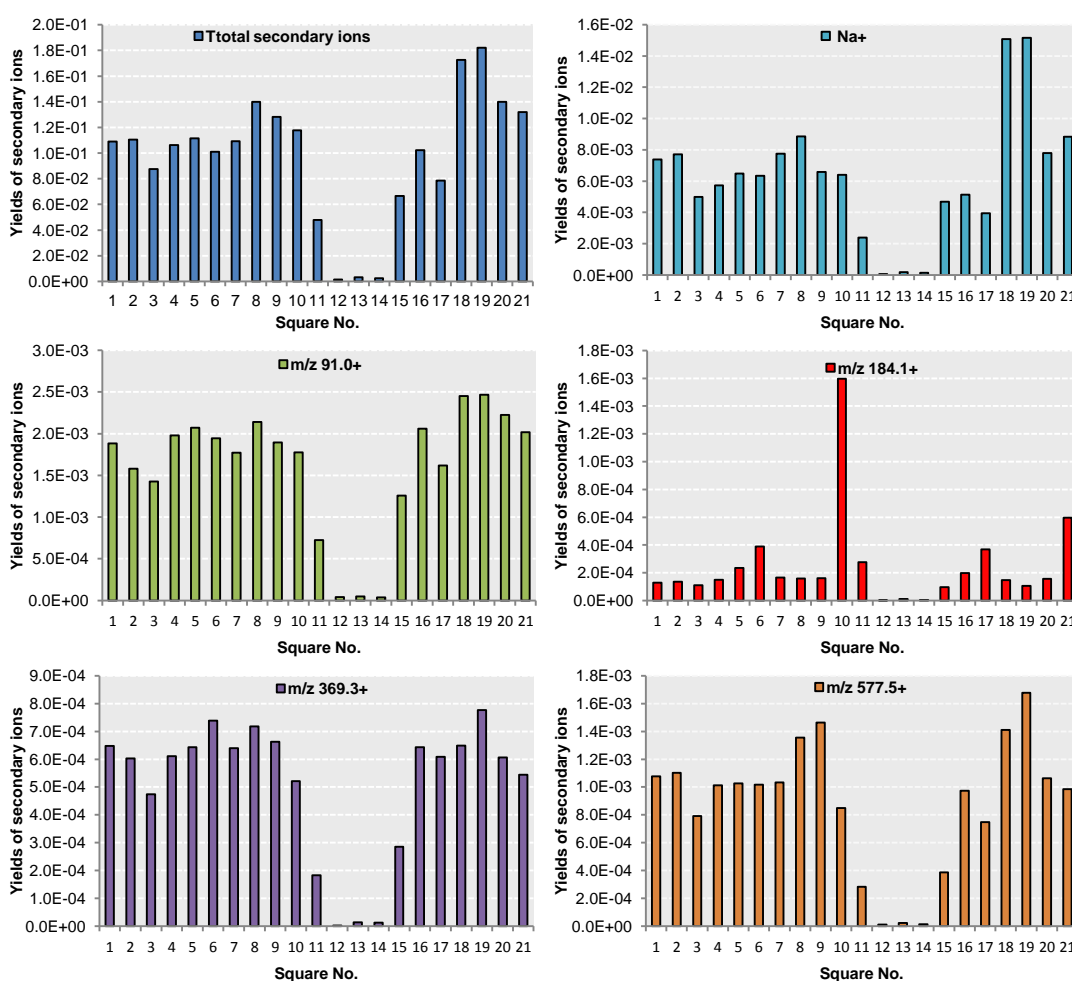


Fig. 3.16 Comparing the yields of total and selected ions cross the animal hemisphere of *Xenopus laevis* zygote 10 min post-insemination using the BioToF-SIMS. The topography has a similar influence on the yields of SI in certain areas, e.g., No.12-14 have lower ion yields compared with other areas, generally No.17-18 have higher yields and SI yields of No.01-10 are intermediate. The exception is for SI m/z 184.1⁺ with the highest yields in square No.10-11 where other SI signal loss is significant.

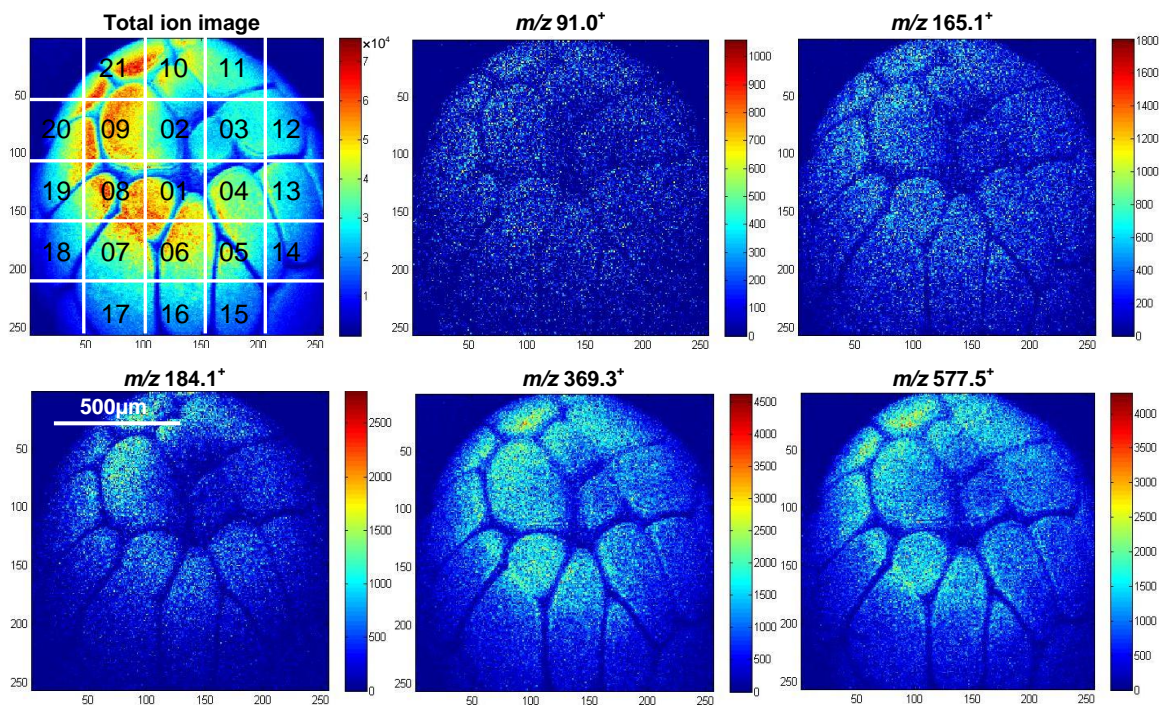


Fig. 3.17 Images (+SIMS) of *Xenopus laevis* 32 cells embryo selected for comparison study of secondary ion yields variation using the J105 3D Chemical Imager. Spectral dose is 4.47×10^{13} ions/cm² over $1200 \times 1200 \mu\text{m}^2$, 256×256 pixels across the image. The total ion image was divided into 25 squares equally, the squares No.01-21 were compared though the yields of total and selected SI at m/z 91.0⁺ ([C₇H₇]⁺), m/z 165.1⁺ ([C₂H₇O₅PNa]⁺), m/z 184.1⁺ (phosphocholine), m/z 369.3⁺ (cholesterol) and m/z 577.5⁺ (DAG) as detailed in Fig. 3.18. The colour scale corresponds to the ion intensity and the counts can be read on the scale bar.

The zygote sampled 10 min after fertilisation of the same batch sample was also analysed with the J105. Significant SI signals loss was not observed across the sample surface. Of particular interest with respect to the J105 analysis is whether it is capable of imaging the big sphere with more features on the membrane such as a blackberry-like embryo. As in Fig. 3.17, the total ion image and selected SI images demonstrate the animal hemisphere of 32 cells embryo of *X. laevis*. It is clear that the blastomeres cells are packed closely on the surface. Yields of total SIs and selected SIs at m/z 91.0⁺, m/z 165.1⁺, m/z 184.1⁺, m/z 369.3⁺ and m/z 577.5⁺ were compared in the squares No.01-21 as plotted in Fig. 3.18. The SI yields are also shown certain distribution pattern. Square No.09 has the highest SI yields, lowest yields occur in square No.14-17, and yields in other squares show a circularly decrease around square No.09. The lower SI yields in central squares No.01-02 compared to adjacent squares can be attributed to the wide junction between the blastomeres stopping the SI leaving.

With contrast to the severe SI yields drop in the edge of the sphere (square No.12-14) using BioToF-SIMS as shown in Fig. 3.16, there are low but still detectable SIs generated in the edge area (No.14-17) using the J105 as displayed in Fig. 3.18. A rather homogenous hydrocarbon ion m/z 91.0⁺ was further selected to compare the ion intensity across the analysis area of the spherical cells with relation to the incident angle of PI beam on both instruments.

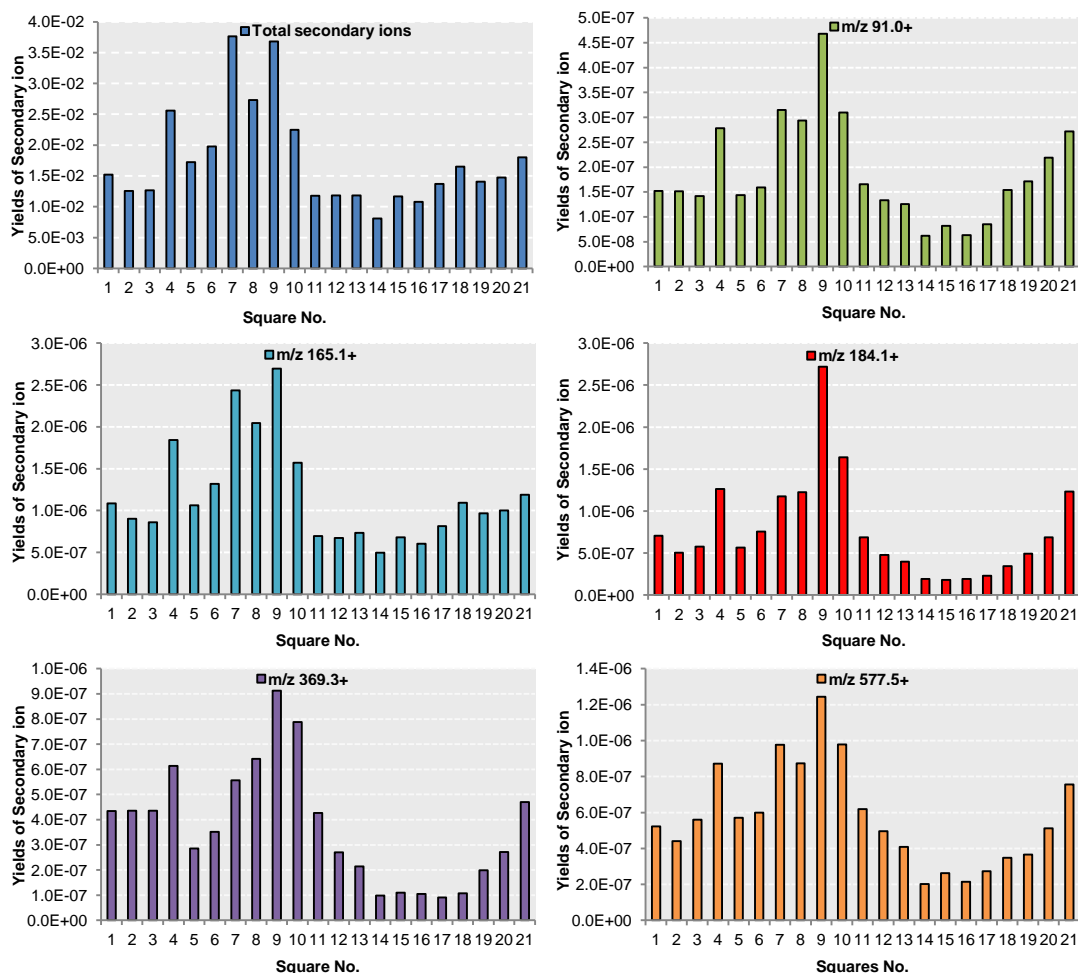


Fig. 3.18 Comparing the yields of total and selected ions cross the animal hemisphere of *Xenopus laevis* 32 cells embryo using the J105 3D Chemical Imager. Similar trends of topographic effects on the SI yields are shown in certain areas. Square No.09 has the highest SI yields, lowest yields occur in square No.14-17, and yields in other squares decrease around square No.09. The central squares 01 and 02 with lower SI yields than adjacent squares can be attributed to the wide junction between the blastomeres stopping the SI leaving.

Furthermore, the intensities of the generic hydrocarbon ion m/z 91.0⁺ in No.01-21 squares are normalised to its maximum intensity across the surface to illustrate the SI loses in different areas as plotted in Fig. 3.19 (a) for the BioToF-SIMS result and Fig. 3.19 (b) for the J105 result. Combined with the PI beam incident direction marked in Fig. 3.19 (a, b), it is obvious that lowest SI yields are from the edge of the sphere facing to the PI beam source. These areas have an obtuse angle with the PI beam as θ_1 shown in Fig. 3.19 (c), which makes the shadow effect largely responsible for the loss of SI, e.g., the squares No.11-14 in Fig. 3.19 (a) and No.14-17 in Fig. 3.19 (b). Further away from the PI ion gun, the incident angles of PI beam with the sample surface tend to equal or less than 90°, e.g., θ_2 and θ_3 in Fig. 3.19 (c). In this region, the SI is not shadowed by the PI beam; in addition, this is where the optical gate is focused on, thus the higher SI yields occur, e.g., in central squares No.01-09 and No.17-21 in Fig. 3.19 (a), and squares No.04-10, 21 in Fig. 3.19 (b). There are some exceptions such as squares No.01-03 in Fig. 3.19 (b). These squares are in the centre but with lower SI that could be caused by the broad junctions between the blastomeres resulting in localised incident angle effects. In some places the PI beam is close to 0° with the sample surface as θ_4 in Fig. 3.19 (c), the SI intensities appear to intermediate, as in the squares No.11-13, 18-20 in Fig. 3.19 (b). Compare (a) and (b) in Fig. 3.19, it seems that the beam shadow effect has more influence for the BioToF-SIMS with the SI falling below 2% in squares

No.12-14 in Fig. 3.19 (a), the severe loss is not seen in the other areas. However, there is not such a reduction of SI intensity using the J105, although the equator areas of the sphere sample still show an apparent decrease of SI intensity [Fig. 3.19 (b)].

In summary, with the extreme topography the SI loss is most severe in where the beam shadow effect plays a vital role, and SI intensity drop is also seen in the edge of the sphere samples. However, both instruments turned out to be useful in imaging the spatial distributions of biological molecules and detailed features in sphere sample to interpret the morphologic changes on the sample surface.

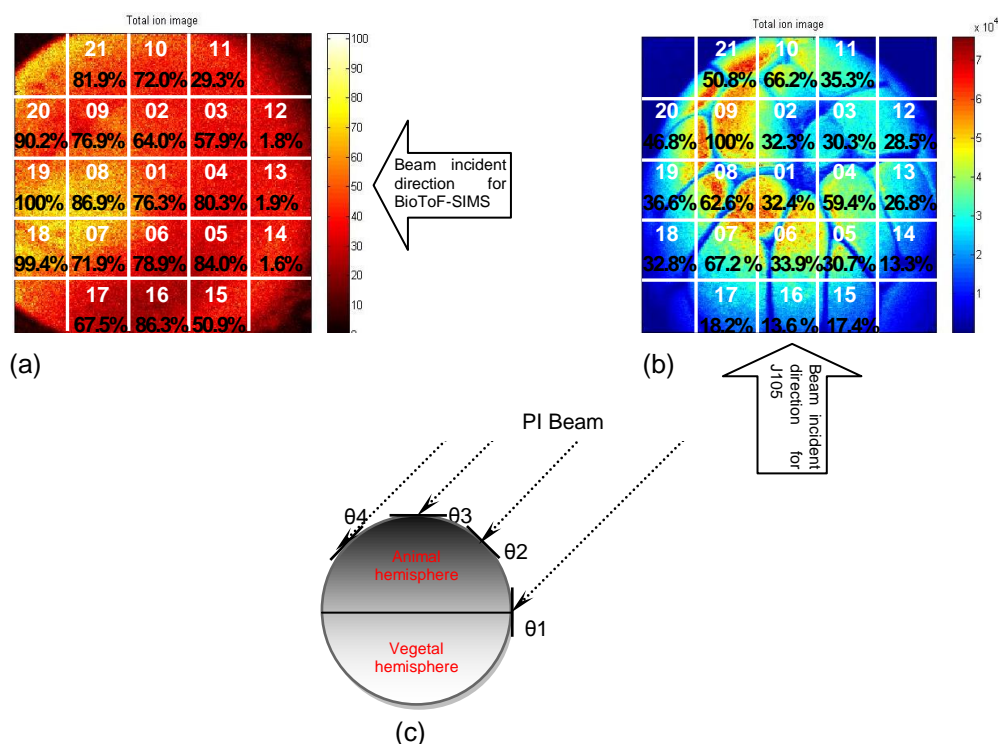


Fig. 3.19 Intensity variation of ion m/z 91.0⁺ cross the surface of spherical sample in relation to the corresponding incident angles of primary ion beam. (a), the percentage of SI m/z 91.0⁺ across the surface of *Xenopus laevis* zygote sampled 10 min post-fertilisation using the BioToF-SIMS. The intensities of m/z 91.0⁺ normalised to maximum intensity of m/z 91.0⁺ at square No.19; (b), the percentage of m/z 91.0⁺ across the surface of *Xenopus* blastula sampled 3.5 h post fertilisation using the J105 3D Chemical Imager. The intensities are normalised to that in square No.09; (c), beam angles in different areas on the sphere sample. With the extreme topography the SI loss is most severe where the beam shadow effect plays a vital role, such as squares No.11-14 in (a) and No.14-17 in (b), and SI intensity drop is also seen in the edge of the sphere samples.

3.3.4 Lipids map of *Xenopus laevis* zygote/embryo in time course study

In this section, the 2D/3D images of *X. laevis* zygote/embryo over a time course period are acquired to *in situ* monitor the important biomolecules on the animal hemisphere and within the depths of a single intact spherical cell, and the further understanding is sought with regard to the lipid arrangement and variations through the embryo development at early stages.

3.3.4.1 Lipid composition in two hemispheres of the zygote

The animal pole and vegetal pole differs not only in colour, but also in the ways they divide and form different germ layers in the gastrulation following the development of the blastula. Of course, the transformation of the different parts of the cell is already encoded into genes, but would biomolecules like lipids also take apart in the biological progress? This experiment is designed to

detect chemical composition of the two hemisphere surfaces by carefully orienting certain sides of the samples onto a special sample holder. The SIMS spectra from the outer layer as well as the corresponding images were acquired to compare the lipids compositions and spatial distributions.

The +SIMS spectra from the animal and vegetal hemisphere of *X. laevis* zygote sampled 10 min post-insemination are present in Fig. 3.20 (a) and (b) respectively. Several main differences are found upon the comparison of the two spectra. Firstly, the animal pole spectrum [Fig. 3.20 (a)] shows the MAG at m/z 313.3⁺, 339.3⁺, cholesterol at m/z 369.4⁺, DAG in the range of m/z 500-650⁺ and TAG in the range of m/z 800-950⁺, while these ions are not obvious on vegetal pole spectrum [Fig. 3.20 (b)]. The existence of these fat components in the membrane of animal hemisphere might be related to the dark appearance in this side, as one study suggested the embryonic pigment requires to mix with fats intimately, probably physically not chemically [89]. Secondly, the two parts share some common ions -- the GPCho and SM fragments at m/z 86.1⁺, 104.1⁺, 125.0⁺, 184.1⁺, 224.1⁺ and GPCho molecular ions at m/z 760.5⁺, 782.9⁺. From the data acquired it can be seen that GPCho lipids are more intense on the vegetal pole than on the animal pole. The relative intensities of selected biomolecules (normalised to the total SI) on both sides are plotted in Fig. 3.21. It is clear that sodium intensities on both sides are in the same level around 1% indicating any salt suppression effects on either side could be counterbalanced. The dominant peak m/z 184.1⁺, representing GPCho and SM, accounts for 8.6% on the vegetal pole compared to 0.91% on the animal pole. Thirdly, m/z 430.5⁺ coming from vitamin E is more visible on the vegetal pole. As for the *X. laevis* egg, similar differences were observed on animal and vegetal spheres.

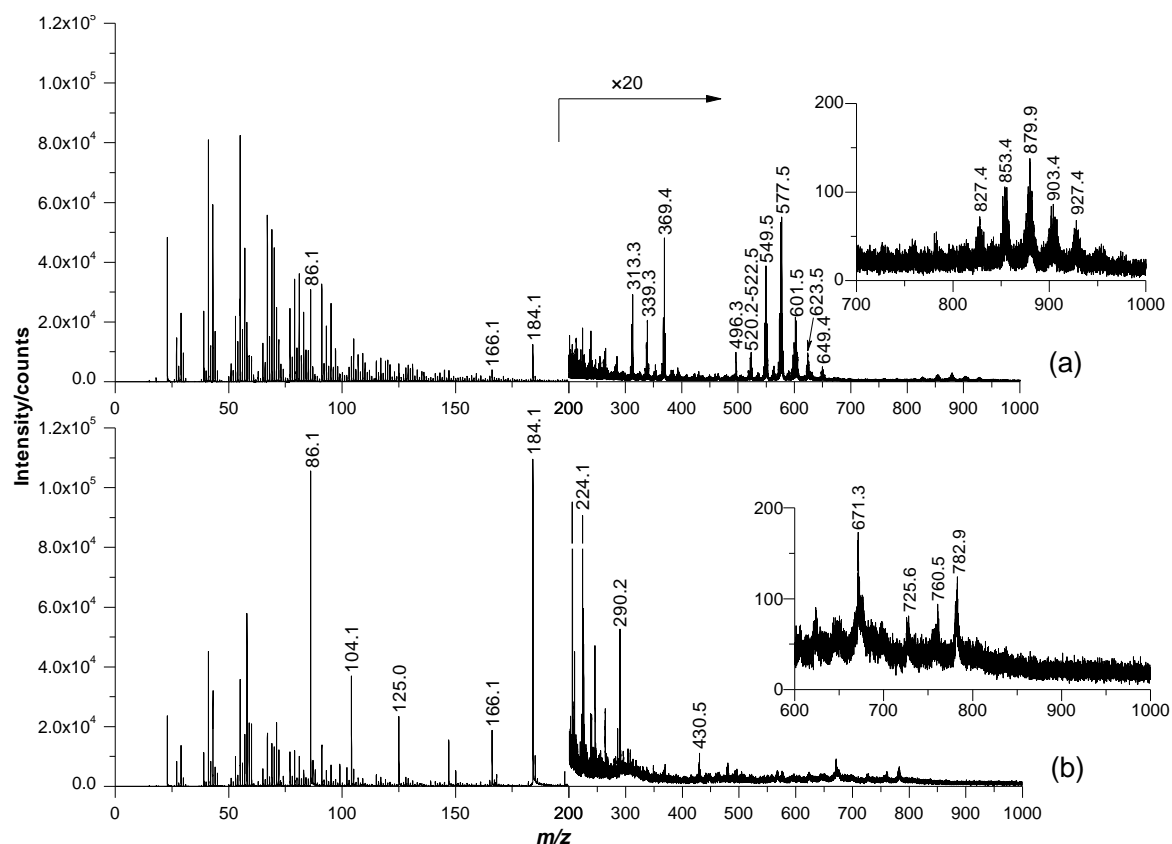


Fig. 3.20 +SIMS spectra of animal hemisphere (a) and vegetal hemisphere (b) of *Xenopus laevis* zygote 10 min post-insemination using the BioToF-SIMS. The spectral dose is 3.27×10^{10} ions/cm² with 20 keV Au₃⁺ PI beam over 600×600 μm² area of sample surface.

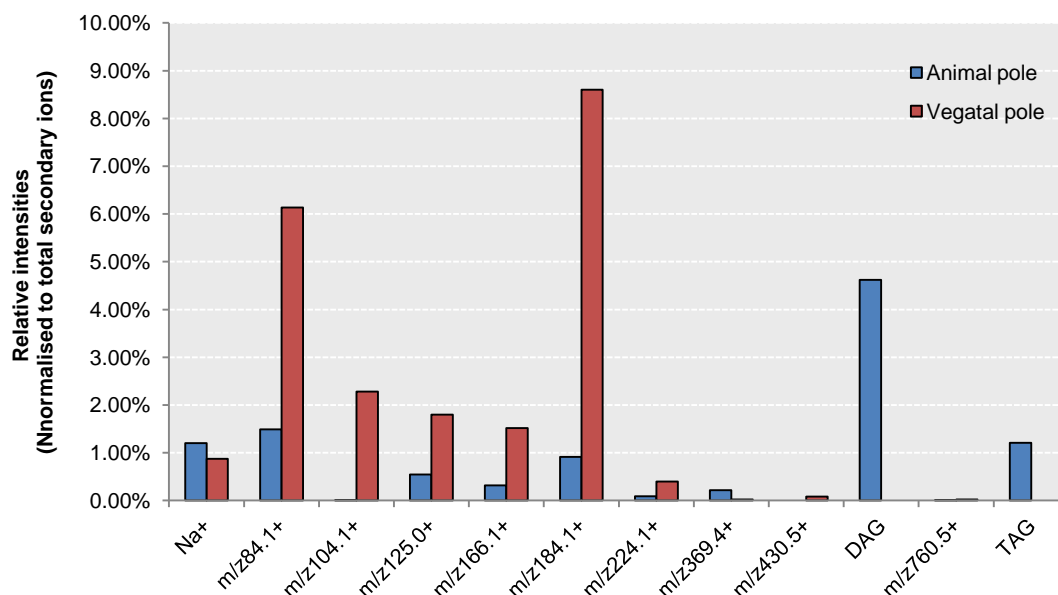


Fig. 3.21 Relative intensities of selected ions from the animal and vegetal hemispheres of *Xenopus laevis* zygote sampled 10 min after insemination using the BioToF-SIMS. The spectral dose is 3.27×10^{10} ions/cm² with 20 keV Au₃⁺ PI beam over 600×600 μm² area of sample surface. On the animal pole, the cholesterol at m/z 369.4⁺, total DAG(m/z 549.5-649.4⁺) and TAG (m/z 827.4-927.4⁺) are the major components; while GPCho/SM lipids fragments at m/z 86.1⁺, 104.1⁺, 125.0⁺, 184.1⁺, 224.1⁺ are dominant on the vegetal pole.

Furthermore, 2D chemical maps were generated to locate the major lipids on the animal hemisphere of the zygote sampled 10 min post-insemination as in Fig. 3.22. It is clear that GPCho/SM lipid fragments at m/z 86.1⁺, 104.1⁺, 125.0⁺, 184.1⁺, 224.1⁺ are concentrated in several spots in the size range 1-10 μm on the membrane. GPSer headgroup at m/z 185.10⁺ and GPGro headgroup at m/z 198.08⁺ are also concentrated in the spots area but less intense than m/z 86.1⁺ and 184.1⁺. MAG at m/z 339.3⁺ and cholesterol fragment at m/z 369.4⁺ cover the whole the surface evenly except for slightly elevated intensity in the right edge. DAG ions at m/z 549.5⁺, 577.5⁺, 603.5⁺ have a complimentary distribution with GPCho, GPSer and GPGro lipid fragments, as shown in the overlay image of ions m/z 184.1⁺ with m/z 577.6⁺.

The ion at m/z 184.1⁺ could be derived from phosphocholine lipids and SM. One feature of SM is long, largely saturated acyl chains which allow them to readily pack tightly together. It has been accepted that the tight acyl chain packing is the key feature of lipid raft organization [90]. The size of the lipid rafts and their stabilities are still not clear and has not been visualized in a biological membrane. Lipid rafts from a few nanometres to micrometres in size have been reported in the literatures [91, 92]. It is possible that the scattered spots on the animal hemisphere are lipid rafts, which may play important role in the process of fertilisation as to accommodating the protein with sperms receptor to function. The further studies in section 3.3.3.2 show more images of the zygotes sampled 10 min after fertilisation with spots scattered on the animal hemisphere. This indicates that the spots could be the sites of egg-sperm interaction and biomolecules identified on the spots area may anticipate in the dynamic process of the gametes fusion.

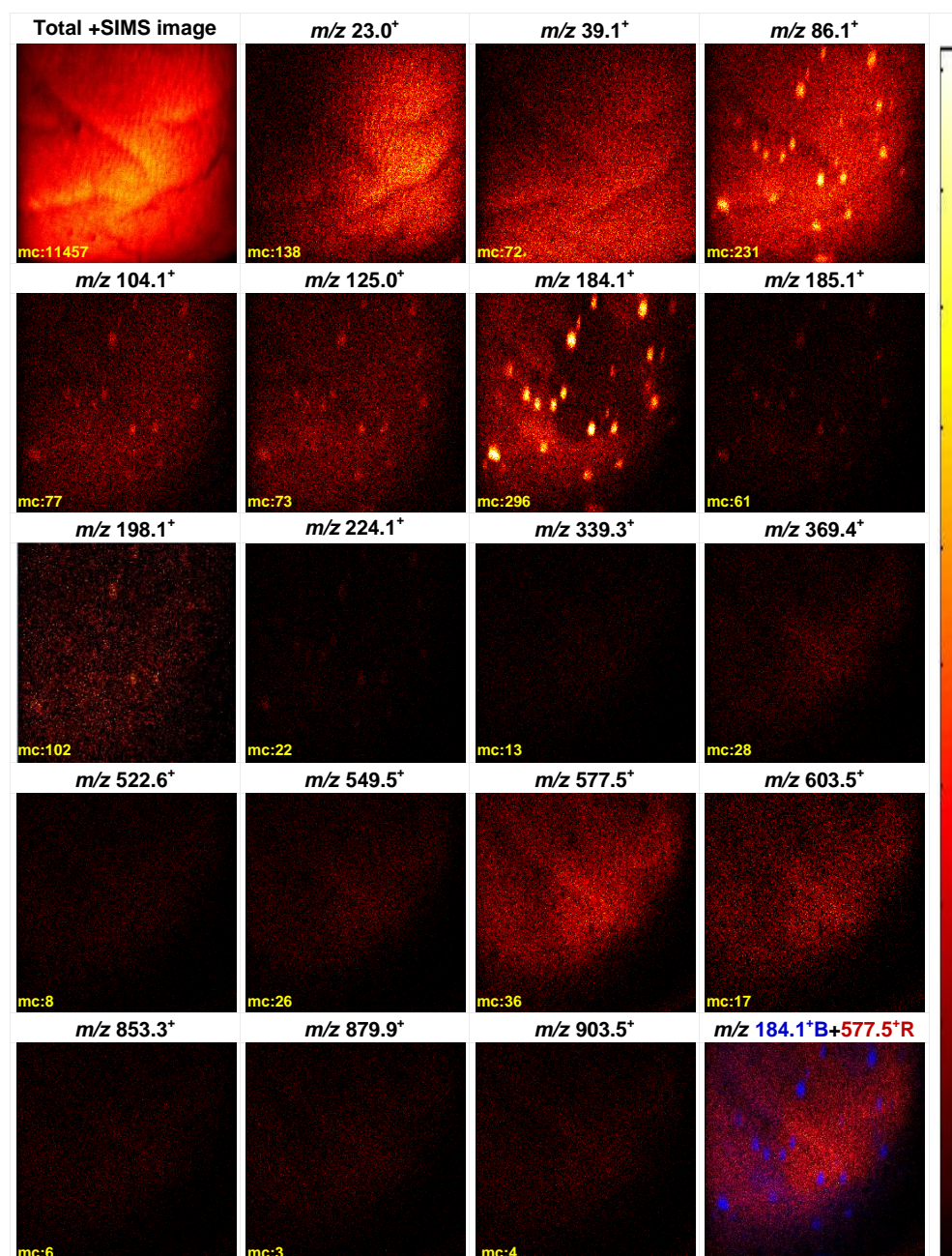


Fig. 3.22 Total positive ion and selected ion images (+SIMS) of the animal hemisphere of *Xenopus laevis* zygote 10 min after insemination using the BioToF-SIMS. Spectral dose is 3.27×10^{10} ions/cm² with 20 keV Au₃⁺ PI beam over 600×600 μm² surface of the zygote. Selected ions are as follows, Na⁺ at *m/z* 23.0⁺; K⁺ at *m/z* 39.0⁺; GPCho and SM fragments at *m/z* 86.1⁺, 104.1⁺, 125.0⁺, 184.1⁺, 224.1⁺; GPSer headgroup at *m/z* 185.10⁺; GPGro headgroup at *m/z* 198.08⁺; MAG at *m/z* 339.3⁺; cholesterol fragment at *m/z* 369.4⁺; phosphoglycerol (C18:0) at *m/z* 522.6⁺; DAG ions at *m/z* 549.5⁺, 577.5⁺, 603.5⁺; TAG ions at *m/z* 853.3⁺, 879.9⁺, 903.5⁺. The thermo scale corresponds to the ion intensity and the maximum counts (mc) per pixel can be read on the ion images.

3.3.4.2 Monitoring the lipids distribution on the animal hemisphere of zygotes sampled shortly after fertilisation

During the fertilisation and early embryo development, all the biological events are shown a sign on the animal hemisphere of the embryo, e.g., pigment granules moving to form colour contrast, membrane repacking into smaller parcels. The question arises, would these visible changes on the membrane also involve the biomolecular rearrangement? Very few *in vivo* image techniques such as photobleaching fluorescence is able to revealed the dynamic distribution of the lipids on the cell membrane [93], however, the chemical information is restricted to the lipid that can be fluorophore-

tagged. The work in this section aimed to visualize the various lipids distribution on a single intact zygote shortly after the fertilisation for understanding the morphologic changes in relation to the variation of chemical gradients, and accordingly possible functions of lipids during the fertilisation.

The zygotes 10, 20, 30 and 40 min after the insemination were analysed using the BioToF-SIMS with 20 keV C_{60}^+ PI beam to image the animal and vegetal hemisphere in both positive and negative ion mode. The \pm SIMS images of total ion and selected SI are shown in Appendix I because of the vast data set. Here just the most interesting images from the zygote 10 min after fertilisation are presented. As in Fig. 3.23, the zygote shows the scattered spots approx. 30-50 μ m on the animal hemisphere, which closely resembles the SEM images in Fig. 3.4 (a) regarding the study of fertilisation of *Rana pipiens* egg. In that SEM image the round patches with diameter of 20-40 μ m on the cell membrane indicate the sperm entry sites on the animal hemisphere of *Rana pipiens* egg fixed 10 min after fertilisation. Although there was one report using SEM to study the morphological changes of *X. laevis* egg surface during fertilisation and early embryo development, no images were produced to show the sperm entry and fusion site [3]. The further investigation of unfertilised eggs revealed that no such features as scattered spots appeared on the animal sides and the phosphocholine lipids are distributed evenly on the uniform surface. Thus, it is highly likely that the SIMS images in Fig. 3.23 shows the egg-sperm fusion sites. Within the spot areas, most abundant ions are m/z 86.1⁺, 104.1⁺, 125.0⁺, 166.1⁺, 184.1⁺ in +SIMS and m/z 63.0⁻, 78.9⁻ in -SIMS, indicating that mainly GPCho and SM lipids are located within the spots.

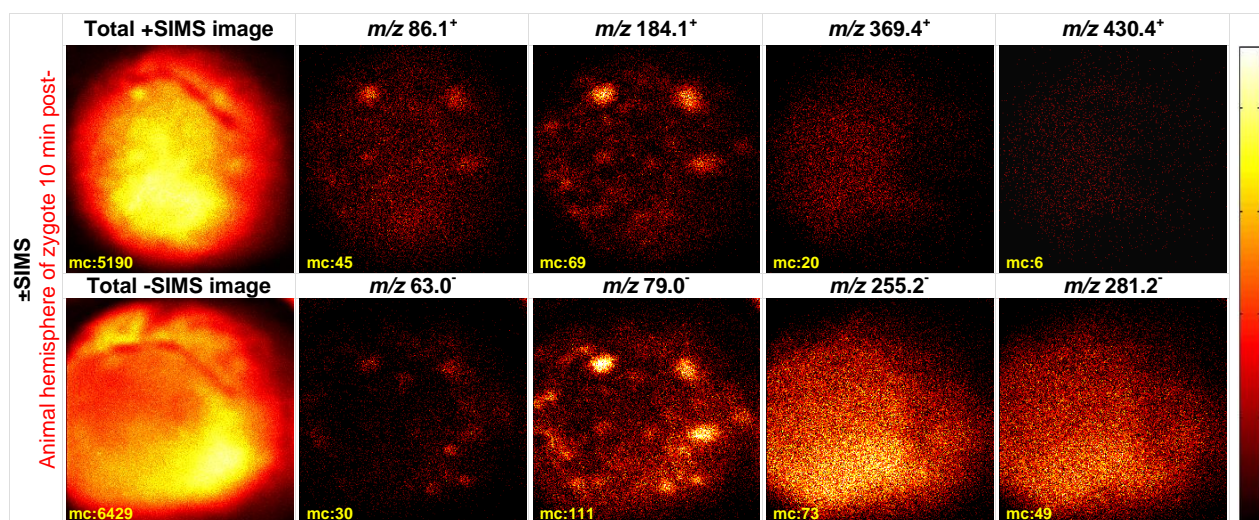


Fig. 3.23 Total ion and selected ion images (\pm SIMS) of the animal hemisphere of *Xenopus laevis* zygote 10 min post-insemination using the BioToF-SIMS. The PI dose is 2.78×10^{10} ion/cm² with 20 keV C_{60}^+ PI beam over $939 \times 939 \mu\text{m}^2$ with 256×256 pixels. Selected ions are as follows, GPCho and SM at m/z 86.1⁺, 184.1⁺; cholesterol at m/z 369.4⁺; vitamin E at m/z 430.4⁺; PO_2^- at m/z 63.0⁻; PO_3^- at m/z 79.0⁻; fatty acids at m/z 255.2⁻ (C16:0) and m/z 281.2⁻ (C18:1). At least 5 zygotes at each time point were investigated to identify any common phenomenon on the animal hemisphere shortly after the fertilisation. At 10 min after fertilisation, most zygotes showed the scattered spots on the animal hemisphere. Within the spots area, most abundant SIs are m/z 86.1⁺, 104.1⁺, 125.0⁺, 166.1⁺, 184.1⁺ in +SIMS and m/z 63.0⁻, 78.9⁻ in -SIMS, indicating that the spots are mainly filled with GPCho and SM lipids. The sizes of the spots are approx. 30-50 μ m calculated by counting the pixels across the spots that is larger than those in Fig. 3.22. The thermo scale corresponds to the ion intensity and the maximum counts per pixel can be read on the ion images.

Compared with Fig. 3.22 which also shows the spotty surface of the zygote 10 min post-insemination, the spots sizes are smaller than those in Fig. 3.23. The reason could be that the individual differences of *X. laevis* eggs induce variation in the fertilisation progress. The study of

fertilisation in *X. laevis* using light microscopy and SEM has revealed that even within the same batch of eggs, fertilisation still occurs at significantly variable time [42]. Moreover, the fertilisation event does contain several consecutive steps as mentioned in the Introduction. It can be speculated that the smaller dots on the egg animal side in Fig. 3.22 show the very early sperm-egg incorporation, *i.e.*, the sperms just binding to the animal hemisphere. Subsequently the gametes membrane fusion happens with more adjacent areas involved, thus in Fig. 3.23 the larger patches appear as on the zygote animal side.

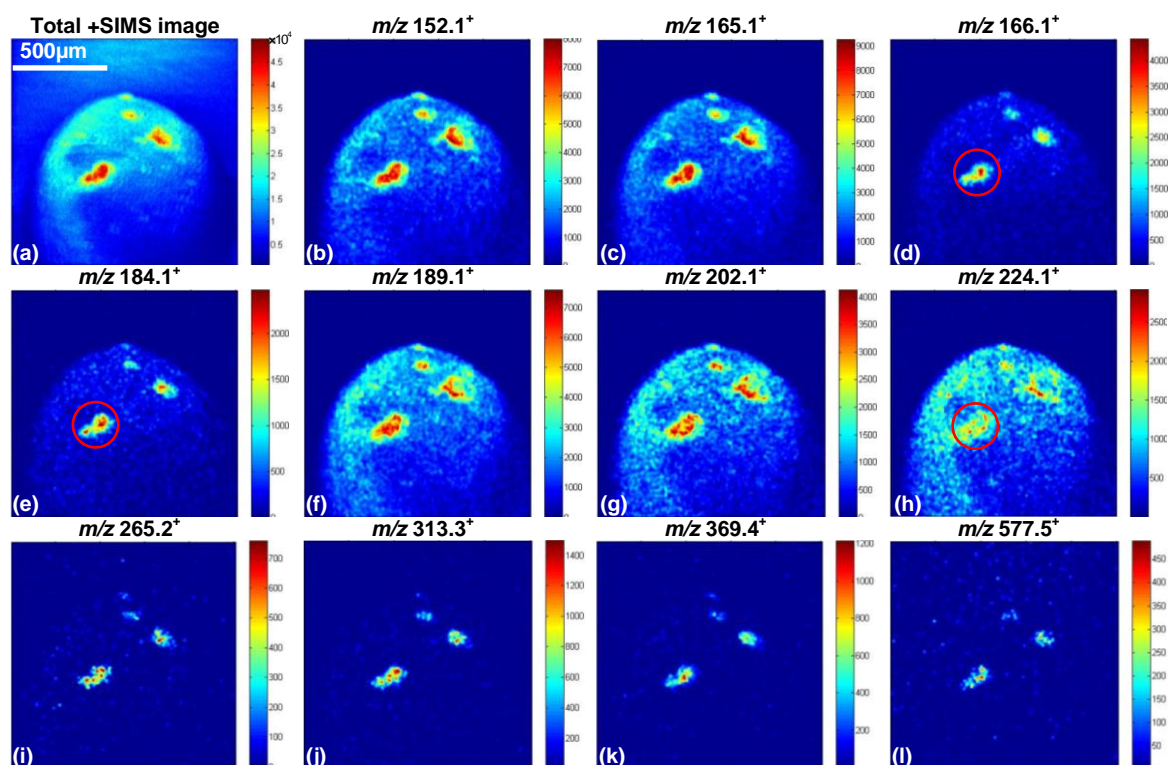


Fig. 3.24 Total ion and selected ion images (+SIMS) of the animal hemisphere of *Xenopus laevis* zygote 10 min post-insemination using the J105 3D Chemical Imager. Spectral dose is 5.33×10^{13} ions/cm² using a 4 µm-focused 40 keV C₆₀⁺ PI beam over 1200×1200 µm² with 256×256 pixels. The patches on the zygote surface are possible sperm and egg fusion sites. *m/z* 165.1⁺ is a common glycerophospholipids fragment; GPCho and SM share the fragments at *m/z* 166.1⁺, 184.1⁺, *m/z* 224.1⁺ is unique to GPCho, *m/z* 265.2⁺ is only for SM; MAG at *m/z* 313.3⁺; cholesterol fragment at *m/z* 369.4⁺; DAG ions at *m/z* 577.5⁺; *m/z* 152.1⁺, 189.1⁺ and 202.1⁺ are unassigned ions. The colour scale corresponds to the ion intensity and the counts can be read on the scale bar.

Owing to the severe sensitivity limitation, the C₆₀⁺ PI beam installed in the conventional BioToF-SIMS could not be focused down to a very small size for high resolution imaging. Therefore the further investigation employed the J105 that uses a DC C₆₀⁺ PI beam to explore more details of the biological process with micron scale resolution. Of particular interest, the zygote fixed at 10 min post-insemination was analysed using a 4 µm-focused 40 keV C₆₀⁺ PI beam, yielding high lateral resolution images over the animal hemisphere of the zygote as shown in Fig. 3.24. The overall morphology is clearly seen in the total ion image. Several patches with sharp outlines are scattered on the zygote surface indicating the possible gametes fusion sites. The abundant biomolecules residing within these patches are mapped cross the animal side of the zygote as in the diagnostic SI images, revealing the varying distribution patterns for different lipids. The common fragment *m/z* 165.1⁺ shared by all glycerophospholipids spread into the whole patch areas; *m/z* 166.1⁺ and 184.1⁺ from GPCho and SM condense in the middle of the patches especially in one patch marked

with a red circle in Fig. 3.24 (d, e); GPGro at m/z 189.1⁺ is spread around the spots; an unidentified ion at m/z 202.1⁺ and GPCho ion at m/z 224.1⁺ appear to circle the patches in Fig. 3.24 (g, h), while another SM fragment at m/z 265.2⁺ [Fig. 3.24 (i)] is dense within the circle of m/z 224.1⁺; the other components such as MAG at m/z 313.3⁺, cholesterol at m/z 369.4⁺ and DAG at m/z 577.5⁺ are concentrated in the centre of the patches as in Fig. 3.24 (j, k, l).

The spatial locations of different biomolecules could reflect their certain functions during the membrane fusion. With further PCA analysis, more distribution difference of various lipids is pulled out as shown in Fig. 3.25. The biomolecules peaks labelled in PC 2 loading are mainly responsible for spatial distribution of the features in the SIMS images shown in Fig. 3.24, particularly the DAG ions at m/z 549.5⁺, 577.5⁺, and 603.5⁺, and MAG ions at m/z 313.3⁺, 339.3⁺ and cholesterol at m/z 369.4⁺. GPEtn lipid ion at m/z 124.1⁺ and m/z 142.1⁺ is also located in the fusion site, along with the other familiar lipids GPCho and SM at m/z 166.1⁺, 184.1⁺, m/z 224.1⁺ and m/z 265.2⁺. The ions at m/z 152.1⁺, 178.1⁺, 189.1⁺ and 239.0⁺ are unassigned.

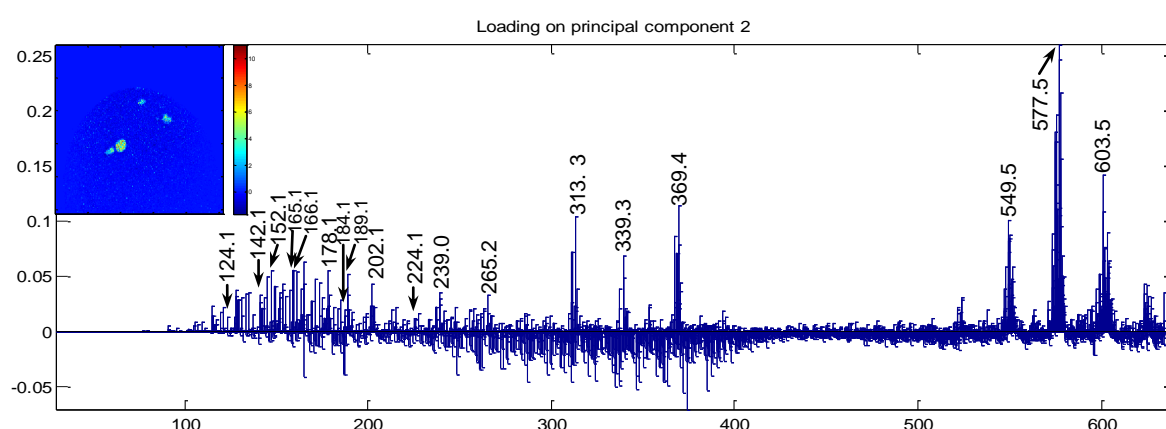


Fig. 3.25 PCA plot of SIMS data of single *Xenopus laevis* zygote 10 min post-insemination. Inset is PC 2 image. The features of fusion site on the animal pole of the zygote are pulled out, and biomolecules located in the fusion sites are labelled.

The variation of identified ions residing in the fusion sites was further analysed in detail by line scanning across one patch as schematically shown in Fig. 3.26 (a). In total 10 scans were made with 10×3 pixels each line. Relative intensities of selected SIs (normalised to the maximum intensity of each ion respectively) cross the scanning site were plotted in Fig. 3.26 (b), including GPEtn fragment at m/z 142.1⁺, the common fragments of GPCho and SM at m/z 166.1⁺, 184.1⁺, m/z 224.1⁺ exclusive to GPCho, m/z 265.2⁺ only for SM, cholesterol fragment at m/z 369.4⁺ and DAG ions at m/z 577.5⁺. The plot indicates that the m/z 577.5⁺ (DAG ion) is most intense in the region of L6 lying the middle of the fusion site, and drops in both sides to approx. 40% of its original intensity at the L5 and L7, then both increase to approx. 65% in the L3 and L8 and drop to nearly 0 in the L1, L2, L9 and L10. The m/z 369.4⁺ (cholesterol) is nearly 0 at the beginning, and then increases suddenly at the L4. It keeps stable in the region L4 to L8 ranged over 80% though some fluctuations and reduces after L8. In contrast to m/z 369.4⁺ and m/z 577.5⁺, m/z 166.1⁺ and 184.1⁺ (common fragments of GPCho and SM) are in the reverse trend in region of L3 to L9. When m/z 369.4⁺ and m/z 577.5⁺ are high, m/z 166.1⁺, 184.1⁺ are low, and vice versa. Away from the region of L3 to L9, both ions drop slightly but still above 20% of their original intensities. The ion at m/z 265.2⁺ (a diagnostic ion of SM) has a very similar trend to m/z 166.1⁺, 184.1⁺ in relative intensity. However, the relative intensity trend of m/z 224.1⁺ (unique ion to GPCho) is slightly

different to m/z 166.1⁺, 184.1⁺, 265.2⁺. It increases gradually from L5 to L7, while the others ions all drop at L6, then drastically drops and an increase happens in both sides away from the region of L5 to L7 with high levels in L2 and L9 where the other three ions are in low levels. The ion at m/z 142.1⁺ (GPEtn fragment) keeps almost at its high level of 80% to 100% in the region L5 to L8, and then decrease radically in both direction away from the region of L5 to L8 to 0 at L4 and 20% at L9. Combined with single SI images in Fig. 3.24, the pattern of SI changes across the scanning area implies circular distribution patterns of the biomolecules. GPCho is in the outer circle of fusion site, then a layer of cholesterol and DAG components lie inside, in the following GPEtn and SM build another circle towards the fusion centre, DAG is most abundant in the centre coexisting with GPCho and GPEtn.

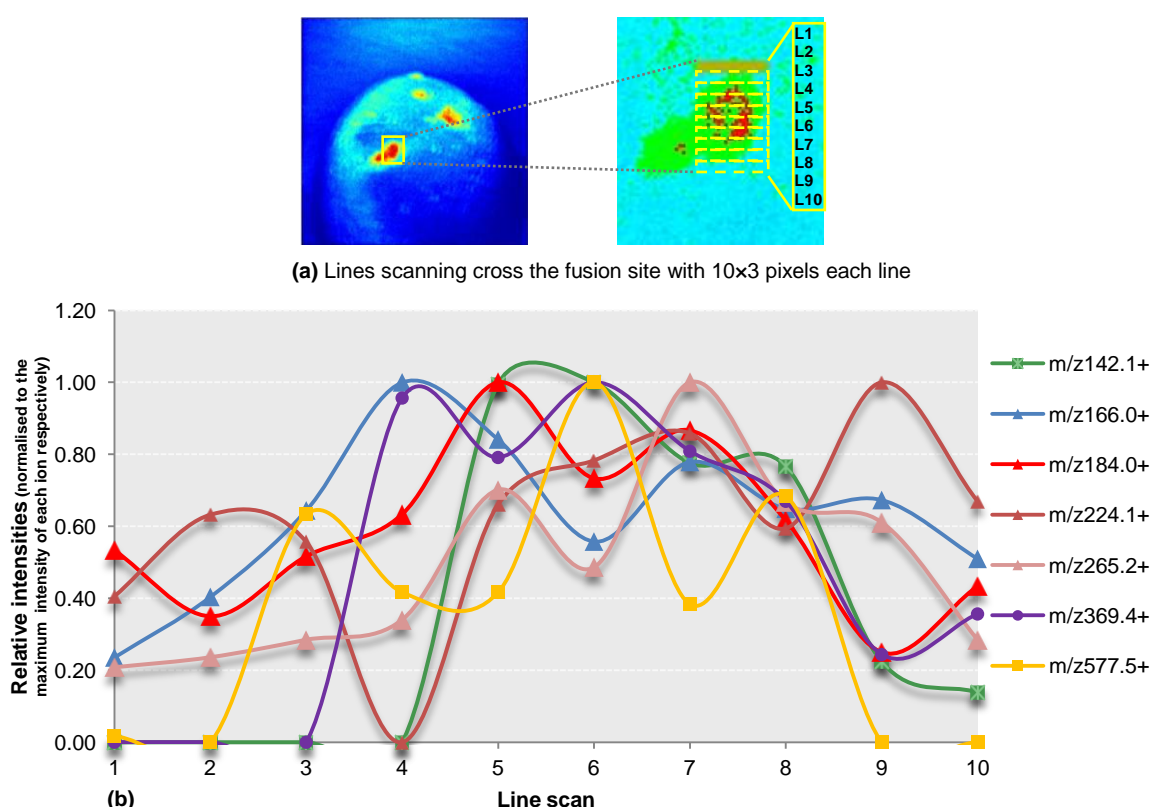


Fig. 3.26 Changes of selected ions across one gametes fusion site on the animal hemisphere of *Xenopus laevis* zygote 10 min post-insemination. (a), illustration of line scanning across one fusion site. In total 10 scanning were made with 10x3 pixels each line; (b), relative intensities of selected SIs across scanning site. The ion intensities are normalised to the maximum intensity of each ion respectively. Selected ions are GPEtn at m/z 142.1⁺, the common fragments of GPCho and SM at m/z 166.1⁺, 184.1⁺, m/z 224.1⁺ is unique to GPCho, m/z 265.2⁺ is only derived from SM; cholesterol fragment at m/z 369.4⁺; DAG ions at m/z 577.5⁺. The tendency of SI changes in the whole scanning area implies a circular structure at fusion site with GPCho in the outer layer, then a layer of cholesterol and DAG components inside, GPEtn and SM form another circle towards the fusion centre and the highest level of DAG in the centre coexisting with GPCho and GPEtn.

Membrane fusion is a profound biological process likely involving lipid rearrangement and possible synthesis initially. Considering that DAG can be rapidly phosphorylated to phosphatidic acid (GPA) which is a commitment step in phospholipid biosynthesis [94, 95], it is speculated that in the centre of the fusion site phospholipase-mediated hydrolysis of SM occurs to generate DAG [96], which quickly builds new lipids such as GPEtn and GPCho to stop the dissolving of the membrane induced by the sperm binding. GPEtn is able to form highly curved structure that could be used to seal a space inside the fusion centre for the release of sperm nucleus. Most synthesized GPCho is

transported away from the centre to form the outer layer of the fusion site. This proposed model involving lipids synthesis and rearrangement can well explain the distribution pattern of selected SIs, *i.e.*, DAG has high relative intensity exclusively in the fusion centre along with low level of SM, GPEtn just exists in the fusion centre and GPCCho is lower in the centre and higher away from the centre. Cholesterol is more evenly distributed over a wider range than DAG to stabilize the newly-formed membrane.

In order to investigate the fusion progression beneath the surface, depth profiling was further performed on the zygote. The 3D view of the total ion images and a SI image of m/z 165.1⁺ are shown in Fig. 3.27 (a, b). These reveal that the fusion sites penetrate the cell membrane and expand to ring-like structures with depth. At this point, it is difficult to identify which fusion site is truly the gametes fusion site with the sperm nucleus being released to the egg. Amphibians contain two groups of mechanisms exhibiting very different blocks to polyspermy [97]. One is a fast electrical block before second sperm-egg fusion by cortical granule exocytosis at fertilization envelope [98]. Another is a slow process that occurs in the egg cytoplasm after the sperms entry, allowing only a single sperm nucleus with a single centrosome to ultimately participate in embryonic development, while the other sperm nuclei and centrosomes degenerate before cleavage. It is likely that the slow block occurs in the sampled zygote as several fusion sites penetrating the *X. laevis* egg membrane as shown in Fig. 3.27.

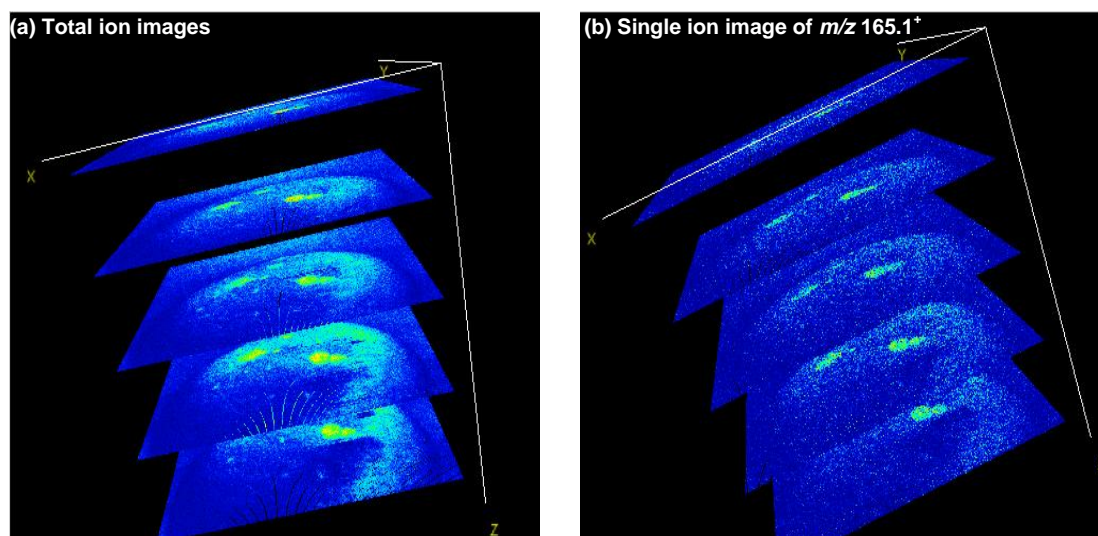


Fig. 3.27 3D visualization of depth profile of *Xenopus laevis* zygote 10 min post-insemination using the J105 3D Chemical Imager. The view of total ion profiles in (a) and single ion m/z 165.1⁺ in (b). The depth profiling was performed on the animal hemisphere. Each depth had a dose of 1.07×10^{13} ions/cm² with 4 μ m-focused 40 keV C₆₀⁺ PI beam over 1200×1200 μ m² area at 256×256 pixels. The 3D viewing shows that the *X. laevis* gametes fusion progressed through the etch depths.

To test whether the phenomenon shown in Fig. 3.22, Fig. 3.23 and Fig. 3.24 is caused by any possible artefacts, *e.g.*, incorrect manipulation of samples or artificial activation of the egg, a control group of the *X. laevis* eggs were pricked in 3 areas on the top of the animal hemisphere of *X. laevis* eggs by a microinjection needle which was to simulate the egg activation. The pricked eggs were incubated 5, 10 min under the same condition as the normal fertilised eggs, and the further sample preparation for SIMS analysis was identical to one used for the zygotes 10 min post-insemination analysed previously. The corresponding lipids distribution on the control group eggs was imaged using the J105, which reveals totally different morphology on the egg surfaces as shown in

Fig. 3.28. At 5 min after pricking the sample membrane appears sagged in the pricked area with three clear holes [Fig. 3.28 (a)]. Major fragment of phosphocholine lipids at m/z 184.1⁺ concentrates around the wounded areas but forming broader patches in Fig. 3.28 (b) compared with those in Fig. 3.24 (e). The sample at 10 min after pricking shows the ruptured membrane in the wounded area [Fig. 3.28 (f)] with phosphocholine lipids surrounding the pricked area [Fig. 3.28(g)] and cholesterol, vitamin E and DAG ions condense in the middle [Fig. 3.28 (h, i, j)]. The morphology of the control eggs indicates this kind of egg activation causes broader congregation site of phosphocholine and additional physical damages to membrane integrity and continuity, which show little similarities to the real sperm-egg fusion site. It can be concluded that the patches on the animal hemisphere of zygote 10 min post-insemination shown in Fig. 3.22, Fig. 3.23 and Fig. 3.24 are not fake activation or the artefact by accidental damage during manipulation of samples but the sites where gametes fusion was occurring.

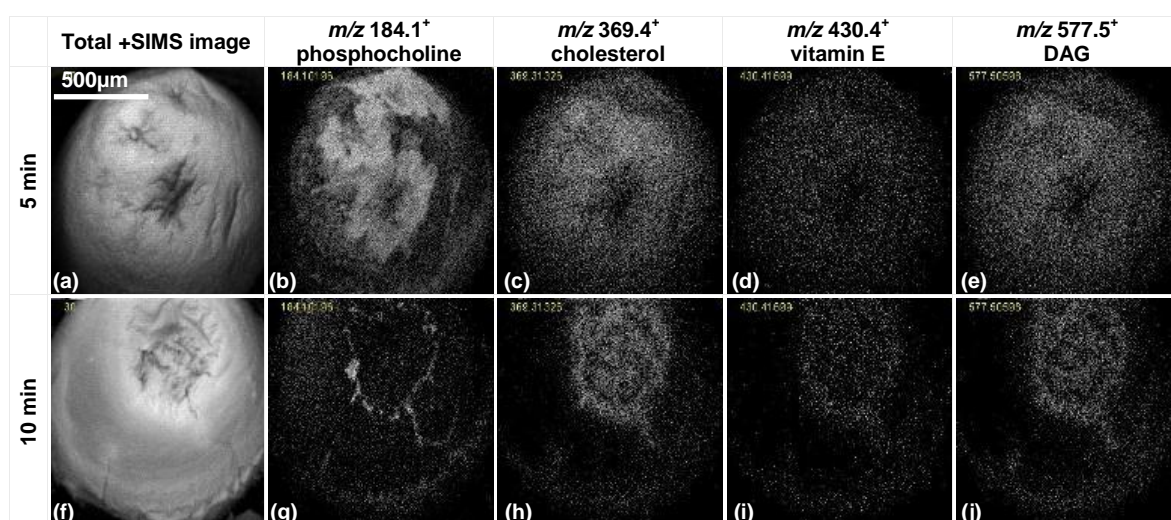


Fig. 3.28 Total ion and selected ion images (+SIMS) of the animal hemisphere of *Xenopus laevis* egg control samples using the J105 3D Chemical Imager. Spectral dose is 1.70×10^{13} ions/cm² with a 4 µm-focused 40 keV C₆₀⁺ PI beam over 1200×1200 µm² area with 256×256 pixels. The eggs were pricked with microinjection needle and sampled 5 min and 10 min after poking with the exactly same sample preparation as *X. laevis* zygote sampling. The morphology of the control eggs indicates this kind of egg activation causes damages to membrane integrity and continuity, and leaves the obvious physical wound on the membrane surface.

3.3.4.3 Subcellular signalling upon the fertilisation of *Xenopus laevis* eggs

Two approaches were used in this section to study the subcellular signalling upon the fertilisation of *X. laevis* egg, one is depth profiling on an intact cell, and another is analysis of serial sections of a single cell. This was for investigate the most profound signalling upon the fertilisation, calcium and IP3 flux. These two molecules have diagnostic peaks in +SIMS, m/z 40.0⁺ for Ca⁺ and m/z 129.1⁺ ([C₆H₁₀O₃]⁺) for IP3.

Depth profiling was performed on the animal hemisphere of a single *X. laevis* zygotes 10 min post-insemination using BioToF-SIMS by alternately etching the surface with 20 keV C₆₀⁺ PI beam and then analysing with the 20 keV Au₃⁺ PI beam to detect the Ca²⁺ and IP3 flux beneath the membrane. The relative intensity changes of selected ions against the etch dose are plotted in Fig. 3.29. With the erosion of the zygote surface, the phosphocholine lipids and cholesterol changes dramatically. The relative intensities of the cholesterol ion at m/z 369.4⁺, MAG ions at m/z 313.3⁺ and DAG ions at 549.5⁺, 577.5⁺ and 603.5⁺ increase at different levels. The ions at m/z 369.4⁺, 549.5⁺, 577.5⁺

increased by over 4 times with the highest increase of ion m/z 577.5⁺ by over 6 times; while the intensity of phosphocholine lipid fragments at m/z 86.1⁺, 104.1⁺, 184.1⁺, 224.1⁺ and GPEtn fragment at m/z 124.1⁺ decreases as they are etched away during sputtering. The ion at m/z 184.1⁺ which falls to half of its initial intensity at the sixth etch and one quarter at the tenth etch indicating that the membrane bilayer was etched away gradually. The intensity of the IP3 fragment, m/z 129.1⁺, remains steady until the etching dose reaches 8.44×10^{14} ions/cm² at sixth etch where the intensities of all phosphocholine lipid fragments drop about 50%, and then increases quickly for the following two etch cycles before becoming stable again. This might be because after the sixth etch, the cytoplasm membrane was penetrated so that IP3 flux under the membrane was exposed for detection. The Ca⁺ ion also has the same trend as the IP3 fragment but with less increase. The DAG fragment at m/z 549.5⁺, 577.5⁺ and 603.5⁺ increase steeply after the sixth etching, indicating the membrane components have a significant change at this point.

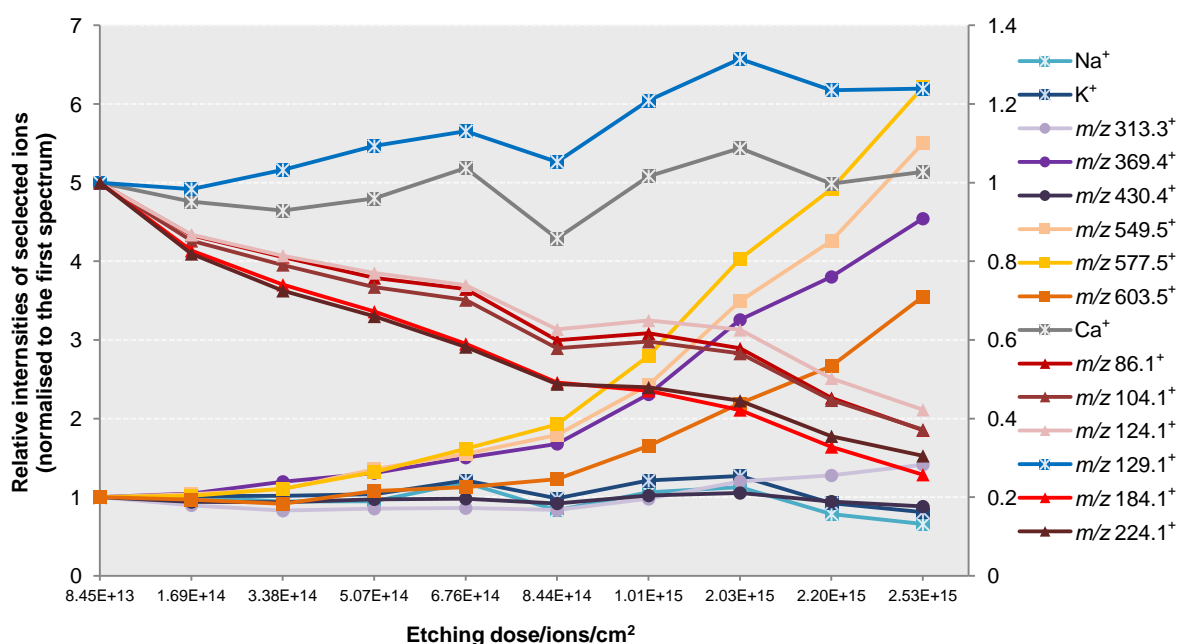


Fig. 3.29 Changes of selected ions during depth profiling of *Xenopus laevis* zygote 10 min post-insemination using the BioToF-SIMS. C₆₀⁺ PI beam was used for etching in an area of $800 \times 800 \mu\text{m}^2$ with a dose of 1.69×10^{14} ions/cm² while Au₃⁺ PI beam for analysis over $300 \times 300 \mu\text{m}^2$ with a dose of 1.72×10^{11} ions/cm². The data lines for ions Na⁺, K⁺, MAG at m/z 313.3⁺, cholesterol at m/z 369.4⁺, vitamin E at m/z 430.4⁺, DAG at m/z 549.5⁺, 577.5⁺ and 603.5⁺ are in the left y axis; for Ca⁺, phosphocholine lipids at m/z 86.1⁺, 104.1⁺, 124.1⁺, 184.1⁺ and 224.1⁺, IP3 at m/z 129.1⁺ are in the right y axis.

According to the experimental data, freeze-dried small cells with approx. 20 μm in width and 4 μm in depth can be sputtered away using an the etch dose of 10^{15} ions/cm². The C₆₀⁺ ion dose between the sixth and seventh etches is from 8.44×10^{14} to 1.01×10^{15} ions/cm², which indicates that the zygote membrane could be etched away. However, it is necessary to perform further investigation using other technique to confirm the etch depth and morphologic change of the zygote membrane. Owing to the topography and quite large size, AFM and SEM are not suitable for investigating the zygote surface. A built-in white light microscope might offer the opportunity to do such analysis following SIMS experiment, which is a future direction of the instrument development.

To etch away the whole of a cell like *X. laevis* zygote will require impractical analysis time using either SIMS instrument. The other alternative method, serial sectioning of a single zygote 10 min post-insemination, was therefore adopted to expose the subcellular structure for the location of IP3

and biomolecules. A total of 19 sections (numbered S01 to S19) were collected from a zygote 10 min after fertilisation in an order from animal pole to vegetal pole. All the sections were subjected to analysis using the J105. Before collecting the data, sputter cleaning with the C_{60}^+ beam were performed on all sections at a dose of 10×10^{13} ions/cm² over $1200 \times 1200 \mu\text{m}^2$ to remove possible surface contamination. With the exception of sections S01 and S07 which were found cracked in the vacuum and sections S18 and S19, which experienced charging issues, images and spectra were successfully acquired from the other sections.

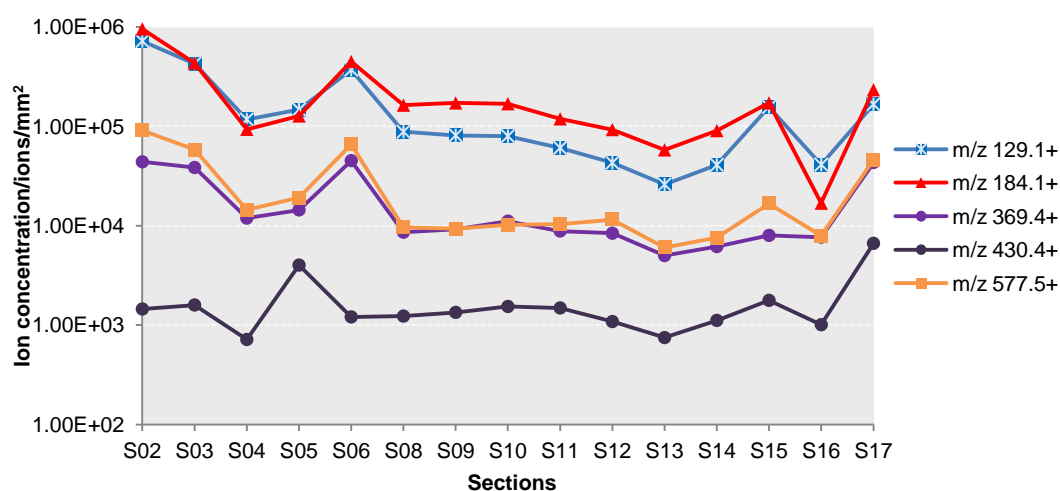


Fig. 3.30 Changes of ion concentrations of selected ions in serial sections of *Xenopus laevis* zygote 10 min post-insemination using the J105 3D Chemical Imager. The zygote was sectioned into total 19 pieces. S01, 07, 18 and 19 were omitted due to sample damage or charging. Each section was cleaned with 40 keV C_{60}^+ PI beam over $1200 \times 1200 \mu\text{m}^2$ with a dose of 10×10^{13} ions/cm². The analysis is performed with a 4 μm -focused 40 keV C_{60}^+ PI beam over $1200 \times 1200 \mu\text{m}^2$ with a dose of 4.26×10^{13} ions/cm² at 256×256 pixels. The ion concentrations are calculated by dividing the total counts of selected ions by the area of the individual section. The selected ions are as follows, IP3 fragment at m/z 129.1⁺; phosphocholine lipids fragment at m/z 184.1⁺; cholesterol fragment at m/z 369.4⁺; vitamin E at m/z 430.4⁺; DAG at m/z 577.5⁺.

Ion intensities of m/z 129.1⁺ and other selected ions of interest are divided by the area of individual section to calculate ion concentration (ions/cm²) at each section as plotted in Fig. 3.30. The area of the section is calculated by measuring the number of pixels of the section diameter in the x and y directions and using the average diameter to calculate the area. The ion concentrations of selected species vary in the different sections. The concentration of m/z 129.1⁺ (IP3 fragment) has the highest concentration in the S02, and then fluctuates down and up and then remains stable until S10 and S11, the sections after S11 showing an apparent trend of slightly decreasing and in the last 3 sections, there is a fluctuation of up-down-up. The IP3 wave starts from the egg and sperm fusion site only occurred in the membrane of the animal side [99]. This could explain why section S02 from the animal side has highest concentration of IP3, as this could close to the sperm entry site where the IP3 flux initiated. In general the sections after S11 on the vegetal side have lower concentrations, because the wave of the IP3 takes 5 min after sperm entry to reach the highest peak and cross the whole egg [16, 17]. The zygote was sampled 10 min after fertilisation when the sperm was entering, so that the concentration gradient could be seen. However, it is not clear why the IP3 concentration fluctuates in the last few sections, and even at the same level as in S08-10 from the animal side. Other biomolecules of interest are also plotted in the Fig. 3.30. Phosphocholine lipid fragment m/z 184.1⁺ follows a similar trend as the IP3, cholesterol fragment at m/z 369.4⁺, vitamin E at m/z 430.4⁺ and DAG at m/z 577.5⁺ almost remain stable in the whole

sections. However, there are very similar trends such as the decrease at S04 and increase at S06 (except m/z 430.4⁺, which increased in S05) and fluctuation in the final three sections. It is possibly that the intensities changes reflected the changes of focusing and extraction from the surface which induced by the sample topography.

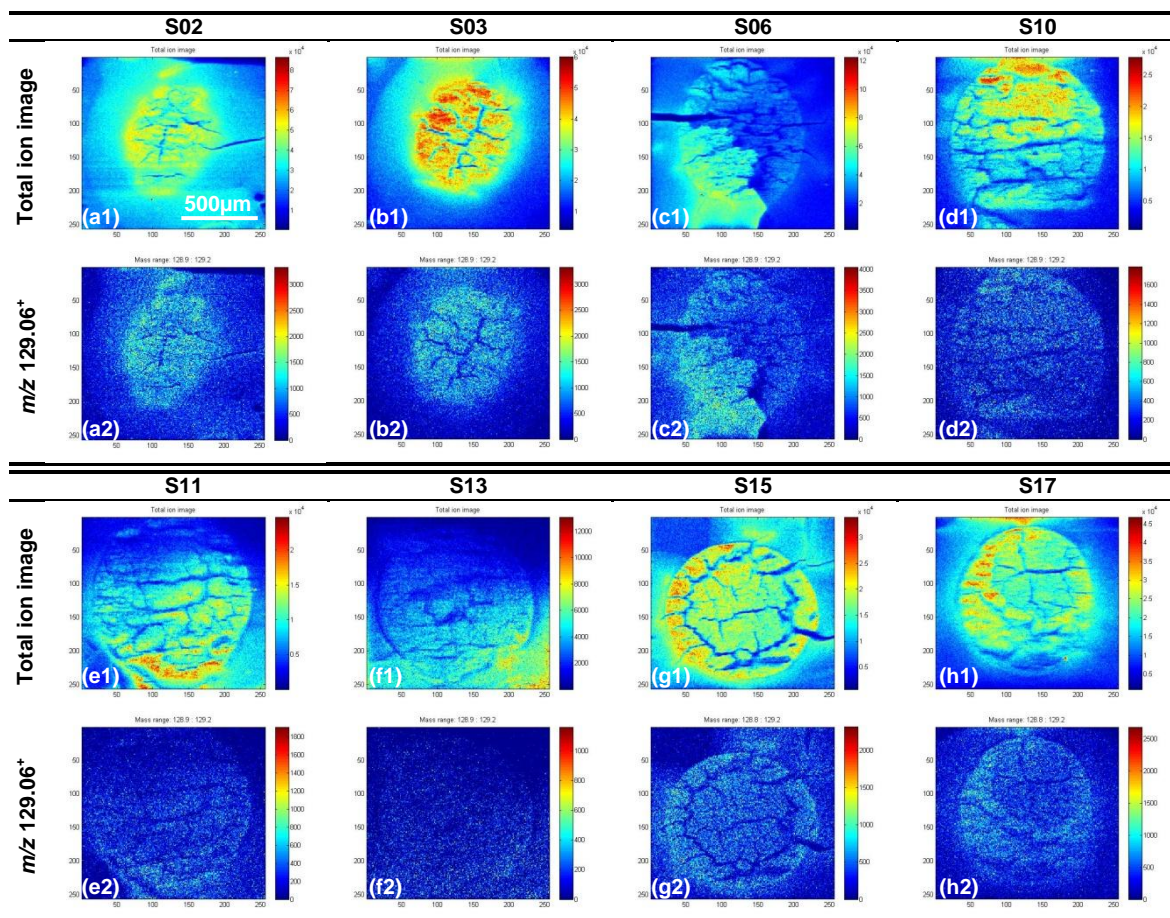


Fig. 3.31 Total ion and selected ion images (+SIMS) in serial sections of *Xenopus laevis* zygote 10 min after fertilisation using the J105 3D Chemical Imager. Each section was cleaned with 40 keV C_{60}^{+} PI beam over $1200 \times 1200 \mu m^2$ with a dose of 10×10^{13} ions/cm². The analysis is performed with a 4 μm -focused 40 keV C_{60}^{+} PI beam over $1200 \times 1200 \mu m^2$ with a dose of 4.26×10^{13} ions/cm² at 256×256 pixels. The colour scale corresponds to the ion intensity and the counts can be read on the scale bar. m/z 129.1⁺ represent IP3 fragment.

The total ion images and distribution of IP3 for each section are shown in Fig. 3.31. Except for S06, the distributions in the sections of animal side are almost homogeneous, and in S17, it spreads like a ring pattern. As shown in the images, the sections were cracked in the vacuum environment of the instrument, this could cause the chemicals diffuse, but the amount of the chemicals should not change in each section, which ensures the ion concentrations calculated in Fig. 3.30 reflect the average level selected species in each section

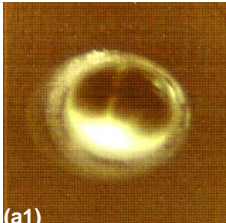
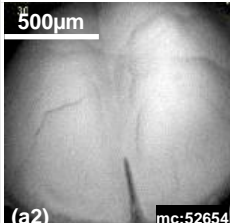
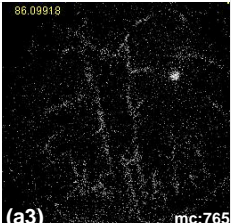
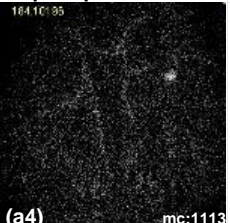
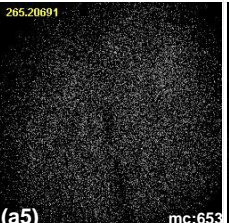
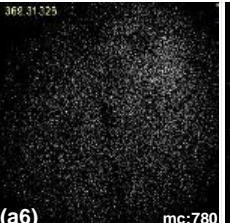
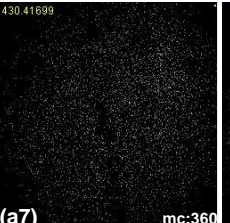
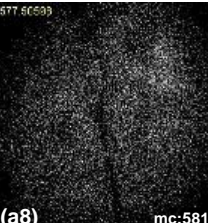
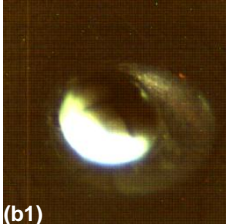
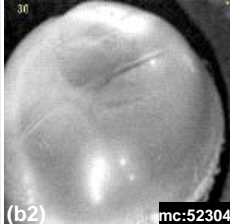
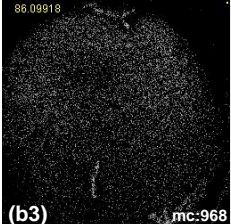
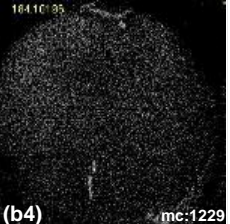
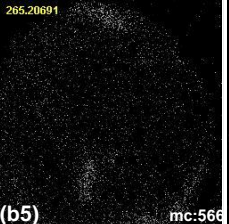
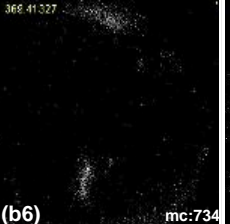


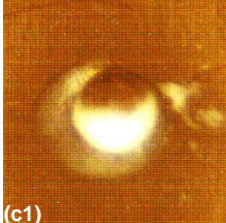

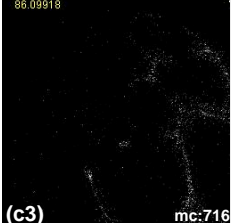
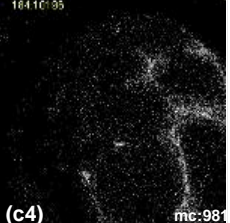
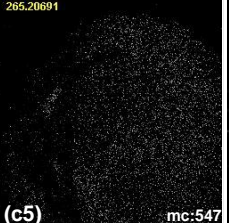
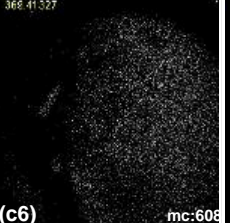
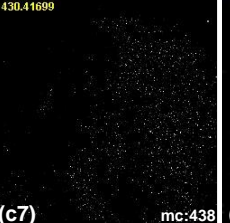
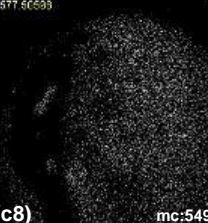
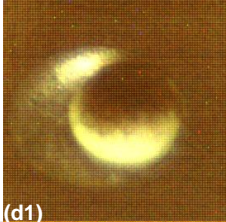
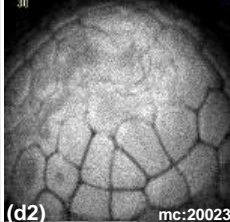
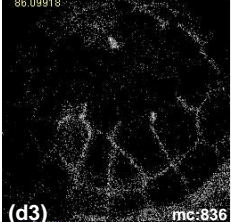
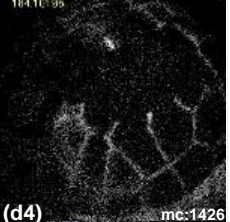
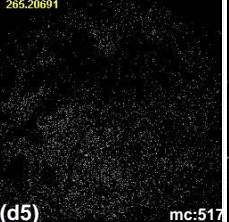
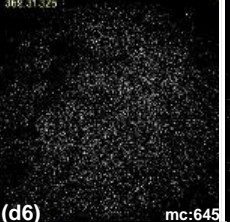
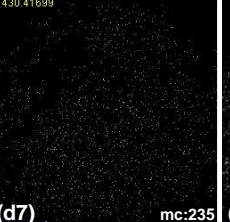
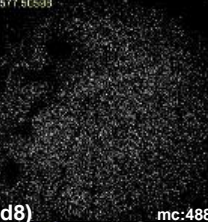
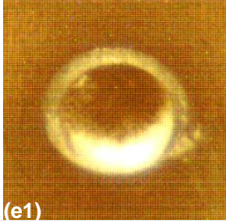
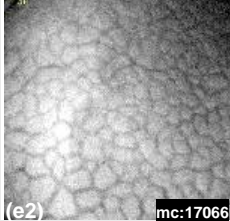
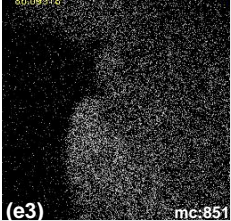
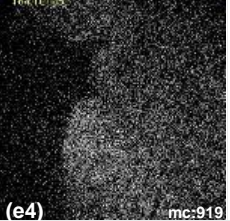
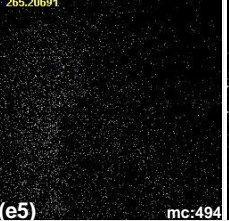
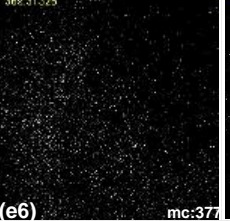
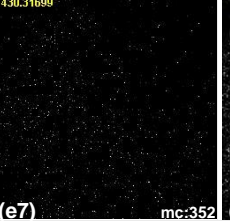
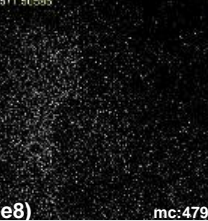
3.3.4.4 Monitoring the lipids distribution on *Xenopus laevis* embryo through the early development stages

Mitotic cell division, a regulated dynamic biological event, is of such central importance for animal development and associated dynamic processes, that the visualization of the mitosis directly in the developing embryo is of great interest. However, only the species featuring transparent embryo that develops extracorporally (e.g., teleosts) can be observed by optical microscopy noninvasively [100]. With regard to amphibian embryo with almost complete optical opacity like *X. laevis* embryo,

observations are restricted. In this section, the J105 is employed to monitor the lipids distribution on the surface and in depths of the embryo through early embryo development offering an alternative noninvasive method for embryonic study.

The biomolecular arrangements on the animal hemisphere of embryos at 2 cells, 4 cells, 32 cells and blastulas 3.3 h and 5.5 h post-insemination are shown by the +SIMS images in Fig. 3.32, as well as the sample photos took before the analysis using the built-in camera. During the cleavage, the embryo will not grow, but divide into smaller cells called blastomeres packed within the sphere. This morphological change is clearly reflected in the total ion images as in Fig. 3.32 (a2, b2, c2, d2, e2). Phosphocholine lipid fragments at m/z 86.1⁺ and 184.1⁺ concentrate in the blastomere junctions, and are less intense on the cell surface as in Fig. 3.32 (a3, a4, c3, c4, d3, d4). Cholesterol at m/z 369.4⁺ and the DAG ion at m/z 577.5⁺ spread on the animal side homogenously as seen in Fig. 3.32 (a6, a8, c6, c8, d6, d8) except for embryo at 4 cells stage. It is worth mentioning that the MAG ions at m/z 313.3⁺, 339.3⁺ and vitamin E at m/z 430.4⁺ Fig. 3.32 (a7, b7, c7, d7, e7) usually share the similar distribution pattern as cholesterol and DAG. The cholesterol lends the membrane with rigidity and mobility [101], which could be a reason why the cholesterol is widely spread on the animal hemisphere to keep the membrane lipids stable and to adapt to fast biomolecular rearrangement during the cell cleavage. SM ion at m/z 265.2⁺ has a high affinity for cholesterol as it locates where the cholesterol is in Fig. 3.32 (a5, b5, c5, d5, e5). These two biomolecules are able to pack tightly to form microdomains that are thought to function as signalling platforms in order to regulate the localization and interactions of proteins [102]. The blastula 5.5 h post-insemination [Fig. 3.32 (e1-7)] have a complementary distribution between phosphocholine lipids and SM/fats which is different with other embryos in Fig. 3.32. The embryo in this stage is ready for further development of gastrulation, forming the three germ layers by pushing part of the blastomeres inwards [40]. The movement requires more fluidity of the biomolecules within the blastomeres membrane, consequently more cholesterol are required in the membrane. This could explain why part animal hemisphere of the blastula 5.5 h after insemination contains more cholesterol than the rest, which could be the starting point of the gastrulation.

Fig. 3.32 Total optical, total ion and selected ion images (+SIMS) of animal hemisphere of *Xenopus laevis* embryos in different cleavage stages using the J105 3D Chemical Imager. The PI dose is 2.13×10^{13} ions/cm² with 40 keV C₆₀⁺ PI beam over 1200×1200 μm² area with 256×256 pixels. The biomolecular arrangements on the animal hemisphere of embryos at 2 cells, 4 cells, 32 cells and blastulas 3.3 h and 5.5 h post-insemination are shown. During the cleavage, the embryo will not grow, but divide into smaller cells called blastomeres packed on the surface of the sphere. The maximum counts (mc) can be read on the ion images. (The figure is in the next page).

	Photos of sample	Total +SIMS image	m/z 86.1 ⁺ -choline	m/z 184.1 ⁺ -phosphocholine	m/z 265.2 ⁺ -SM	m/z 369.4 ⁺ -cholesterol	m/z 430.4 ⁺ -vitamin E	m/z 577.5 ⁺ -DAG ion
2 cells stage	 (a1)	 (a2) mc:52654	 (a3) mc:765	 (a4) mc:1113	 (a5) mc:653	 (a6) mc:780	 (a7) mc:360	 (a8) mc:581
4 cells stage	 (b1)	 (b2) mc:52304	 (b3) mc:968	 (b4) mc:1229	 (b5) mc:566	 (b6) mc:734	 (b7) mc:261	 (b8) mc:486
32 cells stage	 (c1)	 (c2) mc:24239	 (c3) mc:716	 (c4) mc:981	 (c5) mc:547	 (c6) mc:608	 (c7) mc:438	 (c8) mc:549
Blastula 3.5h after Fertilisation (128 cells)	 (d1)	 (d2) mc:20023	 (d3) mc:836	 (d4) mc:1426	 (d5) mc:517	 (d6) mc:645	 (d7) mc:235	 (d8) mc:488
Blastula 5.5h after fertilisation	 (e1)	 (e2) mc:17066	 (e3) mc:851	 (e4) mc:919	 (e5) mc:494	 (e6) mc:377	 (e7) mc:352	 (e8) mc:479

Because of the unsynchronized development of the embryo after the fifth cleavage, the blastula embryo sampled at the same time may look slightly different in terms of the blastomere size. As in Fig. 3.33 (a1), the blastomeres on this blastula embryo have a size of 70-100 μm by counting the pixels cross the blastomeres, appearing bigger than that in Fig. 3.32 (e2) which was also sampled 5.5 h post-insemination. The phosphocholine lipid ion at m/z 184.1⁺ [Fig. 3.33 (a2)] is concentrated in the blastomeres junctions. SM fragment at m/z 265.2⁺ [Fig. 3.33 (a3)] and fats at m/z 369.4⁺ and 577.5⁺ [Fig. 3.33 (a4, a5)] spread almost evenly on the cell surface. The phosphocholine lipids and fats do not have complementary distribution on the animal hemisphere as they do in Fig. 3.32 (e3, e4 and e6 e7), however, it could mean the blastula in Fig. 3.33 (a1) has not developed to the stage as Fig. 3.32 (e2), or it could be the slightly different areas on the animal hemisphere were analysed.

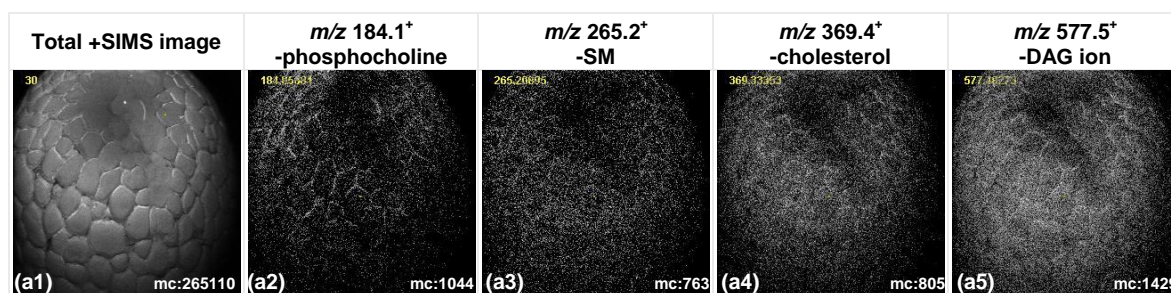


Fig. 3.33 Total ion and selected ion images (+SIMS) of animal hemisphere of *Xenopus laevis* blastula embryo 5.5 h post-insemination using the J105 3D Chemical Imager. Spectral dose is 2.24×10^{13} ions/ cm^2 with 40 keV C_{60}^+ PI beam over $1200 \times 1200 \mu\text{m}^2$ area with 256×256 pixels. Because of the unsynchronized development of the embryo, the blastomeres on this blastula embryo appear bigger than that in Fig. 3.32 (e2) which was also sampled 5.5 h post-insemination.

Furthermore, depth profiling was performed on one of the blastula embryo 5.5 h post-insemination to investigate the 3D distribution of several important biomolecules on the animal hemisphere where is packed with small blastomeres of varying sizes between 10-30 μm . Fig. 3.34 shows the image from the animal hemisphere of the whole blastula embryo after depth profiling the central area and selected biomolecular distributions on the first layer of the central area that underwent depth profiling. The analysis used a 2 μm -focused 40 keV C_{60}^+ PI beam that resolve some fine feature on the small blastomere surface. Particularly, the distribution of m/z 184.1⁺ in the first layer appears as a circle structure around edge of the blastomeres, and with small congregation in the centre that show the Golgi-like structure resembling the fluorescence image of the epidermis of a *X. laevis* embryo in the right panel of Fig. 3.34. As phospholipids are major component of Golgi apparatus [103], it is possible to locate it using most abundant fragment of phospholipids at m/z 184.1⁺. Meanwhile, m/z 184.1⁺ is concentrated in the blastomeres junction to form the circle structure, which is also seen in Fig. 3.32 (c4, d4), indicating the phospholipids play a special role in building membrane in the blastomere junctions that could better tolerate pressure from other blastomeres.

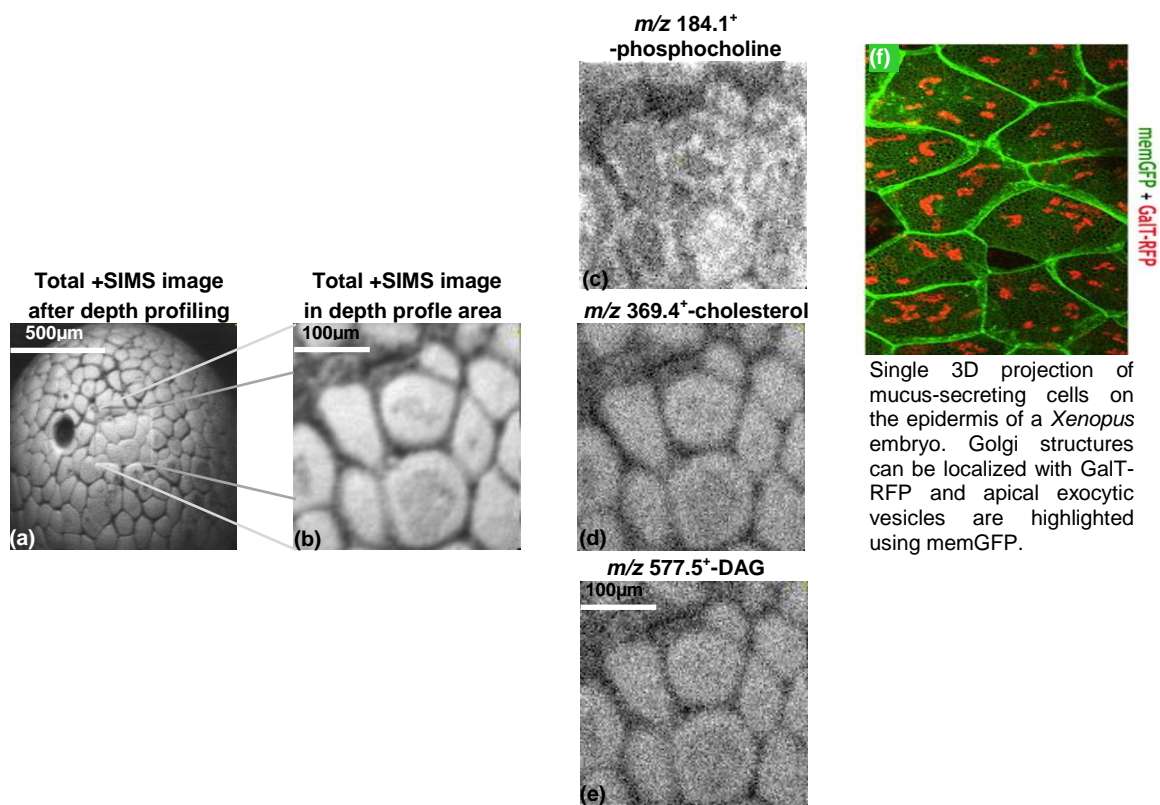


Fig. 3.34 Depth profiling in the central area of *Xenopus laevis* blastula embryo 5.5 h post-insemination using the J105 3D Chemical Imager. (a), total ion image of whole animal hemisphere after depth profiling. Spectral dose is 2.66×10^{13} ions/cm² with 4 µm-focused 40 keV C₆₀⁺ PI beam over 1200×1200 µm² area with 256×256 pixels; (b), total ion image of central area that undergo in first depth profiling. Each depth profiling was performed with 2 µm-focused 40 keV C₆₀⁺ PI beam at a dose of 1.07×10^{14} ions/cm² over 300×300 µm² area with 128×128 pixels; (c-e), single ions +SIMS images of selected biomolecules in depth profiling area. The distribution of *m/z* 184.1⁺ has Golgi-like structure in the middle the blastomere membrane resembling the fluorescence image in (f); (f), single 3D projection of mucus-secreting cells on the epidermis of a *X. laevis* embryo. Golgi structures can be localized with GalT-RFP and apical exocytic vesicles are highlighted using memGFP. Reproduced from reference [104].

On depth profiling, the above structure shown in ion image of *m/z* 184.1⁺ is replaced by a uniform layer of the phosphocholine lipids, and the intensity decreases compared with the first layer as seen in Fig. 3.35. Cholesterol appears evenly spread on the blastomere membrane, and on going through the membrane the intensity doubles after the 24th depth compared with the first depth, and remains steady. MAG at *m/z* 313.3⁺, 339.3⁺ and DAG at *m/z* 577.5⁺ all increase by 1.5 times with no obvious fluctuations after the 9th depth. Vitamin E signal at *m/z* 430.4⁺ has most increase compared with the other ions, up to 2.5 times that of the first depth. The spatial changes of the biomolecules could reflect the membrane structure with cholesterol located under the phosphocholine lipids and MAG, DAG the possible fragments from glycerophospholipids remaining constant in the lipids bilayer structure. The blastula at 5.5 h post-insemination has layers of small blastomeres around the embryo sphere. The depth profiling seems not to go through the layer as seen in the total +SIMS image after the depth profiling in Fig. 3.34. The individual blastomeres are still clear seen and resemble to those before the depth profiling in the central area. The hole to the left of the depth profile area was for testing if the C₆₀⁺ PI beam could penetrate the membrane. The total dose of approx. 3.98×10^{17} ions/cm² was used to drill the hole in the membrane, which means the depth profile a large cell like *X. laevis* embryo will require an impractical time frame.

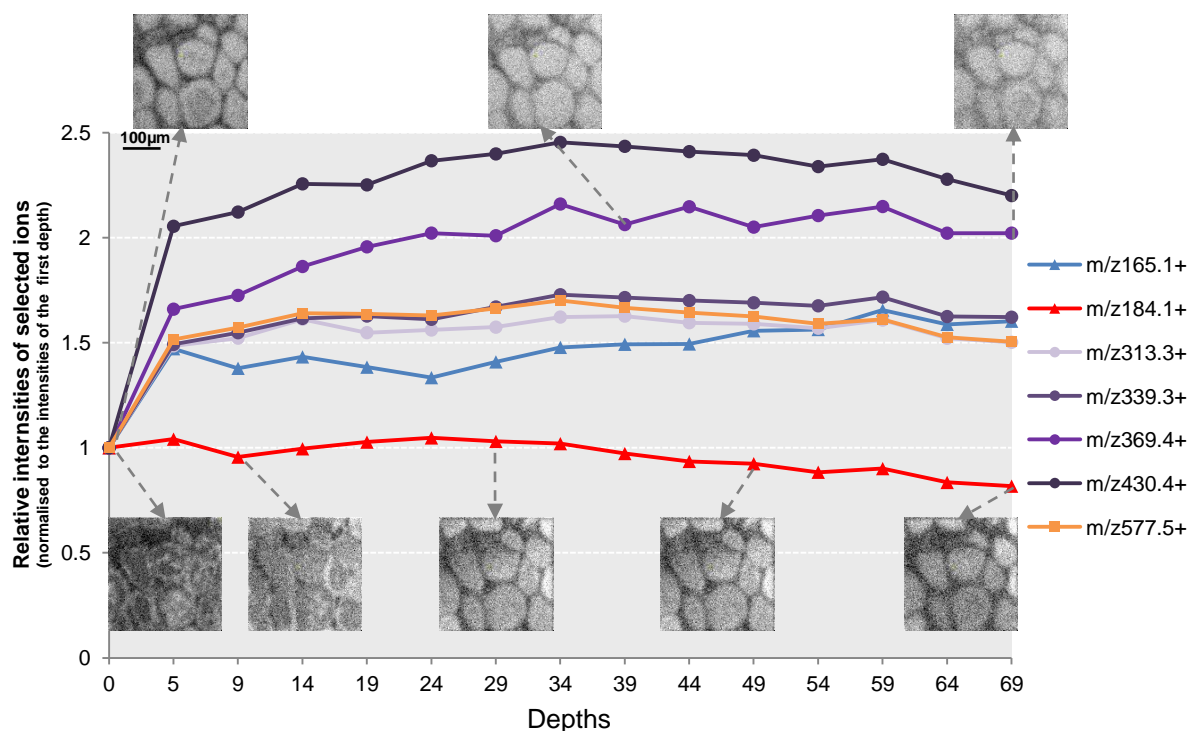


Fig. 3.35 Changes of relative intensities and distributions of selected ions along with depth profiling of *Xenopus laevis* blastula embryo 5.5 h post-insemination using the J105 3D Chemical Imager. The PI dose of each depth is 1.07×10^{14} ions/cm² with 40 keV C₆₀⁺ ion beam over 300×300 μm² area with 128×128 pixels. *m/z* 165.1⁺ is a common glycerophospholipids fragment; GPCCho and SM share fragments at *m/z* 184.1⁺; MAG at *m/z* 313.3⁺, 339.3⁺; cholesterol fragment at *m/z* 369.4⁺; DAG ions at *m/z* 577.5⁺. The distribution changes of *m/z* 184.1⁺ and *m/z* 369.4⁺ are also shown in the inset images with arrow pointing to corresponding depths. The intensity changes of the biomolecules (phosphocholine lipids decreases while MAG, cholesterol and DAG increase) could reflect the membrane structure with cholesterol located under the phosphocholine lipids and MAG, DAG the possible fragments from glycerophospholipids remain constant in the lipids bilayer structure.

3.4 Summary

The total lipids extracted from *X. laevis* zygote were measured with the BioToF-SIMS and the J105 3D Chemical Imager. GPCCho, GPEtn, GPGro, GPI, GPSer, cholesterol and sulfatide were identified by matching the characteristic peaks with the literature data. The results showed that both SIMS instruments were able to identify the lipid species within complex mixtures, and had similarities in detection of lipids species with GC-MS instrument. The J105 displayed the advantage of detecting various fatty acyls, MAG, DAG and TAG species due to its high mass resolution. These biomolecules were highly diverse in structure with varying double bonds along the carbon chain providing the essential building blocks for all the lipids.

The topography effects were investigated by comparing selected SI yields from different areas of the animal hemisphere of *X. laevis* embryos, a spherical object with approx. 1-1.2 mm in diameter. Affected by the extreme topography, the SI loss was most severe where the PI beam had an obtuse angle with sample surface, and SI intensity drop was also seen in the edge of the sphere samples. However, both instruments turned out to be useful in imaging the spatial distributions and detailed features in a spherical sample.

Lipids components and concentrations in the animal and vegetal hemispheres were detected in the membrane of an intact *X. laevis* zygote. MAG, cholesterol, various DAG and TAG appeared in the

animal hemisphere rather than vegetal hemisphere, while the vegetal side showed more intense phosphocholine lipids and vitamin E. The existence of the cholesterol, DAG and TAG components in the membrane of animal hemisphere could be related to the dark appearance of this side, as the embryonic pigment requires mixing with these fat components.

The biological processes of fertilisation were visualised using the J105 3D Chemical Imager at high mass resolution and lateral resolution. The egg-sperm fusion sites were firstly imaged by SIMS, and line scanning across the fusion site revealed possible lipids synthesis mechanisms during the fertilisation. The phospholipase-mediated hydrolysis of SM generated DAG in the centre of the fusion site that swiftly builds new lipids such as GPEtn and GPCho. GPEtn then formed the highly curved structure in order to seal a space inside the fusion centre for the release of sperm nucleus. Most synthesized GPCho was transported away from the centre to form the outer layer of the fusion site. This could well explain why DAG was almost exclusive in the centre along with low level of SM, GPEtn was mainly in the fusion centre and GPCho is lower in the centre and higher away from the centre. Cholesterol was more evenly distributed over a wider range than DAG possibly to stabilize the newly formed membrane.

The subcellular signalling was studied through depth profiling of a single intact *X. laevis* zygote and the serial cell sections of a zygote 10 min post-insemination. The depth profiling showed the intensity of the calcium, IP3 fragment m/z 129.1⁺ and DAG ions at m/z 549.5⁺ and 577.5⁺ increased drastically after the etching dose of 8.44×10^{14} ions/cm². The serial sections of the zygote exposed the interior environment of the cell directly for the SIMS measurement. The ion concentrations of IP3 and other selected biomolecules varied from the animal side to vegetal side. Especially the elevated IP3 was seen in the cell sections from animal side rather than vegetal side, which was coincided with the fact that the IP3 flux initiated from the sperm entry site that is in the animal side and crossed the whole egg.

Further monitoring of the embryonic development showed the different lipid arrangements on the animal hemisphere of *X. laevis* embryo at different cleavage stages. Phosphocholine lipids and possible SM were the main building blocks to the blastomere junction area where the cell membrane was under most pressure from surrounding blastomeres. Partial animal hemisphere of the blastula 5.5 h post-insemination contained more cholesterol than other areas, possibly responding to the further development of gastrulation.

References

- [1] Yan Q., *Membrane Transporters: Methods and Protocols (Methods in Molecular Biology)*. Vol. 227. 2003, Humana Press Inc.
- [2] Bendig M. M. and Williams J. G., *Fidelity of transcription of Xenopus laevis globin genes injected into Xenopus laevis oocytes and unfertilized eggs*. Mol. Cell. Biol., **4**(10): 2109-2119 (1984).
- [3] Monroy A. and Baccetti B., *Morphological changes of the surface of the egg of Xenopus laevis in the course of development. I. Fertilization and early cleavage*. J. Ultrastruct. Res., **50**(2): 131-142 (1975).
- [4] Whitaker M. and Swann K., *Lighting the fuse at fertilization*. Development, **117**(1): 1-12 (1993).
- [5] Gard D. L., *Organization, nucleation, and acetylation of microtubules in Xenopus laevis oocytes: A study by confocal immunofluorescence microscopy*. Dev. Biol., **143**(2): 346-362 (1991).
- [6] Koga M., et al., *A new triple staining method for double in situ hybridization in combination with cell lineage tracing in whole-mount Xenopus embryos*. Dev. Growth Differ., **49**(8): 635-645 (2007).
- [7] Gilbert S. F., *Developmental Biology*, 2006, Sinauer Associates: Sunderland (MA).

- [8] Elinson R. P., *Site of sperm entry and a cortical contraction associated with egg activation in the frog Rana pipiens*. Dev. Biol., **47**(2): 257-268 (1975).
- [9] Stein K. K., Primakoff P., and Myles D., *Sperm-egg fusion: events at the plasma membrane*. J. Cell Sci., **117**(26): 6269-6274 (2004).
- [10] Katagiri C., et al., *Analyses of oviductal pars recta-induced fertilizability of coelomic eggs in Xenopus laevis*. Dev. Biol., **210**(2): 269-276 (1999).
- [11] Gilbert S. F., *Developmental Biology*. 9th ed 2010, Singuer Association.
- [12] [cited 2011 09/08]; Available from: <http://technologysifi.blogspot.com/2010/03/embryology-of-frog.html>.
- [13] Antunes L. C., Davies J. E., and Finlay B. B., *Chemical signaling in the gastrointestinal tract*. Biol. Rep., **3**: 4 (2011).
- [14] Chen G. Q., *Active small-molecule compounds and leukemia: approach from chemical biology*. Zhonghua Yi Xue Za Zhi, **87**(20): 1369-1371 (2007).
- [15] Wagner J., et al., *A wave of IP₃ production accompanies the fertilization Ca²⁺ wave in the egg of the frog, Xenopus laevis: theoretical and experimental support*. Cell Calcium, **35**(5): 433-447 (2004).
- [16] Sato K., Fukami Y., and Stith B. J., *Signal transduction pathways leading to Ca²⁺ release in a vertebrate model system: lessons from Xenopus eggs*. Semin. Cell Dev. Biol., **17**(2): 285-292 (2006).
- [17] Carroll J., et al., *Spatiotemporal dynamics of intracellular [Ca²⁺] oscillations during the growth and meiotic maturation of mouse oocytes*. Development, **120**(12): 3507-3517 (1994).
- [18] Whitaker M., *Calcium at fertilization and in early development*. Physiol. Rev., **86**(1): 25-88 (2006).
- [19] Whitaker M. and Smith J., *Calcium signals and developmental patterning*. Philos. Trans. R. Soc. Lond. B. Biol. Sci., **363**(1495): 1307-1310 (2008).
- [20] Fontanilla R. A. and Nuccitelli R., *Characterization of the sperm-induced calcium wave in Xenopus eggs using confocal microscopy*. Biophys. J., **75**(4): 2079-2087 (1998).
- [21] Chang D. C. and Meng C. L., *A localized elevation of cytosolic-free calcium is associated with cytokinesis in the Zebrafish embryo*. J. Cell Biol., **131**(6): 1539-1545 (1995).
- [22] Schäfer S., Bickmeyer U., and Koehler A., *Measuring Ca²⁺-signalling at fertilization in the sea urchin Psammechinus miliaris: Alterations of this Ca²⁺-signal by copper and 2,4,6-tribromophenol*. Comp. Biochem. Phys. C, **150**(2): 261-269 (2009).
- [23] Kawasumi M. and Nghiem P., *Chemical genetics: elucidating biological systems with small-molecule compounds*. J. Invest. Dermatol., **127**(7): 1577-1584 (2007).
- [24] Berridge M. J., *Inositol trisphosphate and diacylglycerol: two interacting second messengers*. Annu. Rev. Biochem., **56**: 159-193 (1987).
- [25] Sefton B. M. and Buss J. E., *The covalent modification of eukaryotic proteins with lipid*. J. Cell Biol., **104**(6): 1449-1453 (1987).
- [26] Andreyev A. Y., et al., *Subcellular organelle lipidomics in TLR-4-activated macrophages*. J. Lipid Res., **51**(9): 2785-2797 (2010).
- [27] Quehenberger O., et al., *Lipidomics reveals a remarkable diversity of lipids in human plasma*. J. Lipid Res., **51**(11): 3299-3305 (2010).
- [28] Kelly S. M., Butler J. P., and Macklem P. T., *Control of cell volume in oocytes and eggs from Xenopus laevis*. Comp. Biochem. Phys. A, **111**(4): 681-691 (1995).
- [29] Hill W. G., et al., *Isolation and characterization of the Xenopus oocyte plasma membrane: a new method for studying activity of water and solute transporters*. Am. J. Physiol. Renal Physiol., **289**(1): F217-224 (2005).
- [30] Le Caherec F., et al., *Incorporation of proteins into (Xenopus) oocytes by proteoliposome microinjection: functional characterization of a novel aquaporin*. J. Cell Sci., **109**(6): 1285-1295 (1996).
- [31] Sabirov R. Z., Morishima S., and Okada Y., *Probing the water permeability of ROMK1 and amphotericin B channels using Xenopus oocytes*. Biochim. Biophys. Acta, **1368**(1): 19-26 (1998).
- [32] Speake B. K., et al., *The relationship between the fatty acid profiles of the yolk and the embryonic tissue lipids: A comparison between the lesser black backed gull (Larus fuscus) and the pheasant (Phasianus colchicus)*. Comp. Biochem. Phys. B, **115**(4): 493-499 (1996).
- [33] Neuringer M., Anderson G. J., and Connor W. E., *The essentiality of n-3 fatty acids for the development and function of the retina and brain*. Annu. Rev. Nutr., **8**: 517-541 (1988).
- [34] Maldjian A., et al., *The fatty acid composition of brain phospholipids from chicken and duck embryos*. Comp. Biochem. Phys. B, **115**(2): 153-158 (1996).
- [35] Delaunay F., et al., *The effect of monospecific algal diets on growth and fatty acid composition of Pecten maximus (L.) larvae*. J. Exp. Mar. Biol. Ecol., **173**(2): 163-179 (1993).

- [36] Huang C. H., Liang M. F., and Kam Y. C., *The fatty acid composition of oophagous tadpoles (Chirixalus eiffingeri) fed conspecific or chicken egg yolk*. Comp. Biochem. Physiol. A, **135**(2): 329-336 (2003).
- [37] Komoroski M. J., Nagle R. D., and Congdon J. D., *Relationships of lipids to ovum size in amphibians*. Physiol. Zool., **71**(6): 633-641 (1998).
- [38] Koek M. M., et al., *Metabolic profiling of ultrasmall sample volumes with GC/MS: from microliter to nanoliter samples*. Anal. Chem., **82**(1): 156-162 (2010).
- [39] Stewart-Savage J. and Grey R. D., *The temporal and spatial relationships between cortical contraction, sperm trail formation, and pronuclear migration in fertilized Xenopus eggs*. Dev. Genes Evol., **191**(4): 241-245 (1982).
- [40] Stern C. D., *Gastrulation: From Cells to Embryo*. 1st ed 2004, U.S., Cold Spring Harbor Laboratory Press. 341-352.
- [41] Elinson R. P. and Manes M. E., *Morphology of the site of sperm entry on the frog egg*. Dev. Biol., **63**(1): 67-75 (1978).
- [42] Boyle J. A., Chen H., and Bamberg J. R., *Sperm incorporation in Xenopus laevis: characterisation of morphological events and the role of microfilaments*. Zygote, **9**(2): 167-181 (2001).
- [43] Colombo R., Benedusi P., and Valle G., *Actin in Xenopus development: indirect immunofluorescence study of actin localization*. Differentiation, **20**(1-3): 45-51 (1981).
- [44] Chow R. L. and Elinson R. P., *Local alteration of cortical actin in Xenopus eggs by the fertilizing sperm*. Mol. Reprod. Dev, **35**(1): 69-75 (1993).
- [45] Ramirez-Zacarias J. L., Castro-Munozledo F., and Kuri-Harcuch W., *Quantitation of adipose conversion and triglycerides by staining intracytoplasmic lipids with Oil red O*. Histochemistry, **97**(6): 493-497 (1992).
- [46] Rogers W. J., et al., *Characterization of signal properties in atherosclerotic plaque components by intravascular MRI*. Arterioscler. Thromb. Vasc. Biol., **20**(7): 1824-1830 (2000).
- [47] Wenk M. R., *The emerging field of lipidomics*. Nat. Rev. Drug Discov., **4**(7): 594-610 (2005).
- [48] Fletcher J. S., et al., *TOF-SIMS 3D biomolecular imaging of Xenopus laevis oocytes using buckminsterfullerene (C60) primary ions*. Anal. Chem., **79**(6): 2199-2206 (2007).
- [49] Folch J., Lees M., and Sloane Stanley G. H., *A simple method for the isolation and purification of total lipides from animal tissues*. J. Biol. Chem., **226**(1): 497-509 (1957).
- [50] Bligh E. G. and Dyer W. J., *A rapid method of total lipid extraction and purification*. Can J Biochem Physiol, **37**(8): 911-917 (1959).
- [51] Matyash V., et al., *Lipid extraction by methyl-tert-butyl ether for high-throughput lipidomics*. J. Lipid Res., **49**(5): 1137-1146 (2008).
- [52] Greim H. and Reuter U., *Classification of carcinogenic chemicals in the work area by the German MAK Commission: current examples for the new categories*. Toxicology, **166**(1-2): 11-23 (2001).
- [53] Petkovic M., et al., *Comparison of different procedures for the lipid extraction from HL-60 cells: a MALDI-TOF mass spectrometric study*. Z Naturforsch C, **60**(1-2): 143-151 (2005).
- [54] Rose H. G. and Oklander M., *Improved Procedure for the Extraction of Lipids from Human Erythrocytes*. J. Lipid Res., **6**: 428-431 (1965).
- [55] Katagiri C., *Fertilization of dejellied uterine toad eggs in various experimental conditions*. Embryologia (Nagoya), **9**(3): 159-169 (1966).
- [56] Katagiri C., *A high frequency of fertilization in premature and mature coelomic toad eggs after enzymic removal removal removal of vitelline membrane*. J. Embryol. Exp. Morphol., **31**(3): 573-587 (1974).
- [57] Olson J. H. and Chandler D. E., *Xenopus laevis egg jelly contains small proteins that are essential to fertilization*. Dev. Biol., **210**(2): 401-410 (1999).
- [58] Simmons L. W., Roberts J. D., and Dziminski M. A., *Egg jelly influences sperm motility in the externally fertilizing frog, Crinia georgiana*. J. Evol. Biol., **22**(1): 225-229 (2009).
- [59] Zechmann B., Muller M., and Zellnig G., *Membrane associated qualitative differences in cell ultrastructure of chemically and high pressure cryofixed plant cells*. J. Struct. Biol., **158**(3): 370-377 (2007).
- [60] Grimson M. J. and Blanton R. L., *Cryofixation methods for ultrastructural studies of dictyostelium discoideum*. Methods Mol. Biol., **346**: 339-365 (2006).
- [61] Sosinsky G. E., et al., *The combination of chemical fixation procedures with high pressure freezing and freeze substitution preserves highly labile tissue ultrastructure for electron tomography applications*. J. Struct. Biol., **161**(3): 359-371 (2008).

- [62] Puchtler H. and Meloan S. N., *On the chemistry of formaldehyde fixation and its effects on immunohistochemical reactions*. Histochemistry, **82**(3): 201-204 (1985).
- [63] Strauss B., Adams R. J., and Papalopulu N., *A default mechanism of spindle orientation based on cell shape is sufficient to generate cell fate diversity in polarised Xenopus blastomeres*. Development, **133**(19): 3883-3893 (2006).
- [64] Tuan R. S. and Lo C. W., *Developmental Biology Protocols*. 1st ed. Vol. 1. 1999, Humana Press Inc.
- [65] J. D. M. and E. R. L., *Biological electron microscopy: theory, techniques, and Troubleshooting*. 2003, Springer.
- [66] Berntsson K.-E., Haglund B., and Løvtrup S., *Osmoregulation in the amphibian egg the influence of calcium*. J. Cell. Compar. Physi., **65**(1): 101-112 (1965).
- [67] Lee T. G., et al., *Biochemical imaging of tissues by SIMS for biomedical applications*. Appl. Surf. Sci., **255**(4): 1241-1248 (2008).
- [68] Nygren H., et al., *A cell preparation method allowing subcellular localization of cholesterol and phosphocholine with imaging TOF-SIMS*. Colloid. Surface. B, **30**(1-2): 87-92 (2003).
- [69] Li X. H., et al., *Optimization of specimen preparation of thin cell section for AFM observation*. Ultramicroscopy, **108**(9): 826-831 (2008).
- [70] Elinson R. P., *Fertilization of partially jellied and jellyless oocytes of the frog Rana pipiens*. J. Exp. Zool., **176**(4): 415-428 (1971).
- [71] Stewart-Savage J. and Grey R. D., *Fertilization of investment-free Xenopus eggs*. Exp. Cell Res., **154**(2): 639-642 (1984).
- [72] Sommer U., et al., *LC-MS-based method for the qualitative and quantitative analysis of complex lipid mixtures*. J. Lipid Res., **47**(4): 804-814 (2006).
- [73] Pulfer M. and Murphy R. C., *Electrospray mass spectrometry of phospholipids*. Mass Spectrom. Rev., **22**(5): 332-364 (2003).
- [74] Manicke N. E., et al., *Desorption electrospray ionization (DESI) mass spectrometry and tandem mass spectrometry (MS/MS) of phospholipids and sphingolipids: ionization, adduct formation, and fragmentation*. J. Am. Soc. Mass. Spectrom., **19**(4): 531-543 (2008).
- [75] Ostrowski S. G., et al., *Secondary ion MS imaging of lipids in picoliter vials with a buckminsterfullerene ion source*. Anal. Chem., **77**(19): 6190-6196 (2005).
- [76] Roddy T. P., et al., *Proton transfer in time-of-flight secondary ion mass spectrometry studies of frozen-hydrated dipalmitoylphosphatidylcholine*. Anal. Chem., **75**(16): 4087-4094 (2003).
- [77] Passarelli M. K. and Winograd N., *Lipid imaging with time-of-flight secondary ion mass spectrometry (ToF-SIMS)*. Biochim. Biophys. Acta, (2011).
- [78] Amaya K. R., Sweedler J. V., and Clayton D. F., *Small molecule analysis and imaging of fatty acids in the zebra finch song system using time-of-flight-secondary ion mass spectrometry*. J. Neurochem., **118**(4): 499-511 (2011).
- [79] Hannun Y. A., *Sphingolipid second messengers: tumor suppressor lipids*. Adv. Exp. Med. Biol., **400A**: 305-312 (1997).
- [80] Schlame M., Rua D., and Greenberg M. L., *The biosynthesis and functional role of cardiolipin*. Prog. Lipid Res., **39**(3): 257-288 (2000).
- [81] Dargan S. L., Schwaller B., and Parker I., *Spatiotemporal patterning of IP₃-mediated Ca²⁺ signals in Xenopus oocytes by Ca²⁺-binding proteins*. J. Physiol., **556**(2): 447-461 (2004).
- [82] Benninghoven A., *Chemical analysis of inorganic and organic surfaces and thin films by static Time-of-Flight secondary ion mass spectrometry (TOF-SIMS)*. Angewandte Chemie International Edition in English, **33**(10): 1023-1043 (1994).
- [83] Ito H. and Kono T., *Quantitative analysis of organic additive content in a polymer by ToF-SIMS with PCA*. Appl. Surf. Sci., **255**(4): 1044-1047 (2008).
- [84] Kraft M. L., et al., *Phase separation of lipid membranes analyzed with high-resolution secondary ion mass spectrometry*. Science, **313**(5795): 1948-1951 (2006).
- [85] Brown D. A. and London E., *Structure and function of sphingolipid- and cholesterol-rich membrane rafts*. J. Biol. Chem., **275**(23): 17221-17224 (2000).
- [86] Sonnino S. and Prinetti A., *Lipids and membrane lateral organization*. Front Physiol, **1**: 1-9 (2010).
- [87] Rangarajan S. and Tyler B. J., *Topography in secondary ion mass spectroscopy images*. Journal of Vacuum Science & Technology A: Vacuum, Surfaces, and Films, **24**(5): 1730-1736 (2006).
- [88] Lee J. L. S., et al., *Topography and field effects in secondary ion mass spectrometry -- Part I: Conducting samples*. J. Am. Soc. Mass Spectrom.: **22**(10): 1718-1728 (2011).

- [89] Richter H.-P., Hoock C., and Neumcke B., *Morphological and electrophysiological properties of centrifuged stratified Xenopus oocytes*. Biol. Cell, **84**(3): 129-138 (1995).
- [90] Brown D. A. and London E., *Structure and origin of ordered lipid domains in biological membranes*. J. Membr. Biol., **164**(2): 103-114 (1998).
- [91] Simons K. and Toomre D., *Lipid rafts and signal transduction*. Nat. Rev. Mol. Cell Biol., **1**(1): 31-39 (2000).
- [92] Edidin M., *The state of lipid rafts: from model membranes to cells*. Annu. Rev. Biophys. Biomol. Struct., **32**: 257-283 (2003).
- [93] Kahya N., et al., *Probing lipid mobility of raft-exhibiting model membranes by fluorescence correlation spectroscopy*. J. Biol. Chem., **278**(30): 28109-28115 (2003).
- [94] Luo B., et al., *Diacylglycerol kinases*. Cell. Signal., **16**(9): 983-989 (2004).
- [95] Athenstaedt K. and Daum G., *Phosphatidic acid, a key intermediate in lipid metabolism*. Eur. J. Biochem., **266**(1): 1-16 (1999).
- [96] Berridge M. J., *Inositol trisphosphate and calcium signaling*. Nature, **361**(6410): 315-325 (1993).
- [97] Tarin J. J. and Cano A., *Fertilization in protozoa and metazoan animals: cellular and molecular aspects*. illustrated ed 2000, Springer.
- [98] Glahn D. and Nuccitelli R., *Voltage-clamp study of the activation currents and fast block to polyspermy in the egg of Xenopus laevis*. Dev. Growth Differ., **45**(2): 187-197 (2003).
- [99] Gilbert S. F., *Developmental Biology*. 9th ed 2010, Sinauer Associates. 711.
- [100] Papan C., et al., *Time-lapse tracing of mitotic cell divisions in the early Xenopus embryo using microscopic MRI*. Dev. Dyn., **235**(11): 3059-3062 (2006).
- [101] van Meer G., Voelker D. R., and Feigenson G. W., *Membrane lipids: where they are and how they behave*. Nat. Rev. Mol. Cell Biol., **9**(2): 112-124 (2008).
- [102] Milhas D., Clarke C. J., and Hannun Y. A., *Sphingomyelin metabolism at the plasma membrane: Implications for bioactive sphingolipids*. FEBS Lett., **584**(9): 1887-1894 (2010).
- [103] Keenan T. W. and Morre D. J., *Phospholipid class and fatty acid composition of Golgi apparatus isolated from rat liver and comparison with other cell fractions*. Biochemistry (Mosc.), **9**(1): 19-25 (1970).
- [104] Kieserman E. K., et al., *High-magnification in vivo imaging of Xenopus embryos for cell and developmental biology*. Cold Spring Harb. Protoc., (5): pdb prot5427 (2010).

Chapter 4 Subcellular imaging using dynamic secondary ion mass spectrometry

4.1 Introduction

Subcellular imaging could provide direct understanding of cell functions and biological processes. Many techniques have been investigated for this purpose. Imaging Time-of-Flight secondary ion mass spectrometry (ToF-SIMS), as an emerging new tool, is capable of resolving the natural or exogenous molecules at precise locations within biological systems to further the understanding of functioning biomolecules or disease progress at a molecular level. In this study, ToF-SIMS was used to track subcellular organelle, mitochondria (0.5-2 μm), in the murine fibroblast NIH 3T3 BXB-ER cells in response to the activation of the Raf/ERK (extracellular signal regulated kinase) pathway. ToF-SIMS experiments were combined with fluorescence imaging and scanning electron microscopy (SEM). The three imaging modes were employed sequentially to provide complementary information regarding cellular morphological changes and subcellular mitochondria rearrangements following Raf/ERK activation. The fluorophore MitoTracker Red CMXRos, molecular weight 531.52 g/mol, having an intense fragment ion at m/z 495.13⁺ that does not interfere with the mass spectrum of major lipid fragments of biological cells, was selected to highlight the mitochondria in a time course study for 3D confocal and SIMS imaging. SEM images were acquired following SIMS analysis to reveal the morphology of the cells.

The study reported here firstly employed a submicron scale focused C_{60}^+ primary ion beam (500-1000 nm, verified by imaging the filopodia of fibroblast cells with 300-1000 nm in widths) to locate the subcellular organelles in 3D, which is still a challenge encountered by most existing SIMS instruments. The labelled cells were prepared with the same procedure as required for SIMS *in vacuo* analyses, *i.e.*, washing salts followed by freeze-drying. This is also the first time confocal microscopy has been used to image the freeze-dried cells. The identical sampling methodology for both imaging modes is beneficial to assess cell integrity after sample preparation and possible interference induced by the fluorescence tag. This introduction describes previous studies on NIH 3T3 BXB-ER cells reacting to Raf/ERK activation using submicron SIMS imaging, as well as the biological questions this study was trying to answer.

4.1.1 Mouse embryonic fibroblast cells and Raf kinase

As shown in Fig. 4.1 (A), the NIH 3T3 cells appear long and thin with fine tentacles. The cell line has been established from NIH Swiss mouse embryo cultures in the same manner as the original random bred 3T3. The subclone of the cell line after over 5 serial cycles of subcloning has been selected in order to develop better morphologic characteristics for transformation assays. NIH 3T3 BXB-ER cells are derived from NIH 3T3 expressing the fusion protein c-Raf BXB-ER [Fig. 4.1 (B)] at a stable, low level. BXB-ER is a human estrogen receptor fusion protein and the carboxyterminal half (containing the kinase domain) of human C-RAF-1 [1]. c-Raf kinase can be activated by estrogen agonist, 4-hydroxytamoxifene (4-OHT) [2], and also can be stimulated by the addition of β -Estradiol [3]. Therefore, the conditional constructs act as a switch of Raf kinase for mediating cell proliferation, for example, Raf activation can induce a stop of the cell cycle [2].

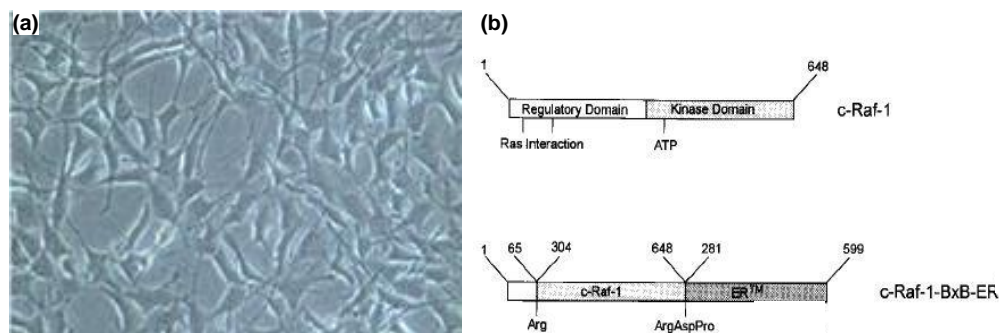


Fig. 4.1 NIH 3T3 BXB-ER cells and the c-Raf-1 derived BXB-ER fusion protein. (a), NIH 3T3 BXB-ER cells; (b), structure of the c-Raf-1-BxB-ER fusion protein. The c-Raf-1 protein consists of a regulatory domain and a kinase domain. Deletion of amino acids 66 to 303 (human c-Raf-1) generates a constitutive active kinase (BxB). Oncogenic c-Raf-1 deletion mutant was fused to the hormone binding domain of the mouse ER (amino acids 281 to 599). Reproduced from reference [4].

Fused with ER, c-Raf BXB-ER protein induces Raf Kinases followed by estrogens treatment, which is vital for regulating mature cells, cancer and organism development. The proteins of the Raf family (A-Raf, B-Raf, and C-Raf) are serine/threonine kinases existing in the upstream of the highly conserved mitogen-activated protein kinase (MAPK)³ signalling module, MEK-ERK [5, 6]. As such, they link ERK activation to different growth signals. Among the Raf family, c-Raf-1 is expressed ubiquitously in mammalian cells [4]. It is well known that the cell cycle progression induced by growth factor greatly relies on Raf-mediated signal transduction cascades. With the inhibition of Raf function, the fibroblasts show the blocks of growth factor-induced G₀/G₁ and G₁/S phase transitions [7]. It has also been proved that in human carcinogenesis a constitutive activation to the protein B-RAF conferred by the mutations are among the most commonly detected genetic abnormalities [5]. Moreover, upon the knock-out of each of the Raf genes various defects were found, implying the distinct function the genes express in mouse development [8]. However, it is uncertain to what extent this could result from their tissue-specific expression pattern and/or from the specific role these kinases might play at cellular level [6, 8, 9].

4.1.2 NIH 3T3 BXB-ER cells in response to the Raf/ERK activation

NIH 3T3 BXB-ER has been widely used to express Raf kinases as the activation can be acutely regulated by estrogen. Galmiche *et al.* [6] demonstrated that C-RAF is the only isoform that directly targets mitochondria, resulting in the direct controlling of important aspects in physiology of these membrane-folded organelles. The consequences followed by the activation of C-RAF on mitochondria using 4-OHT were observed, indicating that C-RAF regulates the shape and the cellular distribution of mitochondria. The mitochondria in green distributed around nuclei in blue evenly and most of them were elongated without C-RAF activation as in Fig. 4.2 (a, c, e); following the activation, the mitochondria migrate close to nuclei with more dense congregation, in addition appearing predominantly spherical as in Fig. 4.2 (b, d, f). However, the result also showed A-RAF also target mitochondria in a lower level, whilst other studies also show mutant B-RAF to be associated with mitochondria in Thyroid cancer cells [10, 11], it could be that different cell types have different RAF-mitochondria interactions.

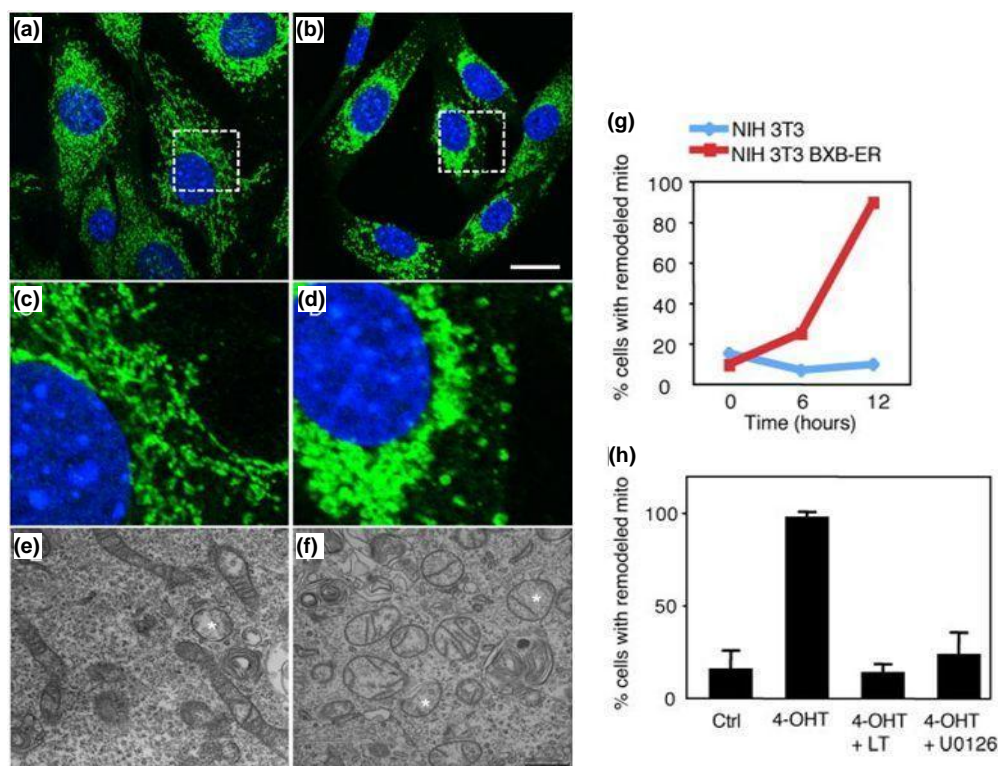


Fig. 4.2 C-RAF activation changes mitochondrial subcellular distribution. (a-d), NIH 3T3 BXB-ER cells were used to analyze kinetically the effects of C-RAF activation on mitochondria. Cells placed in conditions of serum starvation were incubated either with 1 μ M 4-OHT for 12 h. The pictures are representative of findings obtained upon confocal examination after staining for the mitochondrial marker Tom20 (green) and nuclei (4,6-diamidino-2-phenylindole, blue) without (a, c) or following C-RAF activation (b, d). In (c, d), close-ups are presented corresponding to the area enclosed by dotted line boxes in (a, b). (e, f), mitochondrial ultrastructure in control cells and after C-RAF activation (bar: 10 μ m). In control cells (e) the majority of mitochondria have an elongated shape, and only few mitochondria with spherical profiles are visible (indicated here with an asterisk). After 12 h of activation of C-RAF by the addition of 4-OHT (f), notice the predominantly spherical mitochondria (bar: 0.5 μ m); (g), quantification of the percentage of cells with remodelled mitochondria after 0, 6, or 12 h of exposure to 4-OHT in cells expressing C-RAF BXB-ER compared with wild-type NIH 3T3 cells; (h), U0126 and anthrax LT block mitochondrial remodelling induced by C-RAF activation. NIH 3T3 expressing the C-RAF BXB-ER construct were treated with U0126 (10 μ M) or *B. anthracis* LT, immediately before the application of 4-OHT. Both inhibitors abolished the mitochondrial redistribution induced by a 12 h treatment with 4-OHT. Reproduced from reference [6].

Other studies have also showed that Raf/ERK activation can re-organize global nuclei, particularly the structure of major chromatin compartments in mouse fibroblasts, using a conditional form of Raf, BXB-ER. Martin *et al* [3] compared NIH 3T3 cells and NIH 3T3 BXB-ER without and with estrogen treatment. As in Fig. 4.3 (a), the classical chromatin organization was shown in NIH 3T3 cells, NIH 3T3 cells treated with estrogen and untreated NIH 3T3 BXB-ER cells. The euchromatin were scattered and punctuated by few discrete brightly-stained clumps of heterochromatic chromocenters, small dense chromatin clumps are aside nuclear periphery and around nucleoli. Cells with activated BXB-ER appear to have a heterogeneous texture with compact chromatin aggregates [Fig. 4.3 (a), arrows] and discrete chromatin foci around the nucleolar periphery and nuclear lamina [Fig. 4.3 (a), arrowheads]. In addition, it revealed the chromatin changes and nuclear decrease after 15 hours of BXB-ER activation [Fig. 4.3 (b, c)]. The significant difference between NIH 3T3 and NIH 3T3 BXB-ER cells existed in the nuclear diameter, resulting in decreased nuclear volume by 40% in estrogen treated NIH 3T3 BXB-ER cells that were not directly linked to cell cycle distribution.

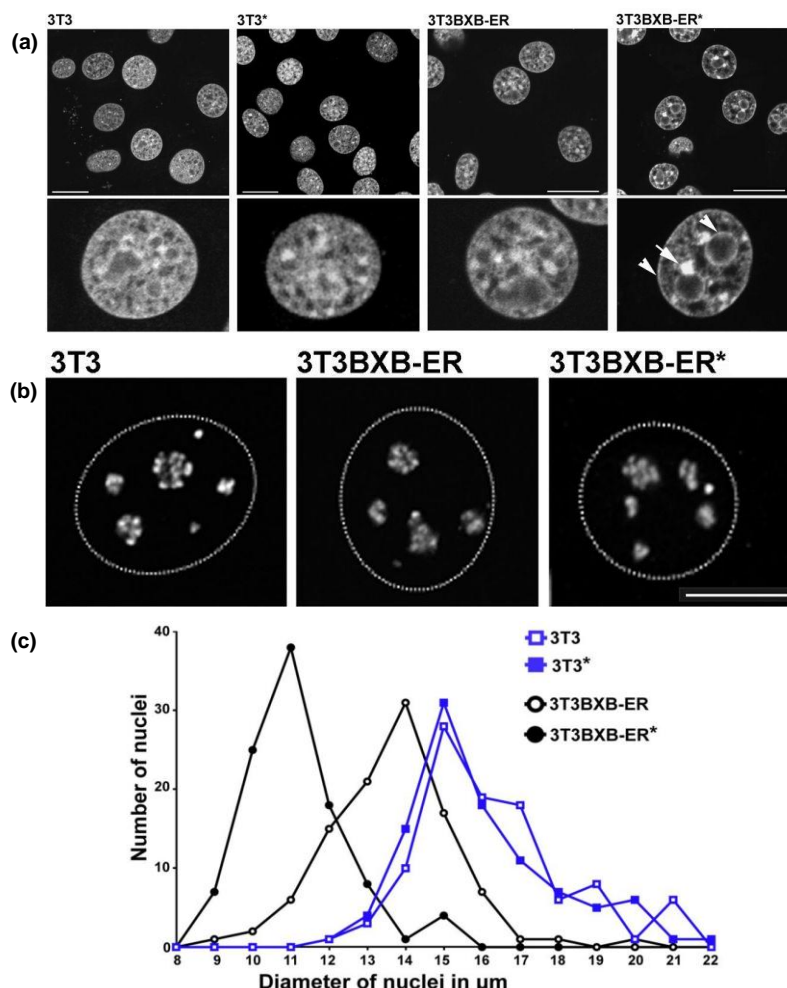


Fig. 4.3 BXB-ER activation induces chromatin rearrangement and reduced nuclear diameter. (a), optical sections of control NIH 3T3 and NIH 3T3 BXB-ER cells stained with Sytox green to show DNA distribution. Enhanced condensed chromatin clumps (arrow) and rims surrounding nucleoli and nuclear periphery (arrowheads) after BXB-ER activation by addition of estrogen for 15 h (*) are indicated. Scale bars: 20 μm ; (b), 3D reconstructions of cells immunoprocessed for fibrillarin show no changes in nucleolar structure. The dotted lines indicate the outline of nuclei. Scale bars: 10 μm ; (c), size distribution of nuclei in untreated and estrogen treated NIH 3T3 and NIH 3T3 BXB-ER cells. The mean diameters of 100 nuclei for each condition were determined and sorted in 1 μm wide bins. Reproduced from reference [3].

4.1.3 SIMS imaging on submicron scale

The advent of new cluster sources such as C_{60}^+ [12, 13], Au_3^+ [14], SF_5^+ [15] and Bi_3^+ [16] have increased secondary ion (SI) yields and open an new era of subcellular investigation using SIMS. However, the SIMS community still faces a big challenge in imaging on a micrometer and submicron scale owing to the limited molecules available for detection in such a small pixel. This has resulted in just a handful of reports on submicron scale imaging of subcellular compartments and metabolic pathway using NanoSIMS [17-27] or ToF-SIMS instruments [28-31].

NanoSIMS combines nanoscale imaging under high mass resolution with stable isotope labelling to locate of subcellular isotope markers quantitatively. Chandra [25] traced the marker of ^{127}I (from IdU) and ^{81}Br (from BrdU) for imaging DNA replication and RNA distribution as well as intranuclear metal ions in fractured freeze dried HeLa cell following heat shock treatment. The study was performed with an O_2^+ ion source focused at 500 nm. It revealed elevated levels of bound calcium located around the nucleus, indicating that calcium might play an important role during RNA transcription and storage. Lechene and co-workers [32] presented extensive applications of stable

isotopes to cell biology using a 100 nm-focused Cs^+ primary ion (PI) beam. ^{13}C -labeled free fatty acid, oleic acid (^{13}C -OA) was used to track adipocytes membrane transport, whereby, quantitative images of ^{13}C in three locations, inside cell but outside the lipids droplets, outside of cell and inside lipids droplets, showed a high level accumulation of ^{13}C in intracellular lipid droplets [18]. In another study, co-localization of RNA and DNA in rat embryo fibroblasts was demonstrated in Fig. 4.4, which indicated $^{12}\text{C}^{15}\text{N}^-$ signal (RNA) was strong within the nucleoli and along the nuclear envelope [Fig. 4.4 (a)], while stronger $^{81}\text{Br}^-$ (DNA) is found along the nuclear envelope than around nucleoli [Fig. 4.4 (b)]. Romer *et al.* [20] measured the membrane binding and internalisation of the protein ^{15}N -STxB in HeLa cells prepared by resin embedding and ultramicrotomy section. The image was acquired with Cs^+ at spatial resolutions of less than 100 nm.

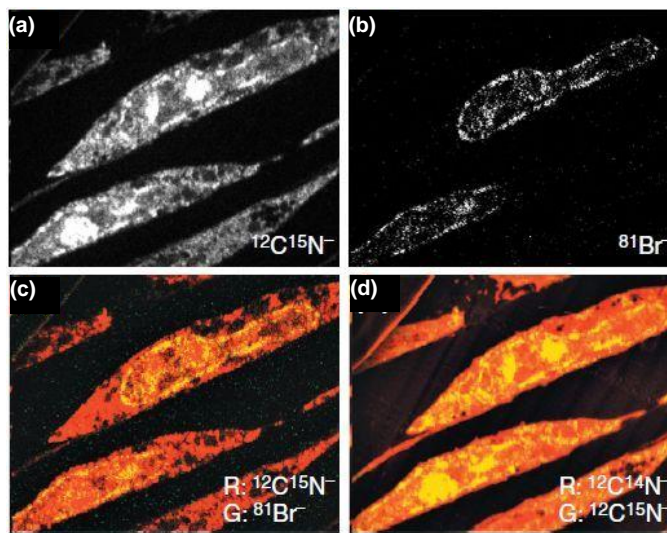


Fig. 4.4 Qualitative co-localization of DNA and RNA through simultaneous NanoSIMS imaging of RNA and DNA. Rat embryo fibroblasts were pulsed with ^{15}N -uridine and BrdU as markers of newly synthesized RNA and DNA, respectively. Parallel mass images at (a) $^{12}\text{C}^{15}\text{N}^-$ and (b) $^{81}\text{Br}^-$; (c), overlay of $^{12}\text{C}^{15}\text{N}^-$ and $^{81}\text{Br}^-$ images. $^{12}\text{C}^{15}\text{N}^-$ is depicted as red (R) and $^{81}\text{Br}^-$ as green (G), the overlap between them shows up as yellow; (d), overlay of $^{12}\text{C}^{14}\text{N}^-$ and $^{12}\text{C}^{15}\text{N}^-$ images. $^{12}\text{C}^{14}\text{N}^-$ is depicted as red (R) and $^{12}\text{C}^{15}\text{N}^-$ as green (G), the overlap between them shows up as yellow. Conditions of the analysis: beam current 2 pA; beam diameter 100 nm; field $20 \times 20 \mu\text{m}^2$. Reproduced from reference [32].

ToF-SIMS has also contributed to cellular imaging and 3D compositional mapping. Most of these studies were carried out with dual PI beams, Bi_3^+ to image and C_{60}^+ or focused Ga^+ to sputter. Szakal *et al.* [31] detected the interior of HeLa cells following focused Ga^+ beam milling, the high lateral resolution was achieved using a Bi_3^+ PI beam with 410 nm spot size. The membrane marker phosphocholine lipids were located along with some unassigned molecules concentrated in the inner region after the beam milling. Breitenstein *et al.* [28] presented the work of dual beams (Bi_3^+ for imaging and C_{60}^+ for etching) analysis for 3D compositional mapping of epithelial MDCK II cells. As shown in Fig. 4.5, xz section of the 3D image showed the distribution of phosphocholine lipids, amino acids and sodium as expected. Ethidium homodimer-1 (EthD-1), a high-affinity nucleic acid stain added to amplify signal from the nucleus, was only detected in 2D imaging of methanol/acetic acid fixed samples (the membrane was stripped). The tag failed to show up within glutaraldehyde fixed samples after several sputtering cycles.

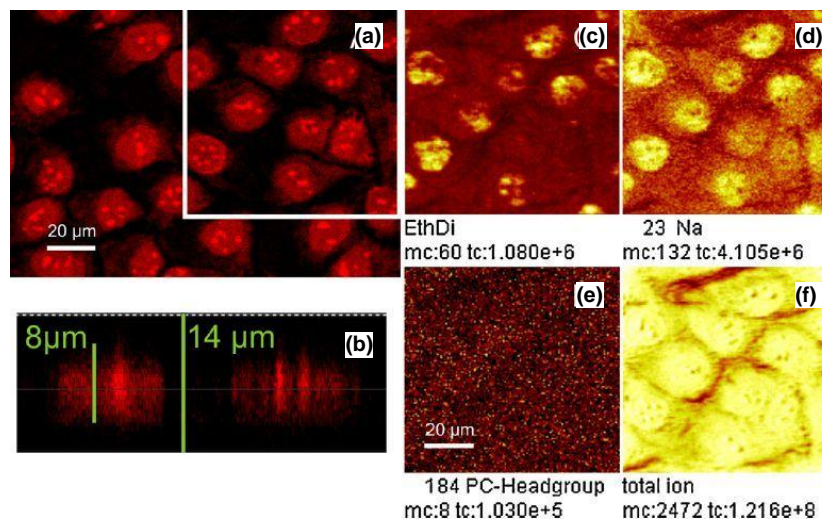


Fig. 4.5 ToF-SIMS imaging (c-f) (a, b) were obtained from the same position of a methanol/acetic acid fixed cell sample. The confocal image xz-section (b) totally ranging 14 μm in depth visualized the thicknesses (8 μm) of the cells, whereas the xy-section (a) revealed the lateral fluorophore distribution at medium height of the cells. By ToF-SIMS ethidium homodimer fragments (c) sum of $C_{19}H_{15}N_3^+C_xH_{2x}$ ($x = 0 \dots 3$) and sodium ions (d) were detectable in high intensities in central parts of the cell. In contrast PC fragments were obtained in very low intensities. From the total ion image (f) the distribution of the cell/cell contacts could be estimated. Reproduced from reference [28].

The dual beams operation mode is a commonly used approach for 3D imaging by SIMS. However, the introduction of a second ion beam further complicates the analysis process with regard to beam alignment and causes a loss of valuable information in the sputter etch cycle that is between two data acquisitions. It has been known for a long time that the C_{60}^+ PI beam is the most promising candidate to do molecular depth profiling [33-35]; however, lower focusability and significant current drop during focusing have impeded its application on conventional pulsed-beam ToF-SIMS instruments. Over the last decade, the Vickerman group (Manchester, UK) has worked to develop a 40 kV C_{60} ion source for high resolution imaging and new concept SIMS instrument -- the J105 3D Chemical Imager (J105) for fully exploring the advantages of C_{60}^+ beam [36-39]. This combination offers 3D imaging and depth profiling at high resolution with a single focused C_{60}^+ ion beam. During the analysis, etching and acquisition of data are simultaneous, that is all the in depth information is collected in voxels so that none of the sample is wasted between the analysis cycles. This approach has been applied to various biological samples for studying the morphology and chemical composition, e.g., HeLa cells [40] and mouse kidney sections with C_{60}^+ beam focused at one to tens of micrometres. However, for most of biological cells with a dimension of 20 μm, the lateral resolution of PI is still not ideal to visualize the subtle cellular structures. More collimated beam means less PI current and lower SI yields according to the SIMS equation 1.1 in chapter 1. In addition to sensitivity and secondary ion transmission, sample topography and charging present more challenges for acquiring high resolution compositional images of biological cells.

4.1.4 Aim of the project

The mitochondria remodelling following the activation of Raf kinases has been imaged by confocal microscopy, however, the questions such as the lipids composition changes of mitochondria and interference of the fluorescence tag during the reaction of fibroblast cells still remain unclear. One possible methodology to identify lipids is physiochemical isolation of mitochondria from cells, but it is a time-consuming process and changes may be induced by the process. Moreover, the estrogen activation takes effect in seconds and minutes [41], isolating the organelles cannot be fast enough

to freeze the biological process. This is why the high resolution imaging ToF-SIMS is introduced for *in situ* measurement. The advantages of the J105 has realised 2D and 3D imaging in high resolution. The work presented in this chapter is to explore the submicron scale imaging of the J105 for tracking the mitochondria rearrangement *in situ* in murine fibroblasts after Raf/ERK activation either by the lipid fragments or by xenobiotic fluorophors. The comparisons with fluorescence images and SEM images were also made to assess the morphological changes and possible effects induced by sample preparation or fluorescence tag.

4.2 Materials and methods

4.2.1 Cell culture

NIH 3T3 cells and NIH 3T3 BXB-ER cell was kindly provided by Dr. Josip Lovrić (the Faculty of Life Sciences, The University of Manchester). The cells were cultured using Dulbecco's modified Eagle medium [DMEM, high glucose, Sigma, with 2 mM L-glutamine, 4.5 g/l glucose, 50 U/ml penicillin, 50 U/ml streptomycin and 10% (V:V) Fetal Calf Serum (FCS)] in Ø100 mm dish. The dishes were placed in a 37 °C incubator with 5% CO₂ for 2-3 days until the cells reached 80-90% confluence. Subculture was performed every three days to keep the sample supply, as follows. The medium from confluent cell dish was removed and the dishes was rinsed with prewarmed (37 °C water bath) Trypsin-EDTA (0.25% Trypsin, and 0.53 mM EDTA, Sigma, BioReagent). At room temperature, additional 1-2 mL of Trypsin-EDTA was added and settled for 5 min until cells begin to disperse (the process could be encouraged by incubating). Then Trypsin solution was removed and the dish was vigorously vibrated. Followed by the adding 4-6 mL fresh culture medium to cells and aspirating to mix the medium. 0.75-1.5 mL suspended cell medium was then dispensed per dish with 7 mL pre-warmed (37 °C water bath) fresh culture medium to achieve the dilution ratios of 1:4 to 1:6.

4.2.2 Sample preparation

To image fluorescence dye using ToF-SIMS, the sensitivities and stability under C₆₀⁺ sputtering of several mitochondria tracker dyes were checked, including tetramethylrhodamine ethyl ester (TMRE), MitoTracker Red CMXRos and MitoTracker Green (purchased from Invitrogen Life Science and provided by Dr. Josip Lovrić). Dyes were dissolved into dimethyl sulfoxide (DMSO, Sigma, BioReagent, for molecular biology, ≥99.9%) at the concentration of 1 μM and diluted to 1 nM to match the concentration used to stain cells. 20 μL solution of each dye were pipetted onto clean silicon wafer (5×5 mm²) followed by vacuum drying to prepare dye film. ±SIMS spectra were acquired to confirm diagnostic peaks which meet the requirements of high intensity and no overlap with major fragments from cells. Depth profiling of the three dye films was performed to monitor any signal decay or fragmentation changes under C₆₀⁺ bombardment simulating the same condition of 3D imaging of cells. The final requirement to satisfy was detectability within cells using confocal microscopy after the cells underwent chemical fixation and freeze-drying. Using these criteria, MitoTracker Red CMXRos was selected for this study. The concentration at which the labelled cell would show diagnostic fragments of the MitoTracker Red CMXRos in SIMS was determined by systemically staining the cells with the fluorescence tag at a series of concentrations. The procedure is as follows.

When the cells were ready for subculture, 0.2 mL suspended cell medium per well (to achieve a dilution factor of 18 to 15 from the Ø100 mm dish) was added to a 6 wells cell culture plate respectively. Each well contained 2 mL prewarmed fresh DMEM medium and two substrates before the cells seeding. The substrates were glass cover slip (Ø10 mm) and 0.1% poly-L-lysine (Sigma, BioReagent) modified silicon wafer (5×5 mm²). All the substrates were sterilised by 75% ethanol and dried before use. The cells were grown in the incubator for 1-2 days until approx. 80% confluence was reached. The cells density at this level facilitated SIMS analysis regarding cells locating on silicon wafer. Higher confluence level would incur severe charging during SIMS analysis because the cells and extracellular matrix secreted by cells would cover the whole silicon and insulate the substrate. The culture medium was then changed to 2.5 mL starvation media (regular DMEM growth medium with FCS reduced to 0.5%) in each well for maximum 16 h.

The starved cells were labelled first and then treated with estrogen. MitoTracker Red CMXRos was diluted to certain concentrations in DMSO, and 1 µL fluorophore solution was added to each well of the culture plate at room temperature for 40 min in the flow cabinet. The final concentrations of the fluorophore in 2.5 mL culture medium were 60 nM, 100 nM, 200 nM, 400 nM, 600 nM respectively. After the labelling, the old medium at each well was exchanged for prewarmed new starvation media, followed by treating the control cells with 0.1% ethanol (β-Estradiol carrier) for 2 h and activating BXB-ER cells at a final concentration of 5 µM β-Estradiol (Sigma, BioReagent, suitable for cell culture) for 20 min and 2 h respectively in the 37 °C incubator.

To comply with *in vacuo* analysis of SIMS and make identical comparison of SIMS and confocal microscopy, all the labelled samples underwent chemical fixation and freeze-drying at -80 °C as follows. The medium after the cells labelling were aspirated and the cells were washed with 4% (V/V) formaldehyde solution (into 1×PBS. Formaldehyde, sigma, for molecular biology 36.5-38% in H₂O) once, and then 100 µL formaldehyde solution was dropped onto each substrate. Upon 15 min at room temperature, formaldehyde solution was aspirated, and the cells were quickly washed with 0.15 M ammonia formate solution twice and milli-Q water once. Then all the liquid was eliminated from the substrates, the cells were then frozen into liquid nitrogen (LN₂), and freeze-dried at -80 °C for at least 6 h. The samples were stored in the desiccator before analysis. During the processes, the samples were covered with foil to protect the fluorophore from light.

The cells were also prepared without labelling. All the samples for this investigation were grouped as follows; Group A without labelling is for SIMS investigation of morphological changes of NIH 3T3 and NIH 3T3 BXB-ER before and after estrogen treatment, as in Table 4.1. Group B is for comparison study of SIMS and confocal image in time course, as in Table 4.2.

Table 4.1 Cell treatments in Group A

No.	Cell and substrate	Treatment	Note
A1	NIH 3T3 on silicon wafer	0.1% ethanol 2 h	As control
A2	NIH 3T3 on silicon wafer	5 µM β-Estradiol 2 h	Clarify the effect of β-Estradiol to the cell without BXB-ER protein
A3	NIH 3T3 BXB-ER on silicon wafer	0.1% ethanol 2 h	As control
A4	NIH 3T3 BXB-ER on silicon wafer	5 µM β-Estradiol 2 h	BXB-ER activation

The cells grow on silicon wafer is for SIMS analysis

Table 4.2 Cell treatments in Group B

No.	Cell and substrate	Treatment
B1	NIH 3T3 BXB-ER on silicon wafer	0.1% ethanol 2 h
B2	NIH 3T3 BXB-ER on silicon wafer	5 μ M β -Estradiol 20 min
B3	NIH 3T3 BXB-ER on silicon wafer	5 μ M β -Estradiol 2 h
B4	NIH 3T3 BXB-ER on silicon wafer	60 nM fluorophore label & 0.1% ethanol 2 h
B5	NIH 3T3 BXB-ER on silicon wafer	60 nM fluorophore label & 5 μ M β -Estradiol 20 min
B6	NIH 3T3 BXB-ER on silicon wafer	60 nM fluorophore label & 5 μ M β -Estradiol 2 h
B7	NIH 3T3 BXB-ER on glass cover slip	60 nM fluorophore label & 0.1% ethanol 2 h
B8	NIH 3T3 BXB-ER on glass cover slip	60 nM fluorophore label & 5 μ M β -Estradiol 20 min
B9	NIH 3T3 BXB-ER on glass cover slip	60 nM fluorophore label & 5 μ M β -Estradiol 2 h
B10	NIH 3T3 BXB-ER on silicon wafer	100 nM fluorophore label & 0.1% ethanol 2 h
B11	NIH 3T3 BXB-ER on silicon wafer	100 nM fluorophore label & 5 μ M β -Estradiol 20 min
B12	NIH 3T3 BXB-ER on silicon wafer	100 nM fluorophore label & 5 μ M β -Estradiol 2 h
B13	NIH 3T3 BXB-ER on glass cover slip	100 nM fluorophore label & 0.1% ethanol 2 h
B14	NIH 3T3 BXB-ER on glass cover slip	100 nM fluorophore label & 5 μ M β -Estradiol 20 min
B15	NIH 3T3 BXB-ER on glass cover slip	100 nM fluorophore label & 5 μ M β -Estradiol 2 h
B16	NIH 3T3 BXB-ER on silicon wafer	200 nM fluorophore label & 0.1% ethanol 2 h
B17	NIH 3T3 BXB-ER on silicon wafer	200 nM fluorophore label & 5 μ M β -Estradiol 20 min
B18	NIH 3T3 BXB-ER on silicon wafer	200 nM fluorophore label & 5 μ M β -Estradiol 2 h
B19	NIH 3T3 BXB-ER on glass cover slip	200 nM fluorophore label & 0.1% ethanol 2 h
B20	NIH 3T3 BXB-ER on glass cover slip	200 nM fluorophore label & 5 μ M β -Estradiol 20 min
B21	NIH 3T3 BXB-ER on glass cover slip	200 nM fluorophore label & 5 μ M β -Estradiol 2 h
B22	NIH 3T3 BXB-ER on silicon wafer	400 nM fluorophore label & 0.1% ethanol 2 h
B23	NIH 3T3 BXB-ER on silicon wafer	400 nM fluorophore label & 5 μ M β -Estradiol 20 min
B24	NIH 3T3 BXB-ER on silicon wafer	400 nM fluorophore label & 5 μ M β -Estradiol 2 h
B25	NIH 3T3 BXB-ER on glass cover slip	400 nM fluorophore label & 0.1% ethanol 2 h
B26	NIH 3T3 BXB-ER on glass cover slip	400 nM fluorophore label & 5 μ M β -Estradiol 20 min
B27	NIH 3T3 BXB-ER on glass cover slip	400 nM fluorophore label & 5 μ M β -Estradiol 2 h
B28	NIH 3T3 BXB-ER on silicon wafer	600 nM fluorophore label & 0.1% ethanol 2 h
B29	NIH 3T3 BXB-ER on silicon wafer	600 nM fluorophore label & 5 μ M β -Estradiol 20 min
B30	NIH 3T3 BXB-ER on silicon wafer	600 nM fluorophore label & 5 μ M β -Estradiol 2 h
B31	NIH 3T3 BXB-ER on glass cover slip	600 nM fluorophore label & 0.1% ethanol 2 h
B32	NIH 3T3 BXB-ER on glass cover slip	600 nM fluorophore label & 5 μ M β -Estradiol 20 min
B33	NIH 3T3 BXB-ER on glass cover slip	600 nM fluorophore label & 5 μ M β -Estradiol 2 h

Fluorophore in the table is MitoTracker Red CMXRos. The cells grow on silicon wafer is for SIMS analysis, on glass cover slip is for confocal microscope. Two substrates were placed in each well.

4.2.2 Confocal microscopy and ESEM analysis

All fluorescence images were recorded using a laser excited confocal microscopy Leica SP5 (the Faculty of Life science, The University of Manchester) using a 100 \times objective. The side of glass cover slip with freeze-dried cells on were glued onto a glass slide with 5-10 μ L Vectashield mounting medium (H-1200, Vector Laboratories Ltd.) and loaded onto the confocal microscope. The fluorescent dye was excited with Kr-Ar laser at 568 nm. All images were recorded with a resolution of 512 \times 512 pixels. For three-dimensional images of mitochondria arrangement at different cell depth, z-scans around 160 nm increments were taken through the top to bottom of the cells in 25 layers. Data processing and display was performed using Fiji software. Comparison of confocal images provides insight into the stability and integrity of the cells undergoing chemical fixation and freeze-drying during typical sample preparation for ToF-SIMS analysis.

FEI Quanta 200 ESEM (School of Chemical Engineering and Analytical Science, The University of Manchester) was used to image the cells after ToF-SIMS analysis on the areas outside C_{60}^+ ion beam bombardment. This revealed the morphology of the cells labelled and grown on the silicon wafer.

4.2.3 Imaging ToF-SIMS analysis

The cells samples grown on the silicon wafer in Group A and B were subjected to analyses using the J105 3D Chemical Imager (School of Chemical Engineering and Analytical Science, The University of Manchester). The instrument is installed with 40 keV C_{60}^+ PI gun oriented 45 $^\circ$ to the sample operated in DC mode. Fine beam tuning was implemented to focus the C_{60}^+ beam at spot

size of 500-1000 nm, and the corresponding beam current was less than 1 pA. To trace the fluorophore fragments inside of the cell, depth profiling was performed. A series of images at 128×128 pixel over 128×128 μm² or 256×256 pixel over 128×128 μm² were collected at room temperature. Mass resolution of this instrument was typically 5000 at m/z 500⁺. Following preliminary data analysis using Analyze software (developed by SAI Ltd.), principal component analysis (PCA) was performed using Matlab (2009a) using analysis routines that were developed by group members Dr. Alex Henderson and Jimmy Moore.

4.3 Result and discussion

4.3.1 Sensitivity and stability of fluorophore-MitoTracker Red CMXRos

MitoTracker Red CMXRos is a heterocyclic compound with a molecular formula C₃₂H₃₂Cl₂N₂O and molecular weight 531.20 g/mol (isotopic, 100%). The structure is shown in Fig. 4.6. As a red-fluorescent dye, it passively diffuses across the plasma membrane and accumulates in active mitochondria, reacting with thiols on proteins and peptides to form fixable conjugates. The probe could be well-retained after aldehyde-based fixatives [42].

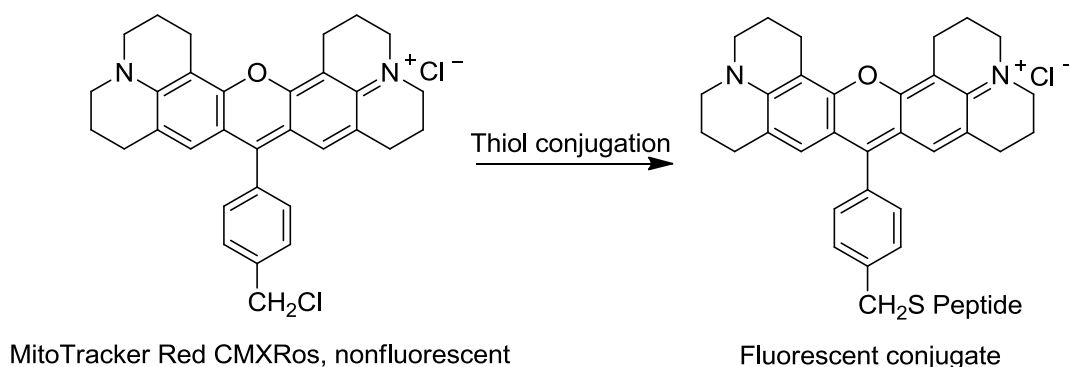


Fig. 4.6 The structure of MitoTracker Red CMXRos and the conjugation with peptide.

The film of the fluorescence dye was measured using the J105. +SIMS spectrum shows that the major fragments are detected in mass range m/z 400-550⁺ with high intensities as seen in Fig. 4.7. According to the chemical structure, the characteristic fragments can be easily assigned and are listed in Table 4.3. The fluorophore can easily lose one chlorine ion to form m/z 495.13⁺ and isotope pattern at m/z 496.13⁺, 497.13⁺, 498.13⁺, 499.13⁺, or lose two chlorine ions resulting in another two intense fragments at m/z 460.16⁺, 461.17⁺. On losing one chlorine and one nitrogen ion followed by the formation of two or three carbon-carbon double bonds, m/z 477.16⁺ and 475.16⁺ are derived. A sequence of fragments generated by the breaking of the heterocyclic ring and losing hydrocarbon are detected with very low intensities. Importantly, no fragments overlapped with biological marker at m/z 184.10⁺. It is therefore promising to trace the diagnostic peaks at m/z 495.13⁺, 477.16⁺ and 460.16⁺ of MitoTracker Red CMXRos in fibroblast cells.

The same sample was also under analysis using the BioToF-SIMS in positive and negative mode as in Fig. 4.8. The +SIMS spectra shows similar fragments at m/z 460-500⁺ as J105 with slightly different mass; the -SIMS spectra demonstrates the intensive fragments are below mass m/z 200⁻ which are not outstanding from other normal peaks in negative spectra, moreover, the fragments around m/z 200-700⁻ are not intense enough to be useful characteristic peaks.

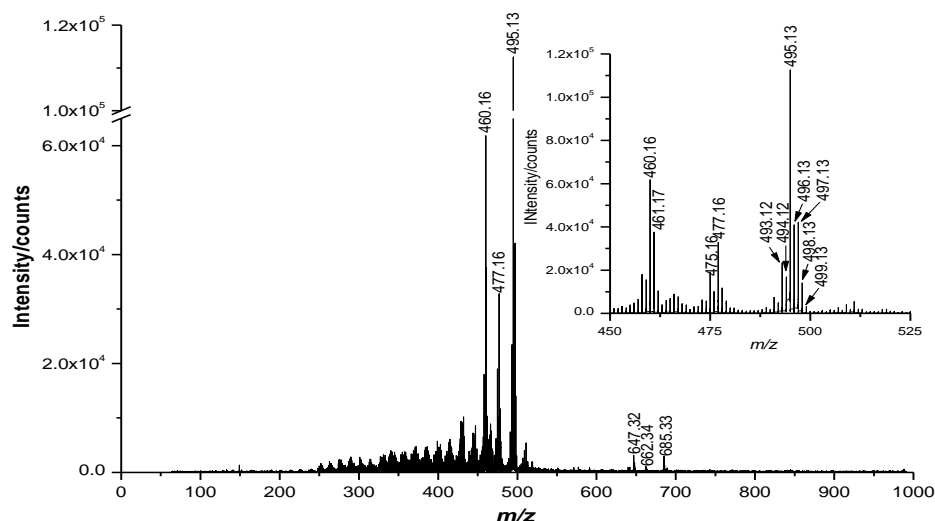


Fig. 4.7 +SIMS spectrum of MitoTracker Red CMXRos using the J105 3D Chemical Imager. Spectral dose is 3.2×10^{12} ions/cm² with 40 kV C₆₀⁺ PI beam.

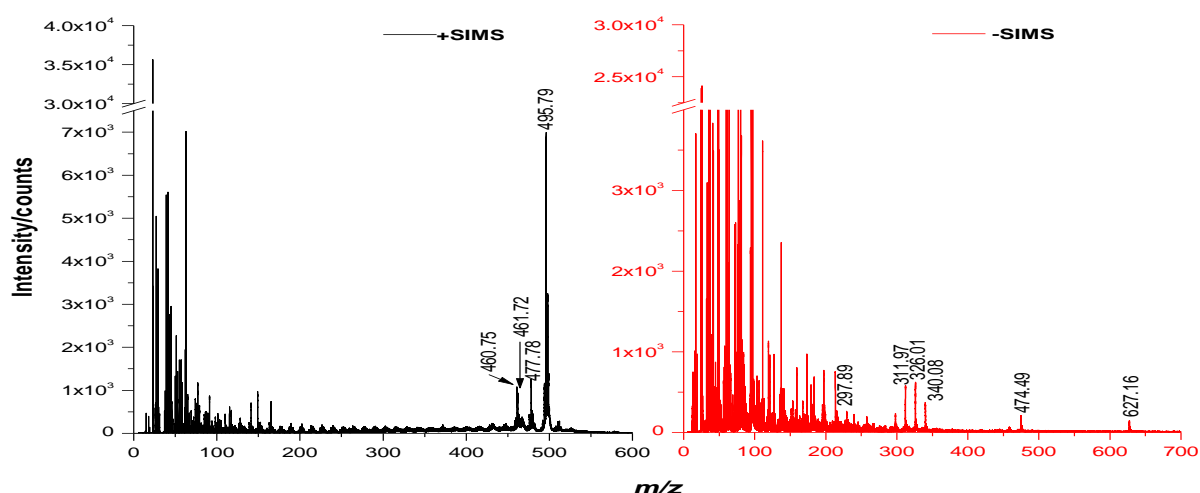


Fig. 4.8 \pm SIMS spectra of MitoTracker Red CMXRos using the BioToF-SIMS. Spectral dose is 1.56×10^{13} ions/cm² with 20 keV C₆₀⁺ PI beam. The +SIMS spectra shows identical fragments at m/z 460-500⁺ as J105; the -SIMS spectra demonstrates the intensive fragments are below mass m/z 200⁻ which are not characteristic from other normal peaks in negative spectra, moreover, the fragments around m/z 200-700⁻ are not intense enough to be characteristic peaks.

Table 4.3 Peak assignment of the fluorescent probe MitoTracker Red CMXRos

Fragments/ m/z	Assignment	Note
460.16	[C ₃₂ H ₃₂ N ₂ O] ⁺	[M-2Cl] ⁺
461.17	[C ₃₂ H ₃₃ N ₂ O] ⁺	[M-2Cl+H] ⁺
475.16	[C ₃₂ H ₂₆ CINO] ⁺	[M-NH ₆ Cl] ⁺
477.16	[C ₃₂ H ₂₈ CINO] ⁺	[M-NH ₄ Cl] ⁺
495.13	[C ₃₂ H ₃₂ CIN ₂ O] ⁺	[M-Cl] ⁺ , m/z 496.13, 497.13, 498.13 and 499.13 are isotope peaks.

Simulating the depth profiling mode under the same conditions of real cell analysis, the fluorophore film was etched through to check the stability under the continuous bombardment of one micrometre-focused C₆₀⁺ ion beam. The changes of selected ions along with depth profiling are plotted in Fig. 4.9 (a). Within expectation, the intensity of m/z 495.13⁺, 477.16⁺ and 460.16⁺ demonstrating the fluorophore decrease gradually along with the etching through the fluorophore film; m/z 167.82⁺ represents silicon adducts from the substrate, increase drastically where the fluorophore peaks plunge down. The positive spectra from 1st, 2nd and 5th etching depth are shown

in Fig. 4.9 (b). It is clear that except for the intensities drop of the diagnostic peaks of the fluorophore marked with the blue asterisks, no new fragments from the dye are induced by the continuous bombardment, indicating the chemical structure of the fluorophore is quite stable and forms several intense fragments even sputtered with high flux of C_{60}^+ PI beam. This offers possibilities to detect and locate the fluorescent probe within the real cell in different depth and investigate the mitochondria rearrangement.

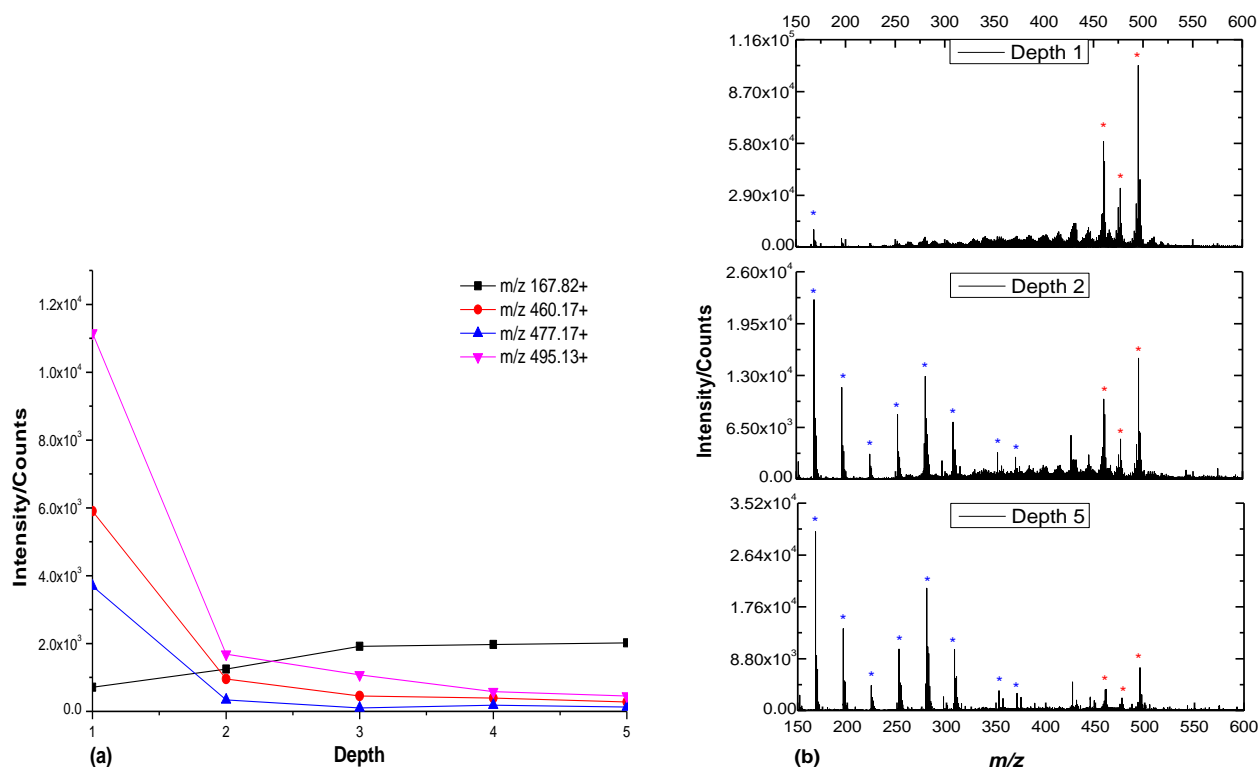


Fig. 4.9 Depth profiling of MitoTracker Red CMXRos film. Each depth is with a dose of 2.8×10^{14} ions/cm² with 40 keV C_{60}^+ PI beam, and the total dose is 1.4×10^{15} ions/cm². (a), changes of selected ions along with depth profiling. m/z 167.82⁺ represents silicon adducts from the substrate; m/z 495.13⁺, 477.16⁺ and 460.16⁺ are fragments from MitoTracker Red CMXRos; (b), +SIMS spectra of 1st, 2nd and 5th depth. Peaks marked with blue star indicate silicon adduct peaks; with red star indicate characteristic peaks of the fluorophore. It is clear that except for the intensities drop of the diagnostic peaks no new fragments from the dye are induced by the continuous bombardment, indicating the chemical structure MitoTracker Red CMXRos is reasonably stable.

4.3.2 Morphological changes of NIH 3T3 BXB-ER cells following Raf/ERK activation in sample Group A

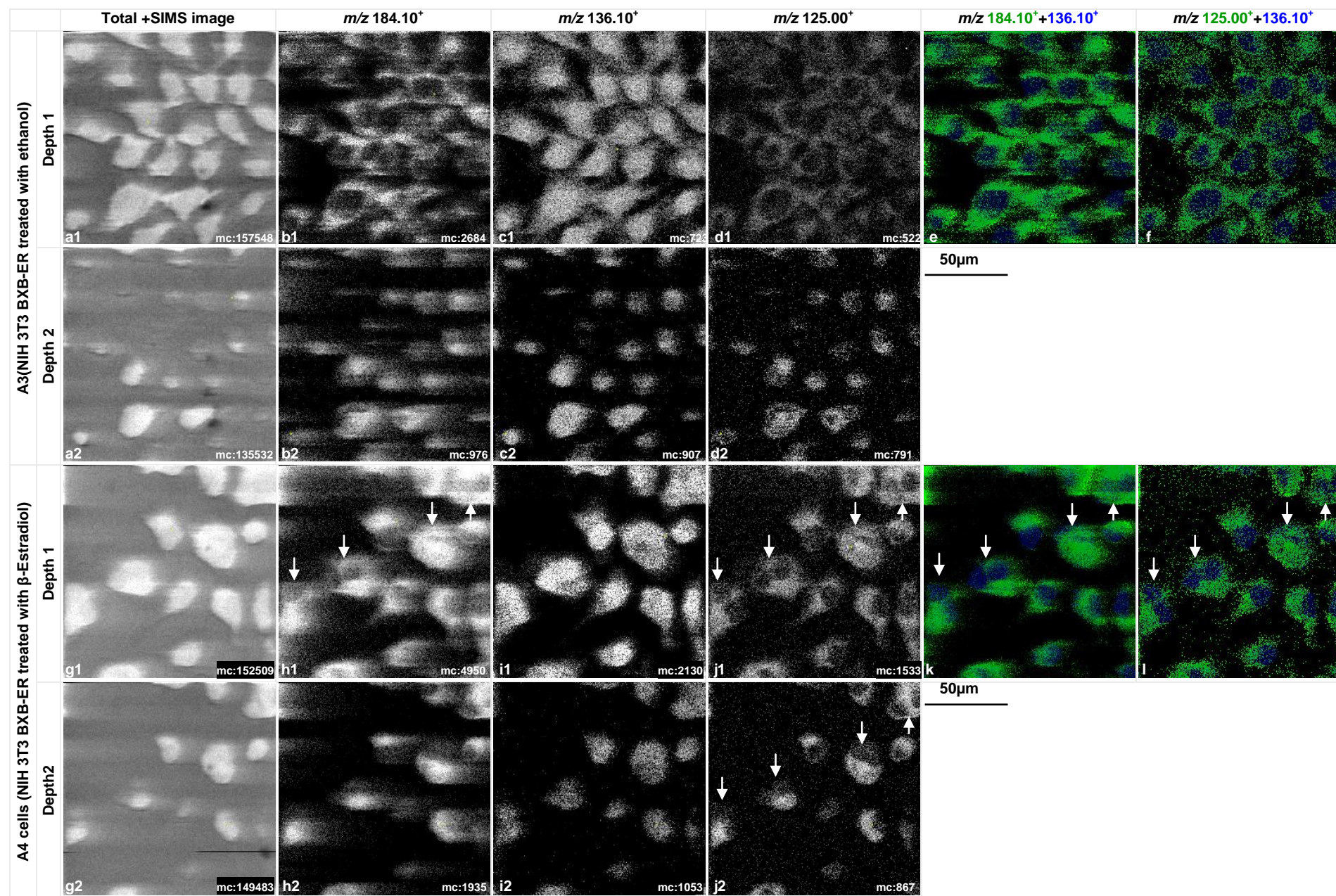
Within sample group A, NIH 3T3 and NIH 3T3 BXB-ER cells were grown on modified silicon wafer and treated with 0.1% ethanol or 5 μ M β -Estradiol for 2 h respectively as listed in Table 4.1. Each sample was prepared on two pieces of silicon wafer in parallel, and analysed at least twice using the J105 on each silicon wafer. A1 and A2 are NIH 3T3 cells, the morphology of the two samples did not show distinct differences either with ethanol (A1) or estrogen (A2) treatment, the data is as supplement shown in appendix II. Without a fused estrogen receptor, it is expected that estrogen cannot trigger the RAF kinase which could have major effects on A1 and A2 cells.

In contrast to the wild-type NIH 3T3, NIH 3T3 BXB-ER cells treated with ethanol (A3) and with β -Estradiol (A4) display distinct differences in morphology as shown in Fig. 4.10. Depth profiling was also performed on both samples with a high C_{60}^+ PI dose of up to 7.49×10^{14} ions/cm² at each depth

for investigating subcellular structure of the cells. After three analysis cycles, the cells were almost etched away with very little cellular materials left in the images of 3rd depth. Only the images from first two depths are therefore displayed in Fig. 4.10. With the C₆₀⁺ beam finely focused making each pixel 500 nm, the filopodia of the cells and the outline of the cytoplasm membrane were clearly shown. Of the most interesting peaks in the SIMS spectra, m/z 184.10⁺ is an important biomarker in SIMS, along with m/z 125.00⁺, since they arise from fragments of phosphocholine lipids, e.g., glycerophosphocholine lipids (GPCho) and sphingomyelin (SM), which are vital building blocks for cytoplasm membrane and subcellular organelles membrane (the peaks assignment is referred to Fig. 3.10 and Table 3.3). In addition, m/z 136.10⁺ is from adenine representing the nucleus [40].

After the first sputter cycle (depth1) the total +SIMS image of A3 cells in Fig. 4.10 (a1) and A4 cells in Fig. 4.10 (g1) show some different features. A3 cells seem to spread out densely on the silicon substrate with filopodia clearly seen, whereas the A4 cells appear to round up following the addition of β -Estradiol. The distributions of cellular components represented by different peaks differ distinctly between the two samples. For A3 cells in Fig. 4.10 (b1 and d1), the ions images indicate that the membrane materials at m/z 184.10⁺ and 125.00⁺ distribute evenly and form the circular structure. As expected, in the middle area where m/z 184.10⁺ and 125.00⁺ are absent allow rooms for nuclei represented by ion image of m/z 136.10⁺; for A4 cells, the membrane materials as seen in Fig. 4.10 (h1 and j1) appear shifted so that it is thicker to one side than the other. Moreover, the nuclei of A3 cells in Fig. 4.10 (c1) are significantly larger than those of A4 cells in Fig. 4.10 (i1) according to the measurement of the size of nuclei by pixel. Additionally, four cells out of the eleven cells in ToF-SIMS image are likely in the mitosis phase or just finishing the division as the arrows indicated in Fig. 4.10 (h1, j1, k and l). It is uncertain if it is the normal division or the cells are resting in the mitosis phase as a consequence of estrogen treatment. Another possibility is the cell nuclei are really close together resulting from the formation of new membrane polarity. All the morphological changes are more clearly shown in the overlay images of m/z 184.10⁺+136.10⁺ and m/z 125.00⁺+136.10⁺ for A3 cells in Fig. 4.10 (e, f) and A4 cells in Fig. 4.10 (k, l).

Fig. 4.10 Comparing the morphological changes of NIH 3T3 BXB-ER cells without and following Raf/ERK activation using the J105 3D Chemical Imager. Depth profiling was performed on A3 (NIH 3T3 BXB-ER treated with ethanol) and A4 (NIH 3T3 BXB-ER treated with β -Estradiol) cells. The cells were etched away in three cycles using a 500 nm-focused 40 keV C₆₀⁺ PI beam with a PI dose of 7.49×10^{14} ions/cm² of each depth over $128 \times 128 \mu\text{m}^2$ at 256×256 pixels. Images were generated using the Analyze software. The membrane materials are represented by m/z 184.10⁺ and 125.00⁺ from phosphocholine lipids; the nucleus is indicated by m/z 136.10⁺ from adenine. As the 3rd depth only shows very little cellular information, here are shown only total ion and selected ion images in positive ion mode from 1st and 2nd depths of A3 and A4 cells, as well as overlay images of m/z 184.10⁺+136.10⁺ and m/z 125.00⁺+136.10⁺ that display the arrangement of the membrane and nuclei. The maximum counts (mc) can be read on the images. (The figure is on next page).



It can be clearly seen that following the estrogen treatment the distribution of m/z 184.10⁺ and m/z 125.00⁺ representing phosphocholine lipids change from an evenly distribution around nuclei in A3 cells to a severely asymmetric distribution to one side in A4 cells, meanwhile, the nuclei are seen to shrink. Compared with 4-OHT treatment which have the similar function to active RAF kinases as β -Estradiol, the mitochondria of the NIH 3T3 BXB-ER showed a similar rearrangement pattern, from an evenly distribution around the nuclei to migrating to the two sides of the nuclei as displayed in Fig. 4.2 (a to b or c to d) [6]. As GPCho are the most abundant phospholipids and comprise 40% of total mitochondrial phospholipids as determined in yeast cells [43], in addition, the most intense fragments from GPCho in SIMS spectra are m/z 184.10⁺ and m/z 125.00⁺, it is highly likely that the rearrangement of distribution of m/z 184.10⁺ and m/z 125.00⁺ could be attributed to the mitochondria remodelling in response to the estrogen treatment. This could be further improved by tracing the fluorescent mitochondria marker in ToF-SIMS analysis as described in section 4.3.3. The nuclei shrinkage as seen in ToF-SIMS images in Fig. 4.10 are in agreement with previous work [3] as shown in Fig. 4.3 (c), which revealed that nuclear volume decreases by 28% in estrogen treated BXB-ER cells compared with control cells treated with ethanol. It was further proved that the decrease is not directly linked to cell cycle distribution.

The comparison study of morphological changes of mouse embryo fibroblast cells in Group A using ToF-SIMS is in good agreement with the existing biological studies [3, 6], and the chemical mapping of the cells indicates the changes that displayed using the membrane lipid fragments m/z 184.10⁺ and m/z 125.00⁺. Although a statistical study involving the analysis of hundreds of cells using SIMS is highly time-consuming and impractical at this stage, the repeated experiment were carried and the results as supplements are provided in the appendix II. This is also one reason for combining the fluorescence study with ToF-SIMS analysis. In doing so, the sample qualities concerning cells integrity and biological processes preservation are checked by fluorescence imaging firstly to ensure the following SIMS analysis acquiring meaningful data that could answer the biological questions more successfully.

4.3.3 Time course study of mitochondrial rearrangement using confocal microscopy and ToF-SIMS in sample Group B

The NIH 3T3 BXB-ER cells in Group B (Table 4.2) were cultured on different substrates, silicon and a glass cover slip for SIMS analysis and confocal microscopy respectively, and labelled with MitoTracker Red CMXRos at different concentrations, followed by estrogen treatment in a time course experiments. This aimed to determine an appropriate dye concentration suitable for both confocal and ToF-SIMS analysis, and to trace the fragments of the fluorescent probe for better understanding of mitochondria rearrangement in reaction to estrogen treatment.

The recommended concentration of MitoTracker Red CMXRos for staining cells in biological studies is in the range from 50-500 nM. The higher the concentration, the more potentially toxic the dye is to the cells. Additionally, the dye could lose the specificity to mitochondria and label other cellular compartments as well. However, a higher concentration might allow the detection of the dye in both confocal fluorescence and SIMS analysis. In this study, the cells underwent chemical fixation, multiple wash steps and freezing-drying, which is different to the standard confocal microscopy protocol in which the cells are kept alive or at least not dried. This requires the fluorescent probe to be traceable after the sample preparation that is identical with the protocol

used in SIMS analysis. Therefore, the concentration of the fluorescent dye must be carefully selected to minimize any disturbance to the ongoing biological process in the cells at the same time being detectable by SIMS.

The initial ToF-SIMS experiments were performed to trace the fluorescent probe peaks in control samples, B4, B10, B16, B22 and B28 cells, which were labelled with 60, 100, 200, 400 and 600 nM MitoTracker Red CMXRos respectively and treated with ethanol. The results showed that the dye fragments at m/z 495.13⁺, 477.16⁺ and 460.16⁺ could be clearly distinguished in the 400 nM and 600 nM fluorophore labelled cells with reasonable intensities for the image, but were in very low intensity in 200 nM fluorophore labelled cells and not seen at all in 60 nM and 100 nM fluorophore labelled cells. SIMS analysis of B22 cells (400 nM fluorophore label & 0.1% ethanol 2 h) are presented as well as PCA data in Fig. 4.11. The dye fragment ions at m/z 461.16⁺ and 461.17⁺ have the reasonable intensity to be detected while the biomarker m/z 184.10⁺ is clearly seen in Fig. 4.11 (b). The PCA data process further separates the dye fragment ions and cellular materials in PCA loading 7 as seen in Fig. 4.11 (d), and the image of PCA loading 7 in Fig. 4.11 (c) shows the scattered fluorescence probe over the area of the cells.

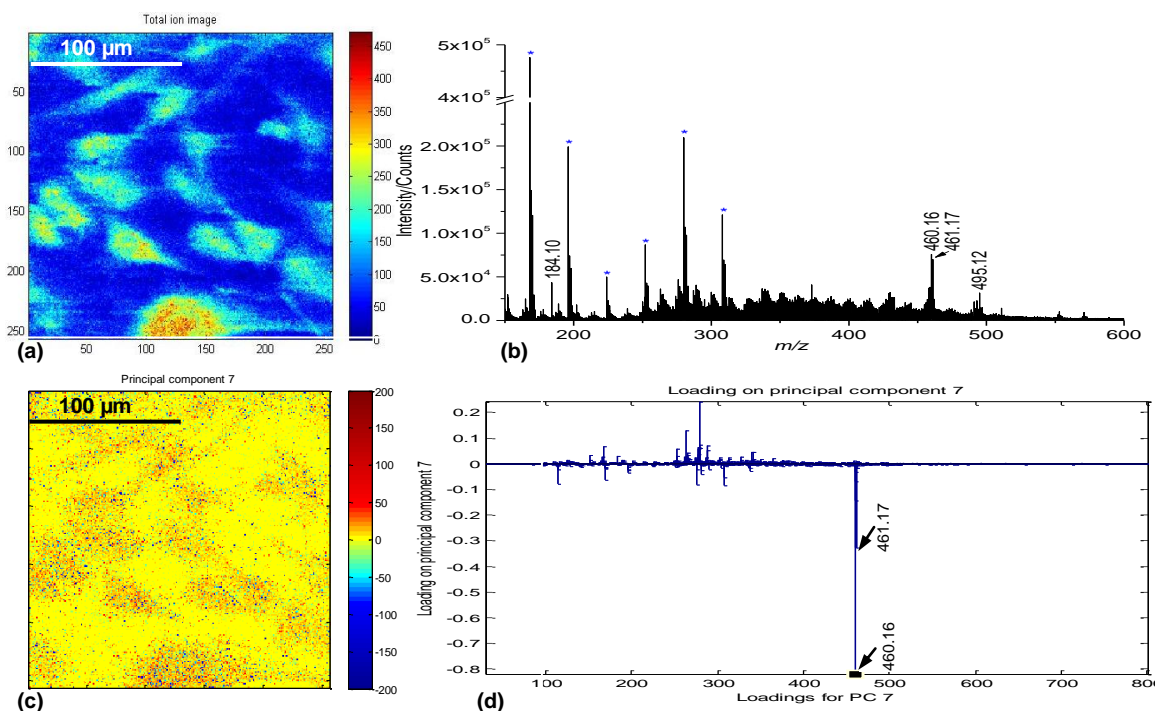


Fig. 4.11 ToF-SIMS analysis of B22 cells (NIH 3T3 BXB-ER, 400 nM MitoTracker Red CMXRos label & 0.1% ethanol 2 h) and PCA data processing. Spectral dose with 1 μm-focused 40 keV C₆₀⁺ PI beam was 1.92×10^{14} ions/cm² over 200×200 μm² with 256×256 pixel per image. (a), total +SIMS image. The colour scale corresponds to the ion intensity and the counts can be read on the scale bar; (b), +SIMS spectrum. The peaks labelled with blue asterisks are silicon adducts peaks from the substrate; (c), principal component 7 image. The colour scale corresponds to positive and negative principal components; (d), the loading plot of principal component 7. (c) and (d) show that PCA can pull out xenobiotic fluorescence dye at m/z 461.16⁺ and 461.17⁺ from the cellular materials.

The confocal analyses were performed at least six times for each sample in parallel on cells labelled with 60, 100, 200, 400 and 600 nM MitoTracker Red CMXRos followed by estrogen treatment in time courses. As labelling concentration greater than 200 nM is required for SIMS analysis, only the fluorescence images of the cells labelled with 200, 400 and 600 nM fluorescent probe followed by estrogen treatment in time courses are shown here for comparison as in

Fig. 4.12. The cells react very differently to labelling with different concentrations. At a concentration of 200 nM, the cells developed naturally with small concentrated spots around the nuclei. The red spots represent the subcellular organelles mitochondria, which are also the targets in the ToF-SIMS analysis. Following the estrogen treatment as a function of time, the mitochondria migrates from evenly spreading around the nuclei in B19 control cells to concentrating in the two opposite sides of the nuclei as shown in B20 cells with 20 min β -Estradiol treatment. In B21 cells incubated with β -Estradiol 2 h, the remodelling of mitochondria to the opposite sides of nuclei is even more pronounced as shown in Fig. 4.12. This behaviour is also repeated in the B26 and B27 cells labelled with 400 nM fluorophore and then added with β -Estradiol for 20 min and 2 h respectively, but with no significant difference between the two samples as shown in the enlarged images (B26 in yellow dashed frame, B27 in blue dashed frame) in Fig. 4.12. The B25 control cells have a the honeycombed structure resembling to B31, B32 and B33 cells labelled with 600 nM fluorescent dye.

The reason for the variation of the reactions of cells to the same concentration of the fluorescence dye is not clear. It is postulated that at the highest concentration, *i.e.* 600 nM, the fluorescent probe becomes too toxic to the mitochondria, subsequently resulting in apoptosis in the B31, B32 and B33 cells. However, the level of toxicity of the fluorescent dye is still unknown. The study of human osteosarcoma 143B TK-(p+) cells and the derived p⁰ 206 cell line devoid of mitochondrial DNA has revealed that chloromethyl-X-rosamine itself has no toxicity to either cell line in the concentration range 100-250 nM unless photoirradiated at light doses greater than 2 J/cm². The photodamaged cells initially exhibited swollen degenerative mitochondria and later the apoptotic nuclei [44]. In this study, the cells have been formalin fixed and then freeze-dried prior to exposure to the laser, so that the photodamage should not have an effect on the dead cells. Owing to the fact that the unnatural subcellular structure is specific to the cells stained with excessively high concentrations of the fluorescent dye, it can also be excluded that the freeze-drying in sample preparation is the reason for the honeycomb-like structure. Therefore, high doses of MitoTracker Red CMXRos could have potentially negative affects to the function of mitochondria, subsequently causing cellular changes and even apoptosis of the cells. However, further investigation is still required regarding the toxicity of the fluorescent dye. With regard to the photosensitising action that induces mitochondria swelling in the living CMXRos labelled cells, the chemical fixation and freeze-drying might be one solution to preserve the original morphology and chemical information in the labelled cells.

The fluorescence images in Fig. 4.12 show the mitochondria rearrangement as a consequence of the estrogen exposure in NIH 3T3 BXB-ER cells. Moreover, the data provides strong evidence of the cells maintaining their cellular integrity and consistent mitochondria rearrangements following the non-routine sample preparation, that is chemical fixation and freeze-drying following the fluorescent tagging to the cells. The images also serve as a reliable indicator for tracking the fluorescent probe using ToF-SIMS.

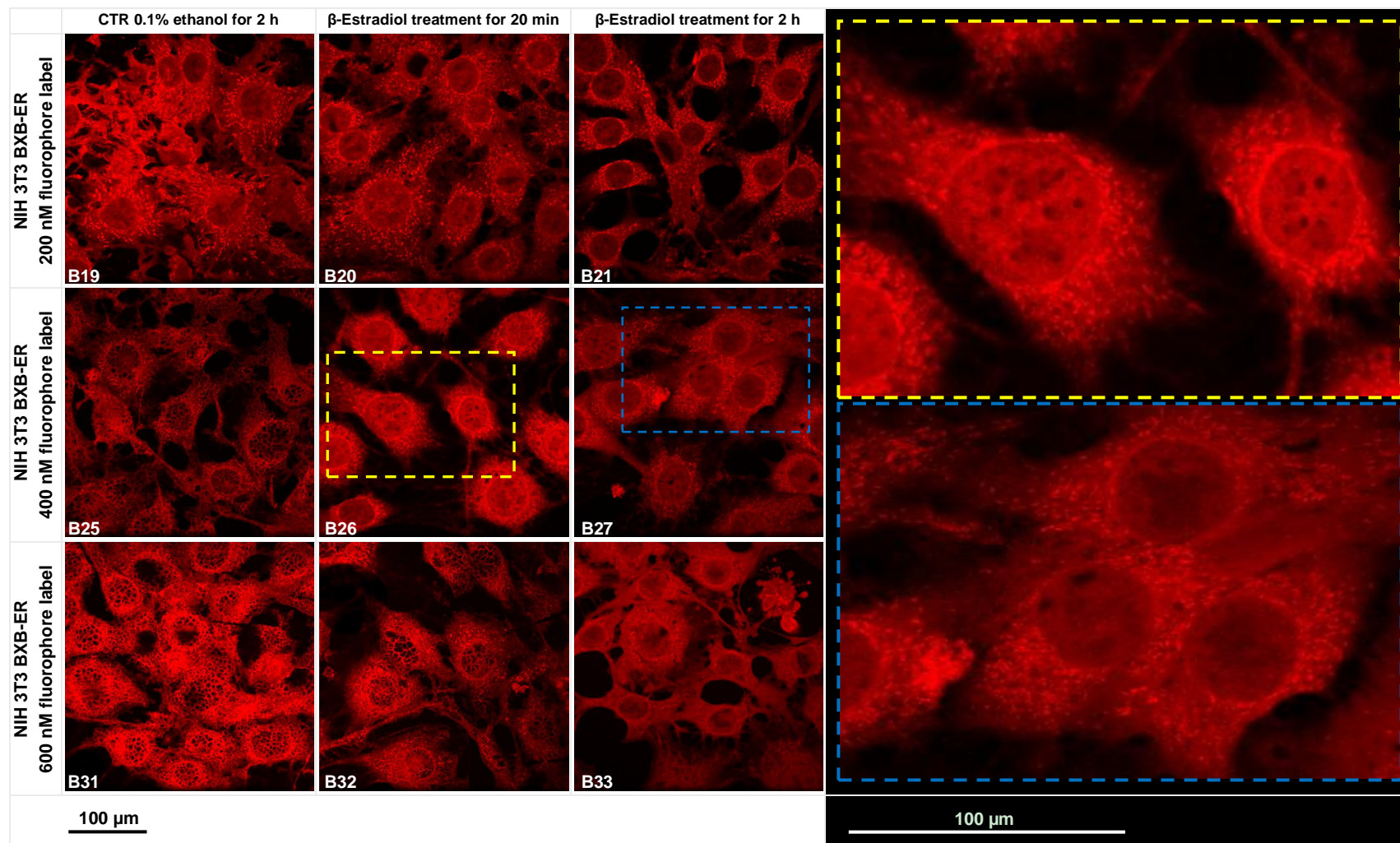


Fig. 4.12 Fluorescence images of NIH 3T3 BXB-ER cells labelled with MitoTracker Red CMXRos at varying concentrations at 200, 400, 600 nM using confocal microscopy. The labels on the images are sample numbers as in Table 4.2.

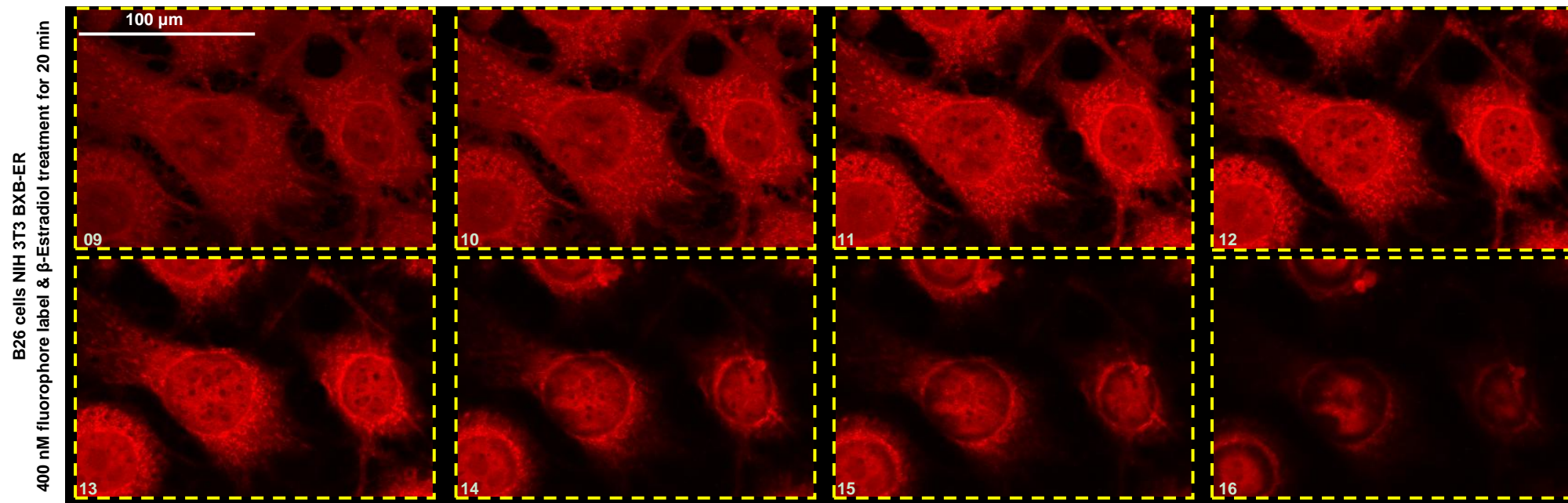


Fig. 4.13 3D depth fluorescence images taken from the yellow frame area of B26 cells (NIH 3T3 BXB-ER, 400 nM MitoTracker Red CMXRos label β -Estradiol treatment for 20 min). Totally 25 stacked images in 4 μ m depth across the whole cells body was taken numbered from 01 to 25 in the stack. Here images 09-16 in the middle part are displayed for better visualization of the scattering of the mitochondria around the nuclei.

To clarify the spatial distribution of the mitochondria, the 3D depth fluorescence images were taken from the area within the yellow frame of B26 cells (NIH 3T3 BXB-ER, 400 nM MitoTracker Red CMXRos label β -Estradiol treatment for 20 min). A total of 25 stacked images within 4 μm depth across the whole cell body were taken, numbered from 01 to 25. Images of No. 09-16 in the middle depth of the cell body are displayed in Fig. 4.13 for better visualization of the scattering of the mitochondria around the nuclei. Apparently, the most intense mitochondria exist in the biggest cross section of the cell body. This also indicates that the fluorescence dye peaks should be expected at different cell depths in the B23 and B24 cells and accordingly the subsequent ToF-SIMS analyses focused were performed in depth profiling mode.

Unlike B26 and B27 cells grown the glass cover slip, B23 and B24 were cultured on silicon wafers but with exactly same treatments correspondingly (400 nM MitoTracker Red CMXRos label and β -Estradiol treatment for 20 min in B23 and B26 cells, 400 nM fluorophore labelling and β -Estradiol treatment for 2 h in B24 and B27 cells). To obtain detail depth information within the cell body, the 40 keV C_{60}^+ PI beam was focused down to 1 μm and rastered across $128 \times 128 \mu\text{m}^2$ on B23 cells. Depth profiles of B23 cells were acquired in 9 depths. The total ion and selected ion images in positive ion mode are shown in Fig. 4.14. The selected ions are representing the membrane (m/z 184.10⁺ and 125.00⁺ from phosphocholine lipids), nuclei (m/z 136.10⁺ from adenine) and the fluorescent probe (m/z 461.17⁺ and m/z 495.13⁺ respectively). It is clear that the integrity of the membrane and nuclei are well preserved and located within expectation in depth 2, 3 and 4. The fragment ions of fluorescent probe at m/z 461.17⁺ and m/z 495.13⁺ have close intensities to m/z 184.10⁺ in +SIMS spectra, and can be imaged in each depth within the cells body. Even with interference from the background noises, the images of the fluorophore ions are shown more intense and concentrated within the cell bodies at each depth. The morphology shown in the total ion image of the 1st depth in Fig. 4.14 is consistent with the ESEM image took following ToF-SIMS analysis as in Fig. 4.16. The filopodia in the ESEM image ranging from 200-550 nm in size are also duplicated in total ion image as in Fig. 4.14.

Though the images in Fig. 4.14 were generated by Analyze software without further image processing, the fluorescence dye ions were clearly located within the cell bodies. The further PCA process was then performed to eliminate background noise arising from the silicon substrate, which aimed to precisely locating the fluorophore and their correlation with membrane and nuclei. Depth 3 and 4 from the depth profiling data of B23 cells were selected to demonstrate the PCA processing due to the two depth sections having bigger nuclei area than the other depths. Once the pixels of substrate peaks mainly silicon adducts were removed, the ion images of m/z 184.10⁺ (representing membrane), m/z 460.16⁺ and m/z 495.13⁺ (representing fluorescence probe) were generated as in Fig. 4.15. It demonstrates that the better distributions of selected ions. The nuclei are expected to reside in the hollow part inside the membrane circle. Interestingly, fluorescent probe ions in the images are scattered around the nuclei as highlighted with the red dashed circles and more intense at the opposite sides of the nuclei in depth 4, which is in good accord with the fluorescence images of B26 cells in Fig. 4.12 and Fig. 4.13. To image the subcellular structures in exquisite detail, further efforts were made to image B24 cells with more collimated C_{60}^+ ion beam.

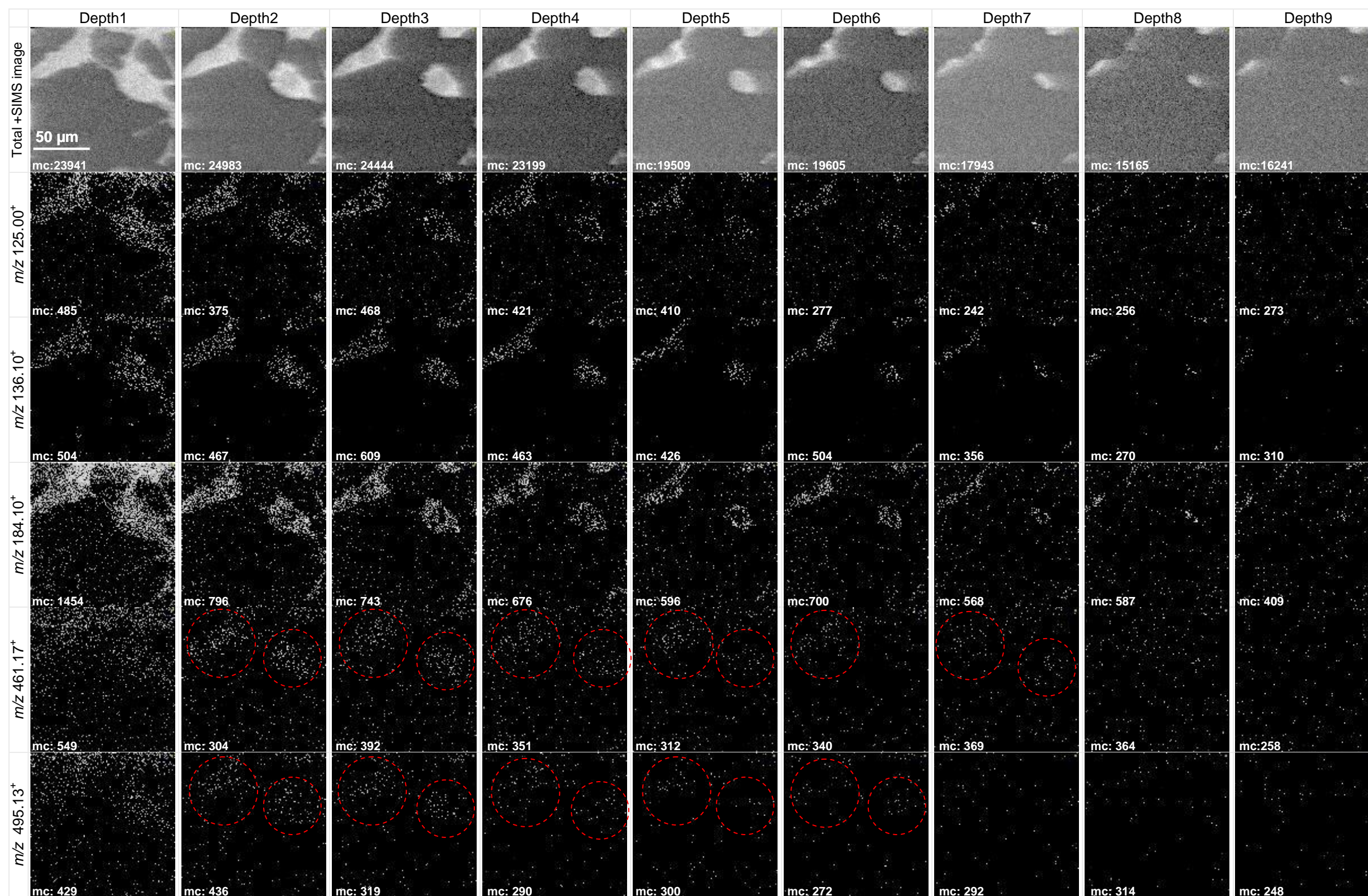


Fig. 4.14 Depth profiling of B23 cells (NIH 3T3 BXB-ER cells, 400 nM MitoTracker Red CMXRos label & β -Estradiol treatment for 20 min) in positive ion mode using the J105 3D Chemical Imager. The spectral dose was 1.17×10^{14} ions/cm² of each depth using 1 μ m-focused 40 keV C₆₀⁺ PI beam over 128 \times 128 μ m² with 128 \times 128 pixels and the total dose of 1.05×10^{15} ions/cm² was used to etch away the cells in nine depths. The membrane is represented by m/z 184.10⁺ and 125.00⁺ from phosphocholine lipids, the nucleus by m/z 136.10⁺ from adenine. Images were generated using the Analyze software. The distribution of the dye fragment ions suggest the dye to be within the cell body. A difference is observed in the most intense fragment ions between this and MitoTracker Red CMXRos standard film spectrum in Fig. 4.14. Here, the most intense fragments from the dye is m/z 461.17⁺ and m/z 495.13⁺ instead of m/z 460.16⁺ and m/z 495.13⁺, but all these peaks are fragments from the fluorescent dye.

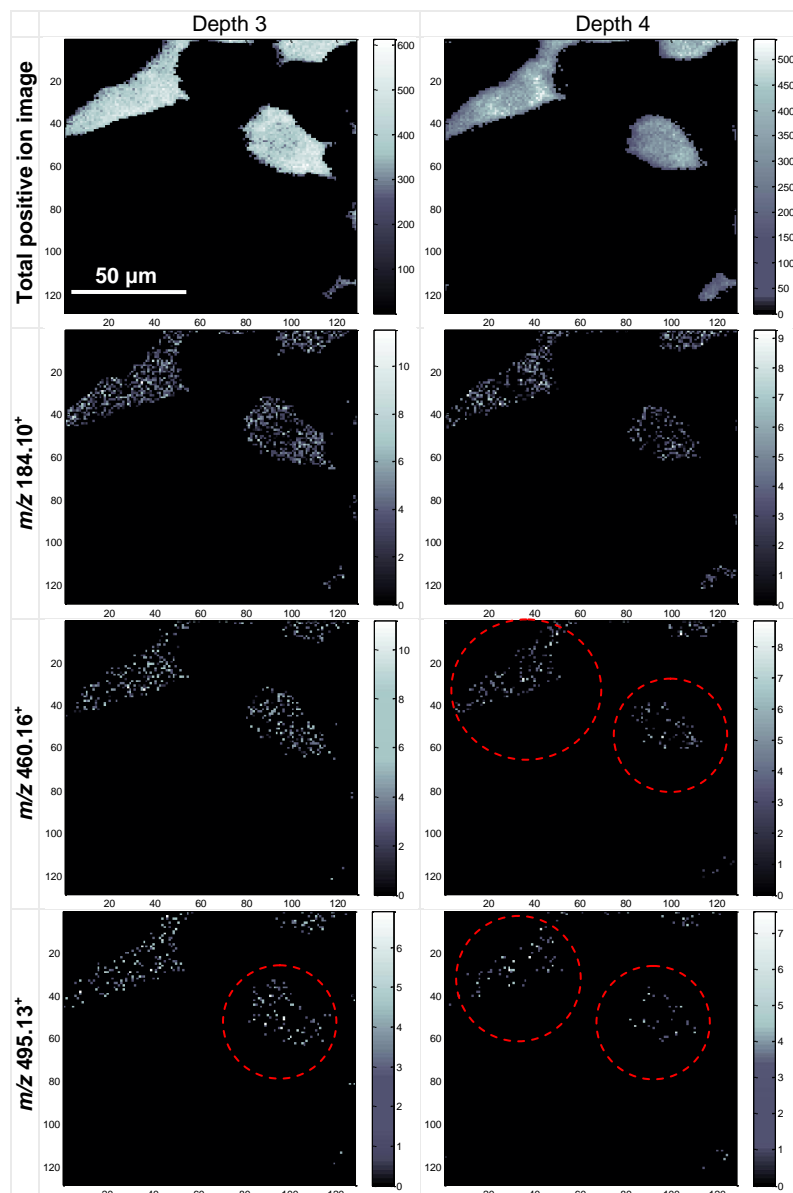


Fig. 4.15 PCA data processing of depths 3 and 4 of B23 cells. The pixels from substrate that mainly yields silicon adducts ions were removed, and then the ion images of m/z 184.10⁺ (represent membrane), m/z 460.16⁺ and m/z 495.13⁺ (represent fluorescence probe) were generated. The gray colour scale corresponds to the ion intensity and the counts can be read on the scale bar. The fluorescence dye ions at the m/z 460.16⁺ and m/z 495.13⁺ show better distributions around nuclei and are within the membrane area. The nuclei are located the hollow part inside the membrane area.

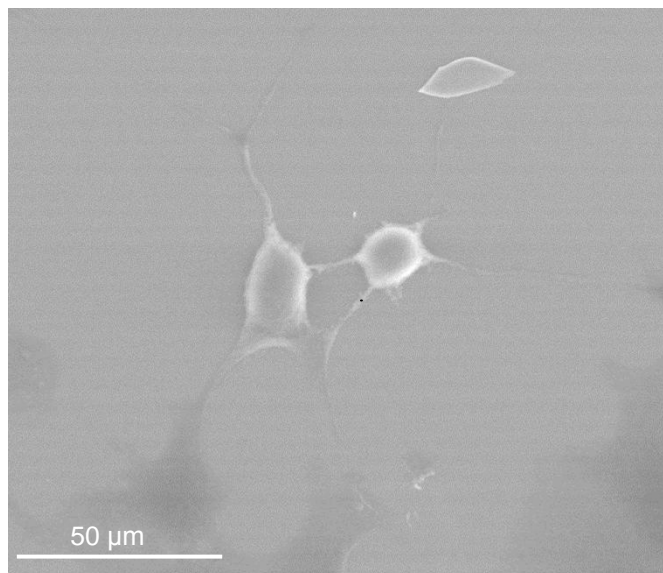
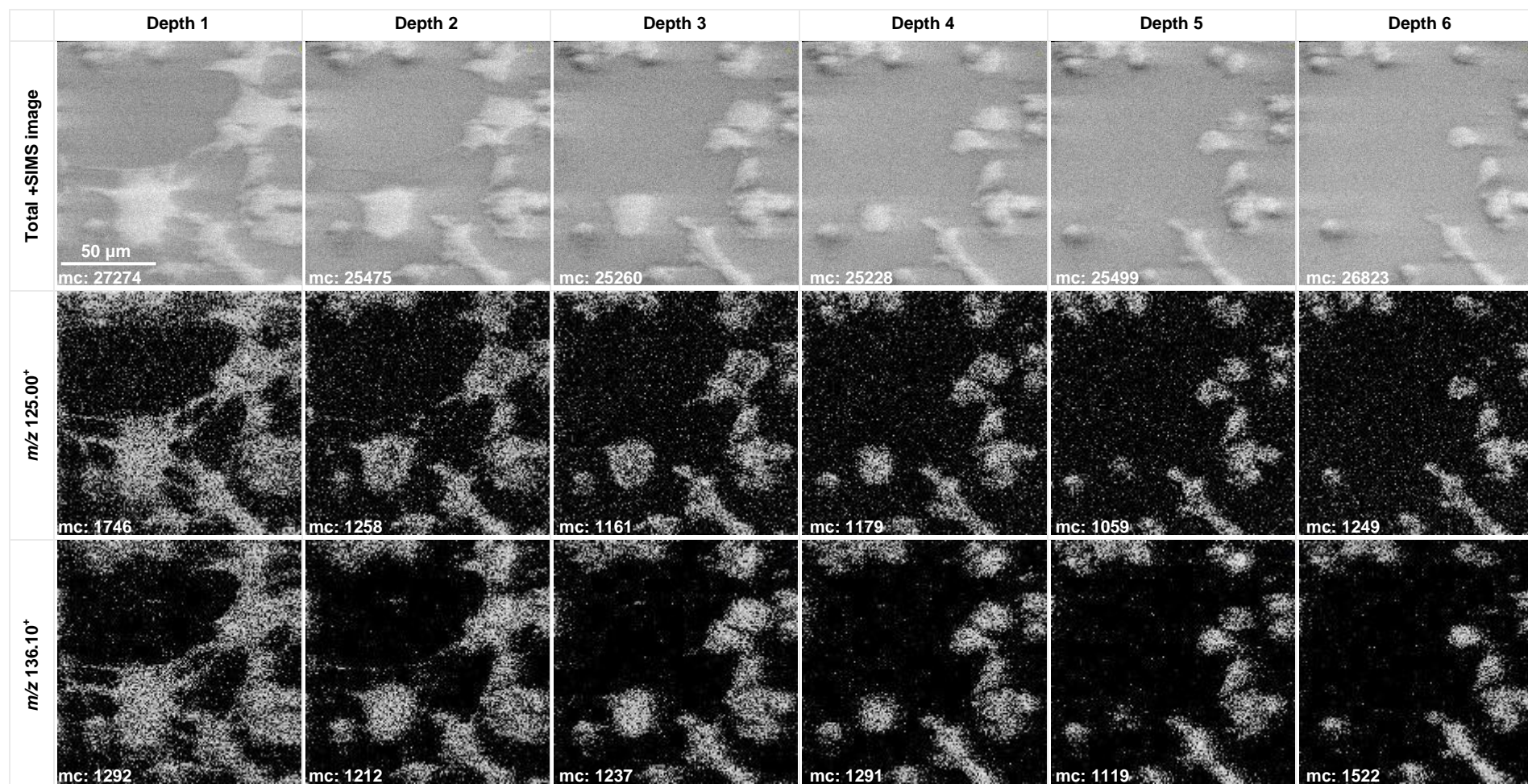


Fig. 4.16 ESEM image of B23 cells. The image was taken after ToF-SIMS analysis over the areas outside of the C_{60}^+ ions bombardment. The analysis was performed using 10 keV electron gun over $160 \times 160 \mu m^2$ with 1600×1600 pixel. The filopodia of the cells is clearly seen extending out from the cell body with a dimension approx. 200-550 nm.

For a high resolution image of B24 cells, 256×256 pixels were acquired over $128 \times 128 \mu m^2$ area using a 500 nm-focused 40 keV C_{60}^+ PI beam. The C_{60}^+ ion beam was finely tuned to pass through a 10 μm aperture whilst avoiding excessive use of the alignment deflectors, so that the collimated beam passes along the central axis of the ion gun with minimal perturbation allowing an ion beam less than 500 nm spot size with less than 1 pA current to be achieved. Images at six depths were obtained on the B24 cells with 500 nm pixel size to match beam diameter as shown in Fig. 4.17. The membrane, nuclei and the fluorescent dye are located by imaging m/z 184.10⁺ and 125.00⁺ (from phosphocholine lipids), m/z 136.10⁺ (from adenine), two groups of peaks m/z 461.17⁺ with the addition of m/z 460.16⁺ and m/z 495.13⁺ with its isotope peaks respectively. Compared to Fig. 4.14, total +SIMS image as well as ion images of m/z 125.00⁺ and 136.10⁺ have clearer outline and sharper edges in filopodia of the cells; in contrast the distribution of m/z 184.10⁺ smudges around the cell body and lose the sharp contour of the cell. This could be caused by some extra cellular matrix spread around the cells body that also comprise GPCho and SM lipids yielding main fragment at m/z 184.10⁺ [45]. Of most interest, in comparison with the location of membrane and nuclei in depth 2, the fluorescence dye fragments m/z 461.17⁺ and 460.16⁺ scatter around two sides of the nuclei as highlighted using red dashed circle in Fig. 4.17. Except for the highlighted area by the red dashed circle, the distributions of the dye ions in other cells in the image lose the certain pattern but still concentrate within the cell bodies at different depths as shown in the green-dash-line circled areas in Fig. 4.17.



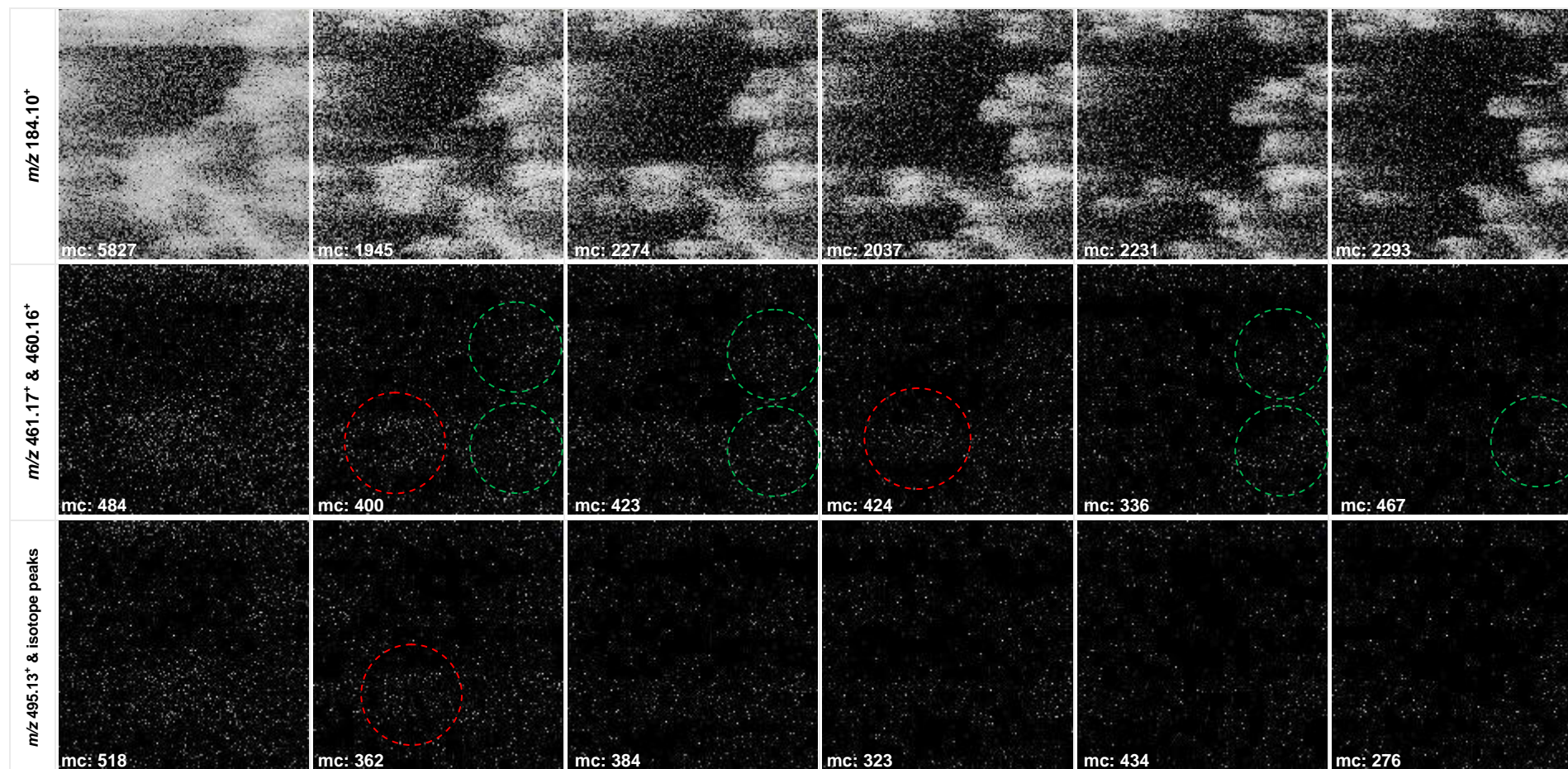


Fig. 4.17 Depth profiling of B24 cells (NIH 3T3 BXB-ER cells, 400 nM MitoTracker Red CMXRos label & β -Estradiol treatment for 2 h) in positive ion mode using J105 3D Chemical Imager. Profiles were acquired at six depths using 500 nm-focused 40 keV C_{60}^+ PI beam at a dose of 9.36×10^{14} ions/cm² of each depth over $128 \times 128 \mu m^2$ with 256×256 pixels and the total dose was 5.62×10^{14} ions/cm² within 6 depths. Images were generated using the Analyze software. The membrane is represented by m/z 184.10⁺ and 125.00⁺ from phosphocholine lipids, the nucleus by m/z 136.10⁺ from adenine, MitoTracker Red CMXRos is presented in two groups of peaks m/z 461.17⁺ with addition of m/z 460.16⁺ and m/z 495.13⁺ with its isotope peaks. Images were generated using the Analyze software. The distribution of the fluorescence dye is correspondingly within the cell body areas even in different cell depths.

As the distribution of fluorescence peaks reveals the location of mitochondria, the pixels containing dye ions are summed up for better understanding the lipids composition of mitochondria. As in Fig. 4.18, the most common fragments from phosphocholine lipids are observed at m/z 125.00⁺, 166.10⁺, 184.10⁺, 204.10⁺, 224.10⁺, 495. 13⁺ (refer to Table 3.3 for peaks assignment). The peak at m/z 384.18⁺ is not seen frequently in +SIMS spectrum of small cells. In the system studied, the activation of Raf kinase in NIH 3T3 BXB-ER causes the migration of the mitochondria and cardiolipin (CL) is exclusive to mitochondria inner membrane [46], it is postulated that m/z 384.18⁺ could be disassociated from CL as in Fig. 4.19. The fragment from the fatty acid chain and phosphate group with calculated mass of m/z 384.21⁺ is in good match with the peak m/z 384.18⁺ in Fig. 4.18. A number of studies provided evidences to support a direct relationship between CL losses or changes in CL molecular species and cytochrome *c* release as an initial step in the pathway to apoptosis [47, 48]. The CL standard from bovine heart was also analysed using the J105, but with the highly salted standard and the presence of abundant amounts of relatively short aliphatic chains in CL, the spectra did not show the characteristic peaks or the peak at m/z 384.18⁺. Since the way to trace the mitochondria has been established, a further study regarding the chemical composition will be carried in the future.

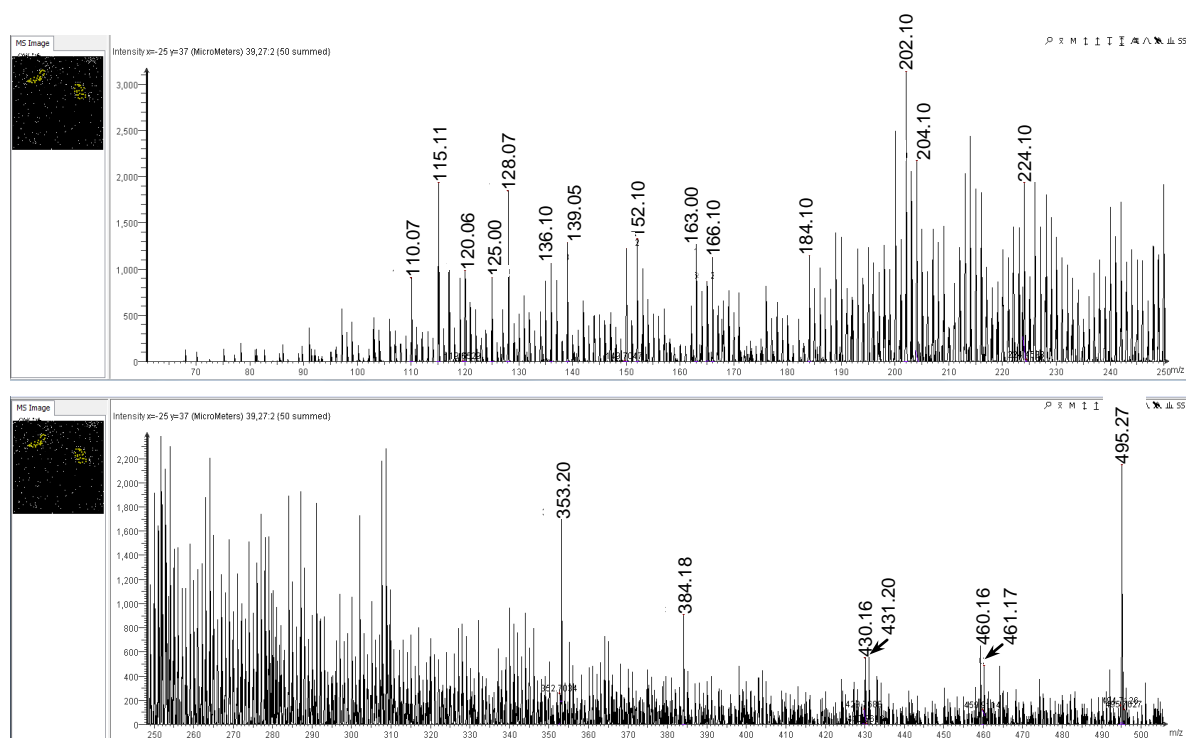


Fig. 4.18 The summed positive ion spectra from the pixels containing fluorescence dye ions. As expected, most fragments from phosphocholine lipids are observed, *e.g.*, m/z 125.00⁺, 166.10⁺, 184.10⁺, 204.10⁺, 224.10⁺, 495. 27⁺ (refer to Table 3.3 for the peaks assignment). It is likely that m/z 384.18⁺ could be a fragment of CL which is exclusive to mitochondria inner membrane.

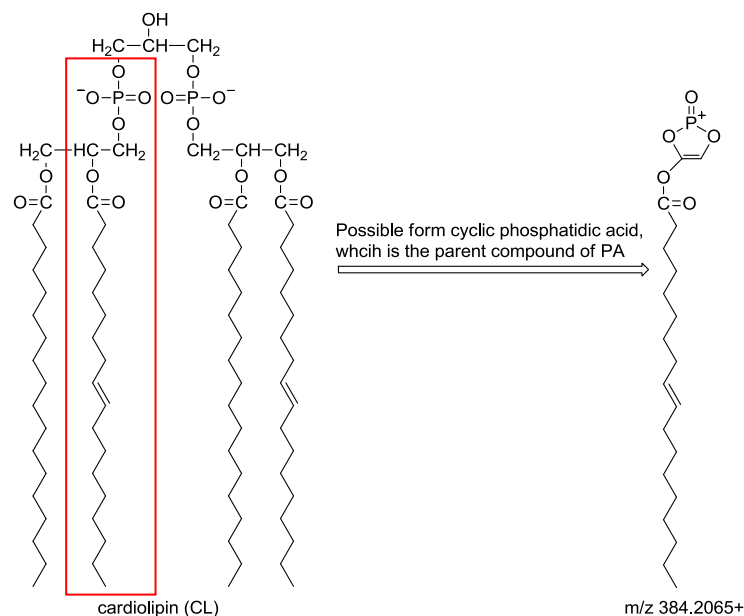


Fig. 4.19 Structure of cardiolipin (CL) and possible fragment by loss of fatty acid chain and phosphate.

4.4 Summary

In this study, a finely focused C_{60}^+ beam was employed for the first time to track subcellular organelle - mitochondria (0.5-10 μm) in fibroblast NIH 3T3 BXB-ER (human estrogen receptor fusion protein) cells following the activation of the Raf/ERK pathway using a novel dynamic ToF-SIMS instrument, the J105 3D Chemical Imager. Morphological changes following the addition of β -Estradiol were observed from even distribution of the cells membrane to a shifting towards the opposite sides of the nuclei in the +SIMS images. The combined confocal microscopy revealed the mitochondria migration and remodelling after the addition of β -Estradiol. The fluorescence probe were also tracked using SIMS to locate the mitochondria that showed the distribution patterns of gathering at the two sides of the nuclei in the +SIMS images, which was in good agreement with fluorescence images. Moreover, a possible cardiolipin fragment was found in +SIMS spectrum through summing the pixels from where the fluorescence probe is located. This is the first time ToF-SIMS has been used to track the exogenous fluorescence dye across small cells body three dimensionally. The three imaging modes, ToF-SIMS, confocal microscopy and ESEM employed sequentially show good agreement with morphological changes before and after Raf/ERK activation, demonstrating an integrated approaching for *in situ* study of the biological processes at subcellular dimension.

Reference

- [1] Lovric J., et al., *Activated Raf induces the hyperphosphorylation of stathmin and the reorganization of the microtubule network*. J. Biol. Chem., **273**(35): 22848-22855 (1998).
- [2] Fueller J., et al., *C-RAF activation promotes BAD poly-ubiquitylation and turn-over by the proteasome*. Biochem. Biophys. Res. Commun., **370**(4): 552-556 (2008).
- [3] Martin C., et al., *Changed genome heterochromatinization upon prolonged activation of the Raf/ERK signaling pathway*. PLoS ONE, **5**(10) (2010).
- [4] Kerkhoff E. and Rapp U. R., *Induction of cell proliferation in quiescent NIH 3T3 cells by oncogenic c-Raf-1*. Mol. Cell. Biol., **17**(5): 2576-2586 (1997).
- [5] Marais R., Wellbrock C., and Karasarides M., *The RAF proteins take centre stage*. Nature Reviews Molecular Cell Biology, **5**(11): 875-885 (2004).

- [6] Galmiche A., et al., *Isoform-specific interaction of C-RAF with mitochondria*. J. Biol. Chem., **283**(21): 14857-14866 (2008).
- [7] Kolch W., et al., *Raf-1 protein-kinase is required for growth of induced Nih/3t3 cells*. Nature, **349**(6308): 426-428 (1991).
- [8] Pelkmans L. and Zerial M., *Kinase-regulated quantal assemblies and kiss-and-run recycling of caveolae*. Nature, **436**(7047): 128-133 (2005).
- [9] Plowman S. J. and Hancock J. F., *Ras signaling from plasma membrane and endomembrane microdomains*. Biochim. Biophys. Acta, **1746**(3): 274-283 (2005).
- [10] Knauf J. A., et al., *Progression of BRAF-induced thyroid cancer is associated with epithelial-mesenchymal transition requiring concomitant MAP kinase and TGF β signaling*. Oncogene, **30**(28): 3153-3162 (2011).
- [11] Ouyang B., et al., *Inhibitors of Raf kinase activity block growth of thyroid cancer cells with RET/PTC or BRAF mutations in vitro and in vivo*. Clin. Cancer Res., **12**(6): 1785-1793 (2006).
- [12] Blain M. G., et al., *Secondary-ion yields from surfaces bombarded with keV molecular and cluster ions*. Phys. Rev. Lett., **63**(15): 1625-1628 (1989).
- [13] Mahoney J. F., et al., *Massive cluster impact mass spectrometry: a new desorption method for the analysis of large biomolecules*. Rapid Commun. Mass Spectrom., **5**(10): 441-445 (1991).
- [14] Benguerba M., et al., *Impact of slow gold clusters on various solids - Nonlinear effects in secondary ion emission*. Nucl. Instrum. Meth. B, **62**(1): 8-22 (1991).
- [15] Hand O. W., Majumdar T. K., and Cooks R. G., *Effects of primary ion polyatomicity and kinetic-energy on secondary ion yield and internal energy in SIMS*. Int. J. Mass Spectrom. Ion Processes, **97**(1): 35-45 (1990).
- [16] Kollmer F., *Cluster primary ion bombardment of organic materials*. Appl. Surf. Sci., **231**: 153-158 (2004).
- [17] Guerquin-Kern J. L., et al., *Ultra-structural cell distribution of the melanoma marker iodobenzamide: improved potentiality of SIMS imaging in life sciences*. Biomed. Eng. Online, **3**: 10 (2004).
- [18] Kleinfeld A. M., Kampf J. P., and Lechene C., *Transport of C-13-oleate in adipocytes measured using multi imaging mass Spectrometry*. J. Am. Soc. Mass. Spectrom., **15**(11): 1572-1580 (2004).
- [19] McMahon G., et al., *CN- secondary ions form by recombination as demonstrated using multi-isotope mass spectrometry of C-13- and N-15-labeled polyglycine*. J. Am. Soc. Mass. Spectrom., **17**(8): 1181-1187 (2006).
- [20] Romer W., et al., *Sub-cellular localisation of a N-15-labelled peptide vector using NanoSIMS imaging*. Appl. Surf. Sci., **252**(19): 6925-6930 (2006).
- [21] Champion C., et al., *Thyroid cell irradiation by radioiodines: a new Monte Carlo electron track-structure code*. Brazilian Archives of Biology and Technology, **50**: 135-144 (2007).
- [22] Elbast M., et al., *Kinetics of intracoloidal iodine in thyroid of iodine-deficient or equilibrated newborn rats. Direct imaging using secondary ion mass spectrometry*. Cell Mol Biol (Noisy-le-grand), **53 Suppl**: OL1018-1024 (2007).
- [23] Azari F., et al., *Intracellular precipitation of hydroxyapatite mineral and implications for pathologic calcification*. J. Struct. Biol., **162**(3): 468-479 (2008).
- [24] Elbast M., et al., *Kinetics of intracoloidal iodine within the thyroid of newborn rats. Direct imagery using secondary ion mass spectrometry*. C. R. Biol., **331**(1): 13-22 (2008).
- [25] Chandra S., *Subcellular imaging of RNA distribution and DNA replication in single mammalian cells with SIMS: the localization of heat shock induced RNA in relation to the distribution of intranuclear bound calcium*. J. Microsc., **232**(1): 27-35 (2008).
- [26] Quintana C., et al., *Morphological and chemical studies of pathological human and mice brain at the subcellular level: Correlation between light, electron, and NanoSIMS microscopies*. Microsc. Res. Tech., **70**(4): 281-295 (2007).
- [27] Lau K. H., et al., *Development of a new bimodal imaging methodology: a combination of fluorescence microscopy and high-resolution secondary ion mass spectrometry*. J. Microsc., **240**(1): 21-31(2010).
- [28] Breitenstein D., et al., *The chemical composition of animal cells reconstructed from 2D and 3D ToF-SIMS analysis*. Appl. Surf. Sci., **255**(4): 1249-1256 (2008).
- [29] Wegener J., et al., *The chemical composition of animal cells and their intracellular compartments reconstructed from 3D mass spectrometry*. Angewandte Chemie-International Edition, **46**(28): 5332-5335 (2007).
- [30] Nygren H., et al., *Bioimaging ToF-SIMS: High resolution 3D Imaging of single cells*. Microsc. Res. Tech., **70**(11): 969-974 (2007).

- [31] Szakal C., et al., *Compositional mapping of the surface and interior of mammalian cells at submicrometer resolution*. Anal. Chem., **83**(4): 1207-1213 (2011).
- [32] Lechene C., et al., *High-resolution quantitative imaging of mammalian and bacterial cells using stable isotope mass spectrometry*. J. Biol., **5**(6): 20 (2006).
- [33] Cheng J., et al., *Direct comparison of Au-3(+) and C-60(+) cluster projectiles in SIMS molecular depth profiling*. J. Am. Soc. Mass. Spectrom., **18**(3): 406-412 (2007).
- [34] Delcorte A., et al., *Sputtering of organic molecules by clusters, with focus on fullerenes*. Appl. Surf. Sci., **255**(4): 1229-1234 (2008).
- [35] Delcorte A., Poleunis C., and Bertrand P., *Stretching the limits of static SIMS with C-60(+)*. Appl. Surf. Sci., **252**(19): 6494-6497 (2006).
- [36] Fletcher J. S., et al., *ToF-SIMS analysis using C-60(+) effect of impact energy on yield and damage*. Anal. Chem., **78**(6): 1827-1831 (2006).
- [37] Fletcher J. S., Lockyer N. P., and Vickerman J. C., *C-60, buckminsterfullerene: its impact on biological ToF-SIMS analysis*. Surf. Interface Anal., **38**(11): 1393-1400 (2006).
- [38] Lockyer N. P., et al., *Development of a C-60(+) ion gun for static SIMS and chemical imaging*. Appl. Surf. Sci., **203**: 219-222 (2003).
- [39] Vickerman J. C., Fletcher J. S., and Lockyer N. P., *Developments in Molecular Sims Depth Profiling and 3d Imaging of Biological Systems Using Polyatomic Primary Ions*. Mass Spectrom. Rev., **30**(1): 142-174 (2011).
- [40] Vickerman J. C., et al., *Exploring subcellular imaging on the buncher-ToF J105 3D chemical imager*. Surf. Interface Anal., **43**(1-2): 380-384 (2011).
- [41] Marquez D. C., et al., *Estrogen receptors in membrane lipid rafts and signal transduction in breast cancer*. Mol. Cell. Endocrinol., **246**(1-2): 91-100 (2006).
- [42] *Molecular Probes Handbook, A guide to fluorescent probes and labeling technologies*. 11th ed, 2010, Invitrogen.
- [43] Zinser E. and Daum G., *Isolation and biochemical-characterization of organelles from the yeast, Saccharomyces-Cerevisiae*. Yeast, **11**(6): 493-536 (1995).
- [44] Nagley P., et al., *Chloromethyl-X-rosamine (MitoTracker Red) photosensitises mitochondria and induces apoptosis in intact human cells*. J. Cell Sci., **112**(14): 2419-2430 (1999).
- [45] Chen W. T., et al., *Development of cell surface linkage complexes in cultured fibroblasts*. J. Cell Biol., **100**(4): 1103-1114 (1985).
- [46] Pulfer M. and Murphy R. C., *Electrospray mass spectrometry of phospholipids*. Mass Spectrom. Rev., **22**(5): 332-364 (2003).
- [47] Cheng H., et al., *Shotgun lipidomics reveals the temporally dependent, highly diversified cardiolipin profile in the mammalian brain: temporally coordinated postnatal diversification of cardiolipin molecular species with neuronal remodeling*. Biochemistry (Mosc.), **47**(21): 5869-5880 (2008).
- [48] Chicco A. J. and Sparagna G. C., *Role of cardiolipin alterations in mitochondrial dysfunction and disease*. Am. J. Physiol. Cell Physiol., **292**(1): C33-44 (2007).

Chapter 5 Conclusion and future work

This study focused on two biological systems, *Xenopus laevis* (*X. laevis*) zygote/embryo and mouse embryonic fibroblast cells NIH 3T3 BXB-ER, to explore the capabilities of ToF-SIMS to image samples with extreme topography and subcellular organelles on the submicron scale three-dimensionally. Two ToF-SIMS instruments, BioToF-SIMS and the J105 3D Chemical Imager were employed for time course studies of dynamic biological processes (e.g., fertilisation, embryo through the early development stages and cells responding to Raf/ERK activation), gaining a new level of insight into the biomolecular arrangement and functions in the subcellular biological processes.

5.1 *Xenopus laevis* embryo

With *X. laevis* embryo, the multiple assay of lipids extraction from the zygotes identified major classes of lipids, including GPCho, GPEtn, GPGro, GPIns, GPSer, SM, cholesterol, ST, various fatty acyls, MAG, DAG and TAG using both instruments. The results were in good agreement with lipids assay of *X. laevis* oocytes using GC-MS instrument. Both SIMS instruments were capable of identifying the lipid species within a complex mixture, not only by molecular ions, but also through abundant diagnostic fragments. Moreover, the J105 showed the advantages over the BioToF-SIMS in detecting various fatty acyls, MAG, DAG and TAG species due to high mass resolution, which facilitated the identification of diverse lipid 'tails' and consequently the lipid structure.

The topography effects were assessed through imaging of *Xenopus* embryo, a spherical object approx. 1-1.2 mm in diameter. The secondary ion loss was most severe where the beam shadow effect occurs using both instruments and a decrease in secondary ion intensity also occurred at the edge of the sphere samples. However, both instruments turned out to be useful in imaging the spatial distributions of biomolecules and to detail features to interpret the morphological changes of the samples.

The lipid profiling of single intact *Xenopus* zygotes revealed different lipid components and concentrations on two poles, the animal and vegetal hemispheres. Cholesterol, MAG and DAG appeared on the animal side rather than the vegetal side, which was relevant to the dark appearance of the animal hemisphere as the embryonic pigment required intimate mixing with cholesterol and DAG. While the vegetal side showed higher intensity of phosphocholine lipids.

To monitor the fertilisation and early embryo development, high resolution imaging and depth profiling were performed on single intact zygote/embryo sampled at different time points after the fertilisation. The egg-sperm fusion sites were visualised on the animal hemisphere of zygote 10 min post-insemination that revealed varying spatial distributions of several biomolecules and the possible lipids rearrangement during the gametes fusion, i.e., in the centre of the fusion site phospholipase-mediated hydrolysis of SM generated DAG which were consumed swiftly to synthesize new lipids such as GPEtn and GPCho to stop the dissolving of the membrane caused by the sperm binding. Further monitoring of the embryonic development showed the different lipid arrangements in response to biological processes on the animal hemisphere of the embryo at different cleavage stages. Phosphocholine lipids and SM are the main building blocks of the

blastomeres junction area, suggesting the tightly packing organisation of SM might have a role in bearing the pressure from surrounding blastomeres.

The IP3 signalling upon the fertilisation was also studied by depth profiling single cell or imaging serial sections of the zygote 10 min post-insemination. The relative intensities of IP3 and calcium increase quickly after a certain sputtering ion dose most likely demonstrating the signalling molecules beneath the membrane. Moreover, the IP3 signals concentration was general higher in the sections from animal side than vegetal side, which was consistent with the fact that the IP3 diffuses from the sperm entry site in the animal hemisphere and across the whole egg.

The study of *Xenopus* embryo has proved that the custom-built instruments in our lab are capable of measuring real world biological samples. For the first time the developing embryos can be imaged almost intact with minimum sample preparation and without considering the embryonic pigment effect as encountered in the microscopic approach using ToF-SIMS. It is hoped that this study will serve as a starting point to explore the mechanism of biological processes as the spatial distribution of functioning lipids in single cells on the micron and submicron scale that cannot be imaged using methods other than ToF-SIMS.

5.2 Murine embryonic fibroblasts

The study of the fibroblast NIH 3T3 BXB-ER cell line firstly adopted a finely focused C_{60}^{+} beam to monitor subcellular mitochondria (0.5-2 μm) in relation to the activation of the Raf/ERK pathway using the J105 3D Chemical Imager. Morphological changes following the addition of β -estradiol were tracked through +SIMS imaging the distribution of representative membrane ions or fluorescence probe of mitochondria, which revealed that the cells membrane rearranged from evenly spreading to uneven distribution at two sides of the nuclei and subcellular mitochondria located by the fluorophore ions showed the distribution pattern of gathering in the two sides of the nuclei. Parallel fluorescence images revealed the mitochondria migration and remodelling of condensing to the nuclei closely after the estrogen treatment. The three imaging modes, ToF-SIMS, confocal microscopy and ESEM, employed sequentially were in good agreement with regard to morphological changes and subcellular mitochondria rearrangement following or without the estrogen treatment, demonstrating an integrated approaching for the study of biological processes at subcellular dimensions.

As a preliminary study, 3D ToF-SIMS imaging has proved to be effective to investigate the cellular processes involved in biomolecular rearrangement and for tracing the xenobiotic fluorophors to confirm the lipids taking part in the processes. The developed methodology has promise to locate natural components and exogenetic markers in complex biological systems to aid the understanding of the mechanism of biological processes (e.g., disease progression) and drug development.

5.3 Future work

5.3.1 Fundamental questions

The new generation J105 3D Chemical Imager is designed to fully exploit the advantages of polyatomic ion beams for molecular depth profiling and imaging on the submicron scale. The

studies of various biological specimens have provided unprecedented insights into chemical gradients and related functions during the biological processes. Nevertheless, there are still fundamental questions regarding the SIMS technique worthy of further investigation.

One important issue is that the sputtering rates are not universally equal for all the components in biological samples. This further complicates the image interpretation and data evaluating of depth profiling. For example, experimentally a flux of C_{60}^+ at a dose of 10^{15} ions/cm² could sputter away the freeze-dried cells with a depth of approx. 4 μ m, but the same dose cannot go through the *Xenopus* embryo membrane. Of course, other factors such as topography and membrane structure that could also tribute to the different sputtering rates. There are studies of sputtering carried out on established model systems mentioned in section 1.2.2.2.2 but with very limited components (two or several) in the systems. Therefore, the assessment of sputtering event on real biological model is necessary. The membrane of *Xenopus* embryo could be an appropriate model. It has relatively large area and known lipid components, and technically it can be isolated as a flat sheet mounted onto a substrate. The depth profiling of the membrane using ToF-SIMS can be combined with atomic force microscopy or white light microscopy that are used to measure the surface morphology change. Coupled with SIMS data, it is possible to evaluate the sputter rates of complex biological membrane and potential beam damage of underlayers. The isolated membrane can also be freeze-fractured for comparison with the depth profiling data to reveal whether the secondary ion signal at different depth reflects the true gradients of biomolecular distribution or the sputtering artefacts.

Another issue of the relatively low ionisation efficiency is deep-rooted in SIMS and other desorption based MS methods. As pointed out by Fletcher and Vickerman [1], a method of globally increasing ionisation of secondary species is the current 'holy grail' in ToF-SIMS development. Associated with low ionisation efficiency, the low yield of molecular ions and high fragmentation in the SIMS spectrum also pose problem on molecular analysis in complex mixture. Thus the question is whether the low ionisation efficiency or high impinging energy of primary ion beam destroys the molecules resulting in the low intensities of secondary ions, particularly molecular ions. Many lipids in the membrane bilayer are already in different ionization states attributed to the interactive or repulsive forces between the head groups in the bilayer [2]. Moreover, according to the experiment of imaging *Xenopus* embryo the primary ion beam with different incident angle was found to favour the different secondary ions. Thus, one practical solution for improved molecular imaging is to optimise the actual bombardment energy of the primary ion beam which requires further adjustment of related parameters, e.g., operation voltage, incident angle of the primary ion beam and intensity of primary ion flux. Or the sample could be analysed in the presence of water/ice which has been proved to enhance ionization through proton transfer [1, 3].

Furthermore, there are other issues related to instrument operation, e.g., cleaning contamination in vacuum and convenient sample mounting methods, need to be addressed as well.

5.3.2 Further biological applications

The new concept ToF-SIMS has been proved to be capable of imaging the biological samples in 2D or 3D with submicron lateral resolution and high chemical sensitivity, offering numerous opportunities to address questions in life sciences.

The work of tracing IP3 signalling has shown the high sensitivity of ToF-SIMS in imaging subcellular signalling. The methodology can be transferred to trace other signalling molecules in *Xenopus* embryo, possibly vitamin A and thyroid hormone. Retinoid, a bioactive form of vitamin A, plays an important role in embryo development, such as regulating homeobox genes, maintaining normal development, triggering of tadpole head and tail growth [4, 5], but its distribution in embryo at early stages remains mystery. Along with thyroid hormone, which induces the complete metamorphosis in vertebrates, its existence and synthesis are still unclear. It has been postulated that the hormone exists in the very early frog embryos possibly eggs [6]. The insufficient sensitivity of current SIMS data might be not enough to confirm or locate vitamin A, however, with the great potential of ToF-SIMS, imaging these chemicals in single cell or series sections is potential direction for the future work. The cell sectioning technique used in the study can be improved by using water as embedding matrix and flash-freezing the sample block in liquid nitrogen, in doing so the effect of smearing matrix can be minimized.

Principal component analysis (PCA) is a powerful tool to uncover variations in large data sets. Coupled with ToF-SIMS, it is promising to study the variation between different embryo stages to reveal the possible driving force for the embryogenesis and possibly to locate the variation ions on the surface and in the depths of the embryos. More importantly, the variations can be narrowed down to lipids, which fall into the mass range of ToF-SIMS analysis. It has been suggested that glycolipids play a pivotal role in embryogenesis. Additionally, sphingolipids have emerged as potential regulatory molecules in signal transducting pathways of cell growth [7]. The study of lipids expression during early development of *Xenopus* has also revealed the sharp increase of glycolipids and glycoproteic sialic acid during the first six days using high performance thin layer chromatography (HPTLC) [8]. The preliminary study on PCA analysis of *Xenopus* embryos in 2 cells, 4 cells and 16 cells stages is shown in Fig. 5.1. The PC2 loading demonstrates the distinct distribution patterns on the hemisphere of different embryos that involves major chemical differences such as fatty acyl, DAG and some lipid headgroups. However, to locate lipid variations among different cleavage stages one needs to conduct parallel experiments in each stage under stable conditions not yet reached by the current ToF-SIMS instrumentation, and requires developing methods to process the huge data sets in the future.

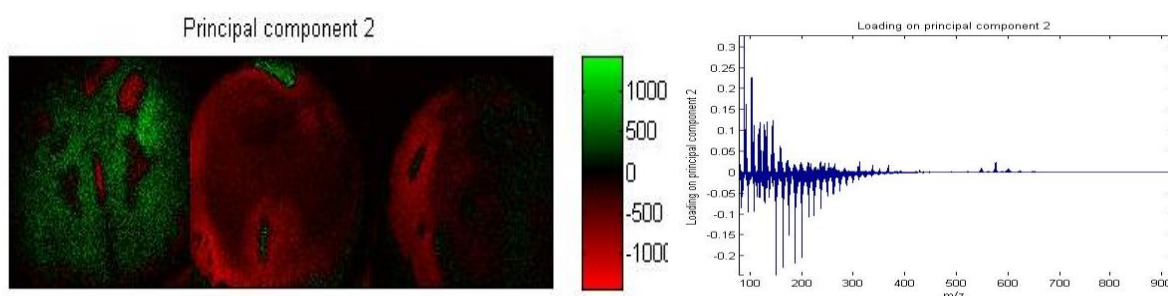


Fig. 5.1 PCA analysis of *Xenopus laevis* embryos in 2 cells, 4 cells and 16 cells stages.

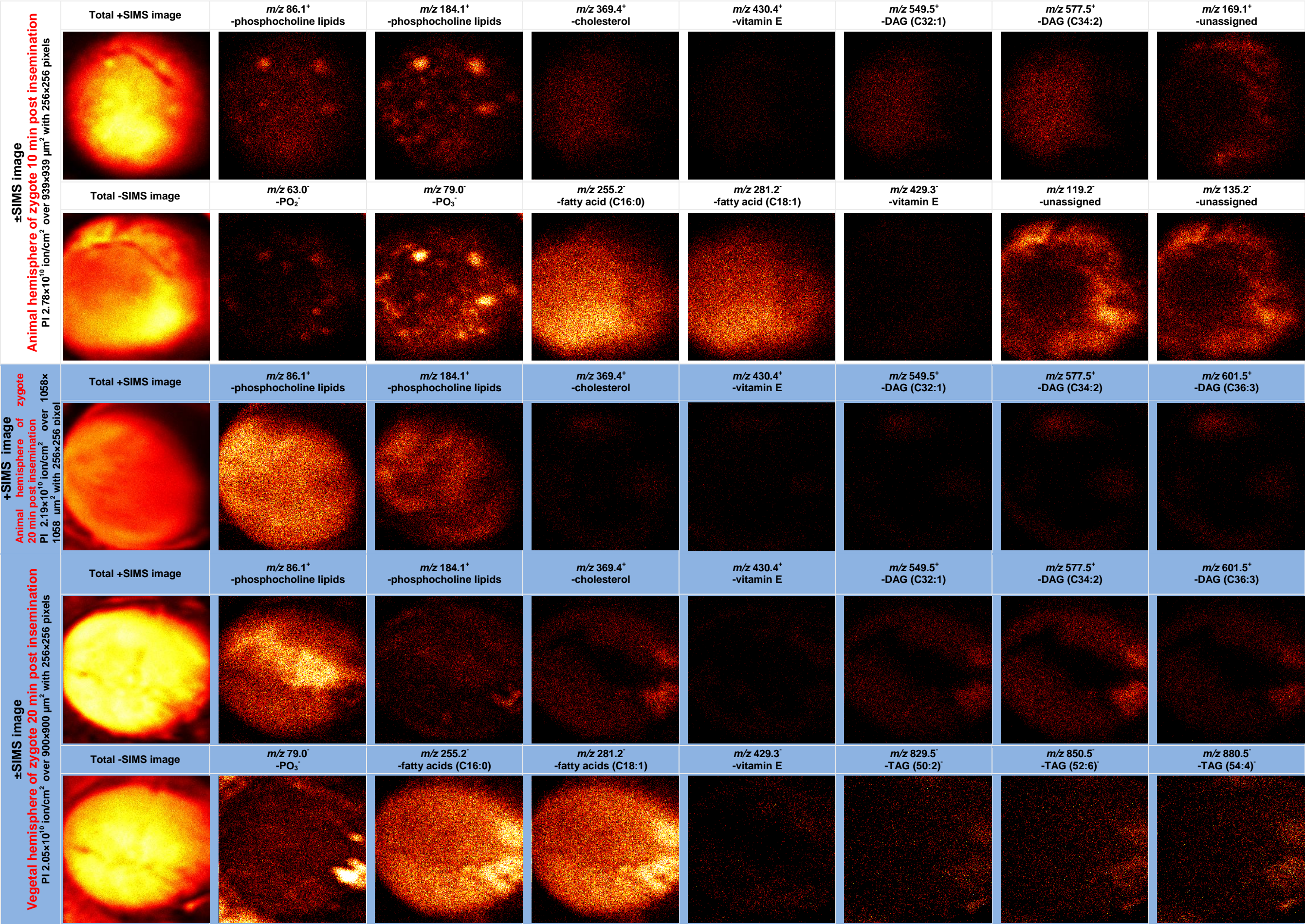
Useful submicron scale imaging using ToF-SIMS has been successfully applied to trace the xenobiotic fluorophors in fibroblast cells. This methodology can be developed to imaging the nuclear tags of the fibroblast cells to understand DNA synthesis and binding, as well as chemical changes upon apoptosis

In summary, imaging ToF-SIMS has entered a new analysis era with 2D imaging and molecular depth profiling on submicron scale, offering promising opportunities to expand its impact to biological studies for answering some burning biological questions.

References

- [1] Fletcher J. S., Vickerman J. C., and Winograd N., *Label free biochemical 2D and 3D imaging using secondary ion mass spectrometry*. Curr. Opin. Chem. Biol., **15**(5): 733-740 (2011).
- [2] Boggs J. M., *Effect of lipid structural modifications on their intermolecular hydrogen-bonding interactions and membrane functions*. Biochem. Cell Biol., **64**(1): 50-57 (1986).
- [3] Cliff B., et al., *Probing cell chemistry with time-of-flight secondary ion mass spectrometry: development and exploitation of instrumentation for studies of frozen-hydrated biological material*. Rapid Commun. Mass Spectrom., **17**(19): 2163-2167 (2003).
- [4] Mohn D., et al., *Mouse mix gene is activated early during differentiation of ES and F9 stem cells and induces endoderm in frog embryos*. Dev. Dyn., **226**(3): 446-459 (2003).
- [5] Ross S. A., et al., *Retinoids in embryonal development*. Physiol. Rev., **80**(3): 1021-1054 (2000).
- [6] Furlow J. D. and Neff E. S., *A developmental switch induced by thyroid hormone: Xenopus laevis metamorphosis*. Trends Endocrin. Met., **17**(2): 38-45 (2006).
- [7] Hannun Y. A. and Bell R. M., *Functions of sphingolipids and sphingolipid breakdown products in cellular-regulation*. Science, **243**(4890): 500-507 (1989).
- [8] Gornati R., et al., *Glycolipid patterns during xenopus embryo development*. Cell Biol. Int., **19**(3): 183-190 (1995).

Appendix I



<div> <div>±SIMS image</div> <div>Animal hemisphere of zygote 30 min post insemination</div> <div>PI 2.19x10¹⁰ ion/cm² over 1058x1058 μm² with 256x256 pixels</div> </div>	Total +SIMS image	<i>m/z</i> 86.1 ⁺ -phosphocholine lipids	<i>m/z</i> 184.1 ⁺ -phosphocholine lipids	<i>m/z</i> 369.4 ⁺ -cholesterol	<i>m/z</i> 430.4 ⁺ -vitamin E	<i>m/z</i> 549.5 ⁺ -DAG (C32:1)	<i>m/z</i> 577.5 ⁺ -DAG (C34:2)	<i>m/z</i> 601.5 ⁺ -DAG (C36:3)
	Total -SIMS image	<i>m/z</i> 63.0 ⁻ -PO ₂ ⁻	<i>m/z</i> 79.0 ⁻ -PO ₃ ⁻	<i>m/z</i> 255.2 ⁻ -fatty acid (C16:0)	<i>m/z</i> 281.2 ⁻ -fatty acid (C18:1)	<i>m/z</i> 429.3 ⁻ -vitamin E	<i>m/z</i> 887.4 ⁻ -sulfatide(C24:1)	
<div> <div>+SIMS image</div> <div>Vegetal hemisphere of zygote 30 min post insemination</div> <div>PI 2.19x10¹⁰ ion/cm² over 1058x1058 μm² with 256x256 pixels</div> </div>	Total +SIMS image	<i>m/z</i> 86.1 ⁺ -phosphocholine lipids	<i>m/z</i> 184.1 ⁺ -phosphocholine lipids	<i>m/z</i> 369.4 ⁺ -cholesterol	<i>m/z</i> 430.4 ⁺ -vitamin E	<i>m/z</i> 549.5 ⁺ -DAG (C32:1)	<i>m/z</i> 577.5 ⁺ -DAG (C34:2)	<i>m/z</i> 601.5 ⁺ -DAG (C36:3)
<div> <div>±SIMS image</div> <div>Animal hemisphere of zygote 40 min post insemination</div> <div>PI 1.61x10¹⁰ ion/cm² over 1027x1027 μm² with 256x256 pixels</div> </div>	Total +SIMS image	<i>m/z</i> 86.1 ⁺ -phosphocholine lipids	<i>m/z</i> 184.1 ⁺ -phosphocholine lipids	<i>m/z</i> 369.4 ⁺ -cholesterol	<i>m/z</i> 460.2 ⁺ -unassigned	<i>m/z</i> 549.5 ⁺ -DAG (C32:1)	<i>m/z</i> 577.5 ⁺ -DAG (C34:2)	<i>m/z</i> 595.5 ⁺ -DAG (C36:6)
	Total -SIMS image	<i>m/z</i> 63.0 ⁻ -PO ₂ ⁻	<i>m/z</i> 79.0 ⁻ -PO ₃ ⁻	<i>m/z</i> 253.2 ⁻ -fatty acid (C16:1)	<i>m/z</i> 255.2 ⁻ -fatty acid (C16:0)	<i>m/z</i> 279.2 ⁻ -fatty acid (C18:2)	<i>m/z</i> 281.2 ⁻ -fatty acid (C18:1)	<i>m/z</i> 459.2 ⁻ -unassigned

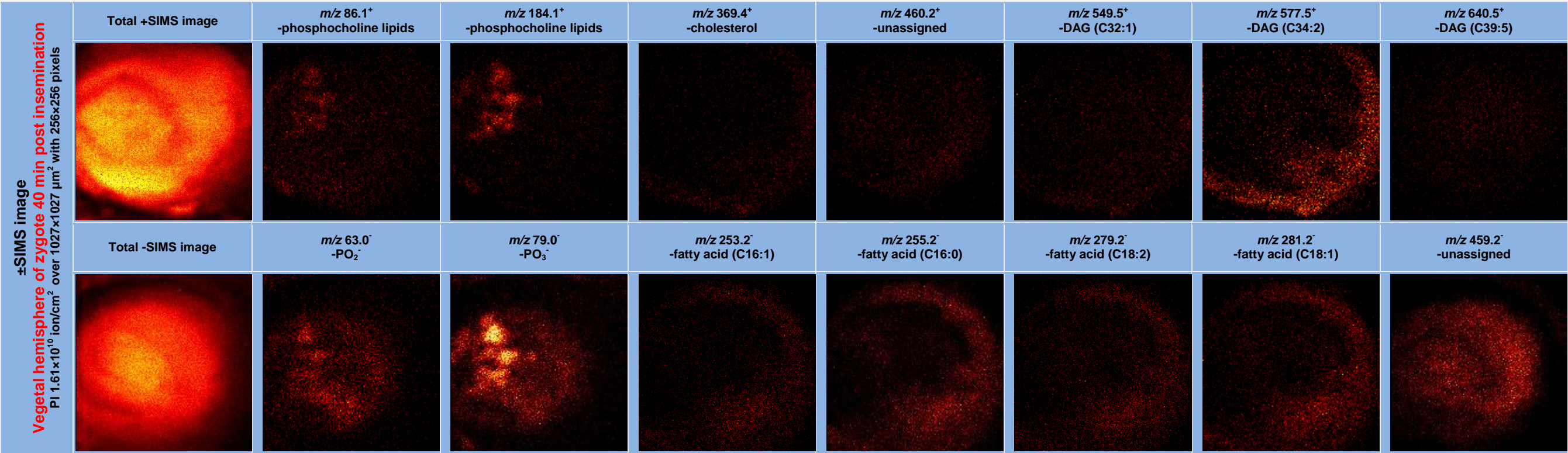


Fig. I.1 Biomolecular distributions on the animal and vegetal hemisphere of *Xenopus laevis* (*X. laevis*) zygotes 10, 20, 30 and 40 min post-insemination. The samples were analysed using BioToF-SIMS equipped with 20 kV C₆₀ PI gun. The total ion and selected SI images in positive and negative mode were generated. At least 5 zygotes at each time point were investigated to identify any common phenomenon on the egg animal hemisphere shortly after the fertilisation. At 10 min after fertilisation, most zygotes show the scattered spots on the animal hemisphere. Within the spots area, the most abundant SIs are *m/z* 86.1⁺, 104.1⁺, 125.0⁺, 166.1⁺, 184.1⁺ in +SIMS and *m/z* 63.0⁻, 78.9⁻ in -SIMS, indicating that mainly glycerophosphocholine (GPCCho) and sphingomyelin (SM) lipids are located within the spots. The sizes of the spots calculated by counting the pixels across the spots are approximately 30-53 μm, bigger than those in Fig. 3.21. The cholesterol, monoacylglycerol (MAG) and diacylglycerol (DAG) spread homogenously in most surface area; at 20min, no congregated lipids dots appear on the animal pole, and GPCCho lipids have a complementary distribution with cholesterol, MAG and DAG, usually the latter three biomolecules share the same location on the zygote surface. After 30 min of addition of sperms, the lipids peaks at *m/z* 86.1⁺, 104.1⁺, 125.0⁺, 166.1⁺, 184.1⁺ are absent in certain round areas on the animal hemisphere, where the cholesterol appears intense. The following 40 min zygote has some small dots residing by GPCCho lipids on the surface, and the other biomolecules distribute evenly.

This interesting lipids organisation on the zygote 10 min after fertilisation could be the egg-sperm fusion sites and the size differences is due to the progress of the fertilisation. The smaller dots on animal hemisphere of the zygote 10 min after fertilisation in Fig. 3.21 could be very early sperm-egg incorporation, in which sperms just binding to the animal hemisphere. In the following the gametes membrane fusion happens with more adjacent area involved in, thus the bigger patches appears as on the zygote animal side sampled 10 min after fertilisation in Fig I.1. Although all samples were fixed at the same time point 10 min after the addition of the sperms, the individual variation could cause the biological progress varying in speed. The observations of fertilisation in *X. laevis* using light microscopy and SEM has revealed even within the same batch of eggs the fertilisation still occurs variably in the timing significantly [1]. Although there is report about using electron scanning microscopy to study the morphological change on surface of *X. laevis* egg shortly after the fertilisation, no mentions were made of any structure which could indicate the sperm entry and fusion site [2]. Study of fertilisation of egg of another frog species, *Rana pipiens*, revealed that the sperm entry site changed from a small, microvilli-free structure at 20 min after insemination to a clump of elongated microvilli at 40 min, then to a distinct patch of microvilli by 2 h. At 40 min, the site was found in a circular depression which was due to the sperm aster and which expanded to a rigid area in the animal half [3]. The SEM images reproduced in Fig. 3.3 and Fig. 3.4, which show the similarities with the SIMS images in Fig. I.1. For examples, the circular spots on the membrane of the zygote fixed 10 min after fertilisation in Fig. 3.4 (a) are about 20-40 μm close to the those on the zygote fixed 10 min after insemination in SIMS images in Fig. I.1; the zygote fixed 40 min after the fertilisation has a circular depression on the membrane as in Fig. 3.3 (c) which similar to the lipids absence area on animal hemisphere of the zygote fixed 40 min after insemination. The zygotes fixed 20 min after the insemination in Fig. 3.3 (b) are not resemble to the one in Fig. I.1, this could be caused by the variability of the biosamples and unsynchronized biological process. ToF-SIMS analysis combined with the time course samples offers an opportunity to investigate the dynamic biological process, which surely would contribute to the developmental biological in terms of identification the important biomolecules that could play important roles in the biological events.

Reference

- [1] Boyle J. A., Chen H., and Bamburg J. R., *Sperm incorporation in Xenopus laevis: characterisation of morphological events and the role of microfilaments*. Zygote, **9**(2): 167-181 (2001).
- [2] Monroy A. and Baccetti B., *Morphological changes of the surface of the egg of Xenopus laevis in the course of development. I. Fertilization and early cleavage*. J. Ultrastruct. Res., **50**(2): 131-142 (1975).
- [3] Elinson R. P. and Manes M. E., *Morphology of the site of sperm entry on the frog egg*. Dev. Biol., **63**(1): 67-75 (1978).

Appendix II

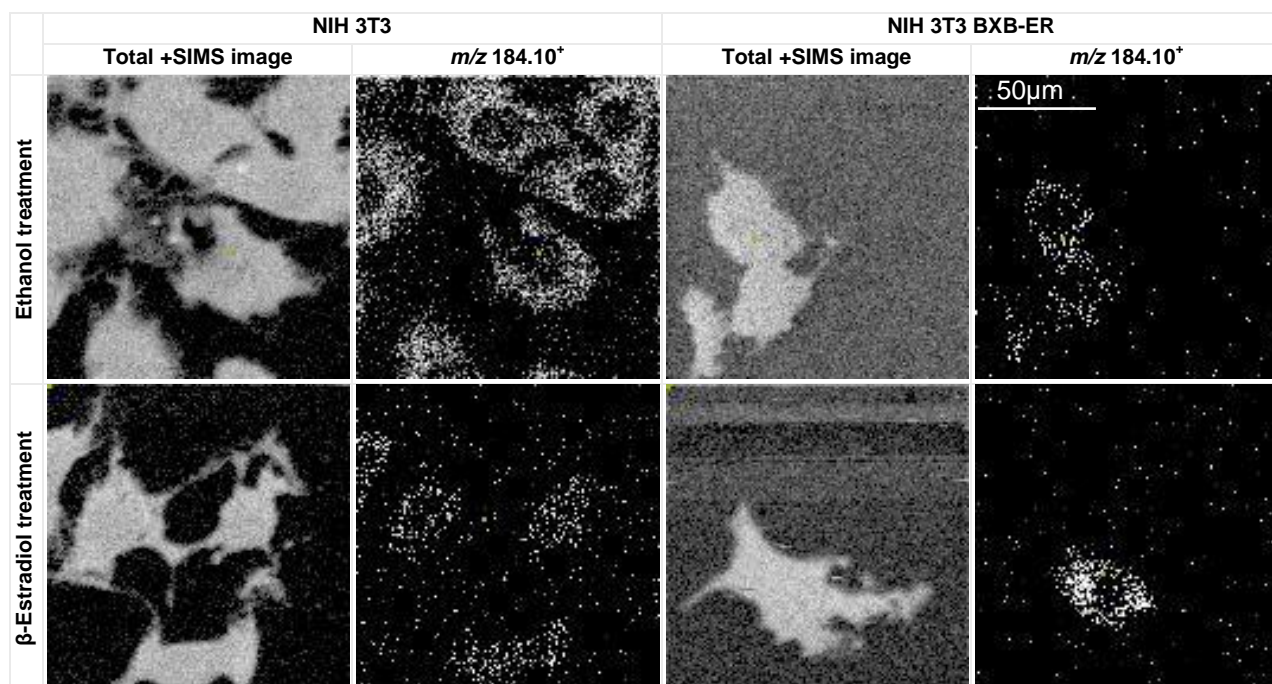


Fig. II.1 Morphological change of NIH 3T3 and NIH 3T3 BXB-ER cells reacting to Raf/ERK activation. The imaging was acquired using 40 keV C_{60}^+ PI beam focused at 1 μm . The spectral dose is 4.68×10^{13} ions/cm² of each depth over $128 \times 128 \mu m^2$ with 128×128 pixels. The estrogen treatment has more influence on distribution of m/z 184.10⁺ in NIH 3T3 BXB-ER cells. The filopodia of the cells are clearly seen, implying the C_{60}^+ ion beam size is equal or less than 1 μm .